8-2008

The Effects of Nanoparticle Inclusions upon the Microstructure and Thermoelectric Transport Properties of Bismuth Telluride-Based Composites

Nick Gothard
Clemson University, gothard@clemson.edu

THE EFFECTS OF NANOPARTICLE INCLUSIONS UPON THE MICROSTRUCTURE AND THERMOELECTRIC TRANSPORT PROPERTIES OF BISMUTH TELLURIDE-BASED COMPOSITES

A Dissertation
Presented to
the Graduate School of
Clemson University

In Partial Fulfillment
of the Requirements for the Degree
Doctor of Philosophy
Physics

---

by
Nicholas Wesley Gothard
August 2008

Dr. Terry M. Tritt, Committee Chair
Dr. Apparao M. Rao
Dr. Chad E. Sosolik
Dr. Catalina D. Marinescu

ABSTRACT

Research into materials that have high efficiencies of thermoelectric heat-energy conversion has been at a plateau since the middle of the last century. During this time, efficiencies have been engineered high enough for several interesting niche applications but not high enough for widespread adaptation into traditional power generation or refrigeration technologies. The past decade has seen considerable advancement, as a number of theoretical works have suggested that lower dimensional structures could hold the key for enhanced efficiency, and several experiments have provided the proof of principle needed to inspire just such a research direction. The benefit of low dimensional structures for thermoelectric efficiency comes from both the potential enhancement of the electronic properties due to quantum confinement effects as well as from the potential for increased scattering of heat-carrying phonons. Widespread application of these principles for technological application requires the creation of composites of nanostructures that can be manufactured easily with dimensions on the bulk materials scale. A good starting point for such materials research is to manufacture composites of materials that are currently known to have high thermoelectric efficiencies by incorporating nanostructures into a bulk matrix.

The goal of this project is to create nanocomposites using bismuth telluride, a compound known to have one of the highest thermoelectric efficiencies at room temperature, as a matrix material. Various methods of synthesizing sufficient quantities of bismuth telluride nanostructures were attempted, including pulsed laser vaporization, chemical vapor deposition, and solvothermal synthesis. The method of solvothermal

synthesis was found to be the simplest approach for producing high yields of bismuth telluride nanostructures. In the initial stages of the project, cold pressing was tested as a means of compaction, but in the end a uniaxial hot pressing technique was adopted in order to consolidate the nanostructures into the bulk matrix.

Nanocomposites were produced using both n-type and p-type bismuth telluride compounds as the matrix material, into which nanostructures of Bi_2Te_3, BiSb, Bi_2S_3, as well as Au and Ag nanoparticles and C_{60} were incorporated. The preferred consolidation technique utilized a 3-axis mechanical mixer, followed first by cold and then hot pressing of the bulk-nano mixtures. The composites were studied with respect to their microstructure and elemental composition, as well as with regard to their thermal and electrical transport properties. The effects of the nanoparticle additions upon the efficiencies of the materials are presented, and the viability of improving the thermoelectric performance of this class of materials by this method is considered.

ACKNOWLEDGEMENTS

First, I thank God for the talents He has bestowed upon me.

Thanks also go to my parents, who have given me counsel and an understanding ear throughout the years. I know that you have always had my best interests in mind, and your support has meant worlds to me.

My wife, Sarah, has listened with patience and understanding in all my darkest hours and has always been there to help me, and I owe her a special debt of gratitude.

I would be remiss not to thank my advisor, Dr. Terry Tritt, for all his help throughout the many stages of this project. In addition to his help in working on the project, his door has always been open and he has been there to encourage and lend perspective along the way.

Especial thanks to Dr. Jian He, who has given very generously of his time to discuss various aspects of this project, and to Dr. Xiaohua Ji for assisting in the solvothermal synthesis of nanoparticles.

I appreciate the help given by Dr. Nathan Lowhorn, especially in the early stages of the project. Thank you for taking the time to show me the ropes of transport measurements and for being a good sounding board throughout my time at Clemson.

Special thanks to all of the group members of the Complex and Advanced Materials Laboratory, who have been a good team to work with. This is a very special group and I am grateful to have been a part of it.

I appreciate the assistance provided by the staff of the Physics Machine Shop, who have been a great help to me by assisting with parts manufacture, without which this project would have been impossible.

Finally, I acknowledge financial support from a DOE Implementation Grant (DE-FG02-04ER-46139) as well as support from the SC EPSCoR Office / Clemson University cost sharing.

TABLE OF CONTENTS

Page

LIST OF FIGURES

Figure Page

LIST OF TABLES

INTRODUCTION

The field of thermoelectrics is concerned with how and with what degree of efficiency solid state materials convert heat to electricity or electricity to heat. All solid state materials exhibit thermoelectric phenomena to some extent, but a good thermoelectric material is defined by having a high degree of efficiency for heat-electricity conversion. Often, such high thermoelectric efficiency materials are referred to simply as "thermoelectric materials." For decades, the area of thermoelectric materials research has focused on improving the efficiencies of the best thermoelectric materials. At the time of this writing, thermoelectric materials operate at efficiencies sufficient for application in several niche applications, but they have yet to be engineered to efficiencies high enough for widespread application.

One of the most promising thermoelectric materials for near room temperature applications is bismuth telluride, stoichiometrically Bi_2Te_3 in its undoped form. Bi_2Te_3 derives its promising thermoelectric performance from a combination of low thermal conductivity (~1.5 W/m-K at 300 K) and a large Seebeck coefficient (~200 μV/K at 300 K). The thermoelectric properties of Bi_2Te_3 were brought to near optimization nearly 40 years ago, and since that time only marginal improvements have been made. Recently, however, it has been suggested that lower dimensional morphologies show promise for further improving the performance of thermoelectric materials. It is the purpose of this work to apply such a concept to the bismuth telluride system in an attempt to further improve the efficiency of this material.

Introduction to Thermoelectrics

Historical Development

Within the past two centuries, the field of thermoelectrics has undergone three main periods of intense research activity. The first of these periods began in 1821 with the discovery by T. J. Seebeck of the effect that bears his name, which describes how a temperature gradient between two dissimilar materials results in a voltage difference across the junction between them [1]. This discovery initiated a period of research that lasted roughly 30 years, during which other notable contributions were made, such as the discovery by J.C. Peltier in 1834 [2] of the heat lost or gained due to electrical current at the interfaces of dissimilar materials, and the effect predicted by W. Thompson, a.k.a. Lord Kelvin, in 1851, which mathematically relates the Seebeck and Peltier effects to each other [3]. These effects are described in more detail in the following section.

Following the development of the novel theories of quantum mechanics that began to be introduced at the turn of the 20^{th} century, a period of investigation into the physical properties of condensed matter materials on the microscopic and atomic levels began. This period of research, beginning in the 1920's and lasting until the 1960's, saw the development of much of modern solid state physics theory, including the introduction by Ioffe of both the concept of a semiconductor and of a parameter that later became known as the thermoelectric figure of merit, a parameter that could be used to gauge the quality of a material with respect to potential thermoelectric device applications [4]. It was during this time that thermoelectrics research became centered primarily upon semiconducting materials, with materials such as bismuth telluride being found to have

the most favorable thermoelectric properties [5]. During the period of intense semiconductor materials research that occurred during the 1950's and 60's, much of the work of optimization via tuning of the electronic properties was completed in bulk thermoelectric materials, and, in fact, many of the materials discovered and developed during that period have undergone scant additional optimization in the years since.

The final era of focused thermoelectric materials research began in the 1990's with the introduction of the "phonon glass / electron crystal" (PGEC) concept, a concept that emphasizes first maximizing a material's electronic properties and subsequently attempting to inhibit thermal conduction while leaving the electronic properties largely unmolested [6]. Concurrent with this approach, theoretical models predicted that enhancement of thermoelectric properties in low dimensional materials could occur due primarily to quantum confinement effects [7]. With the successful manufacture of thin-film superlattices [8], researchers began to see just how promising the realm of low dimensions could be for enhancing the properties of thermoelectric materials.

Thermoelectric Properties

The Seebeck effect, or thermopower, α, describes the establishment of a voltage gradient across a material in response to a temperature gradient (figure 1):

$$\alpha_{ab} \equiv \frac{dV}{dT}, \tag{1.1}$$

where α_{ab} is the relative thermopower across the junction of the materials. Intuitively, the establishment of a temperature gradient implies a higher concentration of charge carriers at the cold end of the sample, which in turn corresponds to the establishment of a voltage differential across the sample. As a corollary, the sign of the Seebeck coefficient is

typically negative for n-type electrical conduction, where electrons are the primary charge carriers, and positive for p-type conduction, where holes are the majority carriers, although there are a few exceptions.

Second, the Peltier effect describes the heat lost or absorbed at the junction between two dissimilar materials. The Peltier coefficient, Π, is expressed as:

$$\Pi_{ab} \equiv \frac{1}{I}\frac{dQ}{dt}, \tag{1.2}$$

where dQ/dt is the rate of heat transfer at the junction, and I is the electrical current (figure 2). The dependence of the Peltier effect upon the current suggests a greater degree of control over the performance of a thermoelectric device than does the Seebeck effect, which simply gauges the propensity of a material for establishing a voltage gradient in response to a temperature gradient, or vice versa.

Finally, the Thompson effect describes the radiation or absorption of heat energy from a material that has both temperature and voltage gradients. The Thompson effect states that in the absence of Joule heating, the heat gained or lost is given by

$$\frac{dQ}{ds} = \tau I \frac{dT}{ds}, \tag{1.3}$$

where s is a spatial coordinate, I is the electrical current, T is the temperature, Q is the heat, and τ is the Thompson coefficient. It should be noted that while the Seebeck and Peltier coefficients describe heat transfer in a system of two materials, the Thompson effect describes heat flow in a single material. From the Thompson effect, it can be shown that

$$\tau_a - \tau_b = T \frac{d\alpha_{ab}}{dT}, \tag{1.4}$$

and consequently that

$$\Pi_{ab} = \alpha_{ab} T \text{ [9].} \tag{1.5}$$

Equation 1.5 is of particular use in providing a link between the thermopower, which is fairly easy to measure, and the Peltier coefficient, which is not.

Thermoelectric Modules

Thermoelectric phenomena in solid state materials can be employed to construct modules that function either as power generation or active refrigeration devices. In either case, a single thermoelectric module is constructed from many individual thermoelectric couples, each consisting of one leg of n-type material and one leg of p-type material, placed electrically in series but thermally in parallel (figure 3). In the power generation configuration, a temperature gradient across the module results in the establishment of a net voltage gradient, since the majority charge carriers in each segment drift towards the cold side of the device. Because electrons and holes move in opposite directions, the net effect is a current that can be used to power a resistive load. The case for active refrigeration is just the opposite. Here, an external voltage source is used to drive a current through the module. In the n-type segment, electrons are drawn towards the positive end of the voltage difference, carrying heat with them, while in the p-type segment, it is the holes that dominate transport and that are drawn to the negative end of the voltage differential, also transporting heat. The net effect is that in both segments of the module, heat is carried by the dominant charge carriers towards the lower end of the

module, resulting in the establishment of a temperature gradient which produces a heat sink on the exterior of the module that can then be used for localized cooling.

When constructing such modules, it is clear that one wants both n- and p-type materials that have high thermopower values, that is, materials that are able to produce substantial voltages in the presence of temperature gradients, and vice versa. Further, these materials must have the ability to sustain a temperature differential, a requirement which in turn implies the need for them to have low thermal conductivities. Finally, they must be reasonably good conductors of electricity. All of these factors are key to evaluating the merit of potential thermoelectric materials with respect to their efficiencies of heat-electricity conversion through a parameter known as the thermoelectric figure of merit, a more detailed review of which is given in the following section.

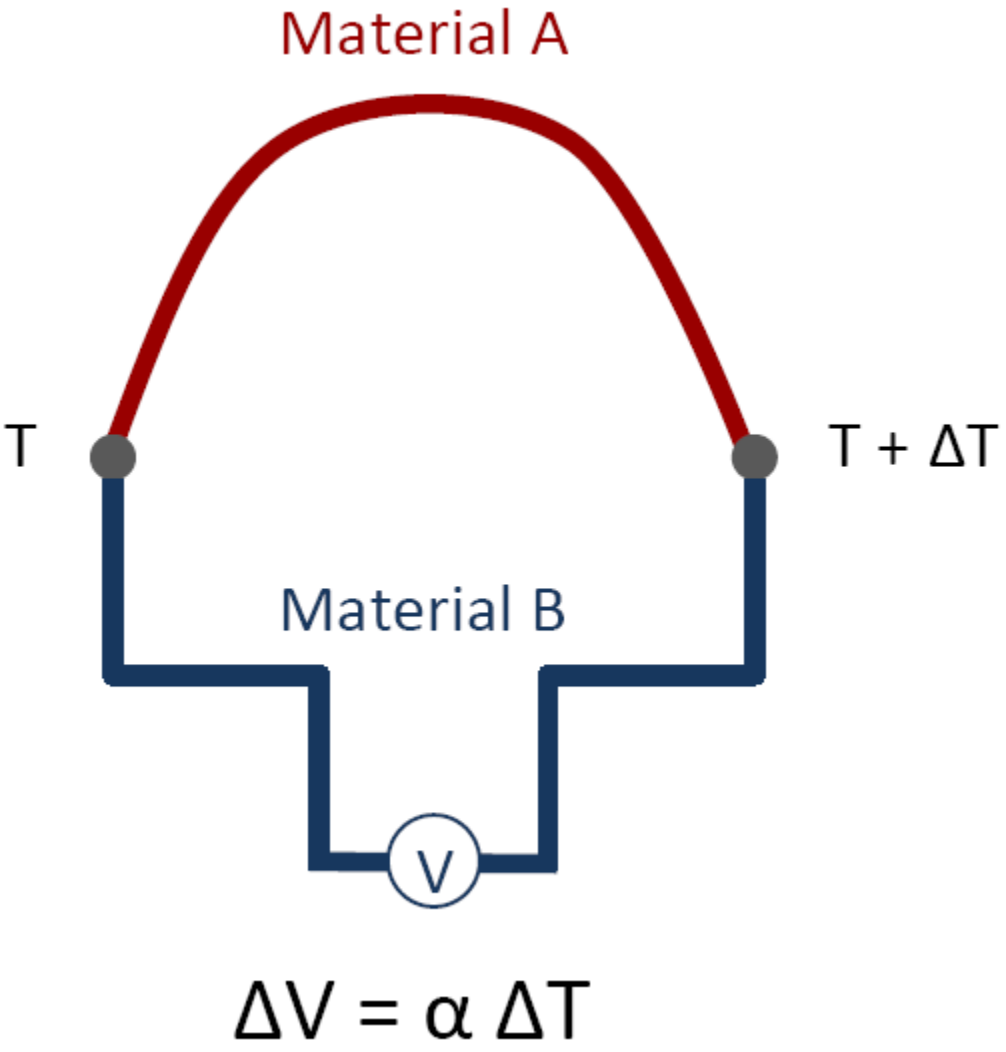

Figure 1. The Seebeck effect occurs between the junction of two dissimilar materials when a temperature gradient is present.

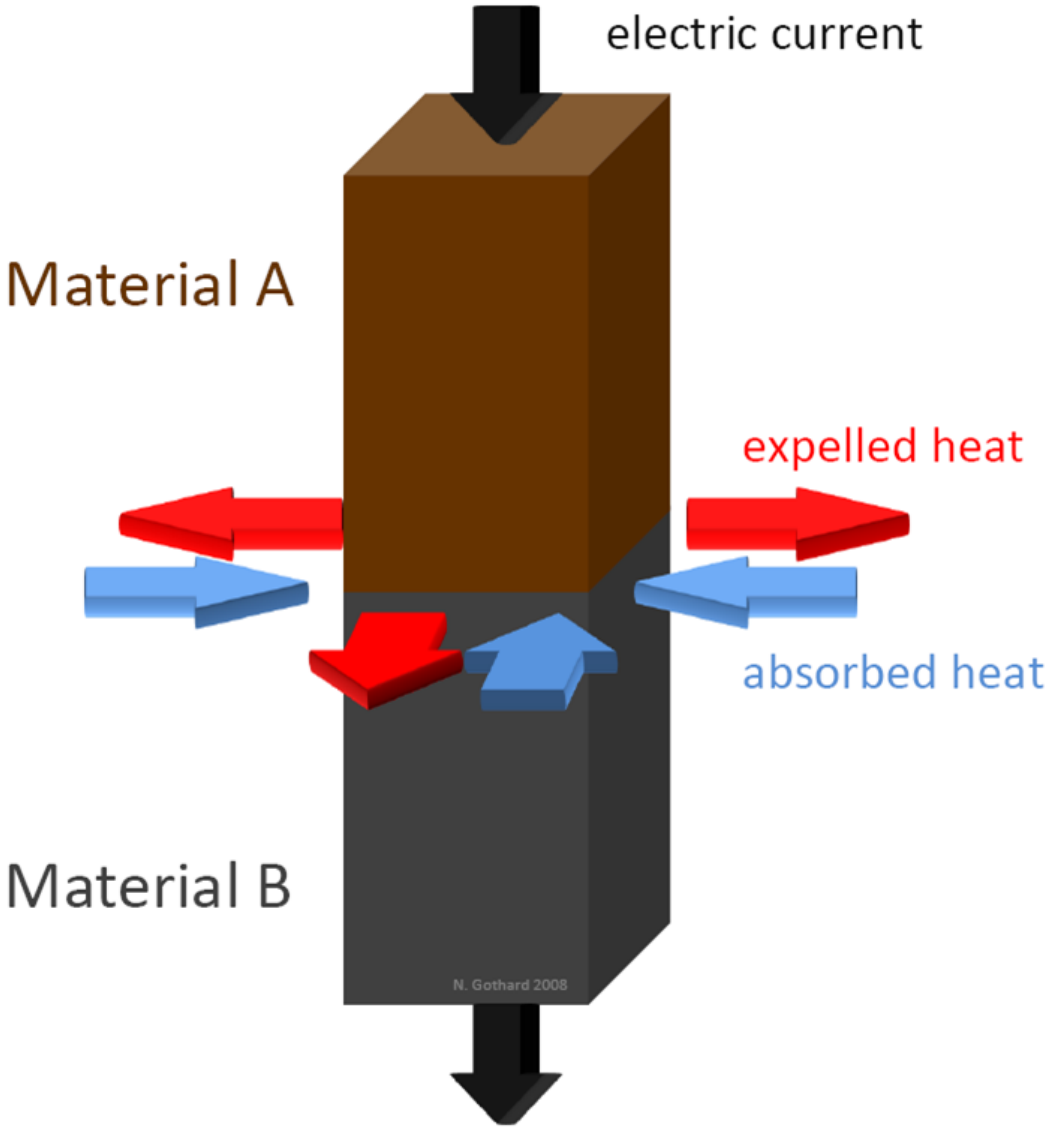

Figure 2. The Peltier effect. Heat is expelled or absorbed at the junction between dissimilar materials when an electrical current is injected.

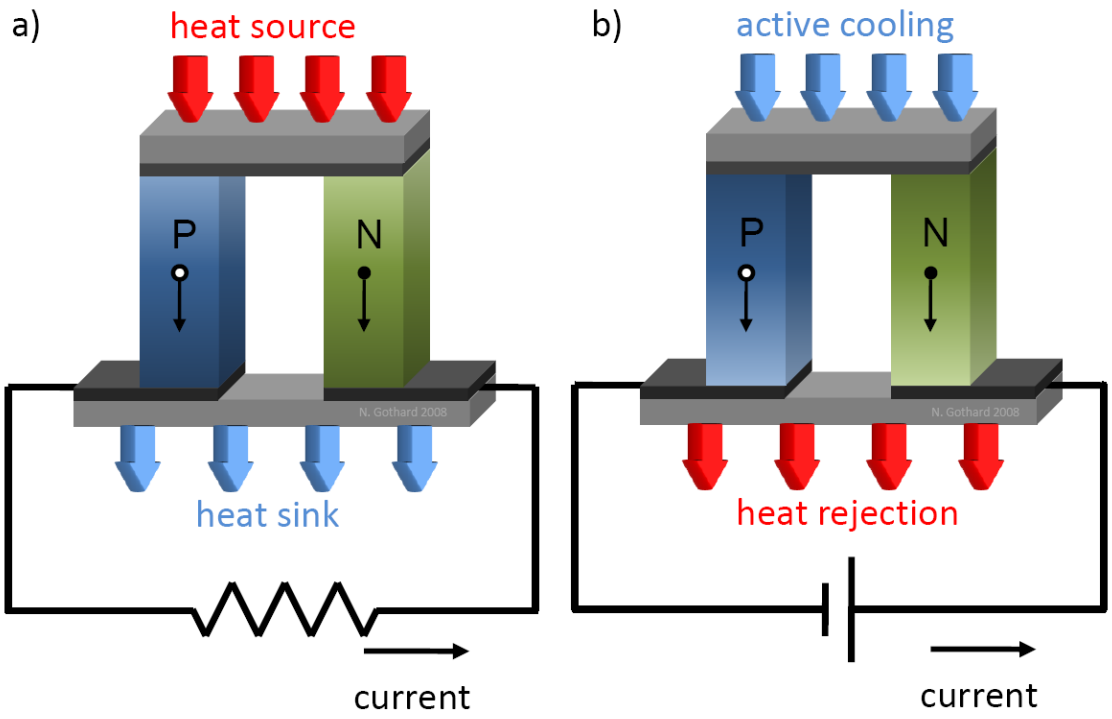

Figure 3. Thermoelectric modules: a) power generation and b) refrigeration. Current is depicted in the conventional sense.

The Figure of Merit

The efficiency of refrigeration modules is characterized by the coefficient of performance (C.O.P.) whereas the efficiency of power generation modules is described in terms of the efficiency of a heat engine. In either case, it is possible to relate the expressions describing the efficiency to a parameter that contains the relevant thermal, electrical, and thermoelectric parameters, the tuning of which is at the center of research into thermoelectric materials. The relation of this parameter, the "figure of merit," to the coefficient of performance and heat engine efficiency is outlined here.

The coefficient of performance, ϕ, is related to the total heat flow, *dQ/dt*, and the power input, *P*, as follows:

$$\phi = \frac{1}{P}\frac{dQ}{dt}. \tag{1.6}$$

Here, *Q* is the sum of heat flow due to the thermal conductance of the material, Q_κ, the Peltier heat flow, Q_Π, and the heat loss due to Joule heating, Q_I. That is,

$$\dot{Q} = \dot{Q}_\kappa + \dot{Q}_\Pi + \dot{Q}_I, \text{ where} \tag{1.7}$$

$$\dot{Q}_\kappa = -K\Delta T, \tag{1.8}$$

$$\dot{Q}_\Pi = I\Pi = I\alpha T, \text{ and} \tag{1.9}$$

$$\dot{Q}_I = -I^2R, \tag{1.10}$$

K being the thermal conductance. The power supplied to the device is given simply by the Joule expression,

$$P = I^2R, \tag{1.11}$$

such that the coefficient of performance (C.O.P.) becomes

$$\phi = \frac{-K\Delta T + I\alpha T - I^2 R}{I^2 R}. \tag{1.12}$$

Maximizing the C.O.P. requires, by differential calculus, that $d\phi/dt$ goes to zero at some value of I, denoted I_{max}. The result is that

$$I_{\max} = \frac{2K\Delta T}{\alpha T}, \tag{1.13}$$

and substituting this value back into equation (1.12) gives, after some simplification,

$$\phi\left(I_{\max}\right) = \frac{\frac{\alpha^2 T^2}{RK} - 4\Delta T}{4\Delta T}. \tag{1.14}$$

The only intrinsic material properties that expression (1.14) depends upon are those in the first term of the numerator, namely the thermopower, α, the thermal conductance, K, and the resistance, R. It is customary to define a new quantity, the figure of merit, Z, as

$$Z \equiv \frac{\alpha^2}{\rho\kappa}, \tag{1.15}$$

replacing resistance and thermal conductance with the dimension-scaled quantities of resistivity, ρ, and thermal conductivity, κ. Dimensional analysis of (1.15) shows the dimensions to be T^{-1}, and as such it is more common to refer to the dimensionless figure of merit, or "ZT", which is given by

$$ZT = \frac{\alpha^2 T}{\rho\kappa}. \tag{1.16}$$

Thus the C.O.P. is given by

$$\phi\left(I_{\max}\right)=\frac{\left(ZT\right)T-4\Delta T}{4\Delta T}\,. \tag{1.17}$$

The figure of merit is also found in the expression for the efficiency of a heat engine, although the derivation is a bit trickier. The efficiency of a heat engine is given by the well-known formula

$$\eta=\frac{W}{dQ/dt}\,, \tag{1.18}$$

where W is the work done by the engine and dQ/dt is the heat flow through the engine. The work done by the device is the contribution from the Seebeck voltage minus a Joule heating term:

$$W=IV_{tot}=I\Delta V_{Seebeck}-I\Delta V_R=I\alpha\Delta T-I^2R\,. \tag{1.19}$$

The expression for heat flow differs from the case of active refrigeration in that heat flow by diffusion and by the Peltier effect are now cumulative, opposed only by Joule heating effects. That is,

$$\dot{Q}=K\Delta T+I\alpha T-I^2R. \tag{1.20}$$

Thus, the efficiency can be expressed as

$$\eta=\frac{I\alpha\Delta T-I^2R}{K\Delta T+I\alpha T-I^2R}\,, \tag{1.21}$$

and it will also have a maximum value for some I_{max}, which is obtained by setting the first derivative of η equal to zero and solving for I. After some simplification, the result is that

$$I_{\max} = \frac{\alpha \Delta T}{R\left(\sqrt{1+\left(\frac{\alpha^2}{RK}\right)T}+1\right)}, \tag{1.22}$$

where the figure of merit, $Z = \alpha^2/RK$, is found in the denominator. Substituting into (1.21) yields $\eta(Z)$, which, after a bit of algebra, can be reduced to

$$\eta = \frac{T_H - T_C}{T_H}\frac{\sqrt{1-ZT}-1}{\sqrt{1+ZT+T_C/T_H}}, \tag{1.23}$$

which again depends on the intrinsic properties of the material solely through the figure of merit, Z [9]. As $Z \to \infty$, the expression for the efficiency given in (1.23) approaches the Carnot limit. Note that while the above derivations are carried out for a single segment of a thermoelectric module, the results will not be changed if the calculation were to be carried out across the entire module. These calculations also assume that there is no heat extraction from the segments due to the Thompson effect.

Recent calculations showing the relationship of theoretical ZT values to the relative Carnot efficiency and the C.O.P. have revealed an interesting trend [10]. Whereas it is generally true from a standpoint of device engineering that the highest possible ZT value is desirable, figure 4 shows that the benefits for improved efficiency of increasing ZT become minor as ZT approaches double digit values. In fact, it was shown that a ZT in the range of 2-3 corresponds to a Carnot efficiency of roughly 40-50% in the power generation scheme or a C.O.P. of 2-3 in the refrigeration configuration. These values are quite competitive with existing engines and mechanical coolers, and are therefore good marks to shoot for in terms of research and engineering effort versus return on investment.

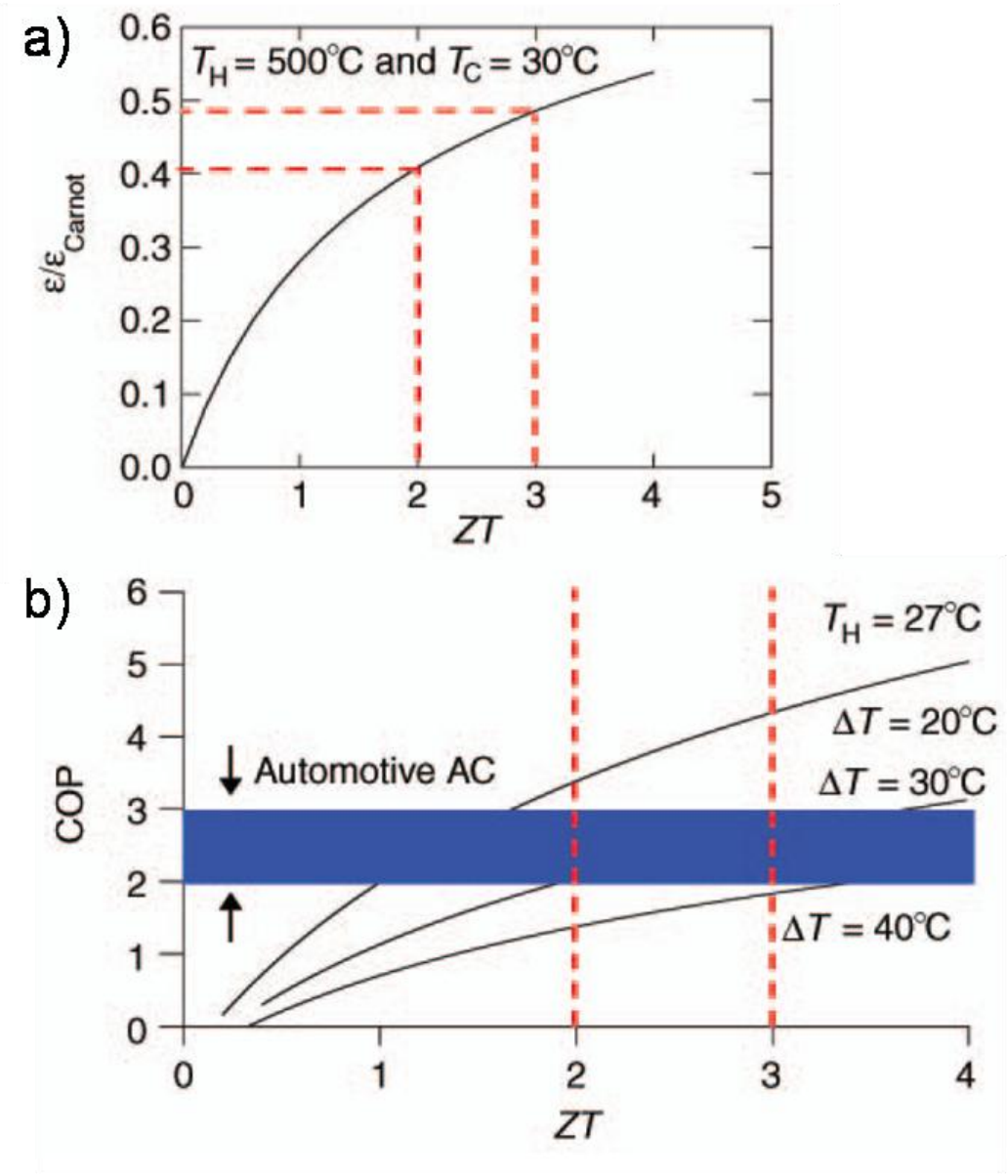

Figure 4. a) Figure of merit, ZT, as a function of relative Carnot efficiency. b) ZT as a function of coefficient of performance, at various temperatures [10].

Current Issues in Thermoelectrics

Difficulties Maximizing ZT

The figure of merit depends entirely on the thermopower, the electrical resistivity, and the thermal conductivity. During the 1950's and 60's, much of thermoelectrics research focused on improving the thermopower and electrical conductivity by judicious doping of promising materials. This approach is quite effective for improving the temperature dependent power factor, defined as

$$PF \equiv \frac{\alpha^2 T}{\rho} = \alpha^2 \sigma T \,, \tag{1.24}$$

but difficulties arise in maximizing ZT because the thermal conductivity for a material is the sum of lattice and electronic contributions, κ_L and κ_e:

$$\kappa = \kappa_L + \kappa_e. \tag{1.25}$$

Further, according to the Wiedemann-Franz equation [11], the electronic thermal conductivity is directly proportional to the electrical conductivity:

$$\kappa_e = L\sigma T \,. \tag{1.26}$$

Here, κ_e is the thermal conductivity due to the charge carriers, σ is the electrical conductivity, and *L* is the Lorenz number, which in the case of degenerate conductors has a value of

$$L \equiv 2.45 \times 10^{-8} W \cdot \Omega / K^2 \,. \tag{1.27}$$

The Lorenz number is only truly constant in the case of metals, but it is customary to use it to help obtain a rough estimation of the electronic contribution to the thermal

conductivity even in the case of semi-conductors. The difficulty presented by the contribution to the thermal conductivity by charge carriers is that any attempt to maximize the electrical conductivity results in a corresponding increase in the thermal conductivity, which acts in opposition to ZT from a standpoint of efficiency. Further, according to the Mott equation [12],

$$\alpha = -\frac{\pi^2 k_B{}^2 T}{3e}\left(\frac{\partial \ln \sigma}{\partial E}\right)\Bigg|_E, \tag{1.28}$$

i.e. the Seebeck coefficient is proportional to the logarithmic derivative of the electrical conductivity. The interrelations of these parameters make maximizing the figure of merit a non-trivial exercise, and a common technique is first to maximize the power factor via doping and then to minimize to lattice thermal conductivity by engineering the lattice or microstructure to include phonon scattering mechanisms that leave the electronic properties largely untouched. This approach was popularized as the "phonon glass / electron crystal" (PGEC) concept [6], where the naming implies that a desirable thermoelectric material would act as a glass with respect to phonons but as a crystal with respect to electrons or holes—i.e. a thermal insulator / electrical conductor. The PGEC approach has helped lead to the investigation of a wide variety of materials for thermoelectric power generation / refrigeration in the past 10-15 years. The range of structures currently being researched in order to achieve a high figure of merit is quite diverse, including materials such as complex chalcogenides [13], skutterudites [14,15], half-Heuslers [16], metallic oxides [17], intermetallic clathrates [18,19], and pentatellurides [20].

Low Dimensional Effects

Much of the initial work towards maximizing ZT for well-known thermoelectric materials such as bismuth telluride was completed by the mid to late 1960s. At this point, there was a good fundamental understanding of how to maximize the thermoelectric performance of a material via doping, to the extent that subsequent decades of research in this area served only to improve the figure of merit by slight amounts. In 1991, however, research into a new morphology class of materials began with the discovery that the growth parameters necessary to synthesize C_{60} could be adjusted to yield an elongated fullerene, which eventually became known as a carbon nanotube [21]. Soon thereafter, a theoretical framework for using low-dimensional structures to enhance the figure of merit even in materials whose parameters have already reached near optimization via conventional techniques was set forth [7]. Specifically, it was proposed that fabricating materials into an effectively 2D "superlattice," a material having layers of alternating composition with an interlayer distance on the order of nanometers, would have the theoretical potential to increase the figure of merit by as much as a factor of 14 over the bulk value, due simply to the morphology of the sample. This claim was the result of applying previously published techniques for calculating the relevant thermoelectric transport parameters α, σ, and κ [22] to a 2D case where thin, alternating layers are treated as multiple quantum wells. Subsequent work has shown that the same phenomenon also to hold for 1D morphologies [23]. The proposed potential increase in the figure of merit was based primarily on an increase in the term $\alpha^2 n$ rather than from any reduction in the thermal conductivity for a system comprised of multiple quantum

wells, when the well width is greater than ~1nm. That is, enhancement of the figure of merit is seen primarily due to quantum confinement effects in the thermopower and in the electronic density of states. Subsequent work in an epitaxially grown PbTe/$Pb_{1-x}Eu_xTe$ superlattice with ~2 nm PbTe layer widths but very thick $Pb_{1-x}Eu_xTe$ barrier widths (on the order of 35 nm) confirmed the predicted thermopower/density of states enhancement in an effectively 2D system, where electronic conduction was constrained to the PbTe layers of the superlattice. Here, $\alpha^2 n$ achieved a maximum of ~50x the value seen in bulk PbTe [24]. In spite of these exciting results, however, it was not until later work in Bi_2Te_3/Sb_2Te_3 superlattices was shown to achieve a ZT value of ~2.4 due to phonon scattering between the layers [8], that low-dimensional structures began to attract widespread interest in thermoelectrics research. It is of note that the layer width in the Bi_2Te_3/Sb_2Te_3 superlattice study was found to be as low as 1 nm, the limit at which phonon scattering was predicted to become a factor in the previous theoretical work. Soon after the Bi_2Te_3/Sb_2Te_3 superlattice results, a similar effect was observed in PbTe/$PbSe_xTe_{1-x}$ superlattices [25]. Other studies have suggested the possibility of improving upon the power factor in a 3D superlattice structure, one in which the alternating layers are all on the order or 2 nm [26], in contrast to the previous power factor enhancement seen only when one layer is effectively isolated by a large buffer layer [24]. It is therefore in principle easy to conceive of a superlattice structure that employs both phonon blocking and quantum confinement effects, though research efforts have yet to produce such a material.

Nanocomposites

However promising superlattices may be for achieving high figures of merit, they are more suited to thin-film applications than to bulk applications due to their thin morphologies. Moreover, they are reliant on labor-intensive epitaxial-growth methods for production. In order to harness the benefits gained by synthesizing materials in low dimensional morphologies within a broader milieu of applications, the concept of a "nanocomposite" was soon to follow the first promising superlattice result. The idea of a nanocomposite is to incorporate some form of nanostructure into a bulk material in such as way that the properties of the composite material benefit from both components, ideally with an overall improvement in the figure of merit. Further advantages such as ease of manufacture and greater potential for scalability may also be achieved. One of the earliest attempts at producing such a composite relied on the incorporation of small-diameter (9-15 nm) Bi nanowires into porous alumina or porous silica and showed an enhancement of the thermopower consistent with the predictions of quantum confinement, but due to the structure of the composite, the resistivity could not be measured, and therefore no figure of merit data could be calculated [27].

In a related vein, previous work with PbSeTe/PbTe superlattices has shown the possibility of spontaneously forming PbSe nanodots within a superlattice layer, and it was subsequently hypothesized that the high density of nanodots in such a "quantum dot superlattice" (QDSL) was almost entirely responsible for the high ZT value (in the range of 1.3 to 1.6 at room temperature) found in this material [28]. Not long thereafter, Ag-Sb-rich "nanodot" regions, having cross sections of 1-2 nm, were found to occur in cubic

$AgPb_{18}SbTe_{20}$ in between regions of PbTe, and were suggested as a possible cause for the ZT value of ~2 that was observed at 800 K [29]. These results were motivational to the field of thermoelectric nanocomposite research, even though QDSLs and cubic $AgPb_{18}SbTe_{20}$ "LAST" materials with Ag-Sb quantum dot precipitates are not nanocomposites in the strict sense. One of the next attempts at producing a thermoelectric nanocomposite relied on the incorporation of C_{60} into a matrix of $CoSb_3$ [30]. Here it was found that although the C_{60} grouped into irregular clusters on the order of microns, the overall effect on the thermal conductivity was still beneficial.

It is the purpose of the current project to synthesize nanocomposites using a bismuth telluride matrix, with an eye towards improving ZT, primarily by reducing the lattice thermal conductivity of the composite.

The Bismuth Telluride System

Crystal Structure

Bi_2Te_3 is a member of the $D_{3d}^5\left(R\bar{3}m\right)$ space group [31], with a rhombohedral unit cell [32], although its crystal structure can also be expressed in terms of a hexagonal unit cell. In the rhombohedral representation, Bi and Te atoms are grouped into layers which are stacked within a unit cell in the [111] direction in the sequence:

Bi – Te – Bi – Te –Te –Bi – Te – Bi – Te [33],

but with two different types of bonding between the Bi and Te atoms. The unit cell contains two Bi and three Te atoms. A transformation of the rhombohedral unit cell into a hexagonal unit cell can be achieved by means of the relations between the basis vectors

of the rhombohedral unit cell, $\mathbf{a}_n^R$, and the basis vectors of the hexagonal unit cell, $\mathbf{a}_n^H$, which are as follows [32]:

$$\begin{cases} \mathbf{a}_1^H = -\mathbf{a}_2^R + \mathbf{a}_3^R \\ \mathbf{a}_2^H = \mathbf{a}_1^R - \mathbf{a}_3^R \\ \mathbf{a}_3^H = \mathbf{a}_1^R + \mathbf{a}_2^R + \mathbf{a}_3^R \end{cases}, \tag{1.29}$$

where $\mathbf{a}_3^H$ is the hexagonal c axis. In this representation, starting at the origin of the unit cell and moving upwards along the c ($\mathbf{a}_3^H$) axis, the sequence of layers is

$$\text{Te}^{(2)} - \text{Bi} - \text{Te}^{(1)} - [\text{Te}^{(1)} - \text{Bi} - \text{Te}^{(2)} - \text{Bi} - \text{Te}^{(1)}] - \text{Te}^{(1)} - ,$$

in which repeating patterns of five atoms in the sequence

$$\text{Te}^{(1)} - \text{Bi} - \text{Te}^{(2)} - \text{Bi} - \text{Te}^{(1)}$$

can be discerned (marked by brackets). Here, the superscripts are used to designate the different types of bonding, and each Bi atom is bonded to three $\text{Te}^{(2)}$ atoms with a 3.22 Å bond length on one side and to three $\text{Te}^{(1)}$ atoms with a 3.12 Å bond length on the other side [34]. The $\text{Te}^{(1)}$ – Bi and Bi – $\text{Te}^{(2)}$ bonds are both covalent, but the $\text{Te}^{(1)}$ – $\text{Te}^{(1)}$ bond is Van der Waals [35]. The hexagonal unit cell is comprised of three quintets of the grouping $\text{Te}^{(1)}$ – Bi – $\text{Te}^{(2)}$ – Bi – $\text{Te}^{(1)}$ [36]. Figure 5 shows the unit cell in the hexagonal representation [37]. The cell parameters for the rhombohedral representation are

$$\begin{aligned} a^R &= 10.473\text{Å} \\ \alpha &= 24^o 9' 32'' \end{aligned}, \tag{1.30}$$

and for the hexagonal representation they are

$$\begin{aligned} a_{1,2}^{H} &= 4.3835\text{Å} \\ a_{3}^{H} &= 30.487\text{Å} \end{aligned}, \tag{1.31}$$

as measured by powder x-ray diffraction [33]. Some differences in the above values are expected for alloys of the substance made by substitutional doping of Bi_2Te_3 with Sb on the Bi site and / or Se on the Te site, e.g., as is typically done when optimizing various aspects of the transport properties.

Electronic Transport and Structure

The Brillouin zone of bismuth telluride is shown in Figure 6 [38]. The energy gap was found to be 0.145 eV for Bi_2Te_3 [39], but this value is expected to vary slightly depending on doping levels within the more general system of $Bi_{1-x}Sb_xTe_{1-y}Se_y$. Qualitative predictions of a conduction band with multiple ellipsoidal valleys were arrived at due to measurements of the magnetoresistance [40,41]. Subsequent Faraday rotation experiments indicated that n-type Bi_2Te_3 would have six ellipsoidal valleys centered on the reflection planes in *k*-space, while optical experiments indicated that p-type Bi_2Te_3 would have only three [42]. This proposed multi-valley model was later found to be consistent with measurements of the band structure via the de Haas-van Alphen (dHvA) effect (of which Shoenberg provides a good review [43]) [44], with the exception that both n- and p-type bismuth telluride were found to have six rather than three-valley valence bands [45]. It was further found that the shapes of the minima are independent of total carrier concentration between $9x10^{17}$ and $2.4x10^{19}$ cm^{-3} [46], in contradiction to previous theories which suggested that the band structure varied with carrier density [47]. Initial calculations of the band structure verified the six-valley

model and also indicated that spin-orbit coupling is an important effect [48]. Shubnikov-de Haas (SdH) measurements [49] on bismuth telluride crystals would later indicate that neither the highest valence band nor the lowest conduction band valley are parabolic [50], and further that a simple two-band model is not an adequate description of the band structure in Bi_2Te_3 [51]. Further, a second type of SdH oscillation indicated the presence of a second type of hole in the p-type Bi_2Te_3 material [50]. More recent band structure calculations have indicated that Bi_2Te_3 is an indirect-gap semiconductor, where the introduction of spin-orbit effects into the model serves to shift the energy bands, thereby accounting for the indirect bandgap [52]. Later, more complete band structure analysis confirmed much of the previous work and noted that the effective masses are highly anisotropic, as might be expected due to the large degree of anisotropy in the crystal structure [53]. The band structure calculated in reference [53] is shown in figure 7.

In the strict 2:3 stoichiometry of Bi_2Te_3, bismuth telluride has been found to be intrinsically p-type, having an electrical resistivity in the range of 2 mΩ cm near 300 K, and it was reported in early literature that no difference in the electrical conductivity was found between the single and poly-crystalline samples, when the measurements were performed parallel to the direction of the cleavage planes [54]. It was also found that a shift from p-type to n-type occurs when Te is present in excess of 62% (figure 8) [36,55,56].

Thermal Transport

Early measurements of the thermal conductivity in several samples of Bi_2Te_3 indicated a relatively low value, below 2.5 W $m^{-1}K^{-1}$ in all samples [57]. Further, the

effects of anisotropy cannot be overlooked as it was observed that the thermal conductivity was much lower, near 0.7 W $m^{-1}K^{-1}$ in samples where the measurement was performed perpendicular to the cleavage planes as opposed to values near 2 W $m^{-1}K^{-1}$ obtained from measurements done parallel to the cleavage planes. It was later discovered that the thermal conductivity value of n-type Bi_2Te_3 was lower than the value observed in p-type Bi_2Te_3 [58], an effect which is perhaps attributable to the fact that Bi_2Te_3 is intrinsically p-type and therefore the addition of impurities or dopants used in this study to produce n-type Bi_2Te_3 would likely also introduce phonon scattering sites. The layered nature of the crystal structure of Bi_2Te_3 provides some explanation for its low thermal conductivity, with the loosely bound Van der Waals layers contributing to phonon blocking but allowing good electrical conduction. This material is consequently a good example of the PGEC concept occurring naturally, and is it this combination of effects that make it an efficient thermoelectric material.

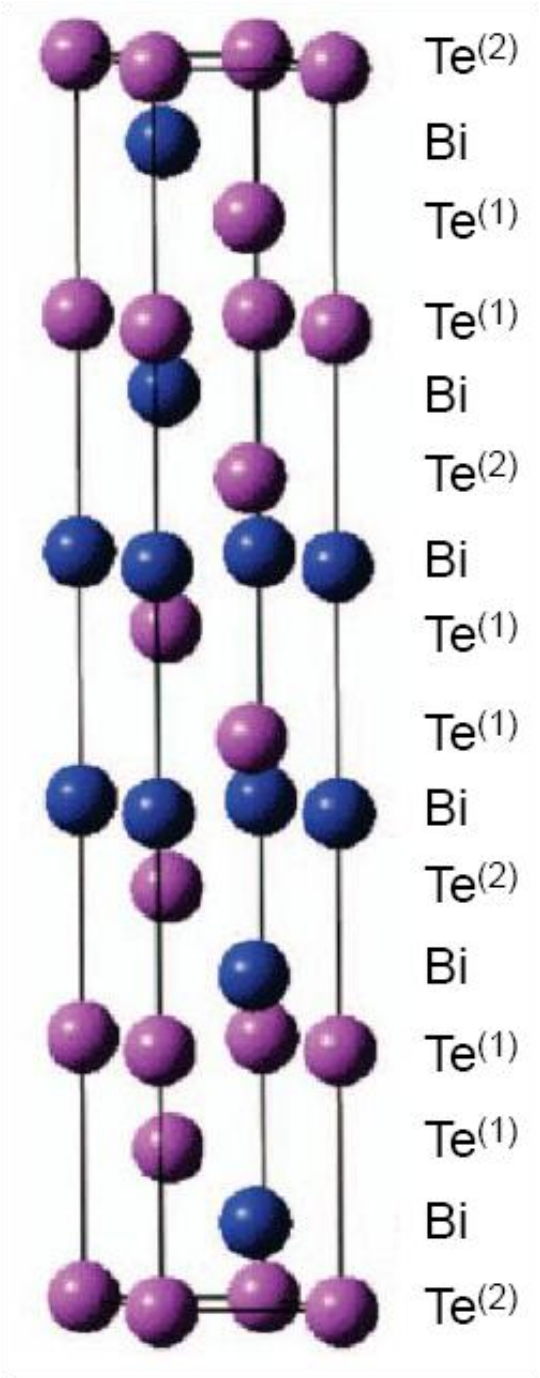

Figure 5. Crystal structure of Bi_2Te_3 in the hexagonal representation [37]. Bi is depicted in blue and Te in pink. $Te^{(1)}$-$Te^{(1)}$ bonds are VdW, while $Te^{(1,2)}$-Bi bonds are covalent.

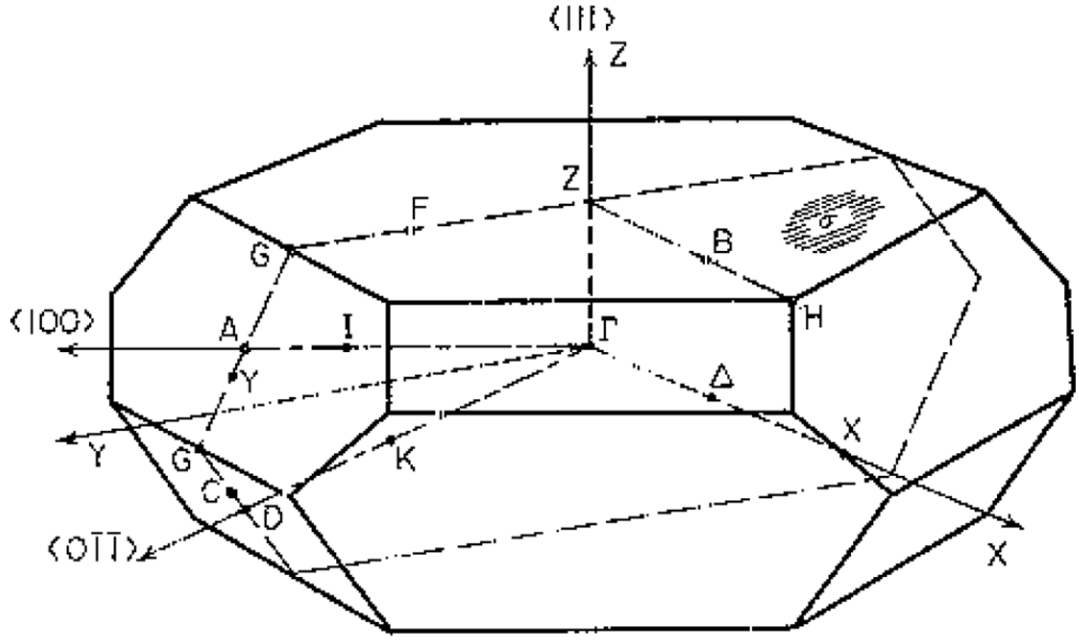

Figure 6. The Brillouin zone of Bi_2Te_3 [38].

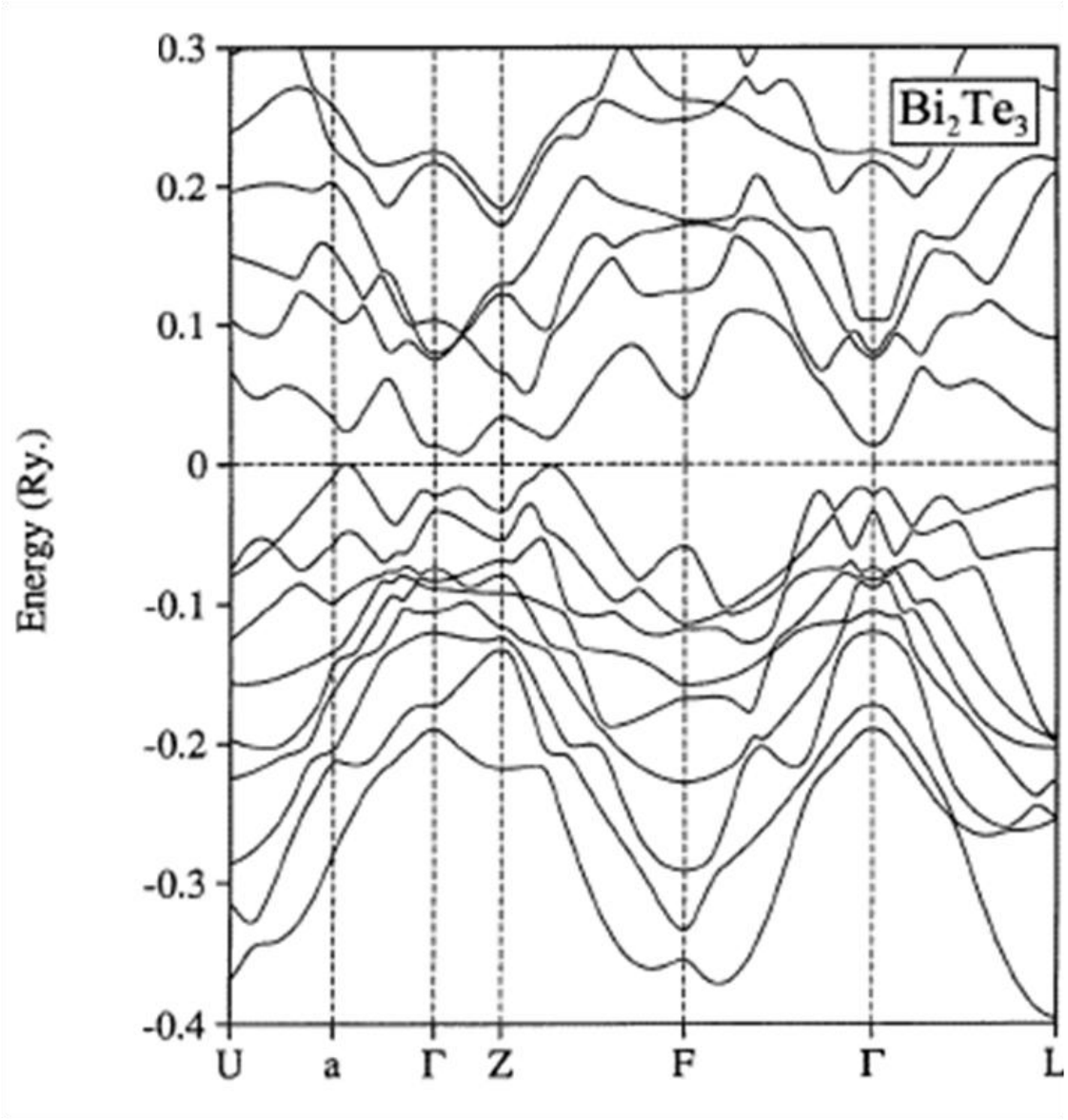

Figure 7. The band structure of Bi_2Te_3 [53].

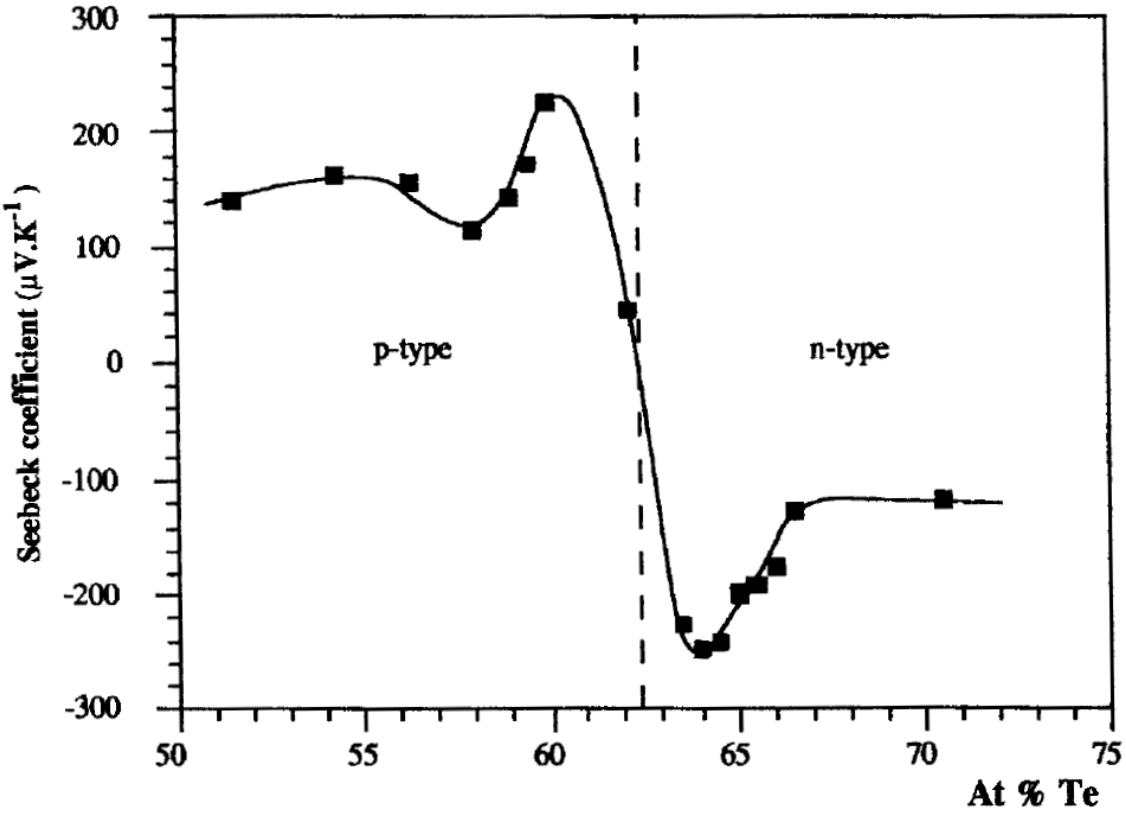

Figure 8. Thermopower of bismuth telluride as a function of tellurium percentage [36].

ELECTRICAL PROPERTIES

Band Structure

Band structure theory results from the application of quantum theory to condensed matter, and it facilitates much of our understanding about electronic transport in solids. Integral to the calculation of the band structure of a material is a calculation of the Brillouin zone, a geometrical construct derived from the crystal structure. The crystal structure for a given solid is generally defined in terms of the unit cell, or "primitive cell"—the arrangement of atoms in real space in the smallest space necessary to completely describe the structure of the entire crystal. In general, a basis of three vectors, the so-called "primitive lattice vectors," $\mathbf{a}_i$, is sufficient to describe the position of any lattice site within the entire structure. Figure 9 shows a sample cubic crystal structure with primitive lattice vectors. As much of the physics of solids in worked out in terms of wavevectors, **k**, which travel in reciprocal space (or "*k*-space"), it is useful to transform the crystal lattice into reciprocal space. The reciprocal lattice vectors, $\mathbf{b}_i$, are calculated from the primitive lattice vectors, $\mathbf{a}_j$, using the following relation [11]:

$$\mathbf{b}_i = 2\pi \frac{\mathbf{a}_j \times \mathbf{a}_k}{\mathbf{a}_i \bullet \mathbf{a}_j \times \mathbf{a}_k}. \tag{2.1}$$

A reciprocal lattice vector, **g**, can then be constructed by forming a linear combination of these reciprocal lattice basis vectors, so that any point in the reciprocal lattice can be located by the appropriate **g**. If one orthogonally bisects all vectors, **G**, that locate another reciprocal lattice point from the origin, the area enclosed is the 1st Brillouin zone. A 2D example is depicted in figure 10, with lines forming the borders of the Brillouin

zone, which is represented as an area. In 3D, the bisectors are planes and the Brillouin zone is a volume. As the condition for Bragg refraction can be expressed as

$$\mathbf{k}\bullet\left(\tfrac{1}{2}\mathbf{G}\right)=\tfrac{1}{2}G^2, \tag{2.2}$$

it follows that the Brillouin zone constructed by the set of reciprocal vectors

$$\mathbf{g}=\tfrac{1}{2}\mathbf{G} \tag{2.3}$$

contains all the relevant physics relating to Bragg reflection in crystals.

The band structure of solids arises in particular from tailoring the theory of quantum mechanical electronic conduction to the constraints of a crystal structure, with a major consideration being the application of the periodic boundary conditions that arise from the periodicity of the crystal structure. From quantum theory it is known that free electron wavefunctions are of the form

$$\psi_{\mathbf{k}}\left(\mathbf{r}\right)=\exp\left(i\mathbf{k}\bullet\mathbf{r}\right). \tag{2.4}$$

In solids, of course, there must always be an external boundary which corresponds at the upper limit to the physical dimensions of the crystal. As such, a first approximation solution for such a boundary would be the familiar particle-in-a-box problem, the solution of which leads to an energy-wavevector relationship such as

$$E\left(\mathbf{k}\right)=\frac{\hbar^2}{2m}\left(k_x{}^2+k_y{}^2+k_z{}^2\right). \tag{2.5}$$

Clearly, a graph of *E* vs. *k* would simply be a parabola, and the wavefunction would take on the appearance of a standing wave within the box, tailored to the appropriate boundary conditions (i.e. it must vanish at the boundaries). Because the lattice is periodic, no information is lost by plotting the *E* vs. *k* result within the first cell of reciprocal space, i.e.

within the 1st Brillouin zone (figure 11). This is done by shifting data that lie outside of the 1st Brillouin zone by the appropriate number of primitive wavevectors.

In a crystal, however, electrons move in the presence of a periodic potential, $V(\mathbf{r})$, generated by the atomic cores that comprise the lattice, and the resulting Schrödinger equation becomes what is commonly known as the Bloch equation [59]:

$$\left[\frac{-\hbar^2}{2m}\nabla^2 + V(\mathbf{r})\right]\psi_{\mathbf{k}}(\mathbf{r}) = E\psi_{\mathbf{k}}(\mathbf{r}). \tag{2.6}$$

The solutions of this equation are of the form

$$\psi_{\mathbf{k}}(\mathbf{r}) = u_{\mathbf{k}}(\mathbf{r})\exp(i\mathbf{k}\bullet\mathbf{r}), \tag{2.7}$$

where $u_{\mathbf{k}}(\mathbf{r})$ has the periodicity of the crystal lattice, i.e. $u_{\mathbf{k}}(\mathbf{r}) = u_{\mathbf{k}}(\mathbf{r}+\mathbf{T})$, where **T** is a translation vector equal in magnitude to the length of the unit cell in the direction of translation. The result of applying periodic boundary conditions to this equation is that one can determine all the possible **k** states within the crystal. There are certain **k** states, however, that do not allow for a solution of (2.6) [60], and it is this restriction which accounts for the origin of the band gap. Figure 12 shows a sample *E* vs. *k* diagram for the case when a nonzero $V(\mathbf{r})$ is used.

For a real crystal, the band structure is typically expressed by a graph of energy, *E*, vs. wavevector, *k*, with the wavevector axis plotted in terms of points in the Brillouin zone (see figure 7). The bandgap is defined as the magnitude of the energy gap between the highest point of the valence band and the lowest point of the conduction band. The bandgap can be either direct, in which case the extrema of the bands occur at the same *k* value, or indirect, in which case there is some separation in *k*-space between the band

extrema. In the case of a direct bandgap, electronic transitions between the two bands can occur without any interaction with the lattice. Indirect bandgaps, however, require a transition between the conduction and valence bands to be facilitated by a phonon, which transfers the electronic energy to the appropriate location in *k*-space—i.e. the location of the opposite band extremum (figure 13).

In the absence of excitations, an electron gas settles into a state of lowest energy, with the organization of the various occupied energy levels being governed by the Pauli Exclusion Principle. In *k*-space, this state can be described by a vector of radius $\mathbf{k}_F$, centered at the origin, so that within $\mathbf{k}_F$ all electronic states are occupied and outside of $\mathbf{k}_F$ no states are occupied. The energy at the surface of this sphere is known as the Fermi energy, E_F:

$$E_F = \frac{\hbar^2}{2m} k_F{}^2, \tag{2.8}$$

and the surface defined by $\mathbf{k}_F$ in *k*-space is the Fermi surface. The Fermi energy is sometimes referred to as the Fermi level.

To apply this situation to electrons within a crystal structure, one needs only to insert the appropriate Brillouin zone, centered at the origin, into the sphere of *k*-states defined by $\mathbf{k}_F$. The spherical Fermi surface then conforms to the Brillouin zone, resulting in a Fermi surface that is a function of the crystal structure as well as of the electron occupancy. The superposition of the Fermi surface and the reciprocal lattice also allows for the Fermi energy to be added to the graph of energy vs. wavevector. This

conceptualization is of great use for classifying the conduction properties of different types of materials.

The many different combinations of band structures and Fermi surfaces can be grouped into four main categories of solids: metals, insulators, semiconductors, and semimetals. If the Fermi level falls into the middle of an energy band, there are empty electronic states in the immediate vicinity of occupied states, and electrons can move about easily under even the slightest external potential. These materials are metals and typically have extremely high electrical conductivity. If the Fermi level lies in between two energy bands so that one is fully filled and the other empty, then the material is either an insulator or a semiconductor, with the difference between the two being the magnitude of the bandgap. If the energy gap between the two bands is substantially large (typically on the order of several eV or more), electronic conduction is nearly impossible and the material is an electronic insulator. If the energy gap is small enough that thermal excitation of electrons or the application of moderate external potentials are sufficient to excite some charge carriers into an unfilled band, the material is a semiconductor and exhibits moderate electrical conduction. A semimetal is a special case in which an indirect bandgap allows the minimum of the conduction band to be at an energy lower than the maximum of the valence band. The Fermi level lies near the top of the valence band (near the bottom of the conduction band), and the result is that conduction is nearly metallic. Bismuth telluride is one example of a semimetal. Schematics of the various scenarios are presented in figure 14.

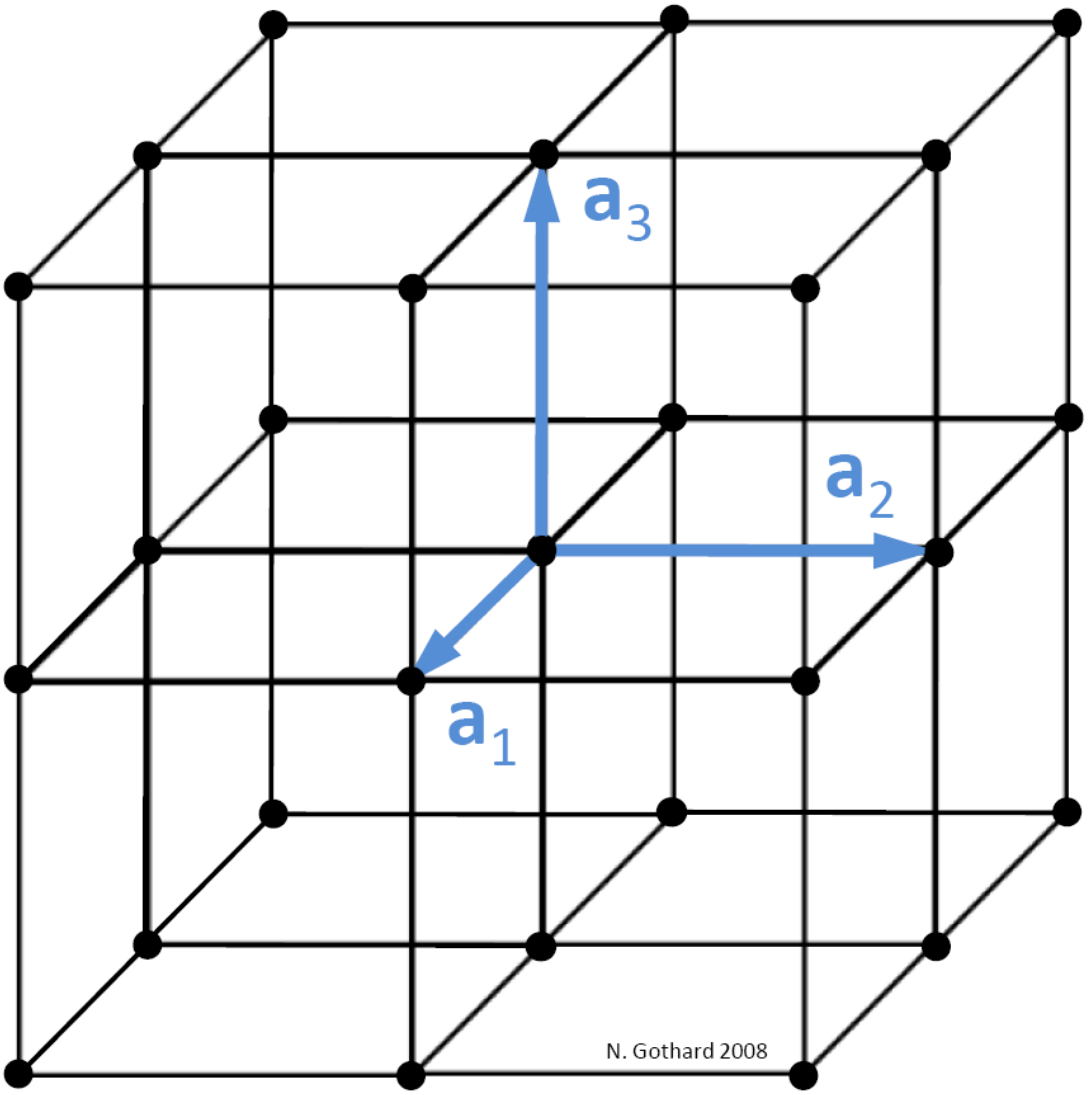

Figure 9. Cubic crystal structure showing primitive lattice vectors $\mathbf{a}_i$, which define the unit cell and form a basis for atomic positions throughout the crystal.

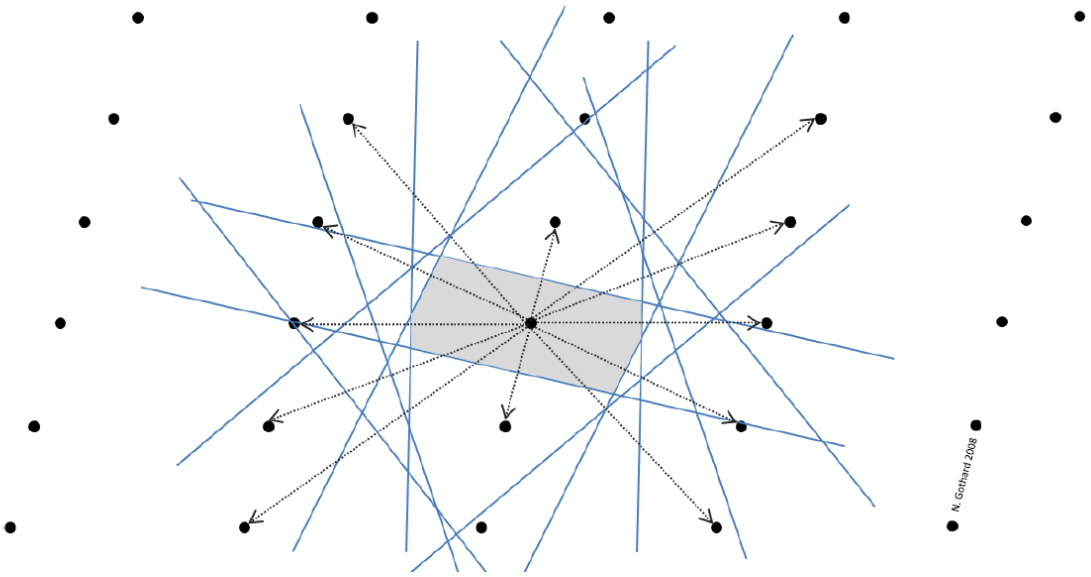

Figure 10. Brillouin zone constructed from a 2D reciprocal lattice. In 3D the lines drawn from the origin would be bisected by planes, and the Brillouin zone would be a volume rather than an area.

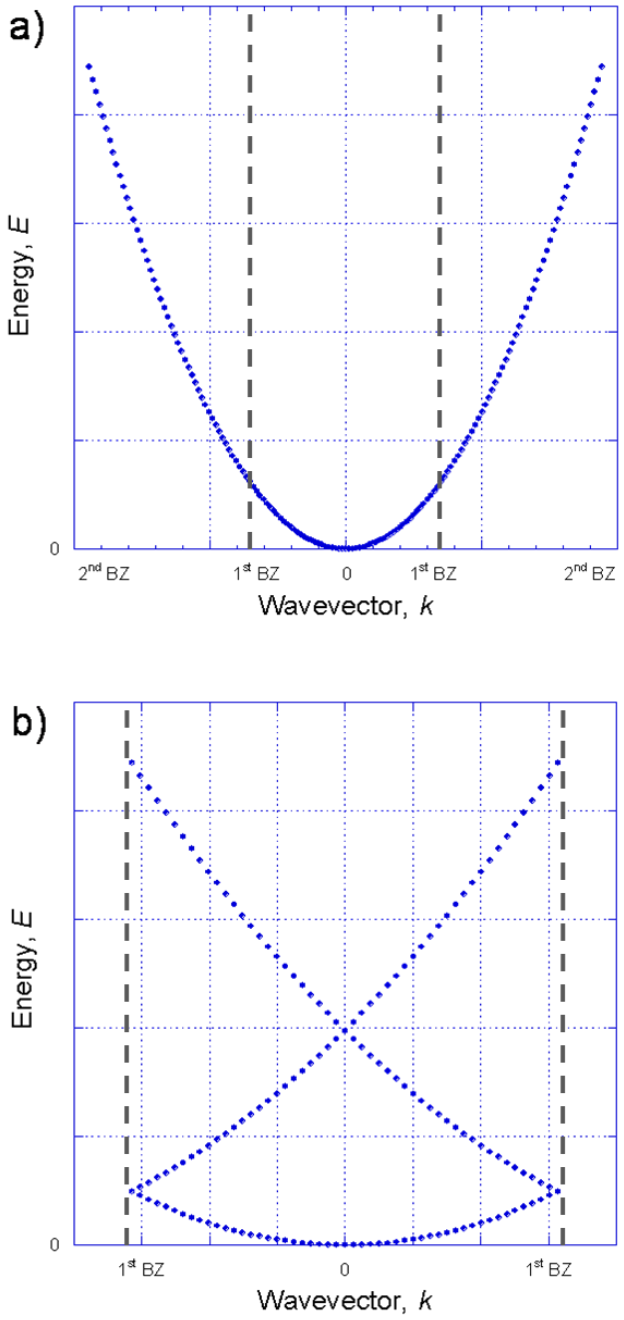

Figure 11. *E* vs. *k* dispersion curve in the absence of a periodic potential. a) The extended zone scheme. b) Reduced into the first Brillouin zone. Brillouin zones are marked by vertical lines and denoted "BZ" on the axes.

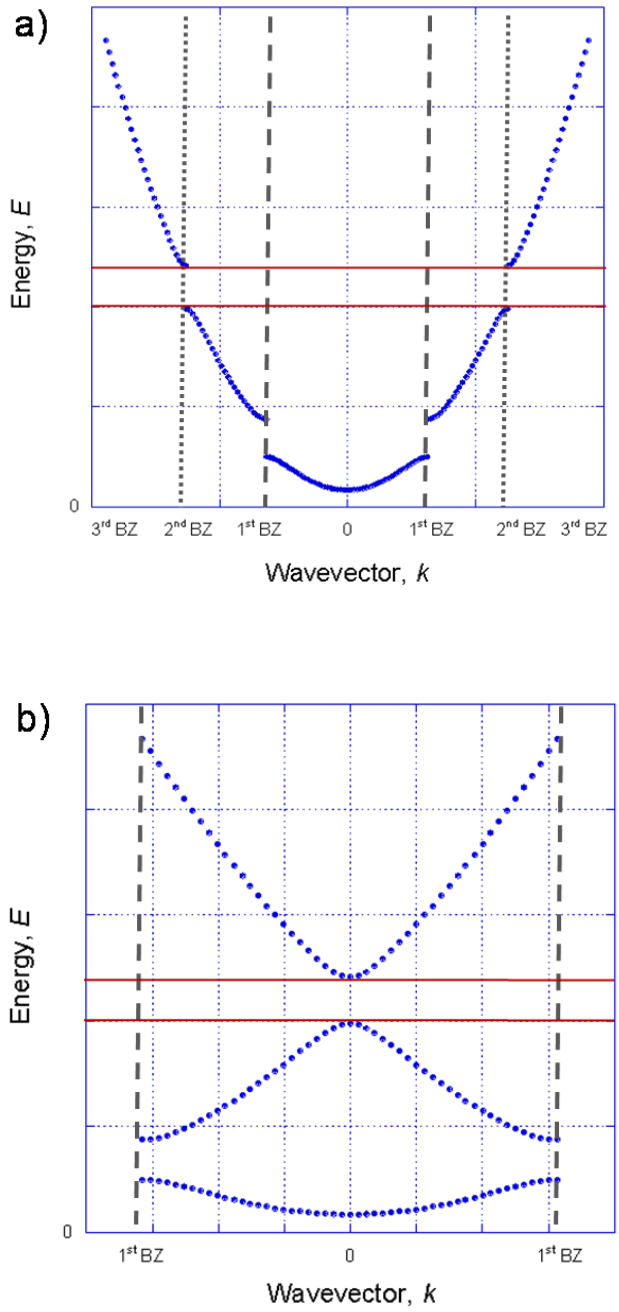

Figure 12. *E* vs. *k* dispersion curve for a periodic potential. a) The extended zone scheme. b) Reduced into the first Brillouin zone. Brillouin zones are again marked by vertical lines, and the bandgap is marked by horizontal red lines.

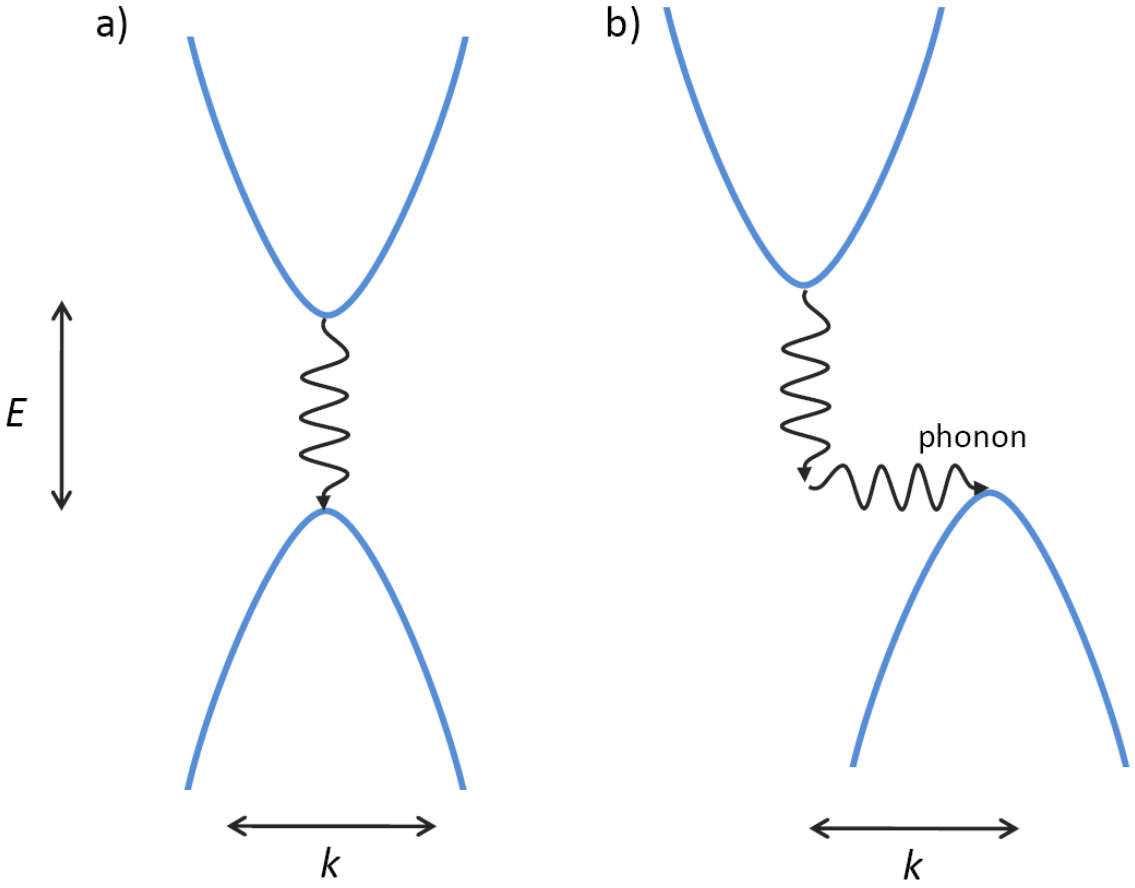

Figure 13. Electronic transitions: a) direct, involving only the electron, and b) indirect, involving the electron and a lattice phonon.

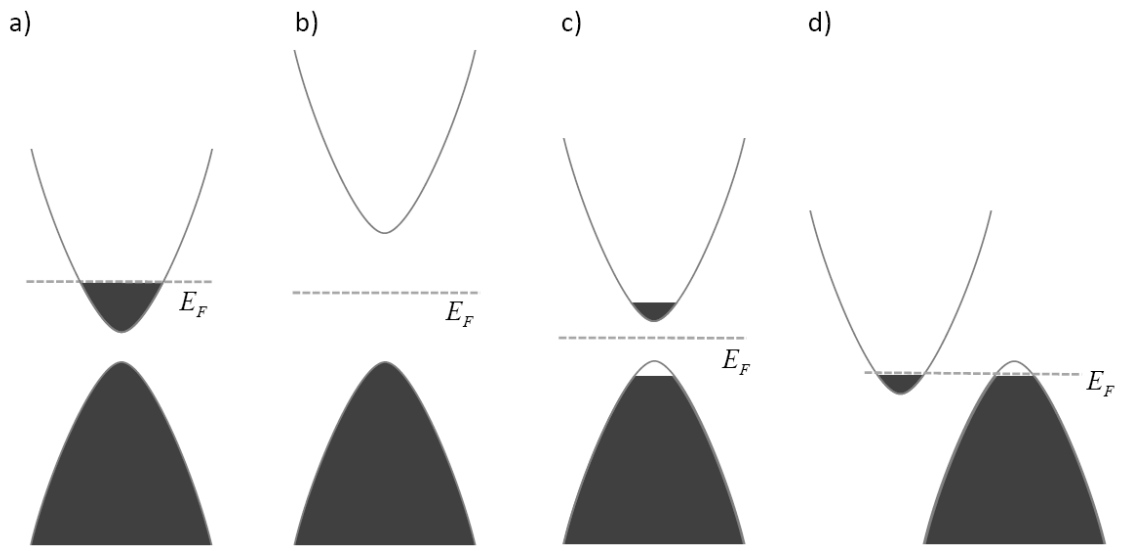

Figure 14. Bandgaps and Fermi levels for four cases: a) metal, b) insulator, c) semiconductor, and d) semimetal. The Fermi level is indicated by the horizontal dashed line for each case.

Electronic Conduction

Electronic conduction in solids is described by the Lorentz force law:

$$\mathbf{F} = q\left(\mathbf{E} + \mathbf{v} \times \mathbf{B}\right), \tag{2.9}$$

which in the absence of a magnetic field can be written more familiarly as Ohm's law:

$$\mathbf{J} = \sigma \mathbf{E}, \tag{2.10}$$

where **J** is the current density, **E** is the external electric field, and σ is the electronic conductivity, given by

$$\sigma = \frac{ne^2\tau}{m}. \tag{2.11}$$

Here n is the number of charge carriers, e is the electronic charge, m is the electron mass, and τ is the relaxation time (the average time between collisions). Charge carriers are either electrons or holes. Holes are simply the absence of electrons, and behave for purposes of calculation as electrons with positive charges. When electrons account for the majority of charge carriers, the material is by definition n-type, whereas if holes are the majority carriers, the material is p-type. In both cases, minority carriers may also account for some degree of electrical conduction.

The resistivity, ρ, is the inverse of the conductivity:

$$\rho = \frac{1}{\sigma} = \frac{m}{ne^2\tau}, \tag{2.12}$$

and is related to the electrical resistance, R, by a ratio of the dimensions of the sample:

$$\rho = R\frac{A}{L}, \tag{2.13}$$

where *A* is the area and *L* is the length. As the resistivity is an intrinsic quantity, it is quite a bit more useful for analysis than is resistance.

The two factors that cause resistivity to vary from sample to sample are the carrier concentration and the collision relaxation time. The carrier concentration can generally be adjusted in compounds by doping atomic sites with similar elements that have excess or fewer charge carriers than the constituent elements of the compound. In the simplest case, for example, electrons could be injected into a IV-VI compound by doping the group IV element site with a group V element. If more holes were desired, a group V element could be doped onto the group VI element site. When electrons are added by doping, the dopant is referred to as a donor, whereas when holes are added, the dopant is an acceptor.

The relaxation time for charge carrier collisions is due to two main types of collisions: collisions with lattice phonons and collisions with impurities or mechanical defects within the crystal structure. As such the net relaxation time is written as

$$\frac{1}{\tau} = \frac{1}{\tau_L} + \frac{1}{\tau_i}, \tag{2.14}$$

where τ_L is the relaxation time for phonon scattering processes and τ_i is the relaxation time for impurity scattering. This allows the resistivity to be rewritten as

$$\rho = \rho_L + \rho_i . \tag{2.15}$$

Since the impurity term is generally temperature independent and the lattice term vanishes as T→0 K, the impurity term is equal to the resistivity at low temperatures,

$\rho(0) = \rho_i = \rho_o$, where ρ_o is known as the "residual resistivity," and the expression (2.15) for the resistivity can be modified accordingly:

$$\rho(T) = \rho_L(T) + \rho_o . \tag{2.16}$$

The residual resistivity is the resistivity due solely to the collisions of carriers with crystal impurities. This is the aspect of the resistivity that can be adjusted by sample preparation techniques.

Measurement Techniques

Resistivity and Thermopower

Measurements of the electrical resistivity and of the thermopower are performed within a custom-built apparatus (termed the R&S system) that is capable of cooling samples to 10 K [61]. Measurement pucks are custom-designed and can be easily inserted into and removed from the measurement system. These pucks can be built to suit the needs of the sample, but they all must fit onto a 24-pin integrated circuit (IC) chips that fit interchangeably into the R&S system. The most common design has a Cu base attached onto the bottom of an IC chip to serve as a thermal base for connecting the sample to the cold finger of the R&S system. This Cu base is attached by use of a commercially available Stycast® epoxy that has relatively good thermal conductivity. Another large Cu block is attached by screws to the Cu base, and its surface is tinned with solder. Samples of appreciable size (approximately 2 x 2 x 8 mm^3) and robustness are soldered onto one end to the Cu block, and then a smaller Cu block is soldered onto the other end of the sample. To this small Cu block, a small 39 Ω resistive heater is

attached by 5-minute epoxy, and it is kept electrically insulated from the sample by a thin layer of cigarette paper. Cu leads are soldered to the Cu blocks at either end of the sample and are used to inject current into the sample. Two more Cu lead wires are attached by solder or by the application of conducting Ag paint to the top surface of the sample, and these serve as voltage probes for measuring the sample resistivity. A differential thermocouple is constructed of 3 mil. Ag-Fe and Chromel wires by spark-welding, and it is inserted into grooves cut into the Cu blocks at either end of the sample. This thermocouple is electrically insulated from the Cu blocks by cigarette paper and is held in place by 5 minute epoxy. A schematic of this 4-probe resistivity and thermopower measurement setup is shown in figure 15.

The measurement cycle is controlled by a custom Labview® program and consists of a series of resistivity and thermopower measurements that are conducted within the space of about a minute at a relatively constant system temperature and with a temperature gradient of approximately 5 K across the sample. After a single measurement cycle, the system temperature progresses to the next set point and the cycle is repeated. Data is taken for both cooling and warming trends. The measurement cycle consists of three thermopower measurements interspersed with two resistance measurements that inject current in opposite directions. The thermopower measurements are averaged to produce a single datum. The voltage probes for the resistivity measurement, attached to the top of the sample, record a total voltage value, V_T of

$$V_T = IR + V_{TE}, \tag{2.17}$$

for a single measurement, where V_{TE} is the thermoelectric voltage, $V_{TE} = -\alpha\Delta T$. Clearly this term is an unwanted addition to the measurement, as the goal is an accurate determination of resistivity, but it can be eliminated by reversing the current and taking an average of the two voltage measurements:

$$V_T = \tfrac{1}{2}\left(IR + V_{TE} - \left(-IR\right) - V_{TE}\right) = \tfrac{1}{2}\left(2IR\right) = IR. \tag{2.18}$$

For a more detailed description of the Labview® algorithm, see reference 62.

Hall Effect

When a current is passed through a specimen in the presence of an external magnetic field, an electric field arises in a direction orthogonal to the magnetic field such that (as can be shown from the Lorentz force law, (2.9))

$$E_j = v_i H_k, \tag{2.19}$$

where v_i is the drift velocity, H_k is the applied magnetic field, and E_j is the Hall field, i.e. the electric field induced by the magnetic field. Note that *v*, *H*, and *E* are mutually orthogonal. In the single carrier model, the electrical current can be expressed simply as the drift velocity multiplied by the electronic charge *e* and the number of charge carriers, *n*:

$$J_i = nev_i, \tag{2.20}$$

so that by multiplication by *ne*, equation (2.19) can be rewritten as

$$neE_j = \left(nev_i\right)H_k = J_i H_k. \tag{2.21}$$

Then, rearranging (2.21) in a manner whose usefulness will become immediately apparent, we get

$$\frac{E_j}{J_i H_k} = \frac{1}{ne} \equiv R_H \,, \tag{2.22}$$

where $R_H = E_j / J_i H_k$ is defined to be the Hall coefficient, which is inversely proportional to the concentration of charge carriers, *n*. Thus, the Hall effect is commonly used as a method of determining the number of charge carriers in a sample.

In the current study, Hall effect measurements were performed in a Quantum Design® Physical Properties Measurement System (PPMS). The sample is affixed by thermally conducting GE varnish upon an electrically insulating layer of transparency film on top of a PPMS measurement puck. This configuration allows the sample to be in good thermal contact with the base while preventing electrical contact. One Cu lead wire is soldered to each end of the sample to provide the current flow, J_i. To measure the Hall voltage, two voltage probes on the top surface of the sample are needed, but a simple 2-wire configuration would require absolute precision in the placement of the probes in order to ensure that the measured voltage is due entirely to the Hall effect and that there is no additional contribution from to the resistance of the sample. Thus, three Cu wires are soldered to the top face of the sample, two on one edge and one on the opposing edge. The single wire on the opposite edge is placed as near as possible to the middle of the sample, and the two opposing wires are placed as symmetrically as possible on the opposite side (see figure 16). Having three voltage leads then provides a 2D probe area that allows the sample voltage measurement to be balanced via a potentiometer on the PPMS. Such balancing overcomes errors in placing the voltage probes precisely, with the net result being that the PPMS is able to measure the Hall effect accurately.

Once the sample has been mounted, it is loaded into the PPMS. The PPMS is able to achieve temperatures as low as 2 K simultaneous with magnetic fields up to 9 Tesla. The measurement cycle for probing the Hall effect consists of a series of magnetic field sweeps at a set temperature. After the room temperature magnetic field sweeps are performed, the sample is cooled to 280 K and the procedure is repeated. The sample is eventually cooled as low as 2 K, with the result being a magnetic field vs. resistance curve for each temperature, and is it easy to show that the slope of these plots is equal to the Hall coefficient:

$$\frac{E_j}{J_i H_k} \sim \frac{V}{IB} = \frac{R}{B} = R_H = \frac{1}{ne}. \tag{2.23}$$

Thus the *n* vs. *T* dependence can be measured, and if the electrical conductivity of the sample is known from an R&S measurement, we can then use the carrier concentration to help arrive at the mobility of the charge carriers, by use of the relationship

$$\sigma = ne\mu. \tag{2.24}$$

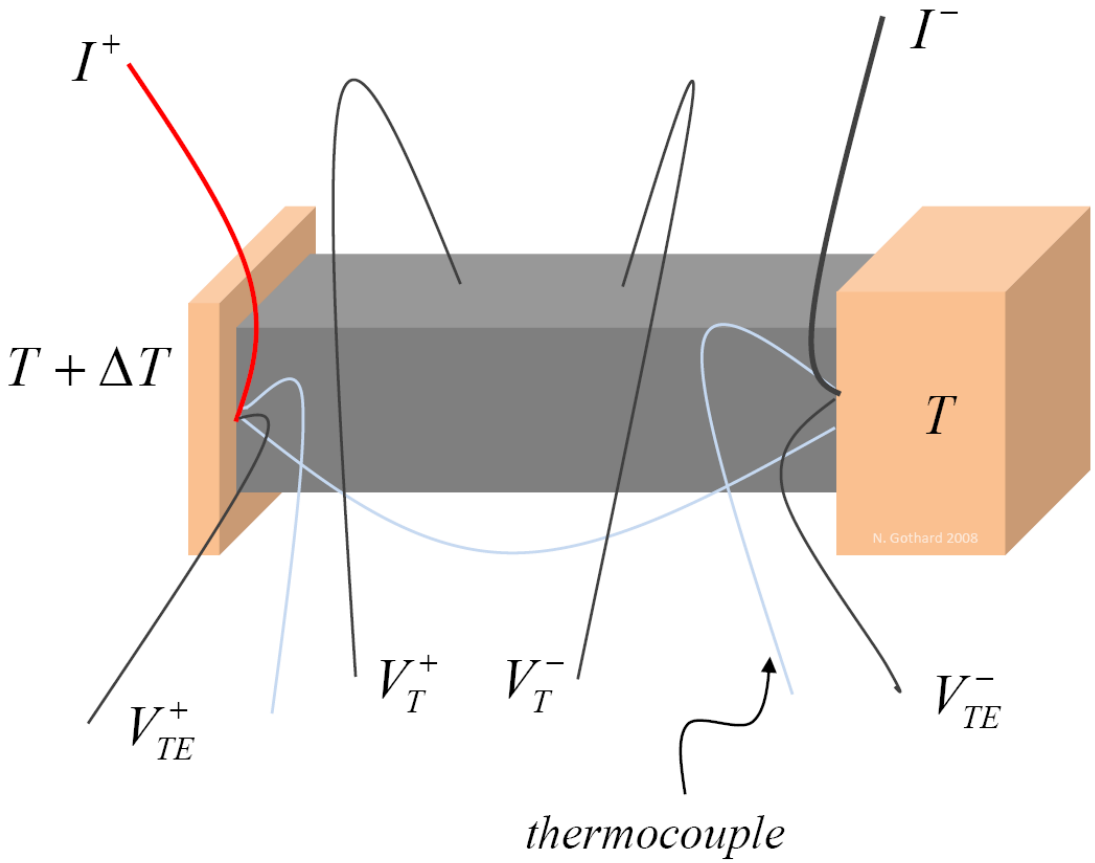

Figure 15. Four probe resistivity and thermopower (R&S) measurement puck schematic.

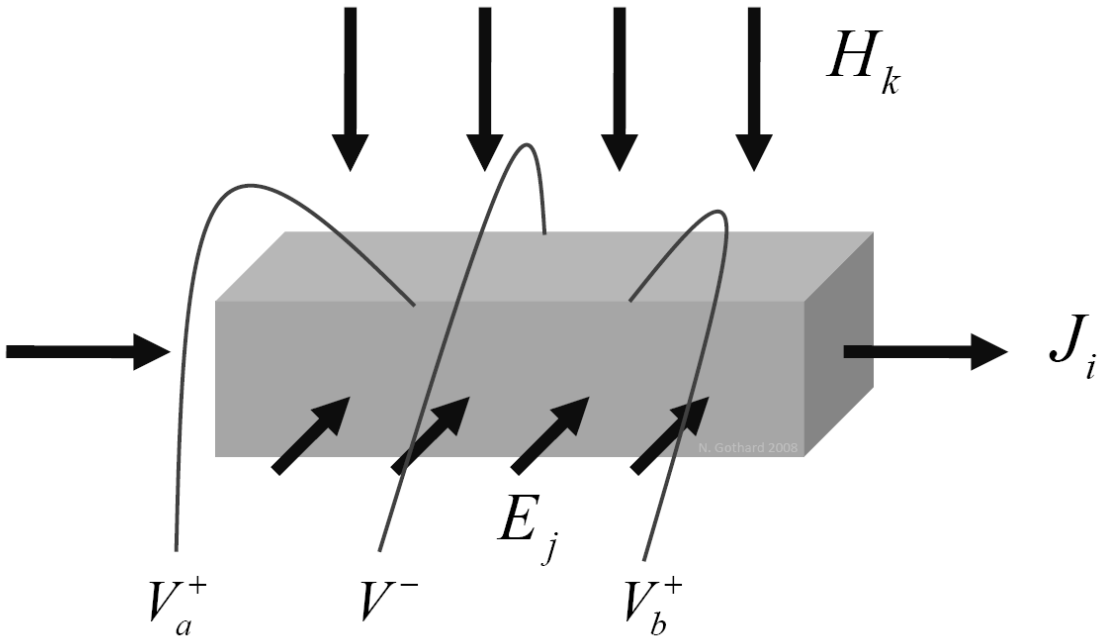

Figure 16. Hall Effect schematic.

THERMAL PROPERTIES

Phonons, Heat Capacity and the Debye Temperature

Before proceeding to a discussion of thermal conductivity, it is first helpful briefly to discuss the concepts of phonons, heat capacity, and the Debye temperature, which are integral to an understanding of thermal conductivity. The following discussion is based that developed in references [11] and [59].

Phonons are essentially quantized vibrations of the crystal lattice. In the simplest case of a cubic lattice, symmetry allows the crystal structure to be visualized in terms of an effectively infinite 1D chain of atoms, where *a* is the equilibrium inter-atomic distance, the locations of individual atoms in *k*-space are given by relative coordinates, q_s, and *T* is a large distance over which translational symmetry,

$$q_s = q_{s+T}, \tag{3.1}$$

holds true (figure 17). For a propagating wave, the general equation of motion holds to the form

$$q_s \sim \exp\left[i\left(sKa - \omega_K t \right) \right], \tag{3.2}$$

where *K* is the phonon wavevector and ω_K is the frequency of the phonon that has wavevector *K*. As in the case of electronic conduction, the system is again subject to periodic boundary conditions,

$$q_s\left(sa \right) = q_{s+T}\left(sa + T \right). \tag{3.3}$$

The phonon wavevector quantization condition,

$$K = \pm \frac{2\pi n}{T}, \tag{3.4}$$

where n = 0, 1, 2, …, $N/2$, arises from applying (3.3) to (3.2). When generalized to 3D, equation (3.4) specifies the set of all allowed phonon modes in a solid. It is clear from (3.4) that the spacing between allowed K values is $2\pi/T$. That is, there is one allowed phonon mode for every $2\pi/T$ in k-space. In 3D, the same condition holds for each K_i, such that there is only one allowed phonon mode for each volume increment of $\left(2\pi/T\right)^3$. Thus, a given K defines a sphere in k-space having a volume $4\pi K^3/3$ to which corresponds a maximum of

$$N = \left(\frac{T}{2\pi}\right)^3 \left(\frac{4\pi K^3}{3}\right) \tag{3.5}$$

phonon modes. In the Debye approximation, K is given by

$$K = \omega/\nu\,, \tag{3.6}$$

where ν is the velocity of sound, assumed to be constant, and ω is the phonon frequency. If the volume in k-space is taken to represent the entire crystal lattice, then (3.5) gives the total number of all phonon modes available to the crystal. As N is a function only of ω, it is apparent that there exists a certain cutoff frequency, ω_D, that corresponds to the point at which all of the phonon modes are activated. This is essentially the maximum allowed phonon frequency. The subscript on ω refers to the fact that the calculation is carried out in the Debye approximation.

By expressing the total number of states in a given volume of k-space as a function of frequency, (3.5) allows a calculation of the density of available states per unit frequency, $D(\omega)$, to be calculated:

$$D(\omega) \equiv \frac{dN}{d\omega}. \tag{3.7}$$

Combining (3.5) and (3.6) into (3.7) and taking the derivative yields

$$D(\omega) = \frac{\omega^2 T^3}{2\pi^2 v^3}. \tag{3.8}$$

This expression will be of use when calculating the specific heat.

Specific heat capacity at constant volume is defined by the Maxwell relation,

$$C_V = \left(\frac{\partial U}{\partial T}\right)_V, \tag{3.9}$$

where *U* is the internal energy, which for purposes of this discussion is the energy of the phonons. Phonon energies are described by the harmonic oscillator problem of quantum mechanics. In such a case, a specified vibrational mode has associated energies given by

$$E_{K,p} = \left(\langle n \rangle + \tfrac{1}{2}\right)\hbar\omega_{K,p}, \tag{3.10}$$

where $\langle n \rangle$ is the number of phonons occupying that particular energy state at thermal equilibrium (the thermal equilibrium occupancy), and the energy is indexed by the particular phonon wavevector, *K*, and polarization, *p*, of the given state. The term $\frac{1}{2}\hbar\omega_{K,p}$, referred to as the zero-point energy, is added to the energy for any given state and as such is typically disregarded in analysis of the energy. The energy can therefore be expressed for convenience simply as $E_{K,p} = \langle n \rangle \hbar\omega_{K,p}$. The thermal equilibrium occupancy is given by the Planck distribution function:

$$\langle n \rangle = \frac{1}{\exp\left(\hbar\omega_{K,p}/k_B T\right) - 1}, \tag{3.11}$$

and the energy of the phonons in a specified mode is therefore

$$E_{K,p} = \frac{\hbar\omega_{K,p}}{\exp\left(\hbar\omega_{K,p}/k_B T\right)-1}. \tag{3.12}$$

The internal energy is the summation of this energy over all wavevectors and polarizations:

$$U = \sum_K \sum_p \frac{\hbar\omega_{K,p}}{\exp\left(\hbar\omega_{K,p}/k_B T\right)-1}. \tag{3.13}$$

The Debye approximation assumes isotropic polarization, so that the summation over *p* may be replaced by a factor of 3, one for each dimension of polarization. Further, the dependence of *K* upon ω can be exploited to replace the summation over *K* with an integral over ω:

$$\sum_K \rightarrow \int d\omega D(\omega), \tag{3.14}$$

scaling by the density of states. Thus the expression for the internal energy, (3.13), becomes

$$U = 3\int_0^{\omega_D} d\omega D(\omega) \frac{\hbar\omega}{\exp\left(\hbar\omega/k_B T\right)-1}, \tag{3.15}$$

where the limits of integration are 0 and the maximum frequency, ω_D. Using (3.8) for $D(\omega)$, a calculation of $C_V = \left(\partial U/\partial T\right)_V$ yields

$$C_V = 9Nk_B\left(\frac{T}{\theta}\right)^3 \int_0^{x_D} dx \frac{x^4 e^x}{\left(e^x-1\right)^2}, \tag{3.16}$$

after a bit of mathematics and a change of variables. Here $x \equiv \hbar\omega / k_B T$ and θ is the Debye temperature, defined in terms of the cutoff frequency, ω_D, as

$$\theta = \frac{\hbar}{k_B}\left(\omega_D\right)^{1/3}. \tag{3.17}$$

Since it depends directly on the maximum allowed phonon frequency, the Debye temperature is often used as a gauge of the thermal properties of a solid. High values of θ imply that the maximum phonon frequencies are also high. Such a system is expected in the extreme to be composed of light atoms bound by heavy interatomic forces. Low values of θ likewise imply heavy atoms and light interatomic forces. Further, θ can be thought of as the temperature at which most of the phonon modes in a material are activated [11,59].

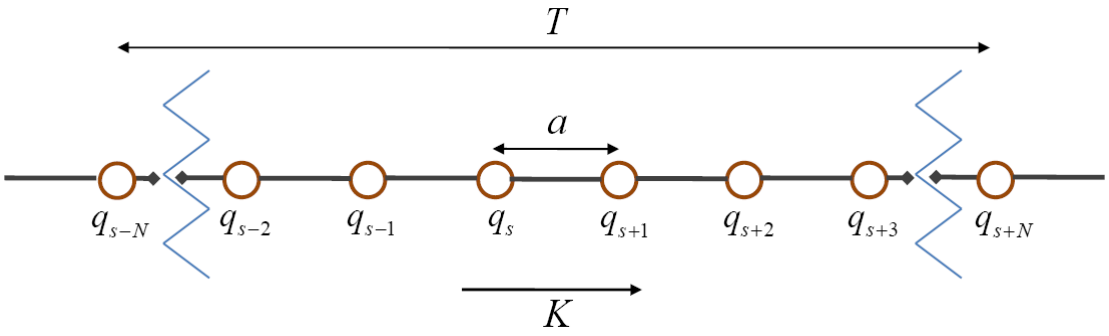

Figure 17. A chain of N atoms represented in *k*-space. Interatomic distance is *a*, and translational symmetry requires that $q_s = q_{s+T}$.

Thermal Conductivity

Heat transport in solids is related to the thermal gradient of the solid by

$$Q = -\kappa A \frac{\Delta T}{\Delta x}, \tag{3.18}$$

where Q is the flux of thermal energy, ΔT is the change in temperature from one end of the sample to the other, κ is the thermal conductivity, and A is the cross sectional area. In solid materials, heat conduction is due to heat transport by the charge carriers, κ_e, as well as by lattice vibrations, κ_L. The total thermal conductivity is the sum of these two factors:

$$\kappa_T = \kappa_e + \kappa_L . \tag{3.19}$$

It can be demonstrated that the electronic contribution to the thermal conductivity follows the following relationship:

$$\kappa_e = A\left(\frac{k_B}{e}\right)^2 \sigma T, \tag{3.20}$$

where k_B is Boltzmann's constant, e is the electronic charge, σ is the electrical conductivity, and A is a constant which assumes a value of 2 for non-degenerate semiconductors and 3.3 in the case of degenerate semiconductors [57]. The complete constant of proportionality takes the form of the Lorenz number,

$$L = \frac{\pi^2}{3}\left(\frac{k_B}{e}\right)^2 \left(\frac{m_e v^2}{2\varepsilon_0}\right), \tag{3.21}$$

which allows (3.20) to be written in the more familiar form known as the Wiedemann-Franz law:

$$\kappa_e = L\sigma T, \tag{3.22}$$

which is used extensively to estimate the electronic thermal conductivity. Though often referred to as a law, the fact that it depends on the Lorenz number, which is strictly not a constant, cautions against using it for hard quantitative analysis. Nevertheless, it is a useful approximation for estimating the contribution of charge carriers to the thermal transport in many semiconductors.

From kinetic theory, it can be demonstrated that

$$\kappa_L = \tfrac{1}{3} C_V v l \,, \tag{3.23}$$

where C_V is the specific heat, v is the speed of sound in the solid, and l is the mean free path of the phonon. Because κ_e is directly proportional to the electrical conductivity through (3.22), attempts to alter the thermal conductivity often focus by necessity on introducing mechanisms that will affect the phonon mean free path.

Thermal resistivity, $W = 1/\kappa$, arises from three main phonon scattering mechanisms: phonon-phonon scattering, scattering by the crystal lattice, and phonon-electron scattering. Phonon scattering by the lattice can be due to grain boundaries, point defects, or dislocations. Phonon-phonon scattering mechanisms can be of two types: normal, "N-processes," or Umklapp, "U-processes." N-processes describe the scattering of two phonons that results in a third phonon that still lies within the first Brillouin zone (figure 18a). Thus, such collisions do not result in a change in the net phonon momentum and consequently do not contribute anything to thermal resistance. On the contrary, U-processes result in the creation of a phonon whose wavevector lies outside of the first Brillouin zone (figure 18b). The point to which this wavevector extends outside of the

first Brillouin zone is physically equivalent to a point within the first Brillouin zone, and it can therefore be mapped back into the first Brillouin zone by the addition of a reciprocal lattice vector, **G**. The result of such a process is a change in the net phonon momentum, and thus these processes do contribute to thermal resistance. At moderately high temperatures, i.e. temperatures approaching and above room temperature, Umklapp processes are the primary phonon scattering mechanism. In this regime, thermal conductivity follows the general form [63]

$$\kappa_L \approx 1/T. \tag{3.24}$$

At low temperatures, the number of phonons is relatively small, and phonon-phonon scattering is not a major effect. Instead, scattering of phonons by the grain boundaries becomes important. Here, the upper bounds on the integral in (3.16) go to infinity, and the result is that

$$C_V \approx \left(\frac{T}{\theta}\right)^3. \tag{3.25}$$

The implication of this for the lattice thermal conductivity is that

$$\begin{aligned} \kappa_L = \tfrac{1}{3} C_V v l &\approx \tfrac{1}{3}\left(\frac{T}{\theta}\right)^3 v l \\ \Rightarrow \kappa_L &\approx T^3. \end{aligned} \tag{3.26}$$

In the intermediate temperature range, a combination of grain boundary scattering and point defect scattering is present [64]. The interrelation of these three scattering processes for a representative κ_L vs. T curve is depicted in figure 19. A high peak in the low to intermediate temperature range indicates a highly ordered crystal structure, whereas a flattening of this peak indicates increased disorder in the crystal structure.

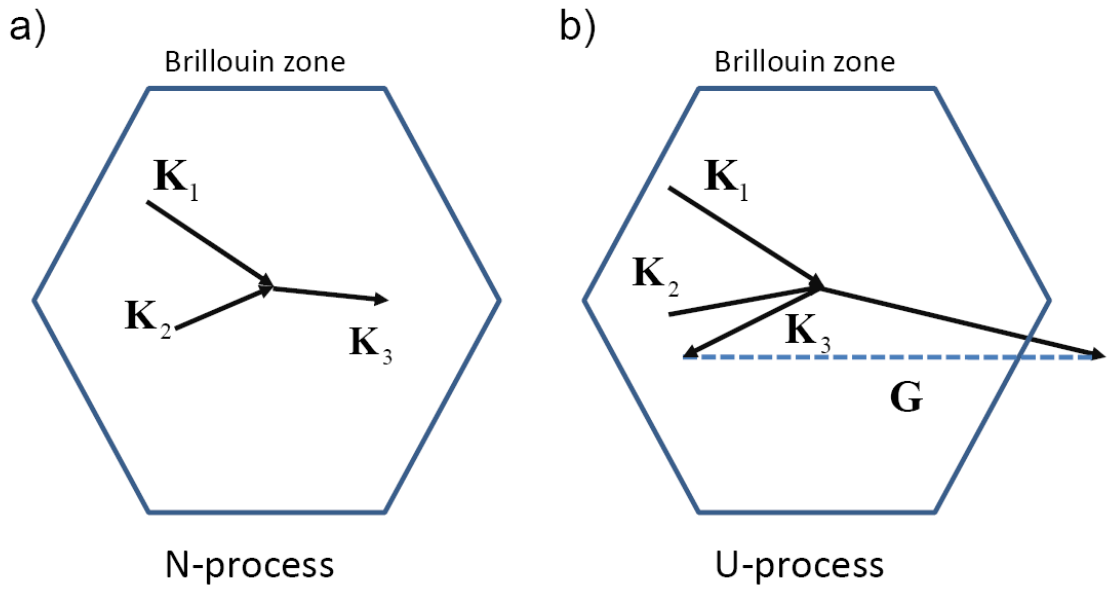

Figure 18. Phonon wavevector scattering within the first Brillouin zone for a) momentum-conserving N-processes, and b) U-processes, in which momentum is not conserved.

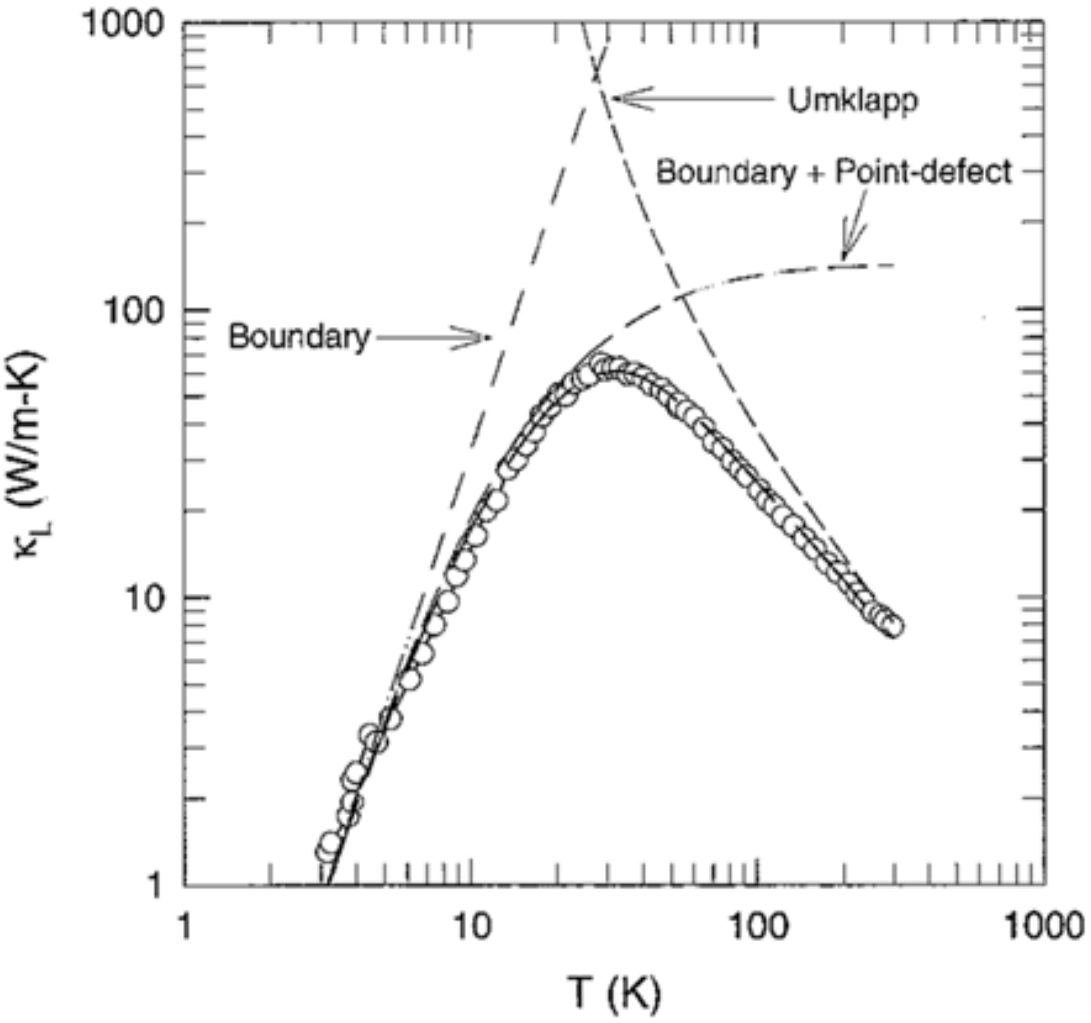

Figure 19. Typical lattice thermal conductivity vs. temperature curve, showing the influence of various scattering mechanisms [64].

Measurement Techniques

Low Temperature

Low temperature measurements of thermal conductivity are carried out in custom built systems attached to closed-cycle He cryocoolers that are capable of cooling the system to 10 K [65]. Similar to the R&S systems, the thermal conductivity (TC) systems feature a removable puck design for quick and easy insertion and removal of samples. The puck and its receptacle are built from commercially available Quantum Design® pucks that are sold for use in the PPMS, but certain modifications are made in order to adapt the puck to the custom TC measurement system. A square Cu block with four holes tapped for screws is affixed by Stycast® epoxy onto the base of the puck, and to this block two smaller Cu sample holders are affixed. Samples of size similar to those used for acquiring low temperature resistivity and thermopower data (2 x 2 x 8 mm^3) are soldered vertically into these sample holders, and a precision strain gage (120 Ω) is attached to the top of the sample by 5 minute epoxy for use as the power source. The Cu block at the base of the sample provides a heat sink that is in contact with the cold finger of the system. Measurements of the temperature gradient across the sample are performed via a 1 mil. constantan-chromel differential thermocouple that is soldered to Cu wires that are in turn affixed to one face of the sample using Stycast® epoxy. A schematic is depicted in figure 20.

Using the ΔT obtained from the thermocouple, the thermal conductance, K, is calculated using

$$P = P_{applied} - P_{lost} = K\Delta T \ . \qquad (3.27)$$

That is, K is simply the ratio of the power flux through the sample to the temperature differential measured at the points of contact of the thermocouple, assuming that the power loss term, P_{lost}, is negligible. Once the thermal conductance is known, the measurement may be scaled by the dimensions of the sample to arrive at the thermal conductivity, κ:

$$\kappa = K\frac{L}{A}, \tag{3.28}$$

where L is the length separating the points at which the thermocouple makes contact with the sample, and A is the cross-sectional area of the sample perpendicular to the direction of heat transport.

In practice, it is virtually impossible to measure the power loss term, which means that the conductivity calculation is based solely on the input power, with the assumption that power losses have been reduced to the point of negligibility. In order to minimize the loss term, a number of measures have been introduced into the system. First, since copper is an effective thermal conductor, with a thermal conductivity of ~400 W $m^{-1}K^{-1}$, the Cu leads from the strain gage heater are cut near to the heater, and phosphor bronze ($\kappa \approx 50$ W $m^{-1}K^{-1}$) wires are soldered in their place to make the electrical connection to the measurement puck. This measure helps reduce any thermal loss from the heater through the connecting wires. Next, after insertion into the system, the sample puck is covered by a small Cu radiation shield that encloses the sample snugly and is thermally sunk with the top of the cold finger. This shield is plated with Au on the interior to increase reflectivity and thereby help prevent heat loss by radiation from the

environment immediately surrounding the samples. Over this, a secondary, larger Cu radiation shield is attached to the base of the cold finger. The cold finger itself is constructed of Cu at the top layer, which is attached to a bronze lower layer, with thermal contact between the two being aided by a thin layer of Apiezon® N grease. The addition of the lower bronze layer helps provide thermal stability to the system, effectively decoupling the sample stage from the rough temperature fluctuations driven by the cryocooler at the base of the system. This enables the fine temperature control to the sample environment that is so vital to accurate thermal transport measurements, while also minimizing the likelihood that the samples will undergo thermal shock. The entire cold finger apparatus is then enclosed under a vacuum shield, and roughing and turbo pumps are employed to bring the pressure down to the order of 10^{-5} Torr, thereby nearly eliminating heat loss due to convection.

In spite of all the precautions, however, some degree of heat loss due to radiation is unavoidable, particularly as the sample temperature approaches room temperature. Such an effect is typically visible in the lattice thermal conductivity data in the range of 200-300 K in the form of a gradual departure from the *1/T* dependence characteristic of the U-processes. The power loss from the sample by radiation is given by the Stefan-Boltzmann law:

$$P_{loss} = \sigma\left(T_{sam.}^4 - T_{surr.}^4\right), \tag{3.29}$$

where $T_{sam.}$ is the temperature of the sample and $T_{surr.}$ is the temperature of the surroundings. During measurements of thermal conductivity, the sample temperature is

$T + \Delta T$, and a Taylor expansion of ($T_{sam.}^4 - T_{surr.}^4$) shows that the first order power loss term is $T^3 \Delta T$. The lattice thermal conductivity data can be corrected for such radiation losses by fitting the portion of the curve that approaches room temperature to the expected $1/T$ form and verifying that the new curve is consistent with (3.29). That is, if $\Delta\kappa$ between the original data and the *1/T*-fitted curve goes as T^3, it can generally be assumed that the data correction is valid. If the correction term, $\Delta\kappa$, is substantially large, however, it is best to attempt to retake the data using a sample of the same material that has a larger cross section. A larger cross section means less surface area by percentage, with the consequence of less percentage of radiation loss. Unfortunately, in this study it was not feasible to produce nanocomposite samples of large enough cross sections to sufficiently minimize radiation effects, and typically the uncorrected lattice thermal conductivity data are presented. This is discussed in greater detail in the relevant sections of chapter 5.

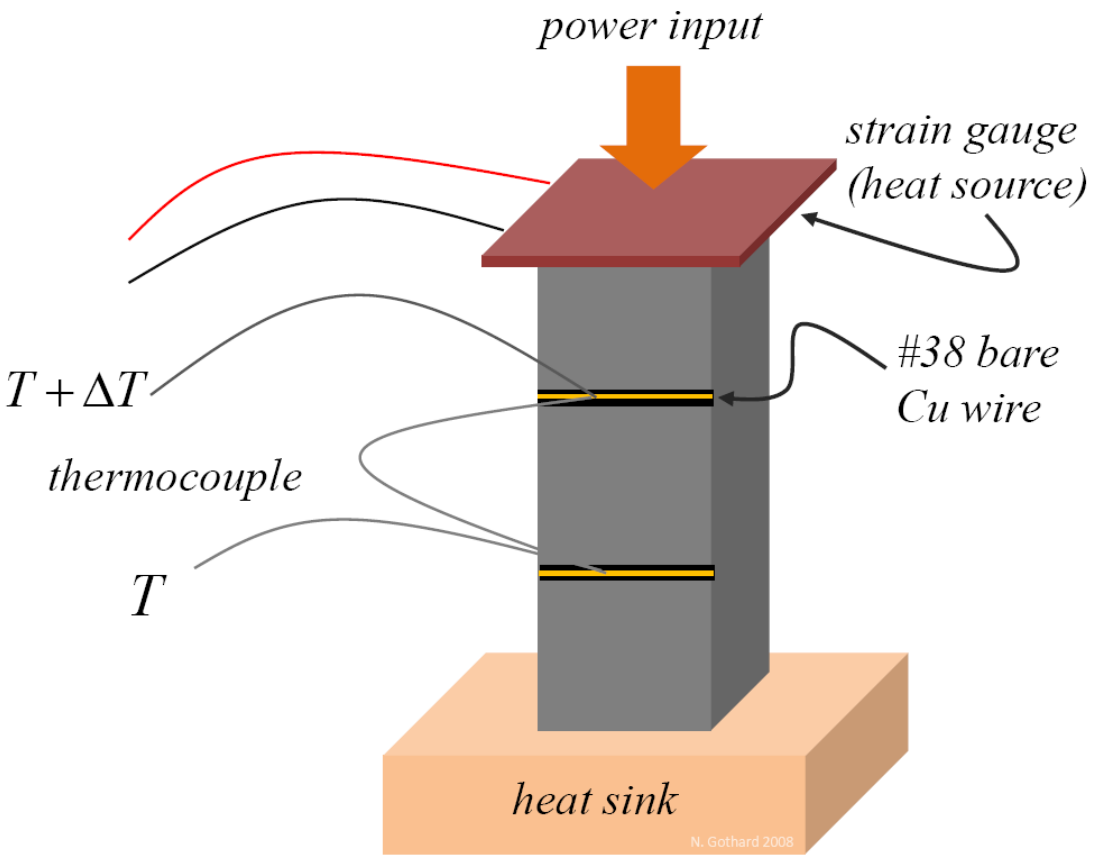

Figure 20. Low temperature thermal conductivity schematic.

High Temperature

Measurements of the thermal conductivity at high temperatures are performed by means of a Netzsch® LFA 457 MicroFlash™ laser flash system together with a DSC 404 C Pegasus® Differential Scanning Calorimeter (DSC). The DSC is capable of measuring the specific heat up to ~1750 K, while the laser flash provides measurements of the thermal diffusivity, *D*, up to ~ 1450 K. Thermal conductivity can then be calculated using

$$\kappa = dDC_V , \tag{3.30}$$

where *d* is the sample density. One disadvantage of this method of measurement is that all the measurements cannot be performed on the same sample piece due to the different geometries of the sample chambers for the DSC and the laser flash. DSC measurements are typically performed on samples on the order of 2 mm on a side, of much smaller size than are used in either the laser flash or the low temperature systems, and which may be fairly irregular. The DSC produces a C_V vs. T curve from which the saturation value of C_V can be taken for use in the thermal conductivity calculations. The laser flash system is able to accommodate samples of various geometries, but the sample size must conform to roughly a 12.5 mm outer diameter by 5 mm thick cylinder, although a thickness of 2 mm is preferable for best results. Conveniently, this is exactly the size of most pellets from the hot press. In order to promote even heating of the surface as well as to inhibit the reflection of incident radiation, the entire sample is sprayed with graphite prior to insertion into the system. One face of the sample is then irradiated with a low energy laser pulse (~15 J / pulse) [66], and as the sample heats up, the opposite face begins to

emit thermal radiation. From the emitted radiation, a graph of ΔT vs. t is created, and the rise half time, $t_{1/2} = t\left(\frac{1}{2}\Delta T_{\max}\right)$, can be estimated. After accounting for the sample thickness, L, the thermal diffusivity, D, can be calculated as follows [67]:

$$D = 0.1388\frac{L^2}{t_{1/2}}. \tag{3.31}$$

A caveat to this approach is that the thermal diffusivity, and consequently the thermal conductivity, is measured in a direction perpendicular to the direction in which it is measured in the low temperature TC system, so one must take care when analyzing data in the case of anisotropic samples.

SYNTHESIS OF MATERIALS

Growth of Bulk Bi_2Te_3

Perhaps the most straightforward method to grow bulk Bi_2Te_3 is by solid state reaction. This method consists of combining high purity elemental Bi and Te in a ratio of 2:3, mixing well, and sealing in a quartz ampoule under vacuum. Initial attempts involved placing a sealed ampoule filled with crystalline Bi_2Te_3 in a furnace and slowly moving the ampoule through a hot zone having a temperature above the melting point of Bi_2Te_3 (585^{o}C) [68]. A typical movement rate is 9 cm/hr. As Te is quite volatile, however, it was found that this method still tends to result in ingots of inhomogeneous composition, particularly at the ends of the sample, but that a high ambient temperature could help minimize Te diffusion [69].

Another growth technique is the directional freezing technique, a method that produces polycrystalline Bi_2Te_3 samples in which the individual crystal grains are aligned. This effect is accomplished by melting Bi_2Te_3 in a furnace with either a vertical or a horizontal orientation and subsequently establishing a temperature gradient across the melt. The gradient is maintained such that the melt begins to solidify slowly from one end to the other, and the individual grains align as the melt freezes. Depending on the speed of withdrawal from the furnace, however, significant Te segregation to the last segment of the melt to freeze can be problematic [70].

Refinements to the directional freezing technique are the use of vertical Stockbarger or Bridgman furnaces. In this method, Bi_2Te_3 is dropped vertically at a very slow rate (on the order of 1 cm/hr) through a double furnace system that has a sharp

temperature gradient between the two furnace segments. The top zone is maintained above the melting point of Bi_2Te_3 while the bottom zone is maintained below the melting point. This technique may be performed with either an open or closed quartz tube, but an open system has a greater tendency to result in the loss of Te. As excess Te has the effect of making the compound p-type, Bridgman furnaces in the open configuration can, in fact, be used to produce n-type bismuth telluride via the controlled loss of Te [71].

Directional freezing and Bridgman techniques are in general unsatisfactory for producing high-quality doped samples of bismuth telluride, however, due to the tendency of the dopants to migrate throughout the sample melt. The solution to this problem is to modify the apparatus to allow only a small portion of the sample to be molten at a given time. This small molten volume limits the diffusion of dopants throughout the sample, with the result being a greater degree of homogeneity in the sample composition. This modification is referred to as the zone melting technique [68]. The rate of freezing has also been shown to have an effect upon the resistivity, thermopower, and lattice thermal conductivity, as, for example, in $BiSbTe_3$ alloys [72].

Nanomaterials Growth Techniques

Pulsed Laser Vaporization

There are a couple vaporization techniques that can be employed to grow nanoscale samples of various solid state materials. The first of these that will be discussed here is the pulsed laser vaporization (PLV) technique. In this method, the sample is attached to a rotating target holder that passes through an O-ring seal into the center of a quartz tube. The opposite end of the tube has a lens that allows a laser pulse

to pass through and strike the sample (figure 21). The energy from the incident laser pulse vaporizes a small section of the sample, and a gentle Ar flow carries the vapor downstream where nucleation may occur. In this study, the laser used was an Nd:YAG laser (1064 nm excitation, 650 mJ/pulse, 10 Hz), and synthesis trials were carried out in an Ar atmosphere at a temperature below the melting point of the material. Such a temperature allows the target material to remain solid while a small portion is vaporized by the laser pulse. The vaporized portion quickly condenses into liquid droplets, which are carried downstream by the gas flow. Nanoparticle nucleation may occur either on a water-cooled Cu cold finger near the exit of the furnace or upon substrates that may be coated with nano-scale catalyst particles. The choice of element for these particles is governed by the requirement that they remain solid at the temperature to which the furnace is heated. An alternative approach to catalysis is the seeding of the target itself with catalyst particles. This growth mechanism is known as the vapor-liquid-solid (VLS) mechanism, and the fact that is has been successfully applied to a variety of semiconducting compounds causes it to be of interest for the production of bismuth telluride nanowires [73].

Early experiments, however, showed the condensation of nanoscale particles to occur in some cases prior to laser ablation of the sample target. An image from transmission electron microscopy (TEM) of such particles is presented in figure 22 [74]. If the laser is not activated, the growth technique is technically that of chemical vapor deposition (CVD), rather than PLV, and CVD growth is discussed in the following section. It was found after many trials that the PLV technique is not well suited to the

growth of bismuth telluride nanomaterials, due both to the relatively low melting point of bismuth telluride as well as to the volatility of Te. Related work has shown, however, that Bi nanorods can be grown via PLV by ablation of a target of densified Bi powder with the addition of a tiny percentage of a nanoparticle Au catalyst particles [75].

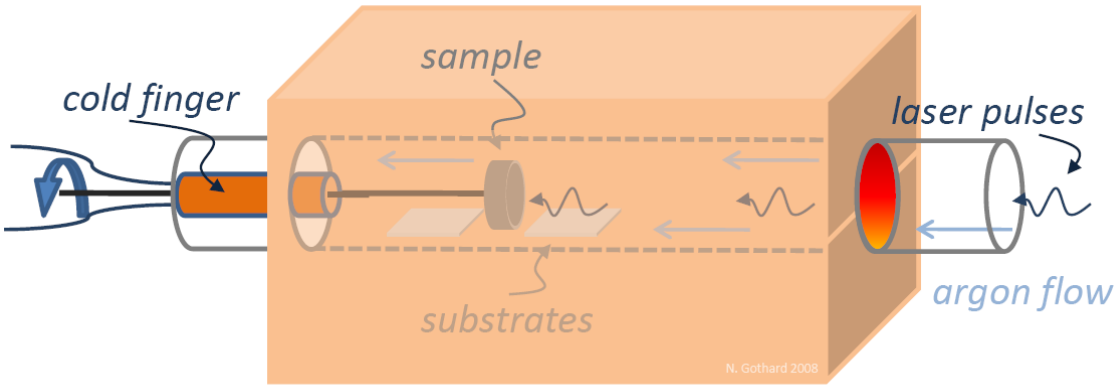

Figure 21. Schematic of the PLV system. A rotating sample is ablated by laser pulses within a sealed quartz tube at temperature and under a gentle argon flow.

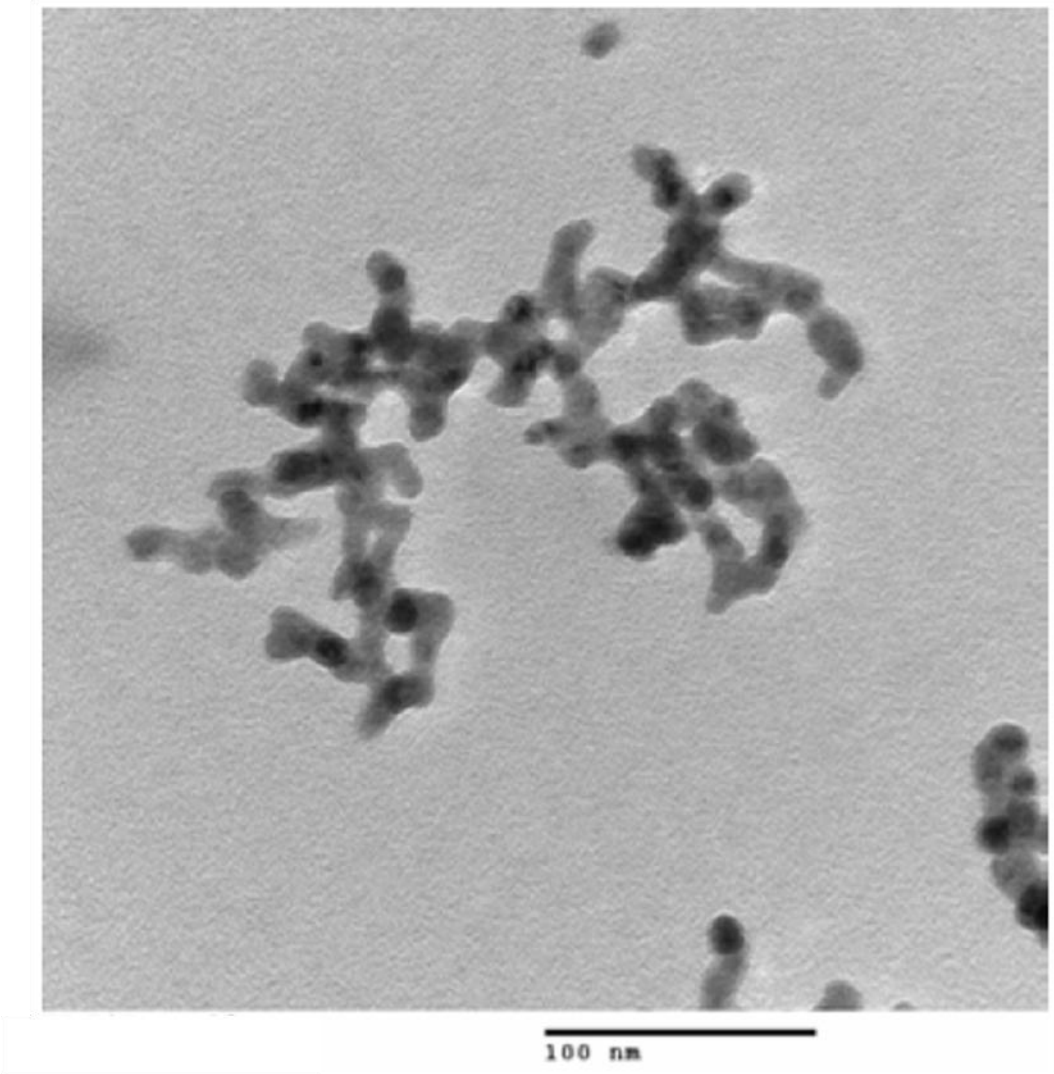

Figure 22. TEM of particles collected from the Cu cold finger during a PLV run in which the laser was not activated.

Chemical Vapor Deposition

The chemical vapor deposition (CVD) technique relies upon the vaporization of source materials at a given temperature under a gas flow in a sealed quartz tube. As vaporization occurs, the vapors are carried downstream to nucleation sites, on the walls of the quartz tube as well as on substrates. A catalyst material may occasionally be mixed with the source powders or dispersed on the substrates. The CVD method has been widely used for several years as a versatile means of growing large quantities of carbon nanotubes [76], including doped carbon nanotubes [77] as well as multi-walled carbon nanotubes with Y-shaped junctions [78]. Further, work done concurrently with the present study within the Tritt research group has shown the CVD method efficacious for producing gram quantities of PbTe nanocubes, where the dimensions of the nanocube can be controlled by adjusting the argon flow rate and the temperature of the furnace [79]. These considerations, combined with the aforementioned observation of the sublimation of bismuth telluride source materials in the PLV system, are the motivation for the use of CVD in the attempt to produce nanoscale bismuth telluride materials.

The experimental setup is pictured in figure 23. Source powders are taken from a slug of a commercially grown p- or n-type $Bi_{1-x}Sb_xTe_{1-y}Se_y$ ingot, generously supplied by Marlow Industries [80]. The slug is placed in a ceramic boat, which is then positioned within a quartz tube that passes through a hinged furnace. Custom designed end caps (not pictured) were machined with O-ring vacuum seals as well as gas and vacuum feedthrough connections. After purging the quartz tube several times to eliminate atmospheric gases, a gentle flow of argon is introduced and the temperature is gradually

increased to a point within the range 700-1200^{o}C, well above the melting point of bismuth telluride (585^{o}C). As the furnace temperature ramps to the set point, a gray / black dusting of powders gradually becomes evident near both the inlet and the exhaust ends of the tube, but primarily at the furnace boundaries. This material is then collected and analyzed with the hope of finding nanoparticles of bismuth telluride.

In this study, material was selected from either an Sb-doped p-type ingot, stoichiometrically $Bi_{0.4}Sb_{1.6}Te_3$, or a Se-doped n-type ingot, $Bi_2Te_{2.7}Se_{0.3}$. When the p-type material was used as a source, examination of the powders by SEM revealed an overwhelming majority of spherical, typically micron-sized particles (figure 24a), although powders that were found deposited on the quartz tube at the upstream boundary of the hot zone tended to have smaller size scales (figure 24b). Occasionally, one of these particles would exhibit nanoscale protrusions giving the appearance that nanowires had nucleated on a core particle and grown radially outward (figure 25). Energy dispersive x-ray analysis (EDX) performed within the SEM chamber revealed the smooth micron-size spheres from figure 24 to be predominantly tellurium. The composition of the parent material is such that if the composition of the particles were pure $Bi_{0.4}Sb_{1.6}Te_3$, the expected percentages of the constituent elements would be Bi : 8%, Sb : 32%, and Te 60%. The Bi : Sb : Te percentages from the EDX data (figure 26) correspond, on the other hand, to nearly a 25% excess of Te in the samples. X-ray diffraction of the samples that evidenced the crystalline protrusions from the core of the particle (see figure 25) revealed the presence of crystalline Te structures (figure 27), while EDX showed that Te is present at nearly 95 atomic percent in those samples. The notable lack of Bi in powders

grown by this method is attributed in part to the relatively low percentage of Bi present in the source material and also to both the high volatility of Sb and Te with respect to Bi. The large mass of Bi may also play a role in its absence in the product material, as such a heavy element would not be expected to travel as far as Sb or Te, which are both considerably lighter.

When the Se-doped n-type bismuth telluride source ingot ($Bi_2Te_{2.7}Se_{0.3}$) was used as the source, the morphology of the nanoparticles produced was in general more diverse that the spherical particles obtained from the p-type ingot material. Although it was still not uncommon to find the predominantly Te spherical particles in the resultant powders, such particles were typically found interspersed with more irregular and often elongated particles, such as those depicted in figure 28. EDX of the powders shown in figure 28 reveals the presence of Bi in much higher quantities than was previously obtained (figure 29). Here, the excess Te is thought to be due to the presence of the spherical particles previously identified as predominantly Te, while the more irregular, elongated particles are presumed to be more Bi-rich. However, the presence of oxygen at over 15 atomic percent suggests that the particles likely are heavily oxidized. Excluding the oxygen peak from the calculation of atomic percentages of constituent elements, so that the atomic percentages of Bi, Te, and Se are calculated relative to the total count of the sum of those elements, the excess Te concentration is approximately 26% (figure 29 inset), comparable to what was found when the p-type ingot was used.

Studies of CVD growth of nanoscale PbTe crystals proposed that a turbulent flow was beneficial for producing nanomaterials in the exhaust region of the tube [79]. It was

found in the current study that higher temperatures (1100-1200^{o}C) tended to increase the complexity of the patterns that were formed by the nanoparticle powder on the walls of the quartz tubing, as well as the number of different regions that could be distinguished, particularly in the upstream section of the quartz tube that protruded from the furnace. Figure 30 is digital camera image of the inside of the quartz tube from the upstream end of the tube after a trial with a temperature set point above 1100^{o}C. It is evident from the patterns of the deposits that the gas flow in this region is rather complex, resulting in a number of visibly distinguishable powder regions. SEM images corresponding to these distinct regions are overlaid on the picture in figure 30. It was found that where complex exhaust patterns such as these were observed, nanoparticles having hexagonal cross-sections and moderately high aspect ratios were formed in higher selectivity than the amorphous Te spheres (figure 31). Elemental analysis of such areas, however, still revealed excesses of Te (figure 32), as well as significant oxidation. The spectrometer also picked up a signal from the carbon tape that was used to secure the sample to the SEM sample mount. Recalculating the atomic percentage values to exclude the O and C inclusions again reveals an excess of Te of nearly 24% from the $Bi_2Te_{2.7}Se_{0.3}$ composition, relative to the total amount of Bi, Te, and Se present. XRD shows the presence of many peaks that can be attributed to a number of phases of bismuth telluride, such as Bi_2Te_3, $Bi_2Te_{2.7}Se_{0.3}$ (source material), Bi_3Te_4, Bi_4Te_3, and Bi_2Te, as well as to an elemental phase of Te that has a hexagonal unit cell (figure 33). Because the conditions of cooling from vapor to liquid to solid in the environment of the CVD cannot be controlled with great precision, consideration of the Bi-Te phase diagram shows how

easily any number of Bi_xTe_y phases may readily be formed when Bi and Te are present in the range of ~30-60 atomic percent Te (figure 34).

A number of pellets were produced via cold-pressing from such powders of the various nanoparticle morphologies obtained by CVD growth, but various problems such as sample compaction and cohesion as well as contact resistances prevented an accurate study of the transport properties of these powders. Further, although the CVD was shown capable of producing sub-micron-sized particles of bismuth telluride, factors such as the relative lack of control over the phase and the low selectivity of particles that were not amorphous Te caused this approach to be set aside in favor of the more reliable hydrothermal synthesis method (described below). It is concluded that although the CVD method does show some promise for producing nanoparticles of bismuth telluride, the inherent lack of control over the conditions of nucleation severely hamper its viability for growing a single phase of a bismuth telluride compound with sufficient purity and in sufficient quantities for incorporation into bulk-nano composites [81].

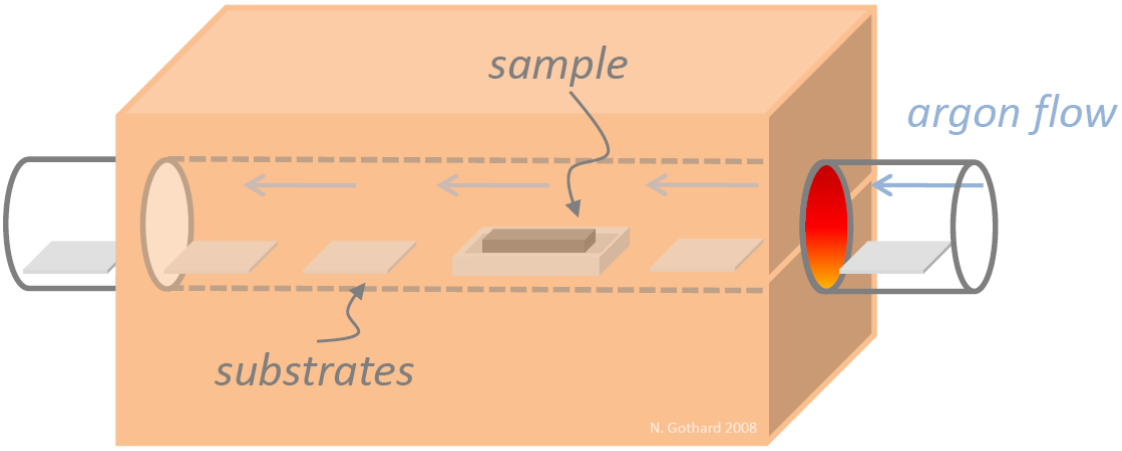

Figure 23. Schematic of the CVD system. A sample is subjected to high temperatures and the resulting vapors are carried downstream by an argon flow.

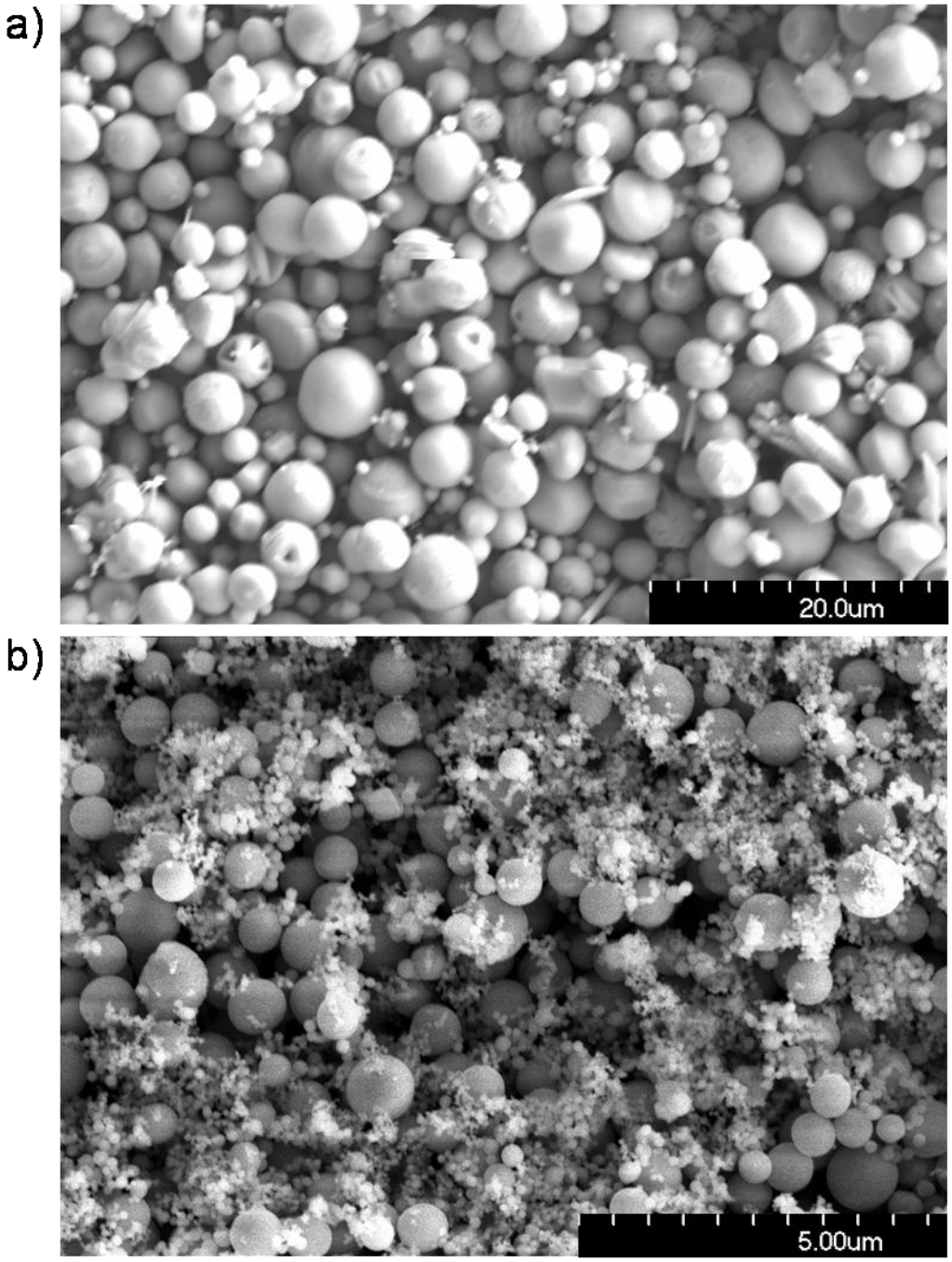

Figure 24. a) SEM image of particles collected from the downstream end of the quartz tube when p-type bismuth telluride is used as the source. b) Particles collected from the upstream end of the quartz tube.

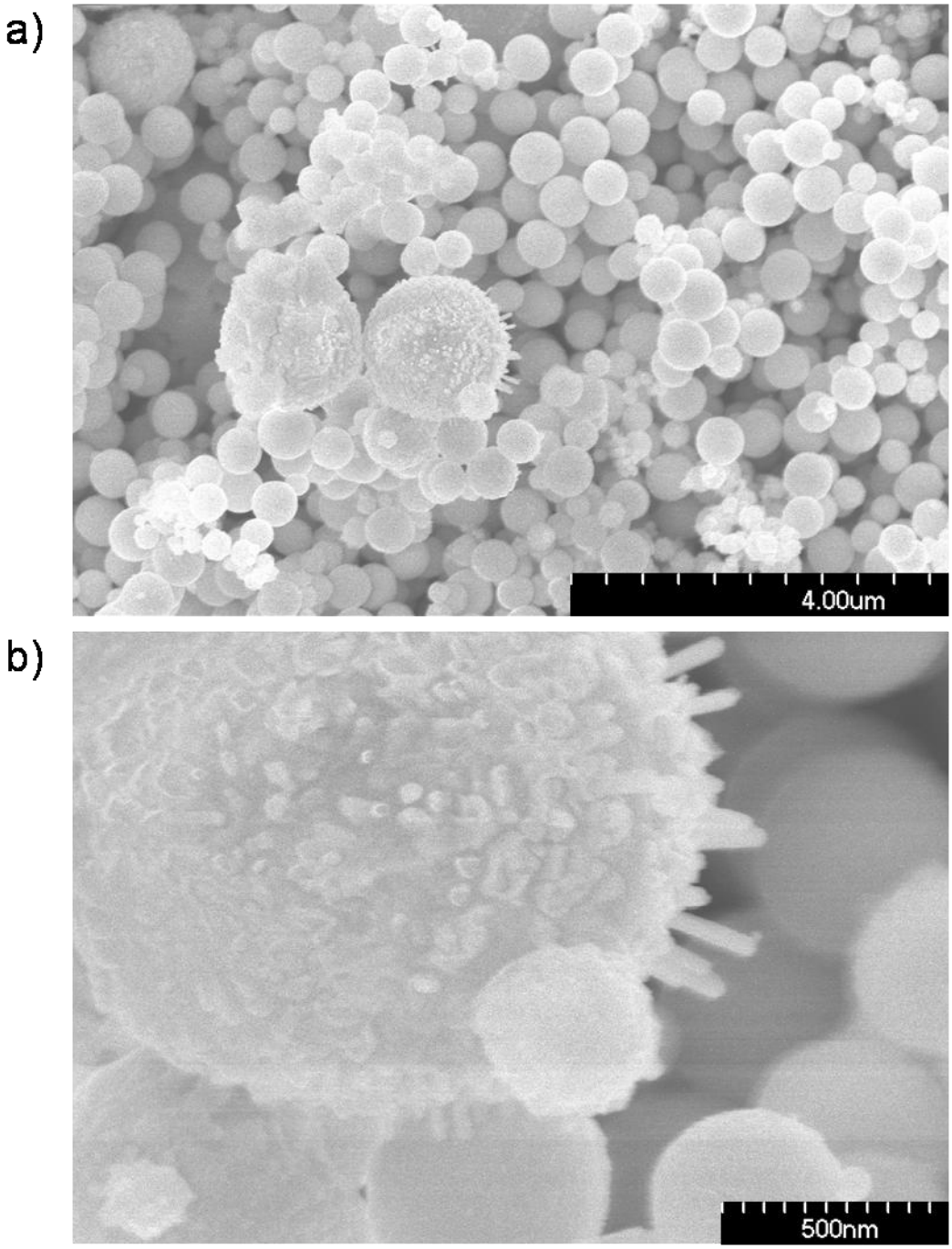

Figure 25. a) Presence of a spherical particle with rod-like protrusions emanating from its core and b) close-up image of the same. The source is p-type bismuth telluride.

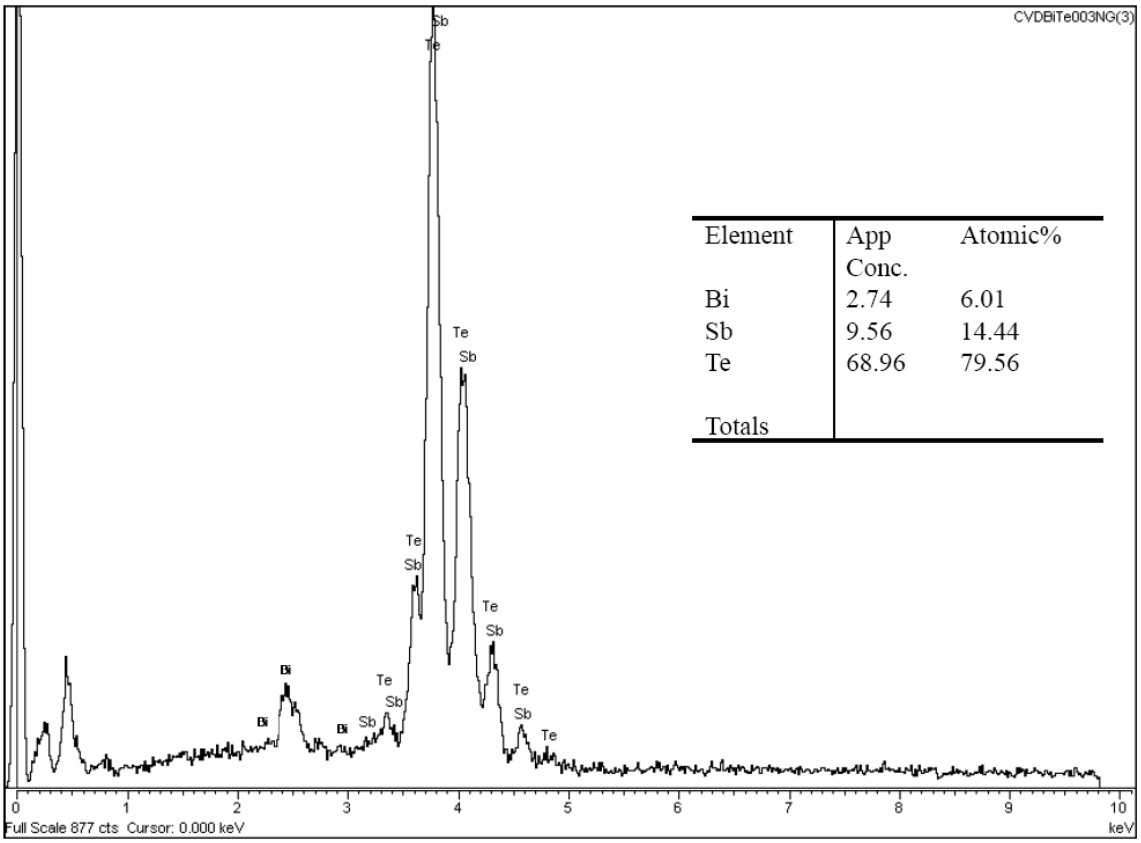

Element	App Conc.	Atomic%
Bi	2.74	6.01
Sb	9.56	14.44
Te	68.96	79.56
Totals		

Figure 26. Elemental composition of micron-size spheres obtained by the CVD method, showing an excess of Te of ~25% as compared to the source $Bi_{0.4}Sb_{1.6}Te_3$ ingot.

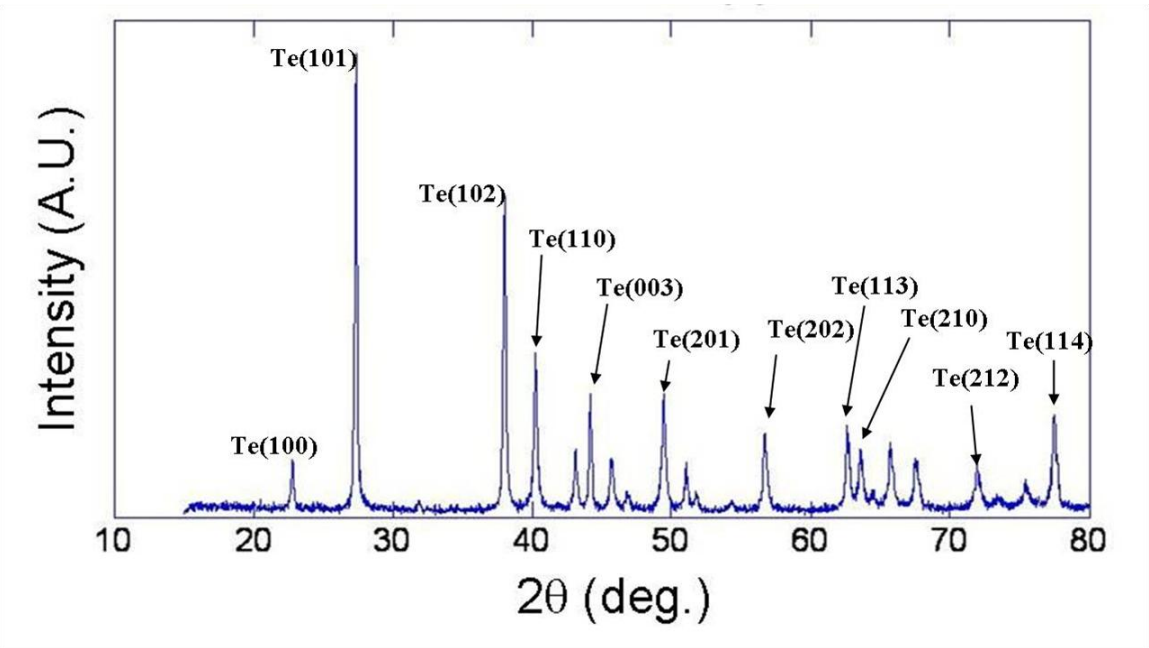

Figure 27. XRD data for the sample that exhibits radial rod-like protrusions (figure 25). All peaks are identified as a crystalline Te phase.

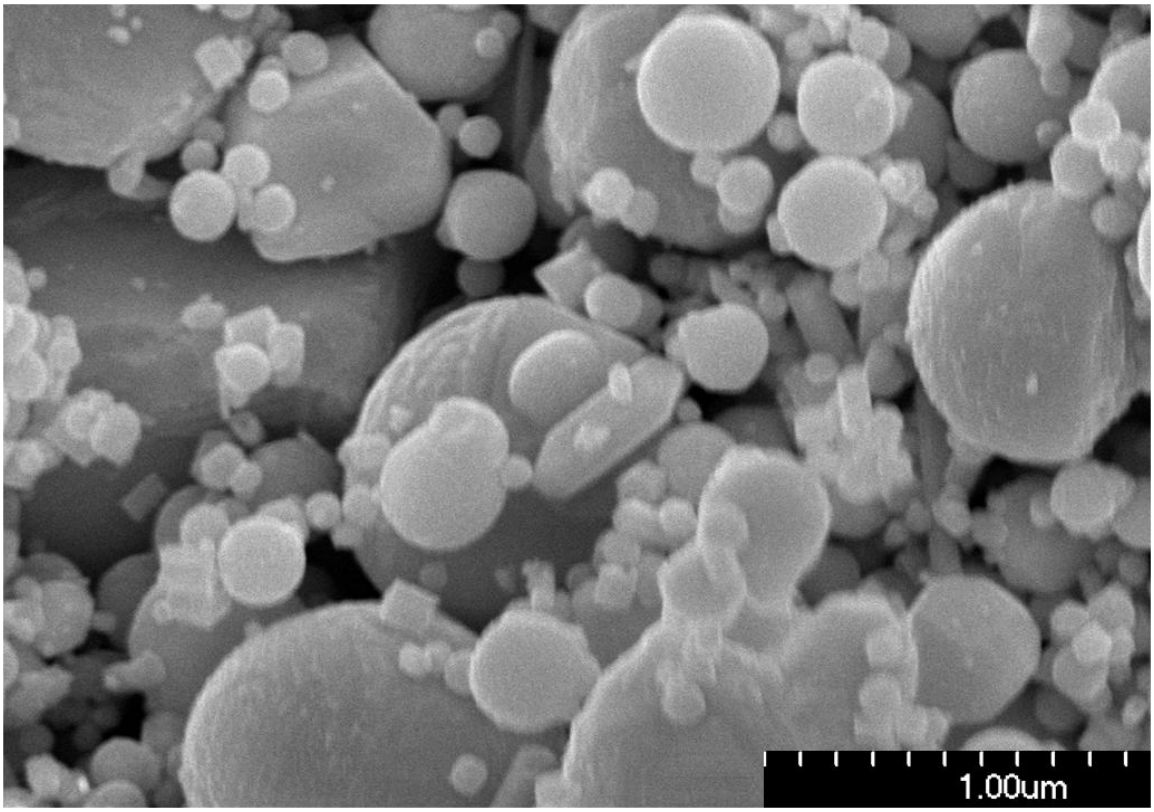

Figure 28. SEM micrograph of particles grown using n-type $Bi_2Te_{2.7}Se_{0.3}$, showing an increase in the number of non-spherical particle morphologies as compared to the p-type synthesis runs.

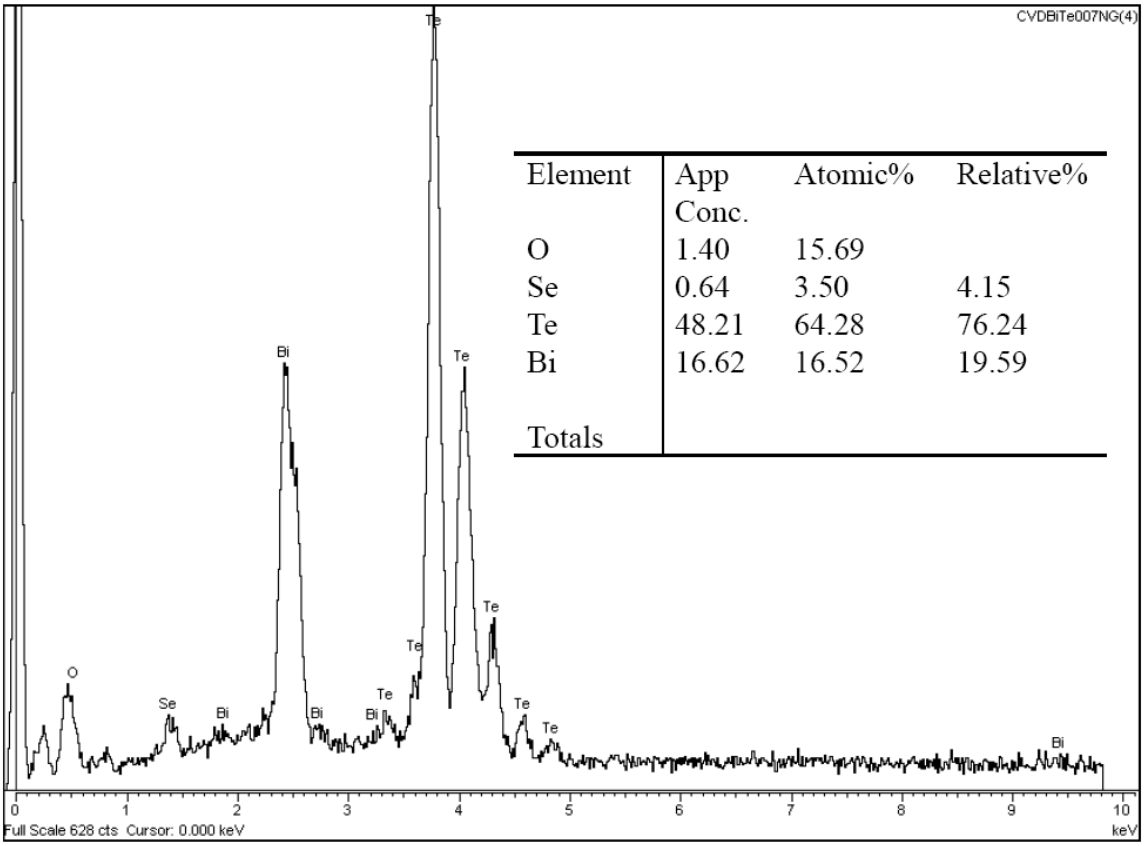

Element	App Conc.	Atomic%	Relative%
O	1.40	15.69	
Se	0.64	3.50	4.15
Te	48.21	64.28	76.24
Bi	16.62	16.52	19.59
Totals			

Figure 29. EDX of powders grown using the n-type $Bi_2Te_{2.7}Se_{0.3}$ source material. The Bi peak is noticeably higher than for the p-type synthesis runs (figure 26), but there is a strong O peak. Relative percentages give the elemental atomic percentages with O excluded from the calculation.

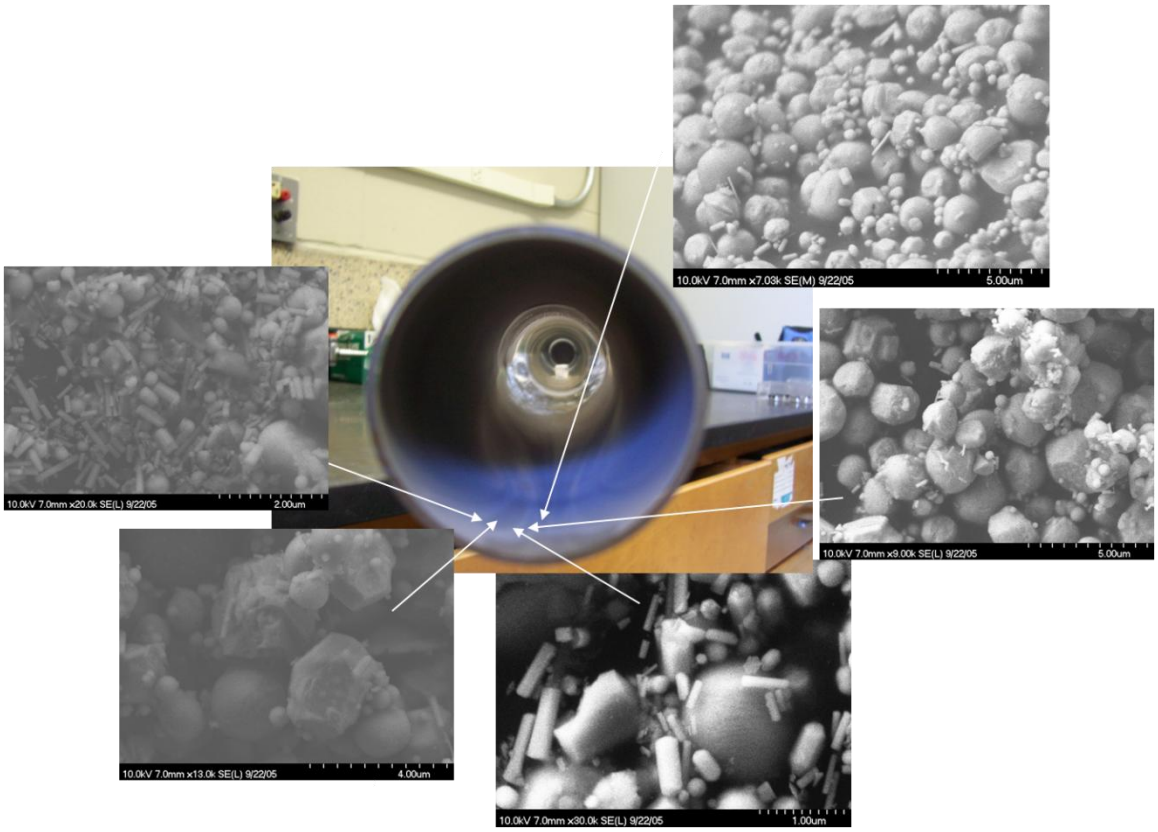

Figure 30. Digital camera image of the interior of a quartz tube following a high temperature CVD run. Swirling exhaust gases created several distinct regions, and the morphology of observed particles was found to vary somewhat as a function of position along the tube.

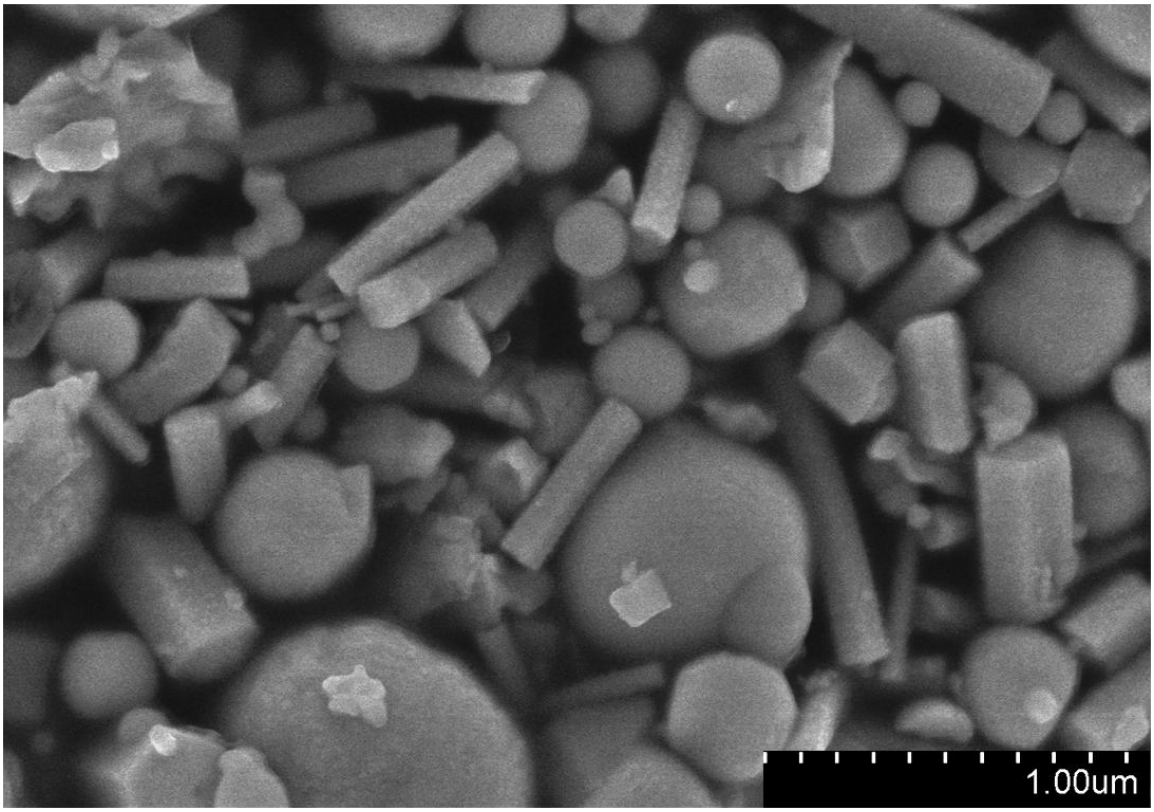

Figure 31. SEM image of particles taken from a taken from a highly active exhaust point for a high temperature CVD run using the n-type bismuth telluride source material. A mixture of spherical and hexagonal cross-sectional particles is visible.

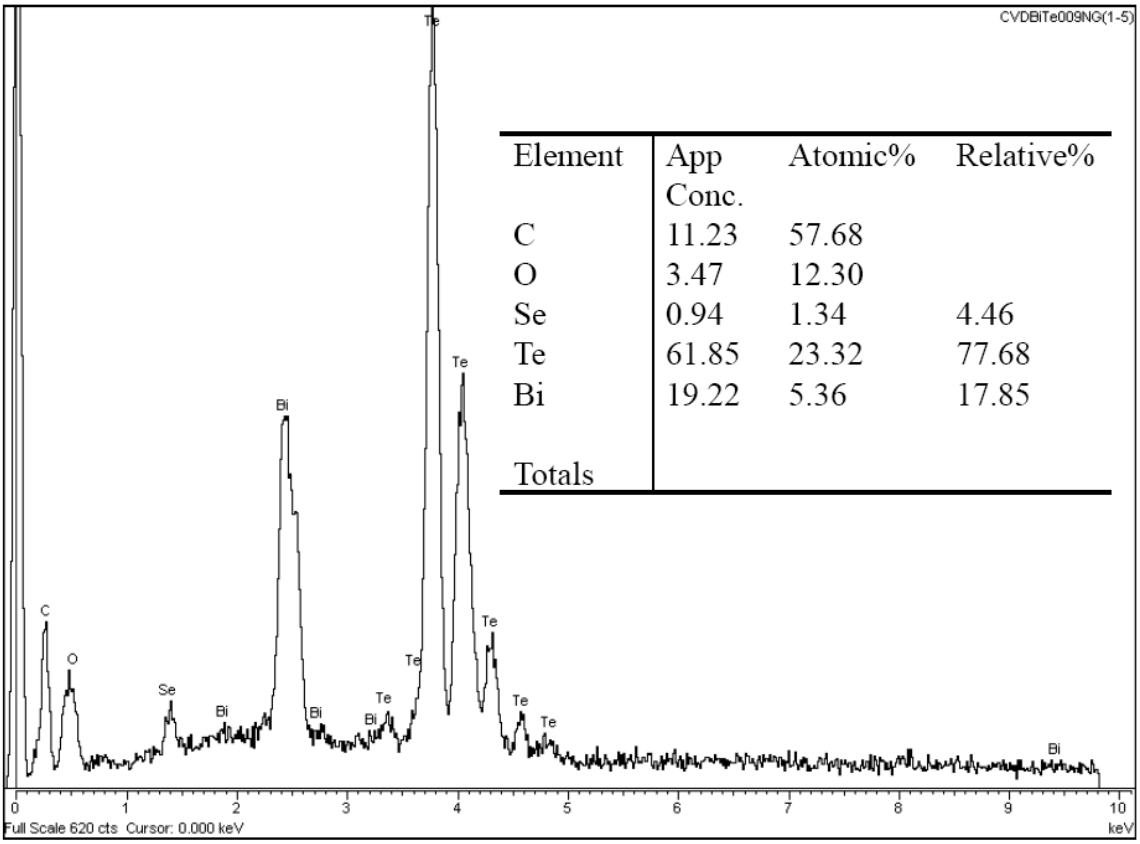

Figure 32. EDX of a mixture of particle morphologies, such as that shown in figure 31. The C peak is due to the C tape that was used to hold the sample, and oxidation is again observed. Te is present in excess of 24%.

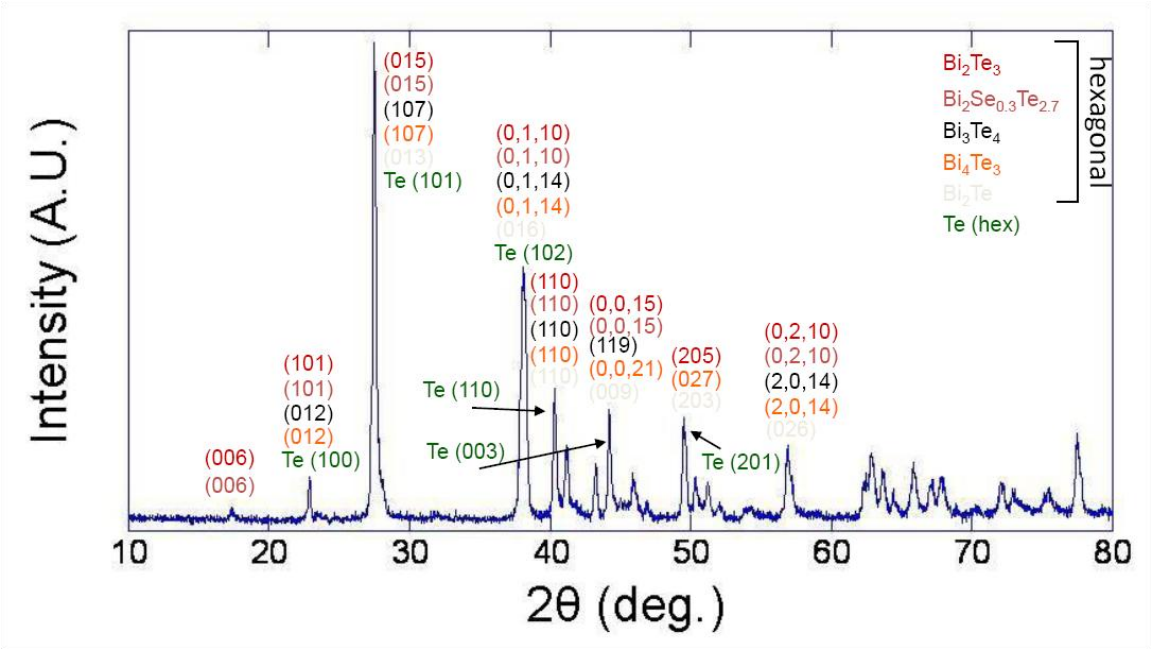

Figure 33. X-ray data of non-spherical particles such as those in figure 31. Five phases of bismuth telluride are identified, as well as one of crystalline Te, having a hexagonal unit cell.

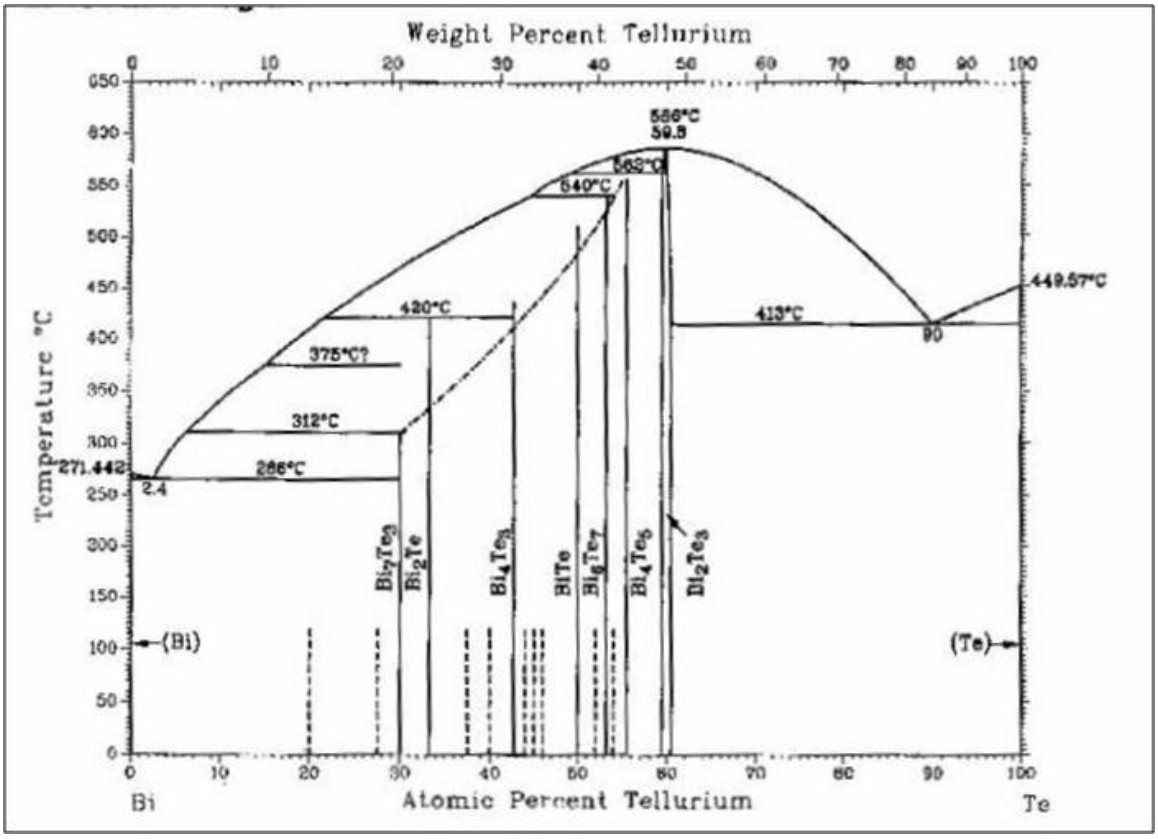

Figure 34. Phase diagram for the Bi – Te system. A variety of Bi_xTe_y compounds may be formed on cooling a mixture of Bi and Te from high temperatures (such as observed in figure 33). (From reference 82).

Solvothermal Method

A more recent technique for growing thermoelectric materials on the nanoscale is the method of solvothermal synthesis. This method relies on a low temperature reaction between compounds in a solvent, where the reactants and synthesis conditions are chosen in such a way that the products are the desired compound plus additional non-reactive byproducts. For example, Bi_2Te_3 was originally synthesized in this way by combining $Bi_2(C_2O_4)_3$ with elemental Te in an organic solvent according to the following reaction [83]:

$$Bi_2\left(C_2O_4\right)_3 + 3Te \rightarrow Bi_2Te_3 + 6CO_2 \,. \tag{4.1}$$

The technique used in the present study is as follows: $BiCl_3$ is combined with either pure Te powder or a compound containing Te, such as Na_2TeO_3 or TeO_2, in a Teflon-lined autoclave. Additional reactants such as NaOH (pH controller) and $NaBH_4$ may be added, and the autoclave is subsequently filled with distilled water to ~85% capacity. After sealing the autoclave, the mixture is heated to 150^{o}C, where it is held for 24 h. Synthesis can also be accomplished in an open beaker, and in this case the temperature is held at 60^{o}C for 24 h and the reactants NaOH and $NaBH_4$ are not added. After the reaction completes, the solute is filtered from the solvent, and the powder obtained from the reaction is washed thoroughly with distilled water, ethanol, and acetone, to remove impurities, and then dried in a vacuum chamber at room temperature [84,85]. If distilled water is selected as the solvent, the technique is commonly called the hydrothermal method.

This method has been found to be quite effective for producing large amounts of Bi_2Te_3 powders with dimensions on the nanoscale. Figure 35 is an SEM image characteristic of such hydrothermally grown bismuth telluride nanoparticles. Particle morphologies are typically irregular-spherical, although occasionally nanotubules may also be formed. XRD confirms the phase to be primarily Bi_2Te_3. Synthesis runs ordinarily yield ~0.5-1 grams of nanoparticle powder, sufficient to produce approximately 2-4 nanocomposite pellets, depending on the volume fraction of nanoparticles used to make the composite. This method of synthesis may also be adapted to grow with a variety of nanoparticles besides bismuth telluride such as, for example, BiSb, Bi_2S_3, and PbTe.

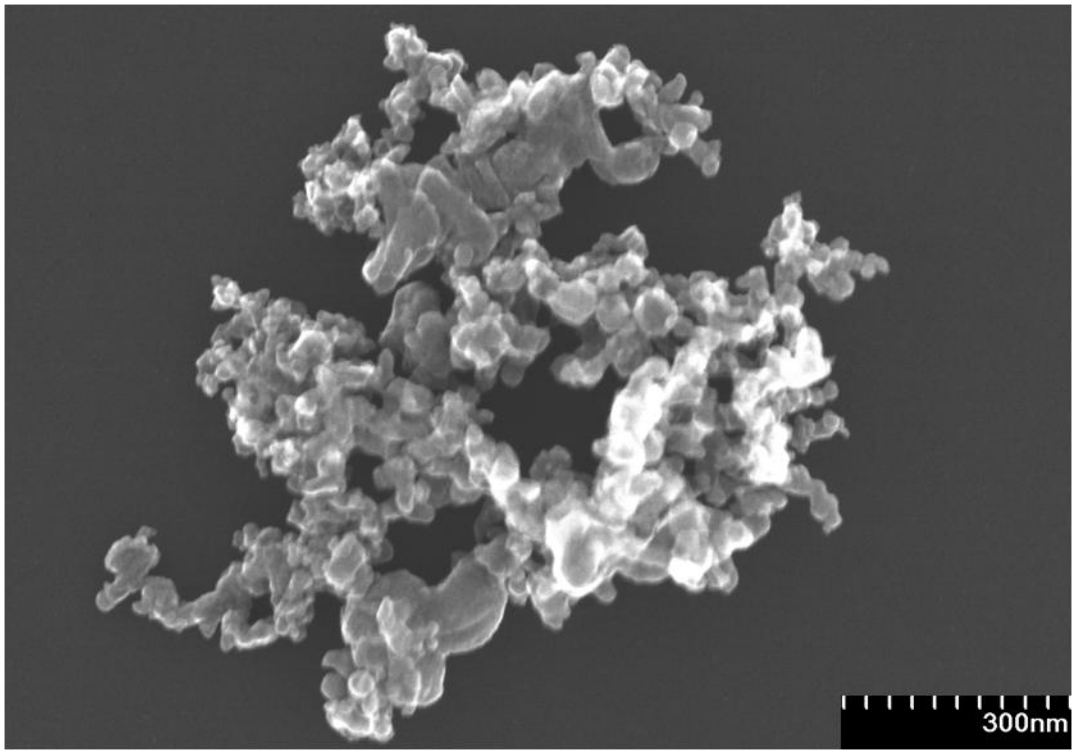

Figure 35. SEM of bismuth telluride nanoparticles grown via the solvothermal method.

Composite Hot Pressing

The production of nanocomposites was accomplished primarily by means of a uniaxial hot press, custom-built by Thermal Technology, Inc [86]. The hot press consists of two vertically aligned steel press rams powered by a hydraulic pump, capable of supplying up to 10 tons of pressure. These built-in rams each have threaded extensions that allow the user to attach custom rams constructed from the material of choice. As the custom attachments, but not the built-in steel rams, will operate within the furnace enclosure, it is important to select a material with a favorable temperature-strength profile in the desired temperature range. In this case, pyrolytic graphite was deemed suitable.

Enclosing the hot press chamber is a water-cooled vertical furnace that uses a graphite heating element to drive the temperature to a maximum of 2000^{o}C. The furnace chamber is raised and lowered by compressed air, and it rests upon an O-ring seal on the bottom when in the lowered position. A set screw is used to adjust the amount of weight the chamber exerts upon the O-ring, giving the user control over the quality of vacuum the chamber is able to achieve. Roughing and diffusion vacuum pumps allow the chamber to be evacuated to the order of 10^{-6} Torr. Typically, however, the press is not operated under vacuum, but rather the roughing pump is used in conjunction with an external gas line to purge the chamber with an inert gas, and hot pressing generally takes place at pressures of 0.3-0.5 psi in a N or Ar atmosphere. It is also possible to pressurize the chamber to 30 psi, but such conditions are not needed for the present work. At high positive pressures, the chamber seal would be maintained by sealing the moveable

furnace chamber to the base of the assembly by use of three set screws. A picture of the hot press system is presented in figure 36.

A small viewport is located on the front of the furnace chamber to allow external instrumentation to monitor such things as mass-flow spectroscopy, e.g., but at high temperatures this window is also useful to examine the system for any evidence of mechanical breakdown such as buckling of the sample press rams under temperature and pressure. Cutoff switches for the furnace power, hydraulic pump, and vacuum system are available on the front panel of the hot press control assembly and two switches are used to set the functionality of the hydraulic press. One switch allows the pressure range to be toggled between "low range", which ranges from 0-600 kg, and "full range", which runs from 600-10000 kg, where 1000 kg is equivalent to one metric ton. The other switch controls the position of the press rams and is used manually to control whether the rams are actively moving up, down, or are in the ready position. When the pressure range is set to "full" and the press ram position is set to "up", the system achieves a baseline pressure of 600 kg and is ready to press samples. The press ram position switch also serves as a safety cutoff for the hydraulic pressure, in the event a problem occurs during hot pressing. Temperature, hydraulic pressure, and chamber gas pressure are all monitored and controlled by a Eurotherm® 2704 control panel mounted on the front control panel of the press assembly. These parameters can be set either manually or by a user-defined multi-step program that auto-ramps them to the desired level.

The press rams are machined from industrial grade pyrolytic graphite cylinders that have outer diameters (O.D.) of 2 1/8 in. and lengths of 12 in. and are commercially

available through Poco Graphite [87]. This material was chosen for a number of performance criteria, including high compressive strength (up to ~0.1 GPa) and a relatively low coefficient of thermal expansion [88]. The machining process consists simply of cutting the rod to the appropriate length and drilling and tapping one end to facilitate the rod being screwed onto the built in steel rams. Sample dies are also manufactured using pyrolytic graphite cylinders and are typically machined to have lengths of 2 in., O.D.'s of 1 7/8 in., and inner diameters (I.D.) of 1/2 in., although the user may define custom dimensions to fit the specific requirements of the sample. For example, dies with lengths of 4 in. have been used in attempts to gain greater horizontal stability while dies with I.D.'s of 0.37 in. have been used to accommodate small sample quantities. The graphite dies are snugly encased within a custom-built stainless steel jacket that serves the purpose of containing the sample and die fragments within the steel jacket should the die break during hot pressing. This precaution is particularly important for protecting the graphite heating element of the furnace from being damaged by fragments of a broken die, as replacing this element is a time-consuming and costly procedure, but it has the added advantage of preventing the loss of the sample material in the event of a die fracture. Occasionally, even though the graphite may crack, the steel shell holds the die together tightly enough for pressing to continue, and a useable sample may still be produced.

Pressure is transferred from the large graphite press rams to the sample via rods constructed from TZM (titanium-zirconium-molybdenum), a Mo alloy with a high melting point (2623^{o}C) [89] and a favorable strength vs. temperature profile: ~700 MPa

at 1000°C (compared to steel, which is on the order of 100 MPa at 1000°C) (figure 37) [90]. In order to help prevent sample cross-contamination as well as to keep the sample from bonding to the TZM punches, a thin circle of Grafoil® flexible graphite, having a diameter slightly above the I.D. of the graphite die, is inserted into the die to serve as a buffer between the sample and the TZM rods.

Prior to hot pressing, the sample powders are inserted into the graphite die assembly and cold pressed to ~2 tons to test the assembly for stability and also to achieve preliminary packing before inserting into the hot press. Based on the pressure set point of the hot press and the I.D. of the graphite die, the effective pressure on the sample can be calculated by first converting the set point value, $m_{s.p.}$, specified in kg, to N, using

$$F = m_{s.p.} g \,, \tag{4.2}$$

and then finding the pressure, *P*, applied to the sample in N/m^2 (Pa) by use of

$$P = F/A \,, \tag{4.3}$$

where *A* is the sample cross sectional area. Thus, for example, a set point of 2000 kg (2 tons), corresponds to an applied force of 19,600 N, and if the I.D. of the die is 0.5 inch (0.0127 m), the cross sectional area will be $1.27 \times 10^{-4}\,\mathrm{m}^2$, such that the applied pressure is ~155 MPa. Table 1 lists applied pressure values as a function of set point, for the case of dies with 0.5 and 0.37 inch I.D.

After hot pressing, the hot press chamber is allowed to cool to below 200°C before removing the sample to help protect the graphite heating element and press rams from oxidation. A schematic of the die assembly is shown in figure 38.

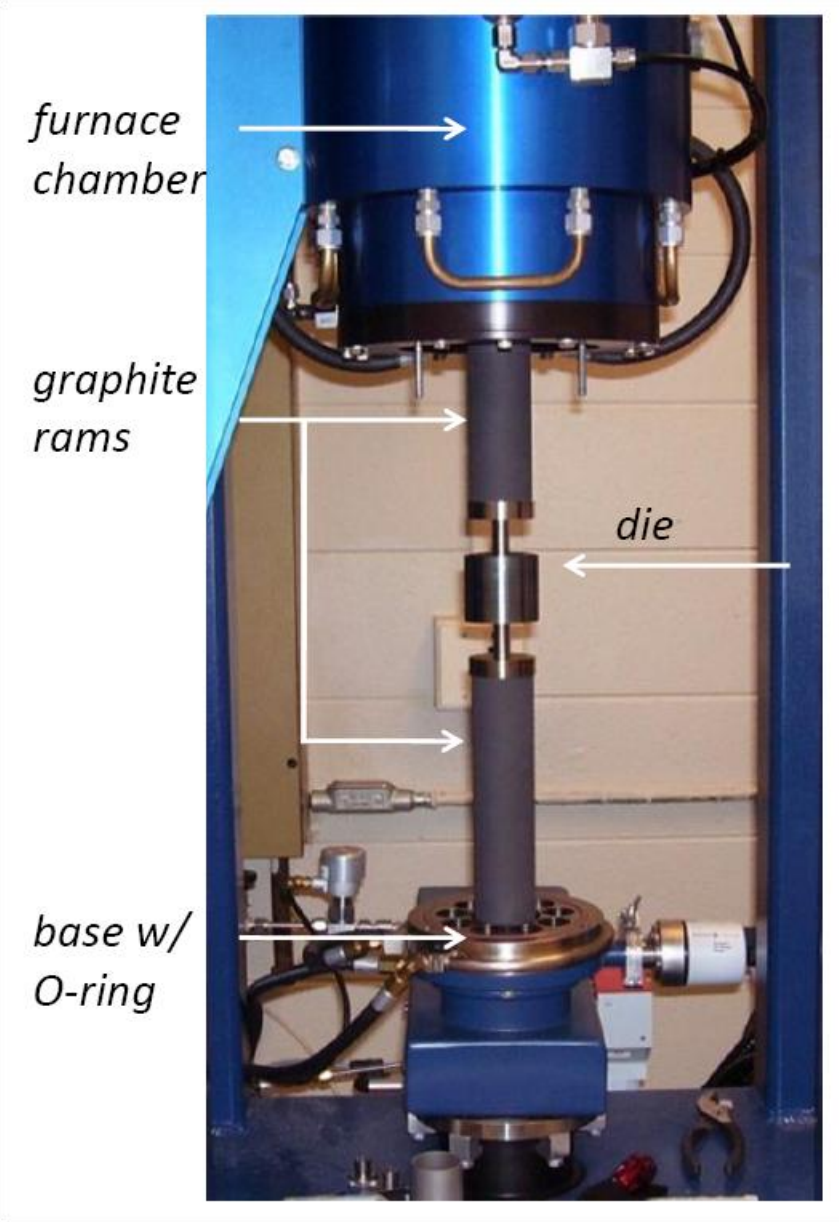

Figure 36. The uniaxial hot press, with the furnace chamber in the raised position.

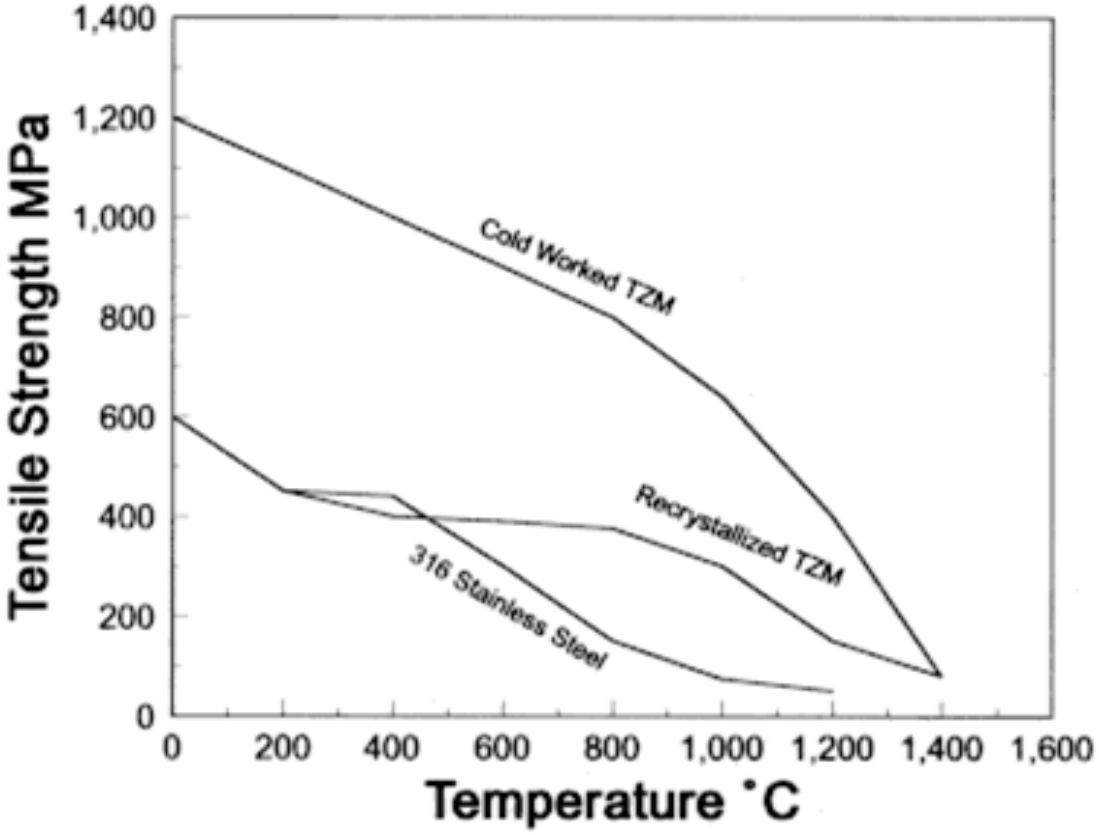

Figure 37. Strength vs. temperature profile for TZM and 316 stainless steel [90].

Set point (kg)	I.D. (in)	Pressure (MPa)	I.D. (in)	Pressure (MPa)
600	0.5	46.42	0.37	84.77
700	0.5	54.16	0.37	98.90
800	0.5	61.89	0.37	113.02
900	0.5	69.63	0.37	127.15
1000	0.5	77.36	0.37	141.28
1100	0.5	85.10	0.37	155.41
1200	0.5	92.84	0.37	169.53
1300	0.5	100.57	0.37	183.66
1400	0.5	108.31	0.37	197.79
1500	0.5	116.05	0.37	211.92
1600	0.5	123.78	0.37	226.05
1700	0.5	131.52	0.37	240.17
1800	0.5	139.26	0.37	254.30
1900	0.5	146.99	0.37	268.43
2000	0.5	154.73	0.37	282.56
2100	0.5	162.47	0.37	296.69
2200	0.5	170.20	0.37	310.81
2300	0.5	177.94	0.37	324.94
2400	0.5	185.67	0.37	339.07
2500	0.5	193.41	0.37	353.20
2600	0.5	201.15	0.37	367.33
2700	0.5	208.88	0.37	381.45
2800	0.5	216.62	0.37	395.58
2900	0.5	224.36	0.37	409.71
3000	0.5	232.09	0.37	423.84
3100	0.5	239.83	0.37	437.97
3200	0.5	247.57	0.37	452.09
3300	0.5	255.30	0.37	466.22
3400	0.5	263.04	0.37	480.35
3500	0.5	270.78	0.37	494.48

Table 1. Applied pressures, calculated based on set point in kg, and I.D. of the graphite die.

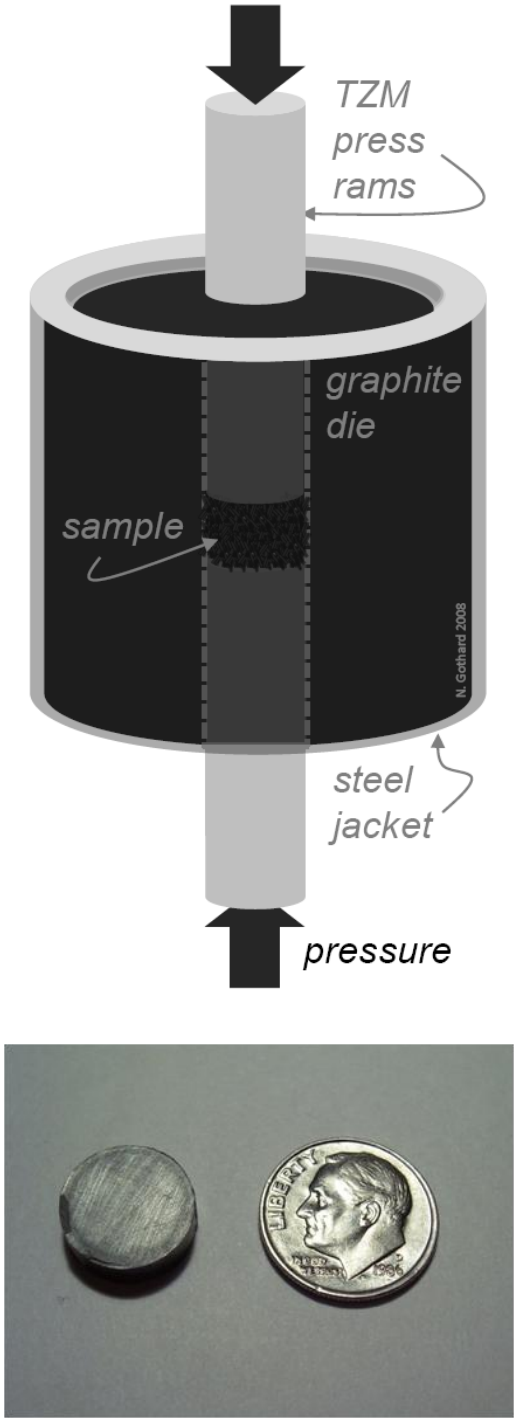

Figure 38. a) Schematic of the die used for hot pressing of nanocomposites. b) Hot-pressed sample

RESULTS

All of the nanocomposites presented in this study were prepared using either $Bi_2Te_{2.7}Se_{0.3}$ n-type bismuth telluride or $Bi_{0.4}Sb_{1.6}Te_3$ p-type bismuth telluride as the matrix material. Nanoparticles of Bi_2Te_3, BiSb, Bi_2S_3, Au or Ag, and C_{60} were separately introduced into the matrix, and the resulting mixture was densified into a composite pellet via the use of a uniaxial hot press. The composite microstructure and composition, as well as the effects of the nanoparticles on the thermal and electrical transport properties are presented below, with a focus on the effect of the nanoparticles on the thermoelectric efficiency of the composite. As the matrix material for each composite is bismuth telluride, the composites are identified in the section headings below simply by the composition of the nanostructure inclusion.

Bismuth Telluride Nanocomposites

Production of bismuth telluride nanoparticles in sufficient quantities for integration into a bulk material was accomplished via the hydrothermal method described in chapter 4. After hydrothermal growth, the nanoparticles were confirmed by powder x-ray diffraction (XRD) to be primarily single-phase Bi_2Te_3, and the particle size and morphology was found by scanning electron microscopy (SEM) to be spherical-irregular, with average sizes on the order of 30 nm (see figure 35). These nanoparticles were then cold pressed, and a temperature gradient was established across the resultant pellet. A measurement of the sign of the voltage across this sample indicated the particles to be n-type semiconductors. Accordingly, n-type $Bi_2Te_{2.7}Se_{0.3}$ was selected for use as the matrix material.

Preparation by Ball Milling

The bismuth telluride matrix material was cut from a commercially grown ingot, then fractured and hand ground via mortar and pestle until a course powder was obtained. This powder was loaded into a ball mill together with a specified amount of nanoparticle powder, calculated by molar percentage (mol. %), and the mixture was ball milled for 20 minutes at 20 Hz. It should be noted that in the current case, the molecular weight of the matrix material ($Bi_2Te_{2.7}Se_{0.3}$) does not differ greatly from that of the nanoparticle powders (Bi_2Te_3), so that a calculation of molar percentage arrives at virtually the same result as a calculation of weight percentage. Ball milling was used for the dual purposes of mixing the nanoparticles and the bulk powders as well as to complete the work of grinding the bulk powders. After ball milling, the mixture was loaded into a 1/2 inch I.D. graphite die, cold pressed briefly to achieve initial compaction, and then hot pressed at 400^{o}C and 2.500 tons (193.4 MPa). A program was created for the hot press to ramp the temperature to the set point, hold for 5-6 minutes to preheat the sample, and then to gradually ramp pressure to the pressure set point and hold for 30 minutes. Following hot pressing, samples were cut from the resultant pellet by use of a diamond saw, and they were prepared for electron microscopy and physical transport properties measurements. The series of samples consisted of Bi_2Te_3 nanoparticles mixed with the bulk powders at 5, 10, 15, and 20 mol. %. Additionally, a 0 mol. % nanoparticle sample was processed under identical ball milling and hot pressing conditions to serve as a reference.

Figure 39a shows the low temperature thermopower vs. temperature data for this series. The curvature of the trend for each nanocomposite shows little change, and the

room temperature thermopower has a mean value of -150 ± 7 μV/K, a reduction in magnitude of approximately 75μV/K in comparison to the commercially available ingot material. Figure 39b shows the room temperature thermopower values as a function of nanoparticle percentage. Following an initial drop in magnitude from the ingot to the 0 mol. % sample, there is little variation with nanoparticle percentage. Electrical resistivity vs. temperature is plotted in figure 40a, wherein it is apparent that there is a mild change in the curvature of the data when progressing from the ingot to the reference sample, and also as an effect of nanoparticle concentration. The residual resistivity (resistivity at 10 K) increases from the ingot to the reference, a trend which, although not 100% systematic, continues as nanoparticles are added. This indicates that nanoparticles tend to increase the amount of disorder in the grain structure. Room temperature resistivity values show a similar trend (figure 40b). The sample having the highest room temperature resistivity is the 15 mol. % sample, with ρ = 1.96 mΩ cm, while the lowest value of ρ is found in the 0 mol % reference sample (ρ = 0.904 mΩ cm). The reason for the ~1 mΩ cm spread is not immediately clear, but a consideration of a plot of the density vs. resistivity at room temperature shows that the effect is not attributable to porosity variations from sample to sample (figure 41). Instead, compositional variations are likely the cause, which sheds some doubt on the reliability of the preparation technique for preparing samples in a uniform manner.

The large uniform decrease in thermopower dominates the trend in the power factor for this series, with the result that the power factor values for all the hot pressed composites, including the reference sample, decrease from the ingot value. Moreover,

the increases in resistivity that are present in all of the composites that contain nanoparticles are cause for further power factor decreases, beyond the decrease exhibited in the 0 % reference sample (figure 42).

Since the total thermal conductivity (TC) depends on the sum of the electronic and lattice parts, with the electronic part being directly proportional to the electronic conductivity, analysis of the thermal conductivity will focus here largely on the lattice contribution. The data for lattice TC is obtained by calculating the electronic TC by use of the Wiedemann-Franz relationship ($\kappa_e = L\sigma T$) and subtracting this value from the total TC. In this series of samples, there is a noticeable reduction in the low temperature peak of the lattice thermal conductivity for all of the hot pressed samples as compared to the ingot, and a further reduction in this peak as compared to the reference for the composites that contain some percentage of nanoparticles (figure 43a). This type of a reduction is typical of increased scattering of phonons by the grain boundaries, and the effect appears to be more pronounced for composites that have higher percentages of nanoparticle inclusions. At temperatures approaching 300 K, significant radiation effects are visible as an upturn in the lattice TC vs. *T* trend in the ingot data, as well as to some degree in each of the nanocomposite samples. Because a correction of these effects would require correcting the data by as much as 25% in many of the samples, the data has been left uncorrected. Since the onset of radiation effects tends to manifest in this series after 220 K, a comparison of the variation in the magnitude of the lattice thermal conductivity data as a function of nanoparticle percentage is best done in the vicinity of 220 K. Figure 43b is a plot of lattice thermal conductivity values at 220 K vs.

percentage of nanoparticles, which shows that there is a slight systematic reduction in lattice thermal conductivity as a function of nanoparticle concentration. From the effect in figure 43a, therefore, one can conclude that a significant effect of the nanoparticles is an increase in the degree of phonon boundary scattering, but figure 43b indicates that point-defect scattering is also in effect to some extent. The latter effect is of greater interest to this study as it decreases the thermal conductivity in the temperature range where these materials would find application.

Regardless of the positive effect of the nanoparticles upon the thermal conductivity, however, the decrease in the power factor is still the dominant effect when considering the figure of merit, as shown in figure 44. As an aside, note that although the lattice TC data presented in figure 43 are not corrected for radiation effects, the effects of radiation upon the total TC data are quite a bit less significant, and it is therefore the corrected total TC that has been used to calculate the figure of merit in these samples, as well as in those to follow in subsequent sections. Figure 44a, then, shows a non-systematic decrease in ZT for all of the hot-pressed samples as compared to the ingot, at all temperatures. From figure 44b, it is apparent that there is a rough inverse proportionality between the percentage of nanoparticles in the composite and the room temperature figure of merit.

In figure 44a, it is clear that the ZT values for this series have not yet achieved their maxima, and consequently the thermal conductivity, resistivity, and thermopower values were measured at high temperatures in order to find these maximum values. However, matching the values from the high and low temperature data trends presents a

number of difficulties, particularly for the thermal conductivity data. Whereas the low temperature systems measure thermal conductivity in a direction perpendicular to the direction in which pressure was applied to the sample in the hot press, the laser flash system measures TC parallel to the direction of hot pressing. Due to the high degree of anisotropy in these samples, a mismatch was found to occur between the high and low temperature values. Such a problem could be eliminated if samples for low temperature measurements could be produced such that the direction of transport is parallel to the direction of hot pressing. Attempts to grow samples having such aspect ratios were unsuccessful, however, due to the additional stress that samples of such height put on the graphite dies in the horizontal direction. The result is a frequent breakage of dies that results in a loss of the sample. Therefore, high temperature data will not be presented in this or subsequent studies. As the high temperature data trends are simply extensions of the low temperature curves, however, an effective assessment of the efficiency of the materials can be arrived at solely from the low temperature data, regardless of the difficulties discussed herein.

Scanning electron microscopy (SEM) of these composites reveals particles on three size scales, each with a distinct morphology. First, hexagonal particles with dimensions on the order of several microns are distinguishable, and clearly represent the matrix material (figure 45a). Such particles often aggregate but may also sit isolated amidst a finer grained background, whose particles display some regularity but the sizes of which are below the micron scale in most cases. Due to their size and morphology (no more than approximately 1 μm), it is quite likely that these particles also belong to the

matrix material. At higher magnification, the final group of particles can be observed (figure 45b). These particles cluster together in the gaps left by the second group and have spherical-irregular morphologies not exceeding 100 nm in most cases. It is concluded that these are the Bi_2Te_3 nanoparticles. The implication of the presence of the second, sub-micron-size group of matrix particles is that using the ball mill to combine the nanoparticles with the matrix material results in many of the matrix grains being crushed to sizes below the desired size scale of several microns. Consequently, the matrix material has on average a larger size distribution and a smaller grain size than expected, with the result being a continuum in size and morphology between the matrix and nanoparticles. Because of this, it is likely that sub-micron-sized matrix grains are masking the effects of the nanoparticles upon the electrical and thermal transport properties. This problem addressed in the following section.

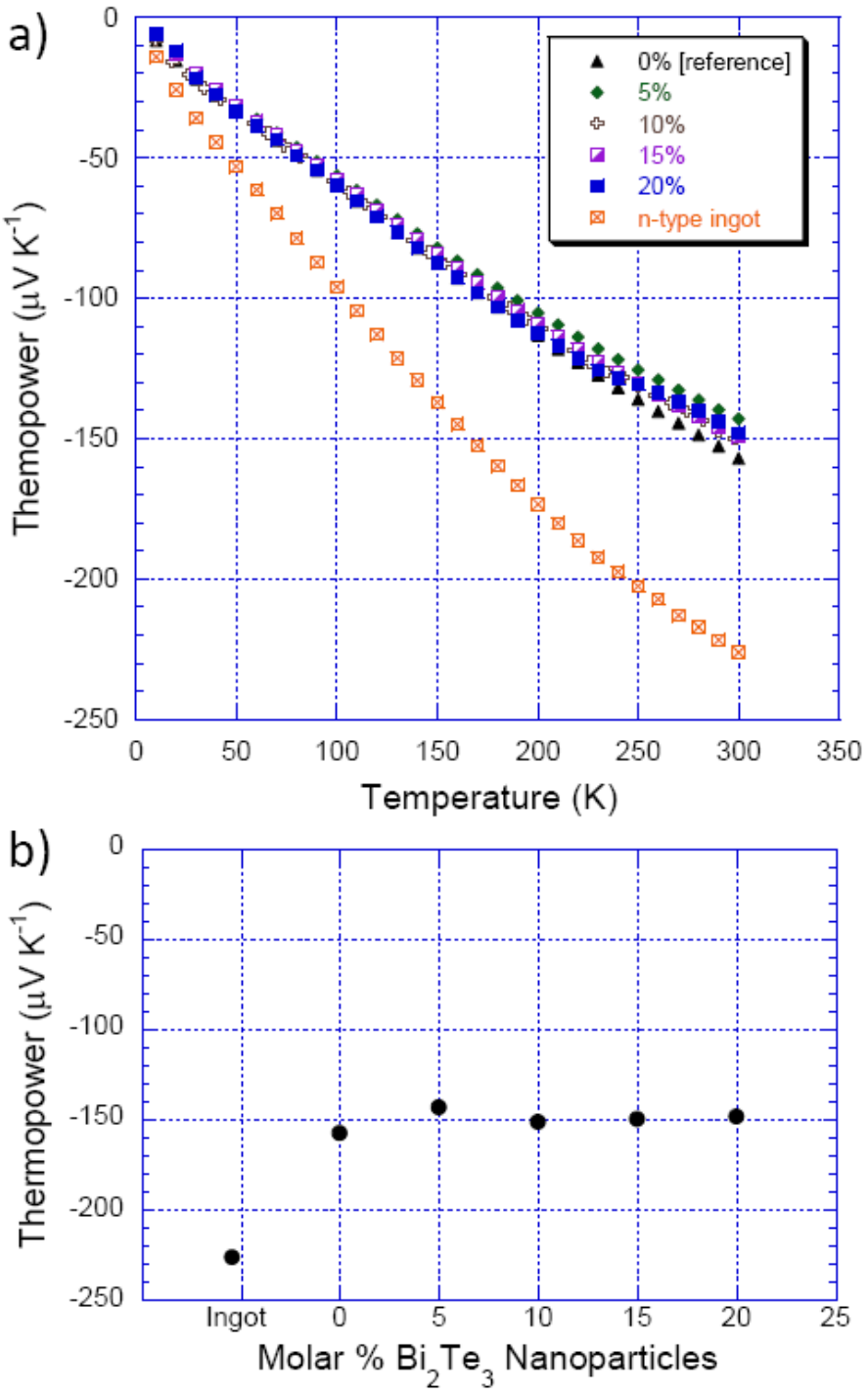

Figure 39. a) Thermopower vs. temperature for the series of ball milled bismuth telluride nanocomposites. b) Thermopower vs. molar % of nanoparticles at 300 K, for the same.

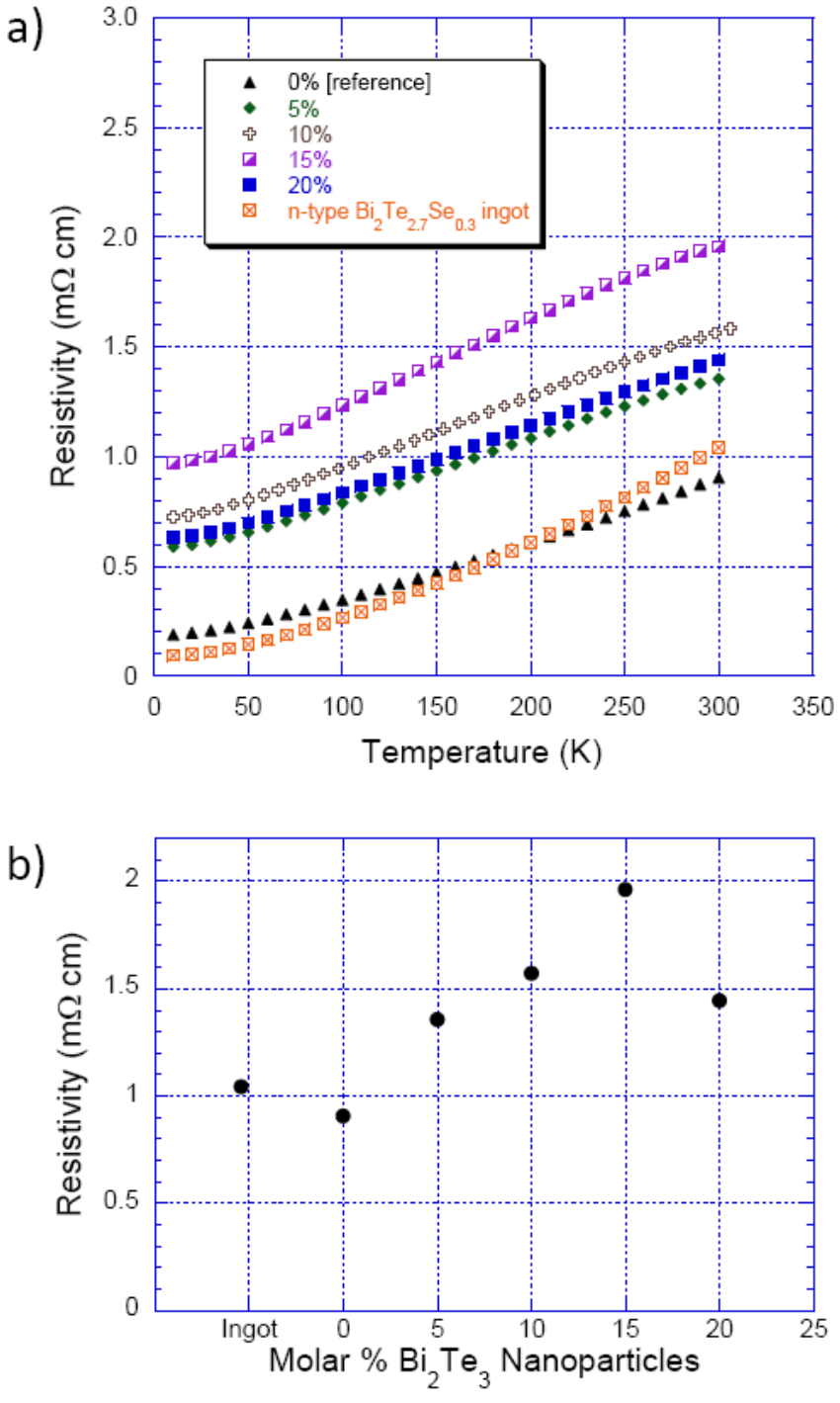

Figure 40. a) Resistivity vs. temperature for the series of ball milled bismuth telluride nanocomposites. b) Resistivity vs. molar % of nanoparticles at 300 K, for the same.

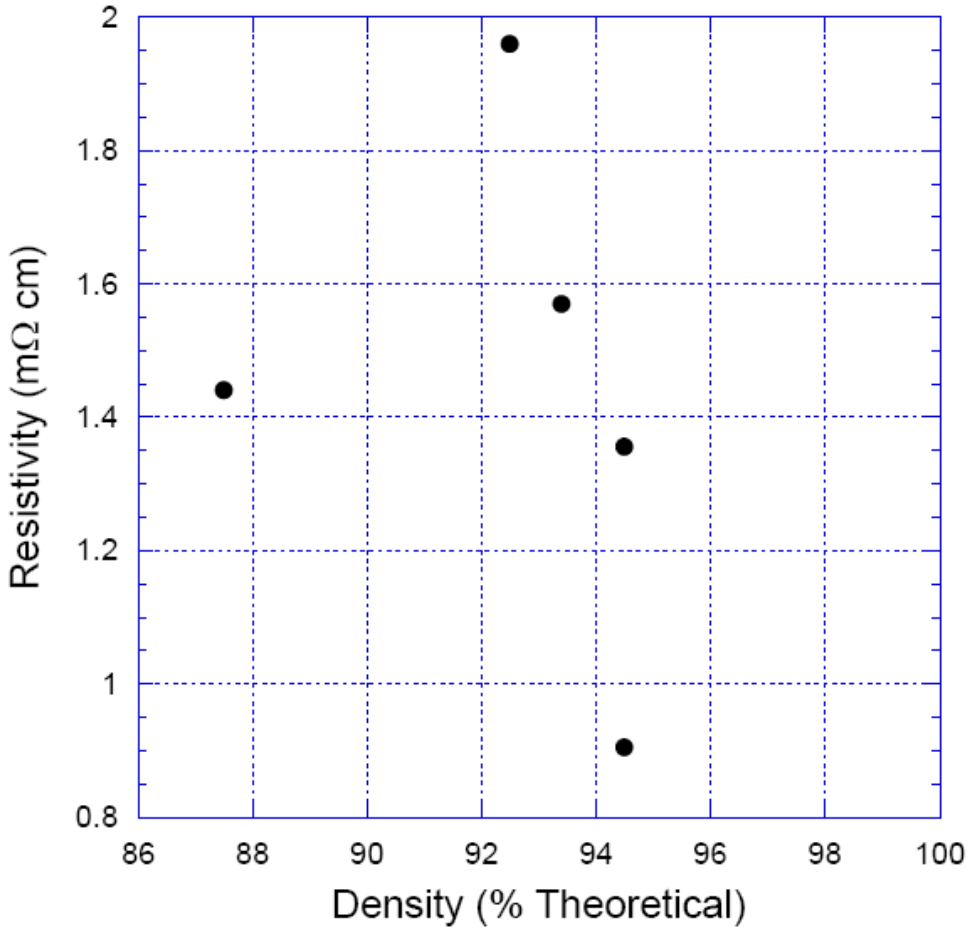

Figure 41. Room temperature resistivity vs. percentage of theoretical density for the ball milled series of bismuth telluride samples. The relationship between resistivity and density is not sufficient to explain the trend seen in figure 40b.

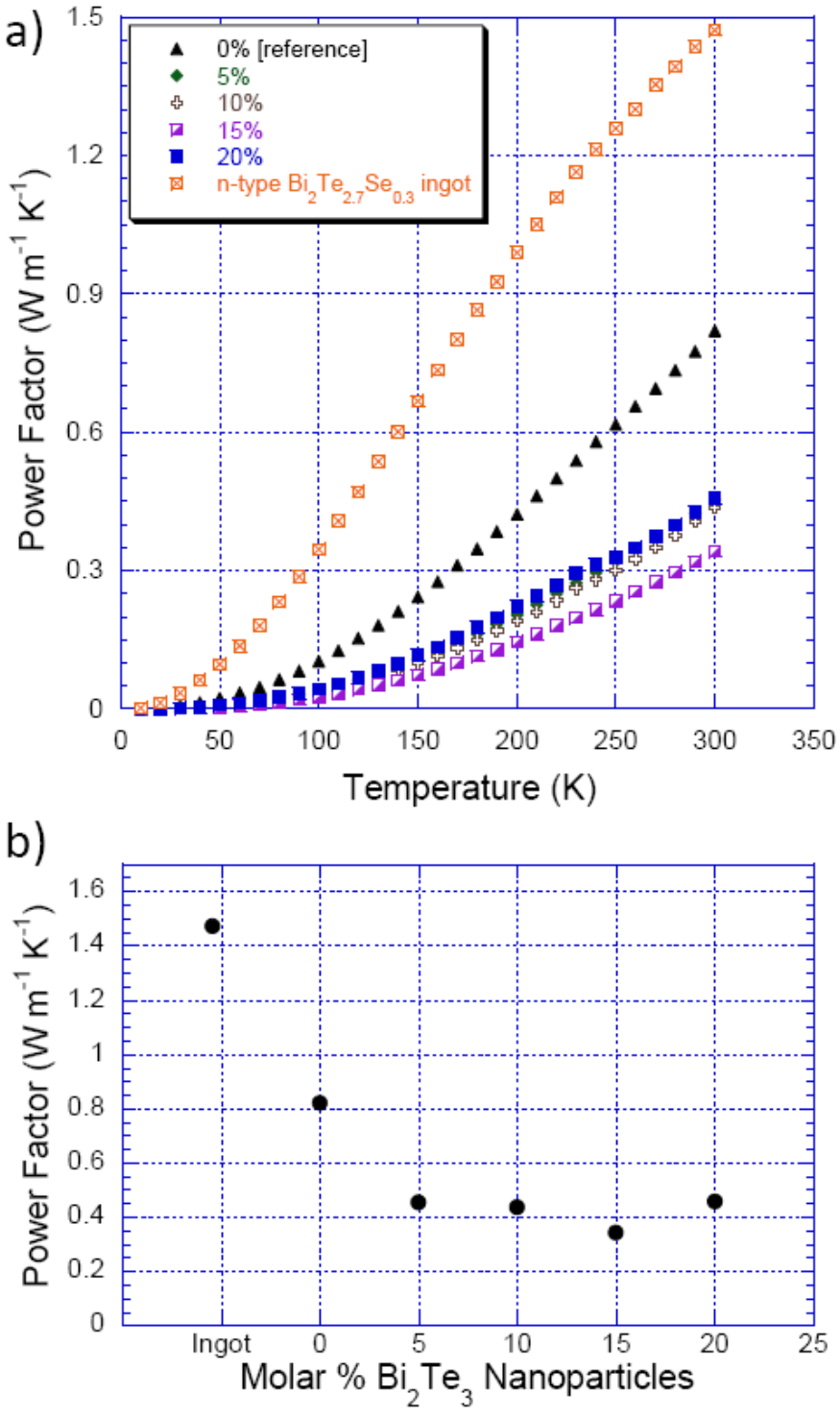

Figure 42. a) Power factor vs. temperature shows a decrease for all nanocomposites with respect to the reference. b) Power factor vs. percentage of nanoparticles, at 300 K.

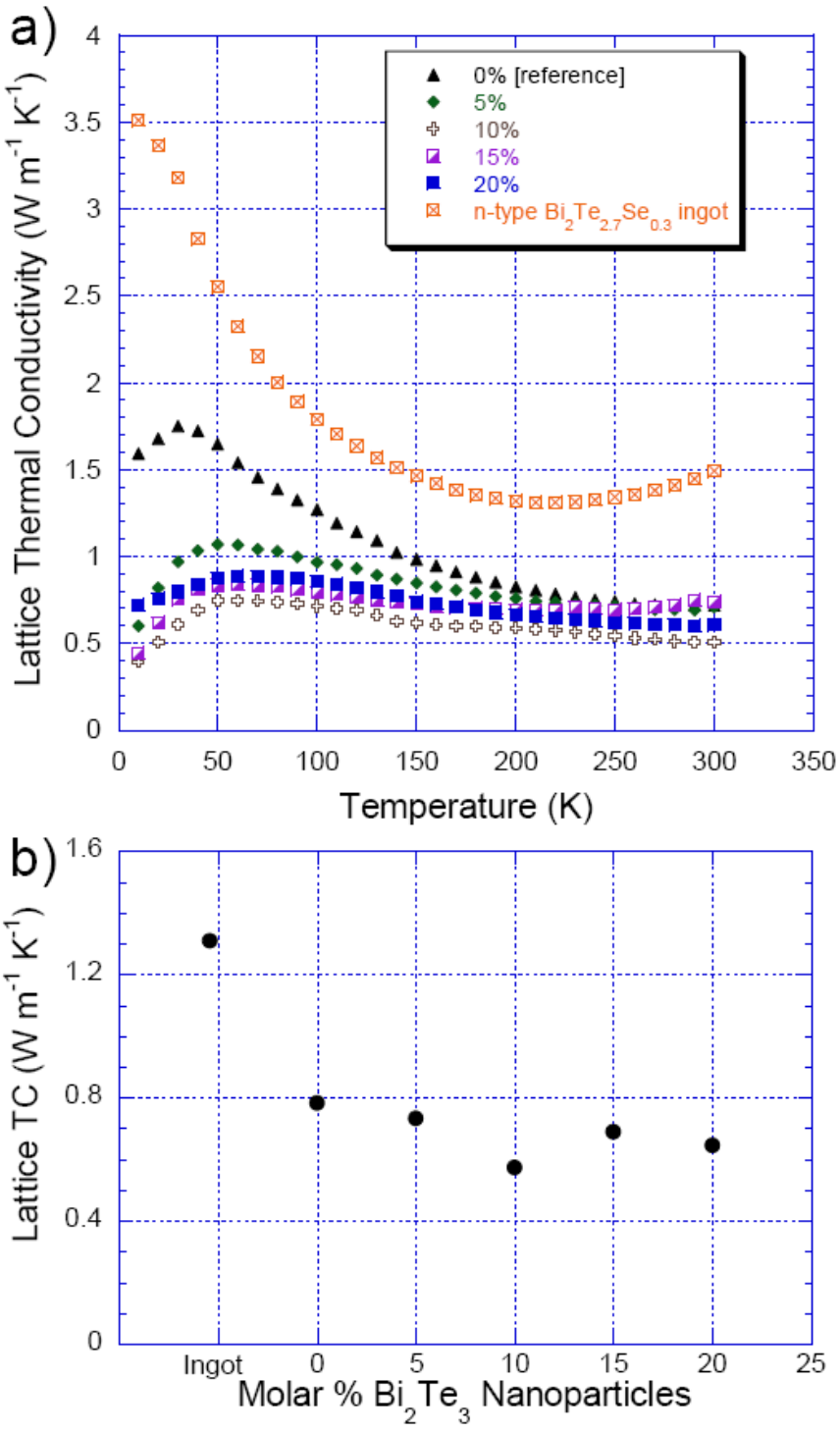

Figure 43. a) Lattice thermal conductivity (κ_L) vs. temperature for the series of ball milled bismuth telluride nanocomposites. b) κ_L vs. molar % of nanoparticles at 220 K, for the same.

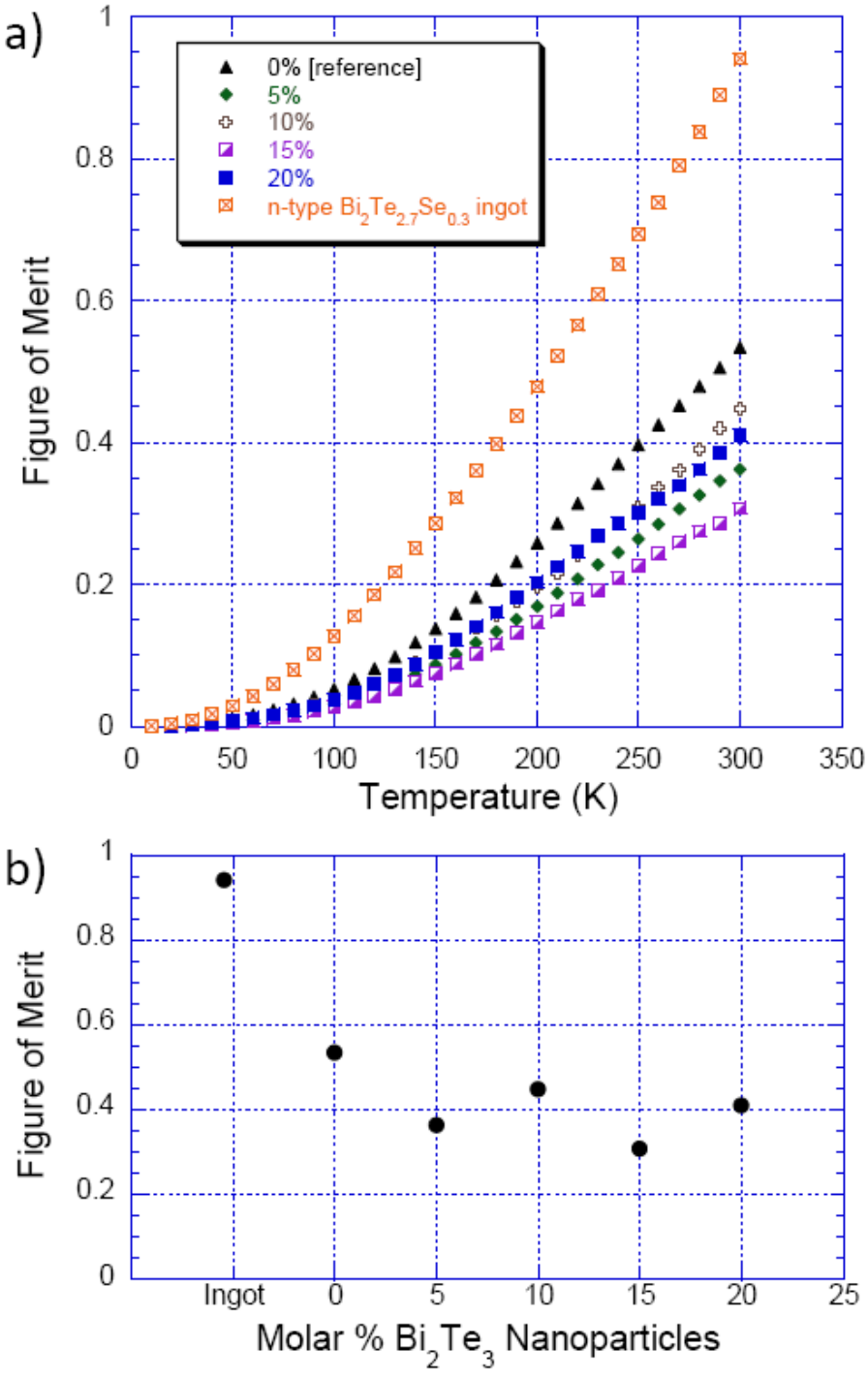

Figure 44. a) Figure of merit (ZT) as a function of temperature for the series of ball milled bismuth telluride samples (calculated using corrected total TC data). b) ZT as a function of nanoparticles percentage at 300 K, for the same.

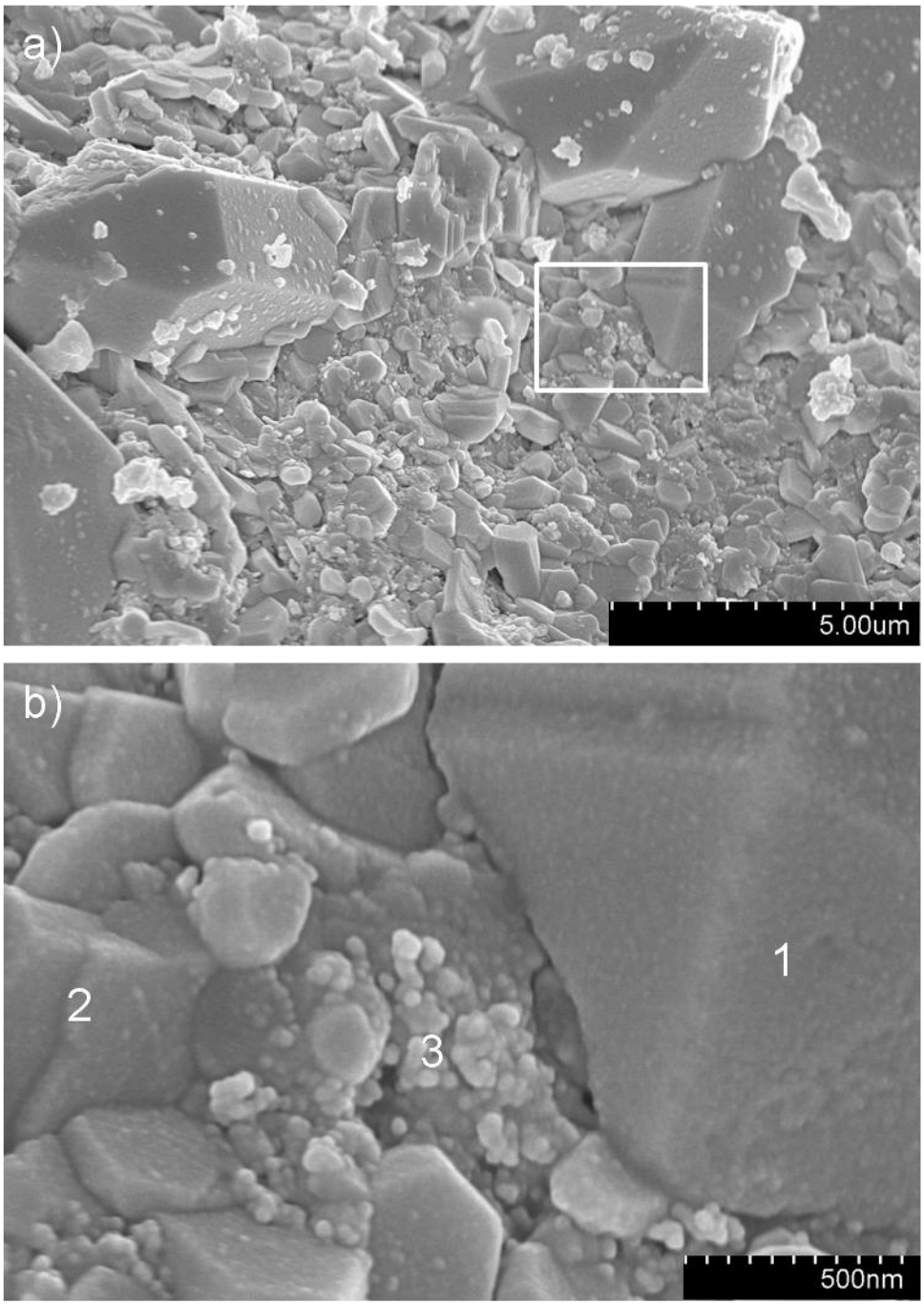

Figure 45. SEM images of bismuth telluride nanocomposite prepared by ball milling and hot pressing. a) Large hexagonal particles in the midst of significantly smaller grain sizes b) Close view of portion from 45a, showing three regions: 1) matrix particles, 2) sub-micron matrix particles, and 3) nanoparticles.

Preparation by Mechanical Mixing

In an attempt to eliminate sub-micron-sized grains from the matrix material and thereby better isolate the role of the nanoinclusions, a second series of samples was produced in which a 3-axis Turbula® mixer was used instead of the ball mill to mix the matrix and nano materials. As before, the matrix material was n-type $Bi_2Te_{2.7}Se_{0.3}$, and the nanoparticles were the n-type spherical-irregular particles obtained by hydrothermal synthesis. Here, however, the matrix material was obtained by grinding a segment of the ingot via mortar and pestle, and then sifting the resultant powders via a system of stacking sieves, from which powders of a specified size distribution could be selected. For the composites studied here, powders collected from between the 450 and 325 meshes were used, such that the powders were expected to have a size distribution of ~32-45μm, corresponding to the sizes of the openings on the sieves. Nanoparticles were incorporated at 5, 15, 20, and 50 molar percent, and again a 0% reference sample was pressed.

After grinding, powders of the matrix material and nanoparticles were weighed out to the appropriate molar percentages, inserted into a glass vial, mixed for 30 minutes, and then loaded into a graphite die with a 1/2 inch I.D. Again, a program was created to ramp the hot press to the temperature set point, hold for 5-6 minutes to preheat the sample, and then gradually ramp to the pressure set point and hold for 30 minutes. The conditions of hot pressing were between 300-400^{o}C, 2.500 tons (193.4 MPa), in a nitrogen atmosphere at 0.3-0.5 psi with an open exhaust line. The temperature was varied slightly in attempts to achieve higher densification.

SEM of a single particle of powder after grinding, sifting, and mixing, but prior to hot pressing, reveals it to be a loose aggregation of smaller particles (figure 46a). Although the total particle size is approximately 40 μm, in the range of the size distribution dictated by the sieves, the largest individual grains appear to be on the order of 5-15 μm. A closer look (figure 46b) shows evidence of fractures and distortions in the larger size particles, presumably attributable to the grinding process. Adhering to the exterior of the particle are several large agglomerations of nanoparticles, and in the lower right of figure 46b, a particle with a high aspect ratio is discernable. Figure 46c provides a closer look at this structure, which may possibly be a Bi_2Te_3 nanotube or nanowire of the sort reported to occasionally form during hydrothermal growth of bismuth telluride [84], although in this case it appears to be coated with the more customary spherical nanoparticles that hydrothermal growth is known to generate. From these results, it does appear as though hand grinding and sifting results in significantly fewer sub-micron-sized matrix grains, although the average grain size is still smaller than the target size of 32-45 μm. SEM of a cross-section of a fragment from a hot-pressed pellet is shown in figure 47. Here, the overall morphology is quite similar to that presented in figure 46, with the exception of being more tightly packed. Two types of regions are visible: those on the scale of ~5-15μm, and smaller, sub-micron-sized regions. In the micron-sized areas, the structure appears similar to what appears in figure 46 to be the matrix material, and there are a greater number of distortions like those in figure 46b, likely as a result of the hot-pressing. The sub-micron-sized regions appear to be aggregations of nanoparticles.

Figure 48a shows thermopower vs. temperature data for these samples. Similar to the ball milled series, the thermopower vs. temperature curve shows minimal change in curvature as compared to the ingot. Also, while there is some variation of thermopower with concentration of nanoparticles, there is not a clear trend, except that all the hot pressed samples have absolute thermopower values at room temperature that are lower than the ingot material (figure 48b). As compared to the 0% reference, there is an initial drop followed by an increase in thermopower for the 20 and 50% samples.

The resistivity vs. temperature data reveals little variation for the samples with less than 20% nanoparticles, but a dramatic increase in resistivity for the 20 and 50% samples (figure 49a). Also, the curvature of these two samples is noticeably different than the reference sample and the samples that contain smaller percentages of nanoparticles, especially at temperatures approaching 300 K. In spite of the high thermopower values for these two samples, however, their high resistivity values effectively negate any benefits to their power factor values (figure 50). In fact, the room temperature power factor values decrease as a function of nanoparticle concentration, although the decrease is very small for the 5% sample (figure 50b). None of the hot pressed samples, including the reference, are competitive with the commercial ingot in terms of the power factor.

Lattice thermal conductivity data as a function of temperature are presented in figure 51a. As with the nanocomposite series prepared by ball milling, there is again a decrease in the low temperature lattice TC peak, with stronger suppression of this peak appearing for the highest nanoparticle percentage samples. Thus, the addition of

nanoparticles again tends to increase the degree of boundary scattering of phonons, an effect that is especially prominent in the 20% and 50% samples. The fact that the lattice TC data for these two samples remains noticeably suppressed as compared to the reference sample until after 150 K also suggests that increased point-defect scattering of phonons is a factor in these samples. Approaching room temperature, there is again a noticeable upturn in the data due to radiation effects, which has also been left uncorrected here due to the percentage change in the data that a radiation correction would impose. Figure 51b presents the lattice TC data as a function of nanoparticle percentage prior to the onset of radiation effects, which occur after 200 K in these samples, showing a slight trend towards lower thermal conductivity as nanoparticle percentage increases. Due to the small magnitude of the decrease, however, it is expected that the negative effects of the nanoparticles upon the power factor will be enough to overcome the advantages gained by the slight decrease in the thermal conductivity from a standpoint of the figure of merit. Indeed, the figure of merit was found to decrease as a function of increasing nanoparticle concentration (figure 52).

In order to gain a better understanding of the interplay between the nanoparticles and the electronic transport properties, measurements of the Hall effect have been performed, and both the carrier concentration, n, and the electronic mobility, μ, have been calculated. The carrier concentration does not change appreciably from that of the ingot material, but it does evidence a slight inclination towards lower carrier concentration with higher nanoparticle volume fractions (figure 53a). It is possible that the modulations in carrier concentration are due to the differing carrier concentrations of

the nanoparticles, as the nanoparticles should not be expected to have identical electronic properties between synthesis batches. It is of interest, however, that the 20% and 50% samples, which have the lowest carrier concentrations, also have the highest thermopower values. In general, it is expected that the thermopower should follow the approximate relation $\alpha \sim 1/n$ [9], which may shed light on the increase in the thermopower values for these two samples. In fact, a rough trend of $\alpha \sim 1/n$ is noticeable in a plot of α vs. $1/n$ (figure 53b).

Electronic mobility data are presented in figure 54, both as a function of temperature and as a function of percentage of nanoparticles at room temperature. Here, the electronic mobility shows a slight decrease as a function of nanoparticle concentration. It is also evident that at temperatures above ~75 K, the temperature dependence of the mobility goes as $T^{-3/2}$, indicating that acoustic phonon scattering of charge carriers is the predominant scattering mechanism in this temperature range, rather than effects caused by the nanoparticles, such as increased boundary or point-defect scattering. Below 75 K, however, the $T^{-3/2}$ fit breaks down, indicating that another scattering mechanism is dominant. It can be shown that when charge carriers are predominantly scattered by grain boundaries, the mobility can be expressed as

$$\mu = \left(el \Big/ \sqrt{8 k_B T \pi m^*} \right) \exp\left(-E_B / k_B T \right), \tag{5.1}$$

where e is the electron charge, l is the average grain size, E_B is the activation energy required to traverse the grain barrier, and k_B, T, and m^* assume the usual values of

Boltzmann's constant, temperature, and effective mass, respectively [30,91]. Equation (5.1) can be rewritten as

$$\ln\left(\mu T^{1/2}\right) = -E_B / k_B T + \ln\left(el / \sqrt{8 k_B \pi m^*}\right), \tag{5.2}$$

which shows that the log of $\mu T^{1/2}$ goes as a factor of $1/k_B T$ plus a y-intercept term that includes the average grain size, *l*. A plot of $\ln\left(\mu T^{1/2}\right)$ vs. $1/k_B T$ is presented in figure 55, with temperature marked on the upper x-axis. Here, the linear nature of the data above 200 $(eV)^{-1}$ (below 50 K), indicates that (5.2) holds for this series of samples below ~50 K, the implication of which is that at low temperatures scattering by grain boundaries is the primary charge carrier scattering mechanism. Moreover, since the magnitude of the y-intercept term,

$$\ln\left(el / \sqrt{8 k_B \pi m^*}\right), \tag{5.3}$$

is governed by the average grain size, *l*, the general trend of decreasing y-intercept with increasing nanoparticle percentage implies a lowering of the average grain size as the volume fraction of nanoparticles in the composites increases.

The primary effect of nanoparticle incorporation in this series of samples, then, is an increase in boundary scattering of both phonons and electrons, an effect which is dominant primarily at low temperatures. At room temperature, the effect of the nanoparticles upon the thermal conductivity is mild, and the increase in electrical resistivity dominates changes in the power factor values, with the net result being a decrease in the figure of merit as a function of nanoparticle percentage, similar to the effect observed for the ball-milled series. In this, case, however, the decrease in ZT is

milder than for the ball-milled composites, particularly at low nanoparticle volume fractions, and it therefore appears as though mixing is a viable method of consolidation when Bi_2Te_3 nanoparticles are used as the composite inclusions [92].

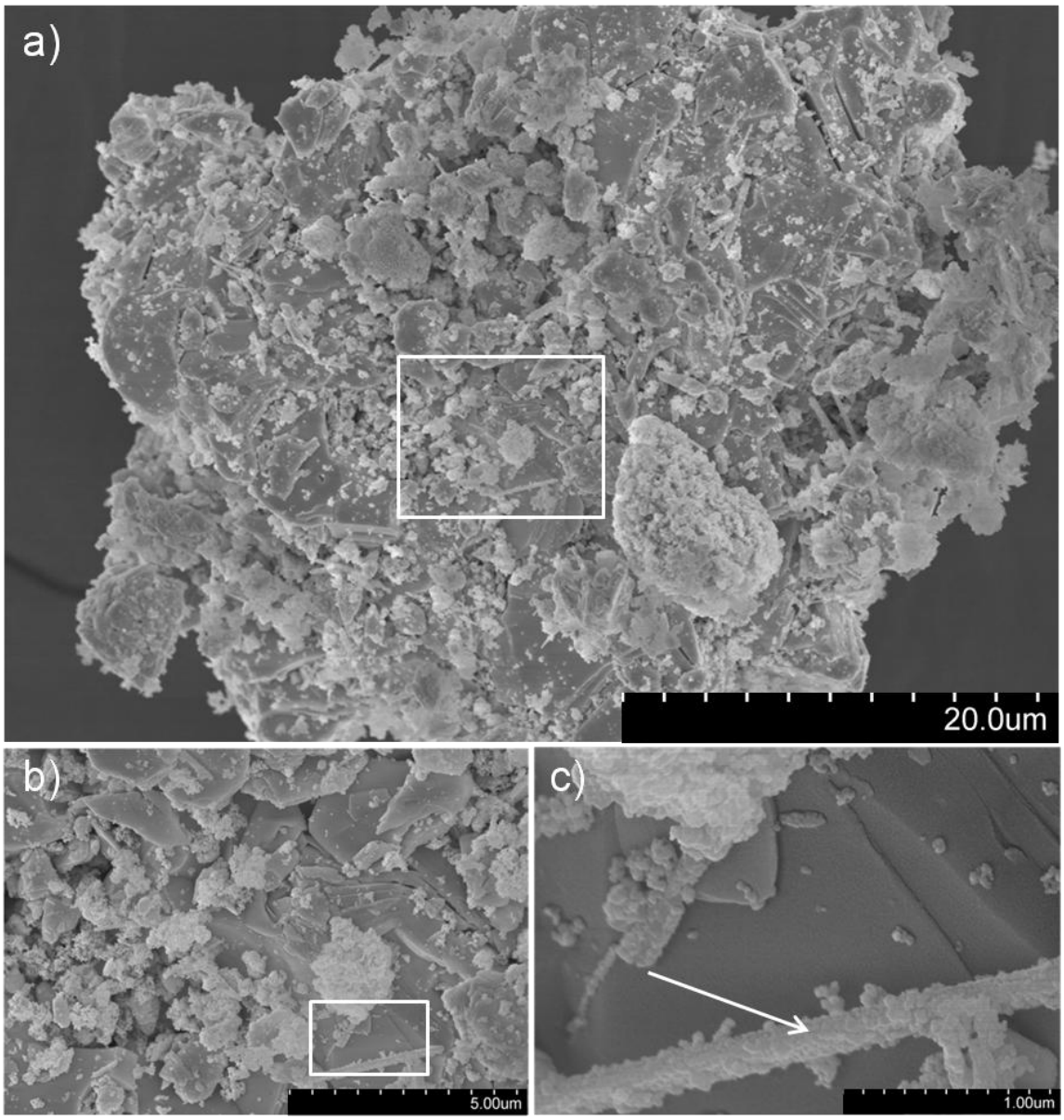

Figure 46. a) SEM of an aggregate particle obtained by sifting ground $Bi_2Te_{2.7}Se_{0.3}$ particles. Total particle size is on the order of 40 μm. b) Close-up of the region marked in 46a. c) Close-up of the region marked in 46b. An arrow indicates the presence of an apparent nanowire.

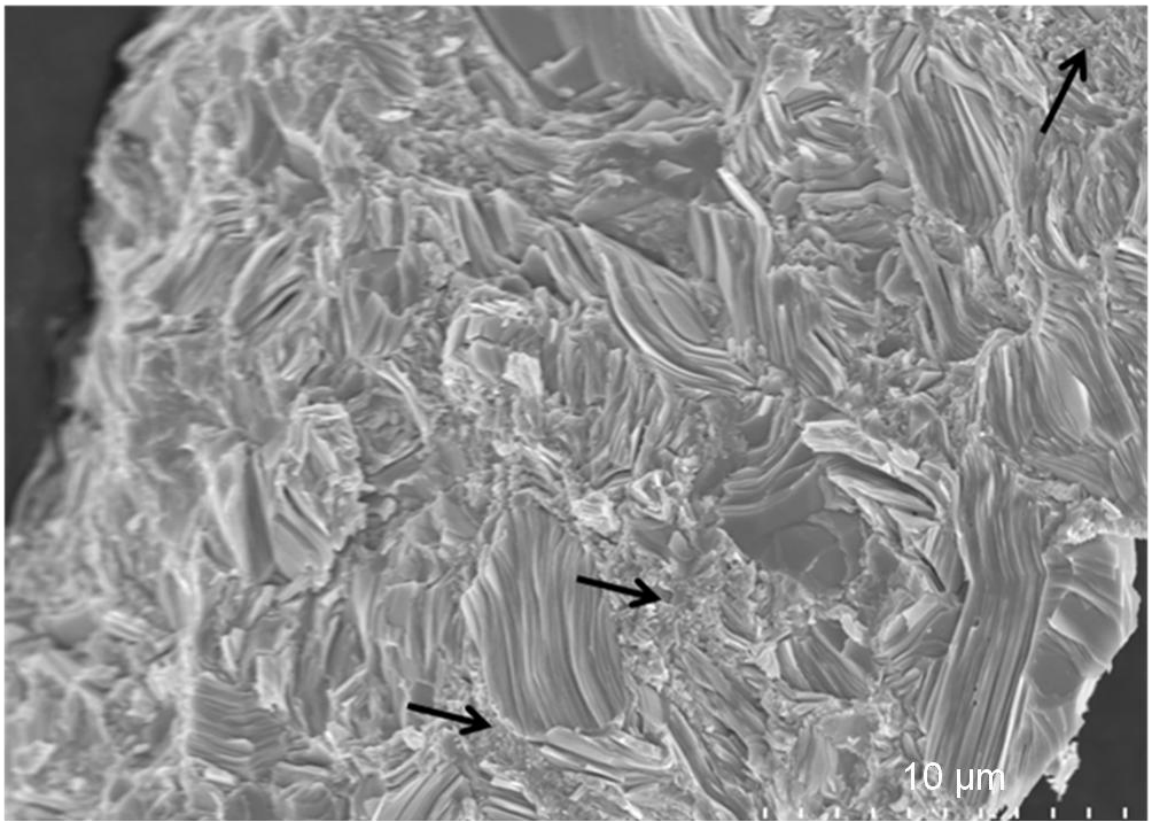

Figure 47. Fragment of a hot-pressed pellet from n-type $Bi_2Te_{2.7}Se_{0.3}$ source. Arrows indicate regions of nanoparticles aggregation.

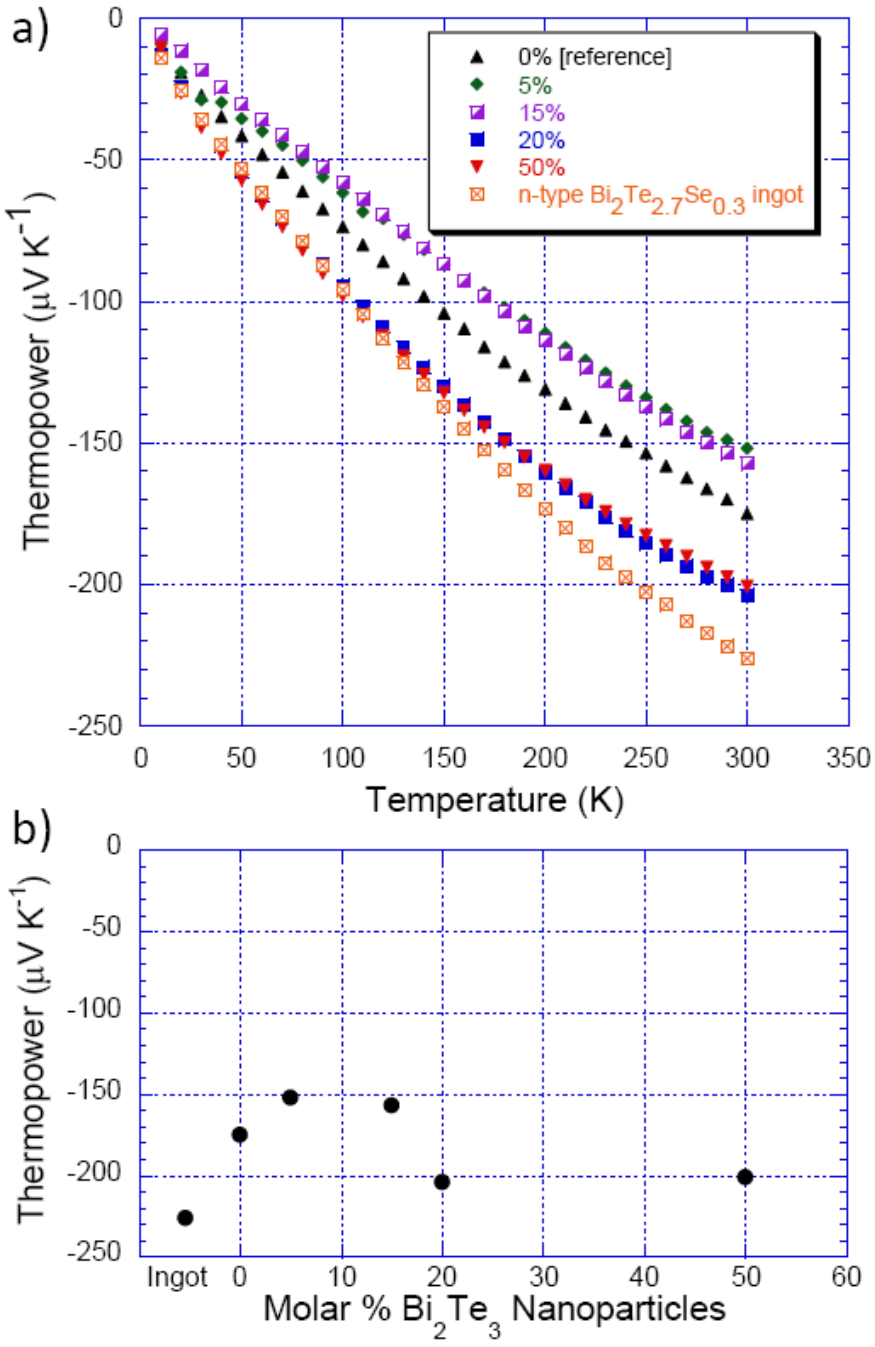

Figure 48. a) Thermopower vs. temperature data for the series of mixed n-type bismuth telluride nanocomposites. b) Thermopower as a function of percentage of nanoparticles, at 300 K.

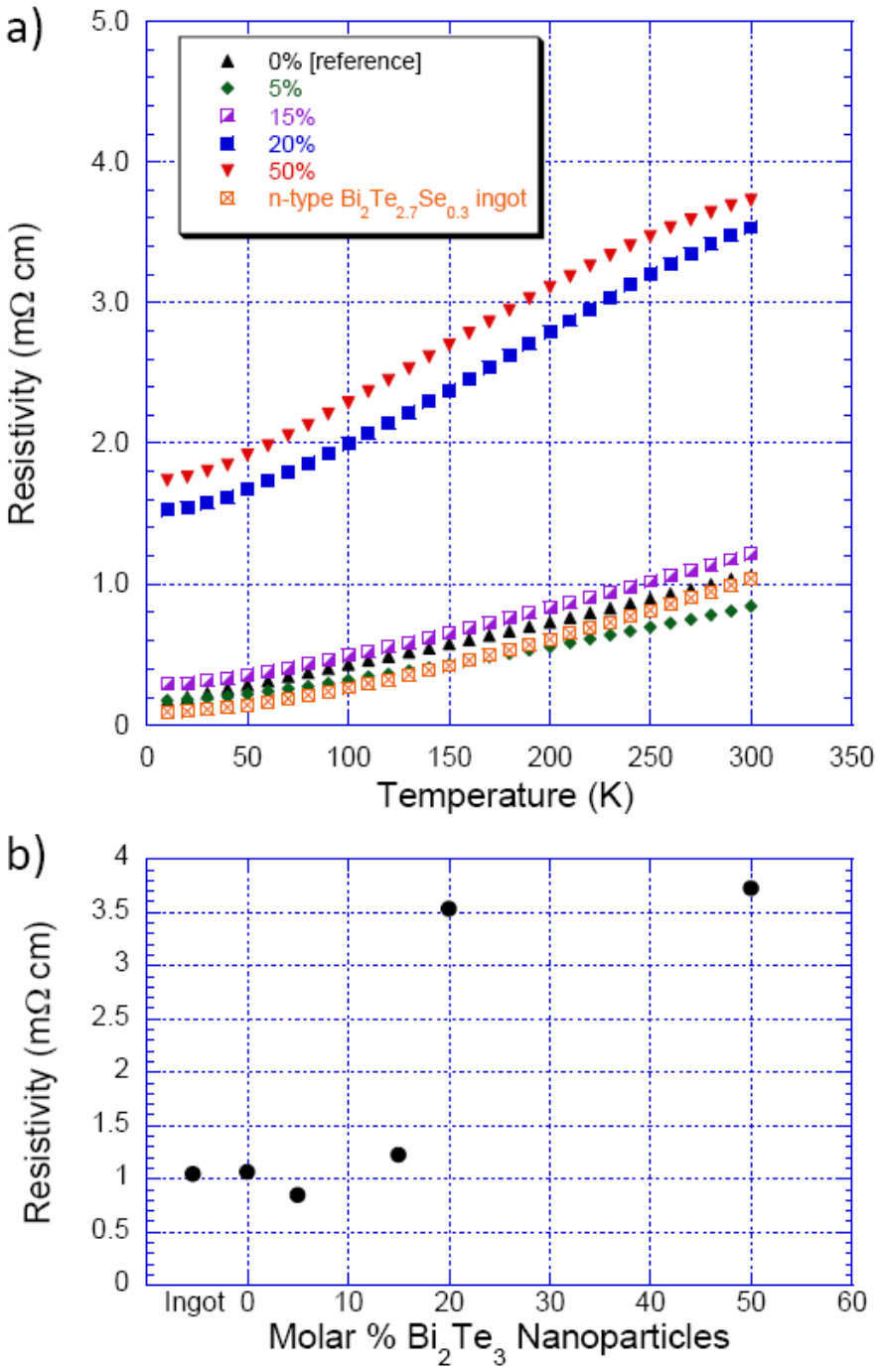

Figure 49. a) Resistivity vs. temperature data for n-type bismuth telluride nanocomposites prepared via mixing. b) Resistivity vs. percentage of nanoparticles, at 300 K.

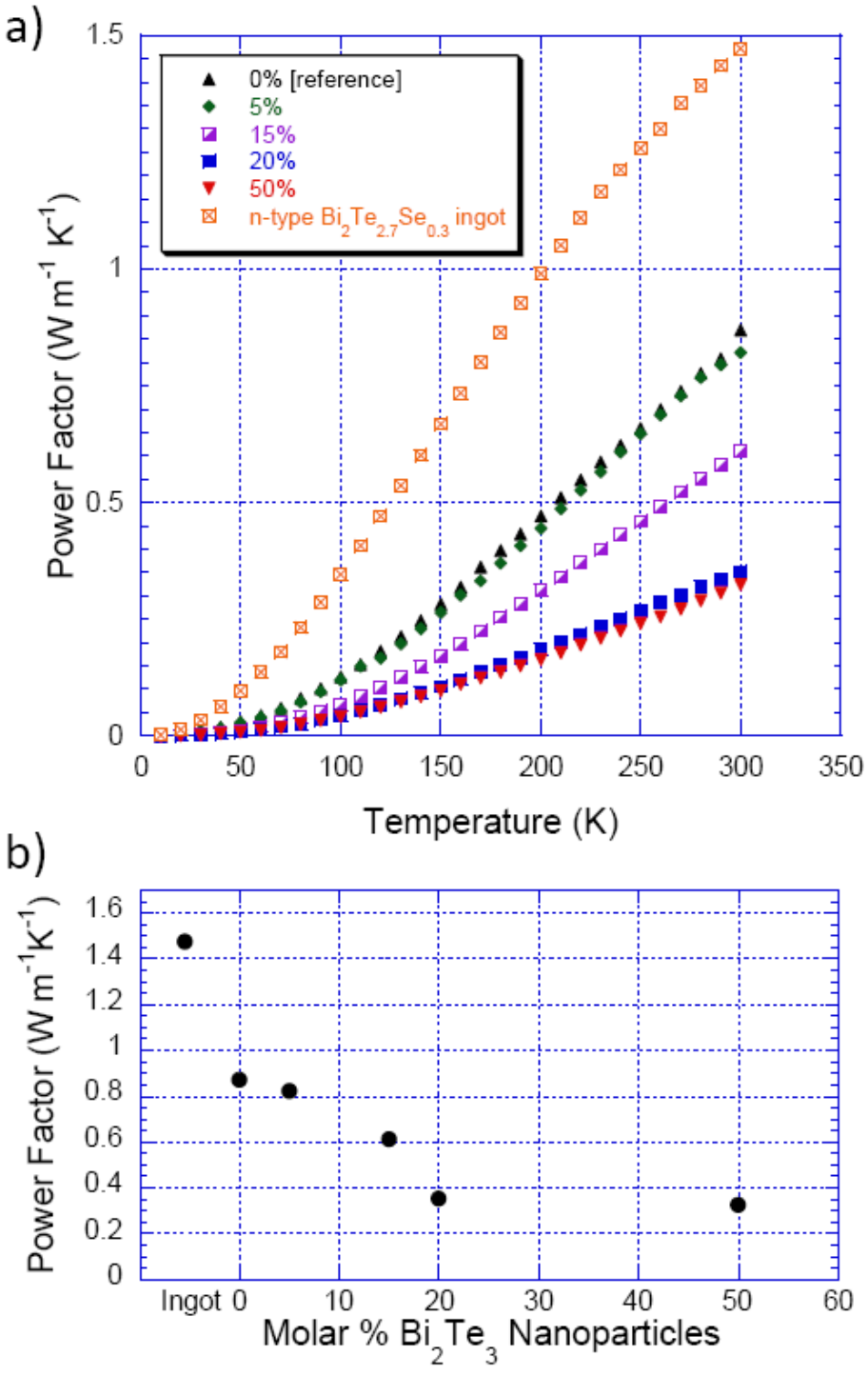

Figure 50. a) Power factor vs. temperature data for the n-type bismuth telluride nanocomposite series, prepared by mixing. b) PF vs. percentage of nanoparticles, at 300 K.

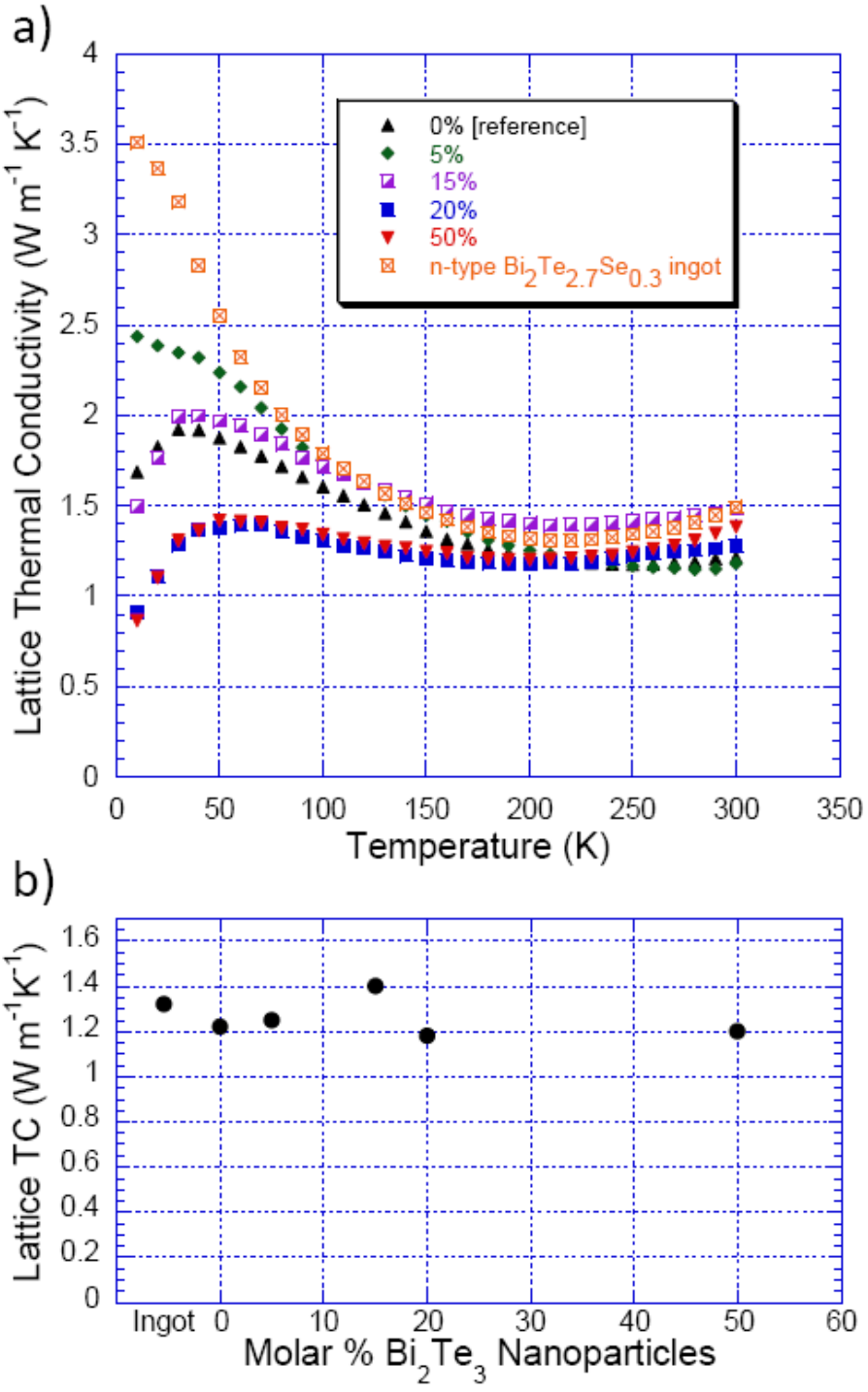

Figure 51. a) Lattice thermal conductivity vs. temperature data for n-type bismuth telluride nanocomposites. b) Lattice TC as a function of percentage of nanoparticles at 300 K.

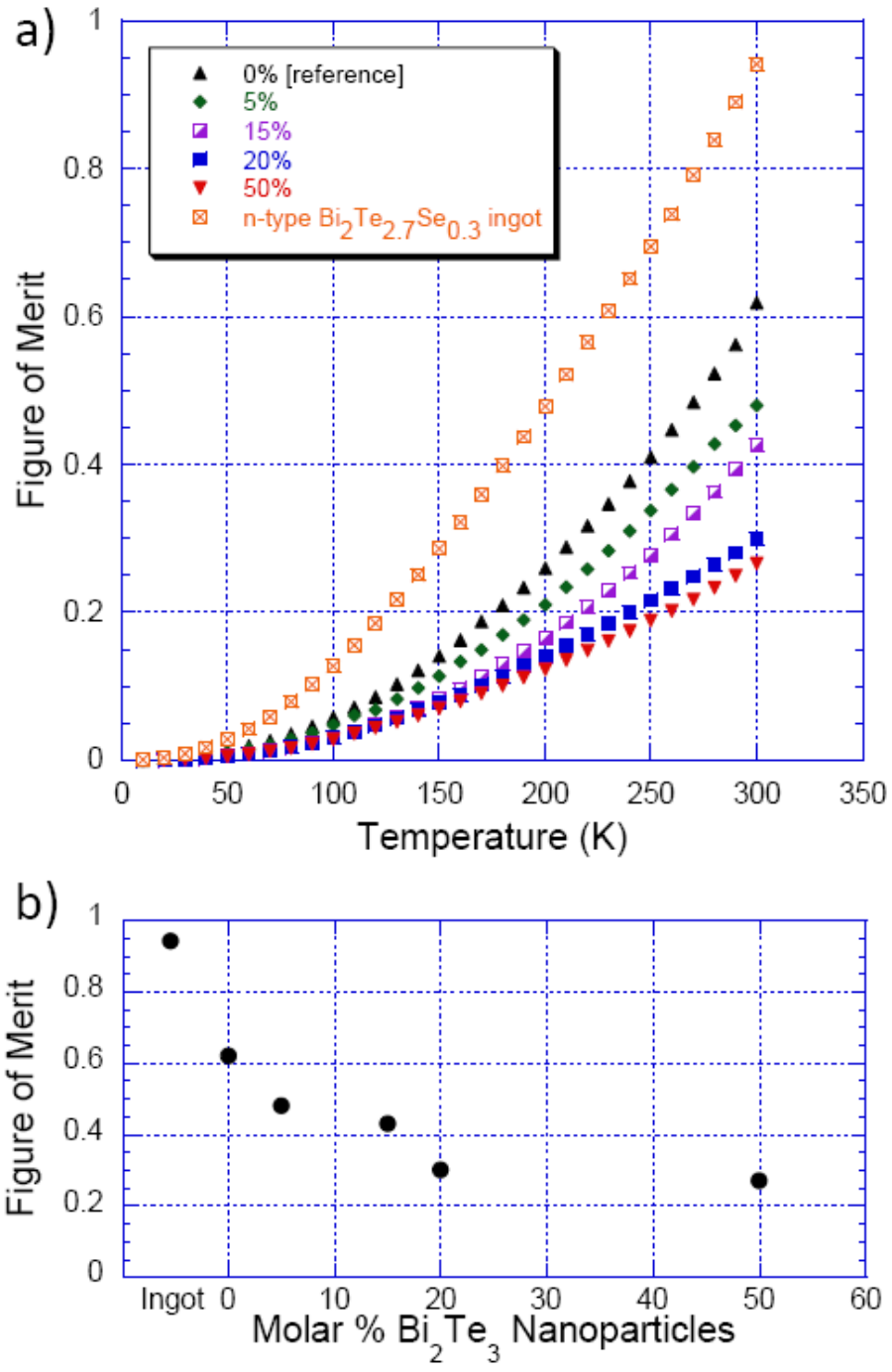

Figure 52. a) Figure of merit (ZT) vs. temperature data for the series of n-type bismuth telluride nanocomposites (using corrected total TC values). b) ZT as a function of percentage of nanoparticles, at 300 K.

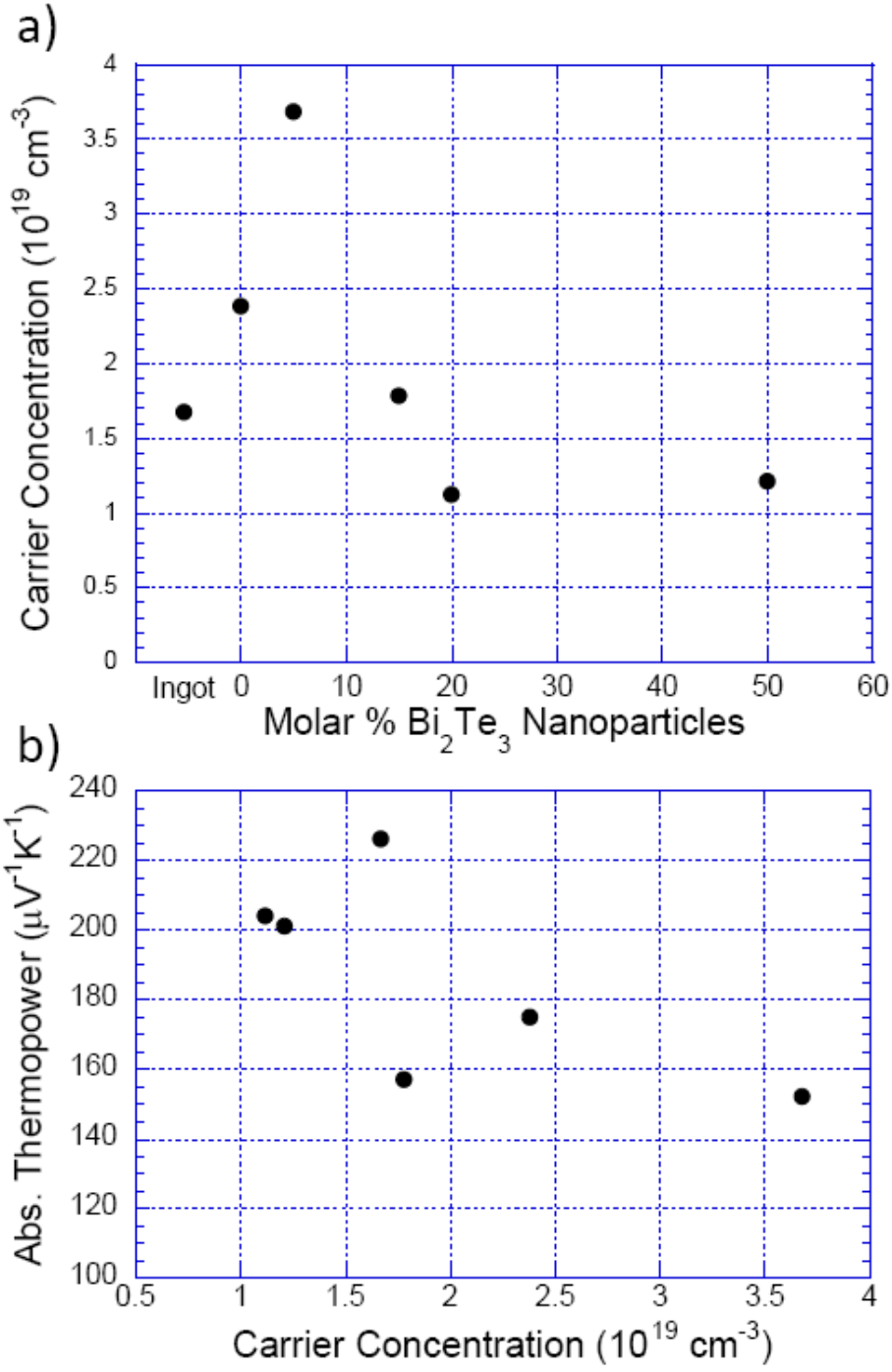

Figure 53. a) Carrier concentration as a function of nanoparticle percentage. b) Thermopower magnitude vs. carrier concentration, showing a rough α vs. $1/n$ dependence. Each graph shows the values at 300 K.

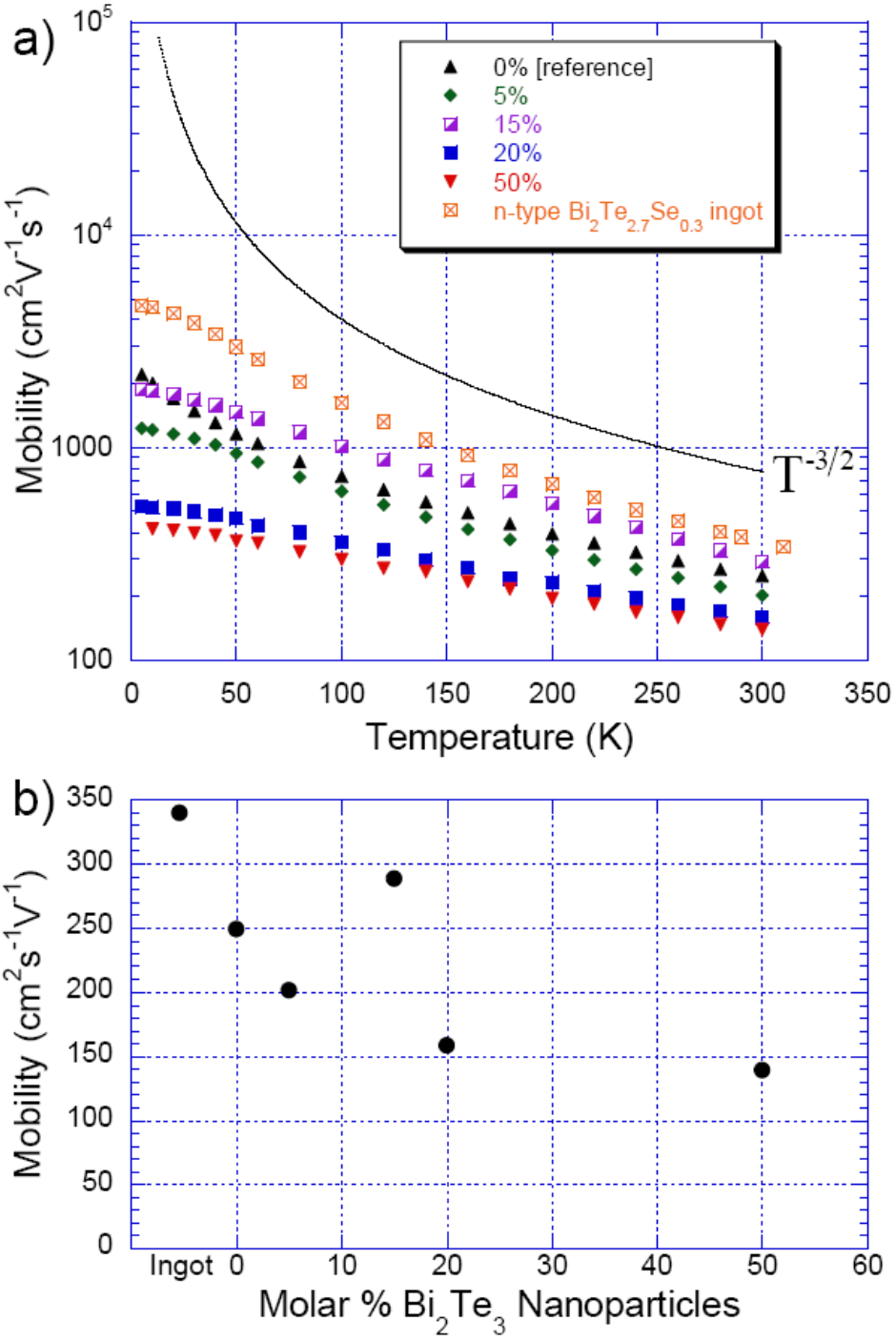

Figure 54. a) Electronic mobility vs. temperature data for the series of n-type bismuth telluride nanocomposites, following a $T^{3/2}$ trend above 75 K. b) Mobility as a function of percentage of nanoparticles, at 300 K.

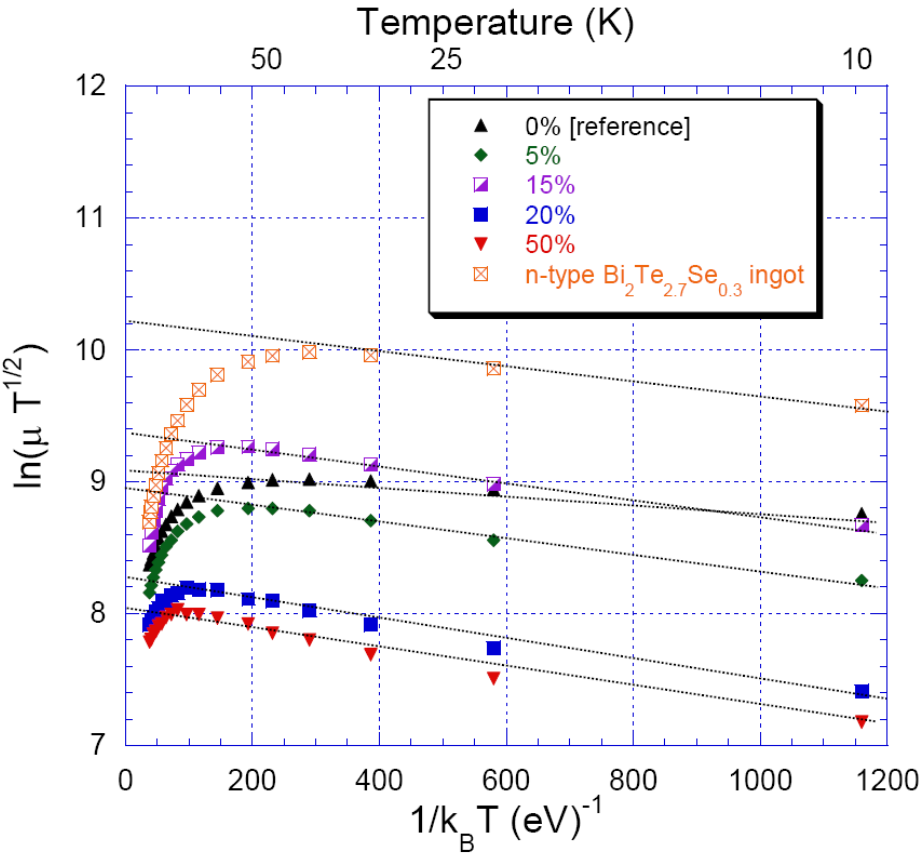

Figure 55. $\ln\left(\mu T^{1/2}\right)$ vs. $1/k_B T$ for the n-type bismuth telluride nanocomposites. Temperature is indicated along the top of the graph.

BiSb Nanocomposites

Nanocomposites formed using nanoparticles of compounds other than bismuth telluride are of interest for a variety of reasons. For example, difficulties in isolating the effects of the nanoparticles upon the transport properties of the composites arise when the nanoparticles and the matrix particles are of the same material, particularly when then matrix material has an abundance of sub-micron-sized grains, as in the case of the ball-milled Bi_2Te_3 nanocomposites. Selecting nanoparticles from a different material than the matrix could make their effects upon the transport properties, particularly the electronic transport properties, easier to distinguish, regardless of the average size of the matrix grains. Further, the different electrical properties of nanoparticles of various compounds could have interesting effects upon the electronic transport properties of the composites, and any differences in lattice structure between the matrix and the nanomaterials could have beneficial effects upon the lattice thermal conductivity.

To this end, BiSb nanoparticles (n-type) were incorporated with n-type $Bi_2Te_{2.7}Se_{0.3}$ matrix powders into a densified composite. One consideration in choosing BiSb is its high thermopower that approaches peak value in the vicinity of 70 K [93], in contrast to the peak for bismuth telluride, which occurs closer to 400 K. Incorporating BiSb into a bismuth telluride composite, then, could have the effect of boosting the thermopower of the composite in the low temperature region. Another consideration was the ease of synthesizing large quantities of BiSb nanoparticles by a modification of the hydrothermal method. To synthesize BiSb nanoparticles, compounds such as $SbCl_3$ or $SbNO_3$ are reacted in an ethanol solution within the temperature range of 150-200^oC. An

SEM image of the typical particle size and morphology obtained by this method is presented in figure 56. The particles are again irregular, but have on average larger sizes than the Bi_2Te_3 nanoparticles, with sizes on the order of hundreds of nm. Following nanoparticle synthesis, matrix material was again ground via mortar and pestle from the n-type $Bi_2Te_{2.7}Se_{0.3}$ ingot, sieved to a distribution between the 32-45μm sieves, and then mixed with the appropriate quantity of nanoparticles, calculated by molar percentage. Mixing was accomplished by the 3-axis mechanical mixer, and the mixtures of matrix and nanoparticles were hot pressed at 350 K and 2.800 tons (~216.6 MPa) in a nitrogen atmosphere. The 0% reference used in the previous section, i.e. a sample pressed using the same processing conditions but without the addition of nanoparticles, is again used as a reference sample for these composites. By this procedure, BiSb nanocomposites were produced with 5 and 20 mol. % BiSb inclusions.

Figure 57a is an SEM image of a particle aggregate after mixing but prior to hot pressing. As before, even though the total particle size is on the order of 40 μm, the particle appears to be an aggregation of smaller matrix particles, with nanoparticles dispersed on the surface and in between the matrix particles. Examination of the finer structure of this particle reveals the presence of sub-micron-size particles (figure 57b), the size and morphology of which is presented in figure 57c. Comparing this image to figure 56 shows that the size and morphologies of these particles are consistent with the BiSb nanoparticles. An SEM image of a nanocomposite after hot pressing is presented in figure 58. The grain structure here also looks quite similar to what was observed for the Bi_2Te_3 nanocomposites, with grains on the size scale of 5-15μm that show some degree

of structural deformation of the matrix particles, as well as regions that have much smaller size scales. In particular, it appears as though nanoparticles of BiSb have aggregated in between the grains of $Bi_2Te_{2.7}Se_{0.3}$, as indicated by the arrow.

Plots of thermopower vs. temperature and vs. percentage of BiSb nanoparticles are presented in figure 59. It is difficult to identify much of a trend in the magnitude of the room temperature values (figure 59b), but there are slight differences in curvature for the nanocomposites data in the thermopower vs. temperature curve (figure 59a). This effect is especially pronounced in the 20% sample and is likely caused by the different temperatures at which the BiSb and bismuth telluride systems achieve their thermopower maxima. Although the effect is more pronounced in the 20% curve, the effect is perhaps more noticeable in the data for the 5% sample, as this data curve nearly overlays the data curve for the ingot. In fact, this 5% sample has higher thermopower values than the ingot at temperatures up to ~125 K, as well as thermopower values well above those of the reference sample. The downside of the effect of the low temperature thermopower enhancement, however, seems to be a reduction in the thermopower of these composites at room temperature, an effect that is strongest in the 20% sample.

Both of the nanocomposites with BiSb additions have residual resistivities that are higher than the reference sample by just over 0.2 mΩ cm (figure 60), an effect that is attributable to increased scattering of the charge carriers by nanoparticle-induced disorder. The effect of the high thermopower value for the 5% sample is noticeable when the power factor is calculated (figure 61), as this sample surpasses the reference sample at all temperatures, but most noticeably at low temperatures. The high resistivity values

exhibited by this sample, however, keep it from having a power factor that surpasses that of the ingot.

Of particular interest for this series of samples is a large systematic decrease in the lattice thermal conductivity (figure 62). Not only do the nanoparticles cause a suppression of the low temperature peak, but in this case there is a significant reduction of the lattice TC throughout the measured temperature range. Since the low temperature reduction can be attributed to additional grain boundary scattering brought on by the addition of nanoparticles, it is likely that the reductions seen at higher temperatures are facilitated by the lattice mismatch between the matrix $Bi_2Te_{2.7}Se_{0.3}$ material and the BiSb nanoparticles. The effects of such reductions upon the figures of merit for these composites are that both the 5% and 20% samples have ZT values higher than the reference sample, if not the ingot, at temperatures up to 275 K (figure 63). Even though the 20% sample shows a tremendous decrease in thermal conductivity, the high thermopower value of the 5% sample causes it to be better, from a standpoint of efficiency.

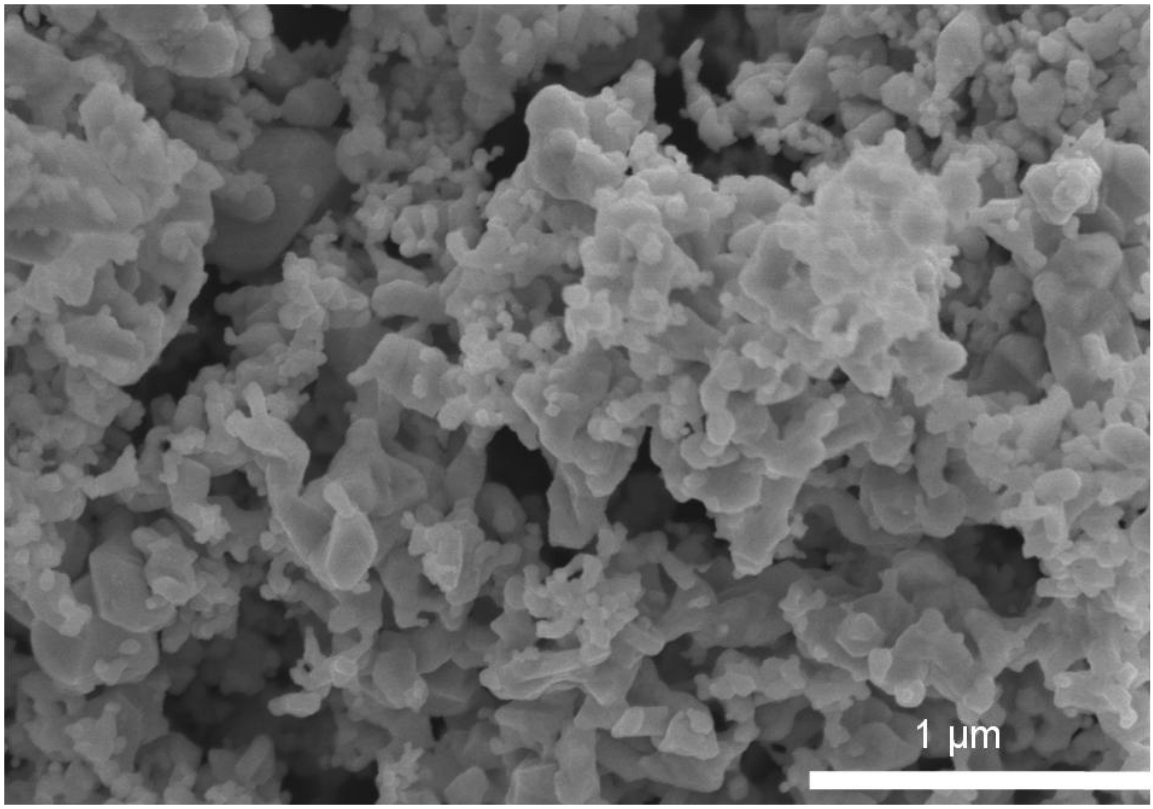

Figure 56. SEM of BiSb nanoparticles grown by the hydrothermal method.

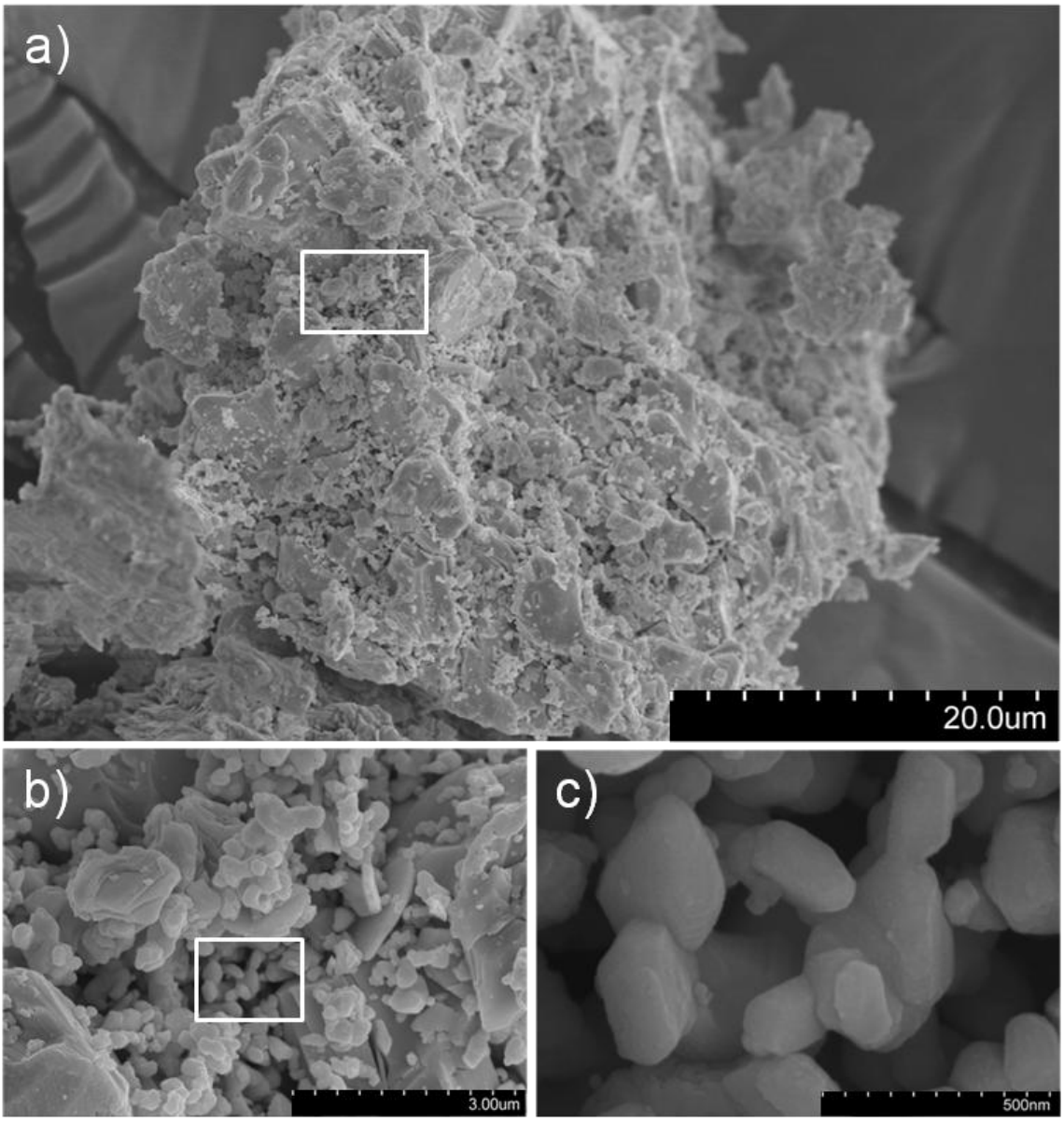

Figure 57. a) SEM of a particle of the n-type bismuth telluride matrix with BiSb nanoparticles intermixed. b) Close-up of the region marked in 57a. c) Close-up of the region marked in 57b, showing the BiSb nanoparticles.

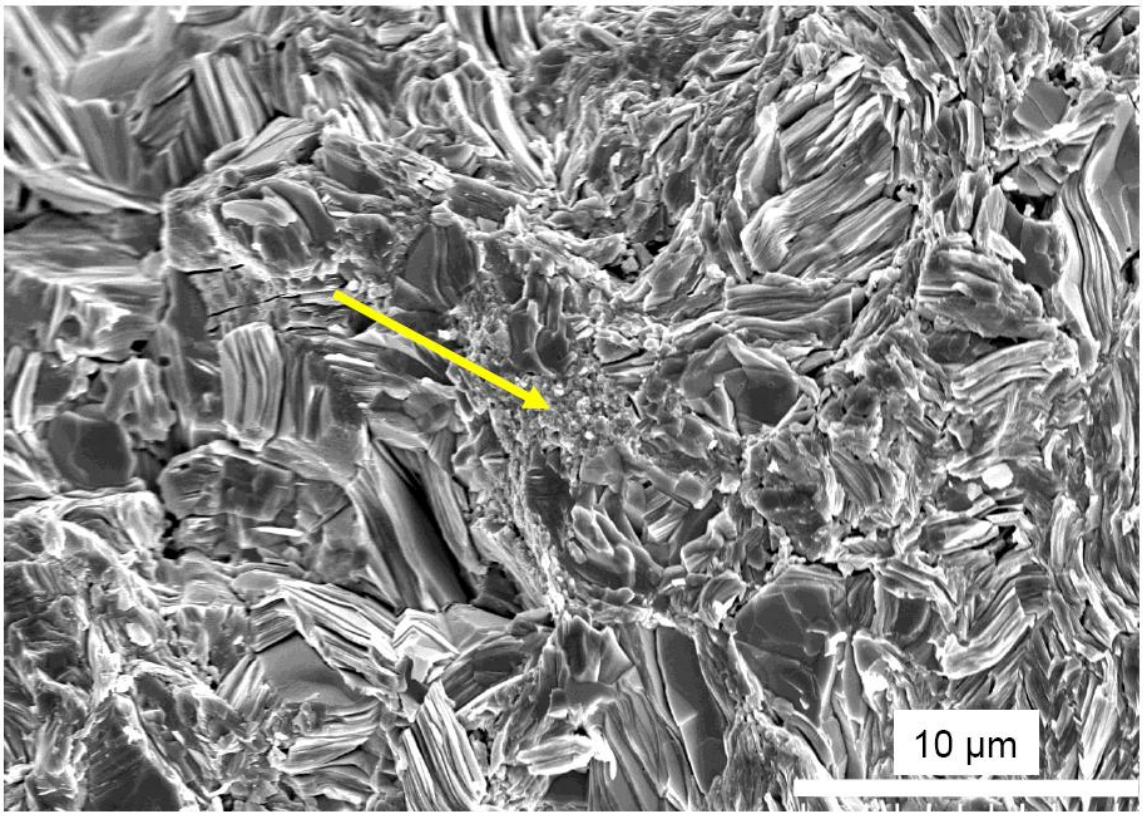

Figure 58. SEM image of the cross section of a BiSb nanocomposite, following hot pressing. The arrow indicates an aggregation of BiSb nanoparticles.

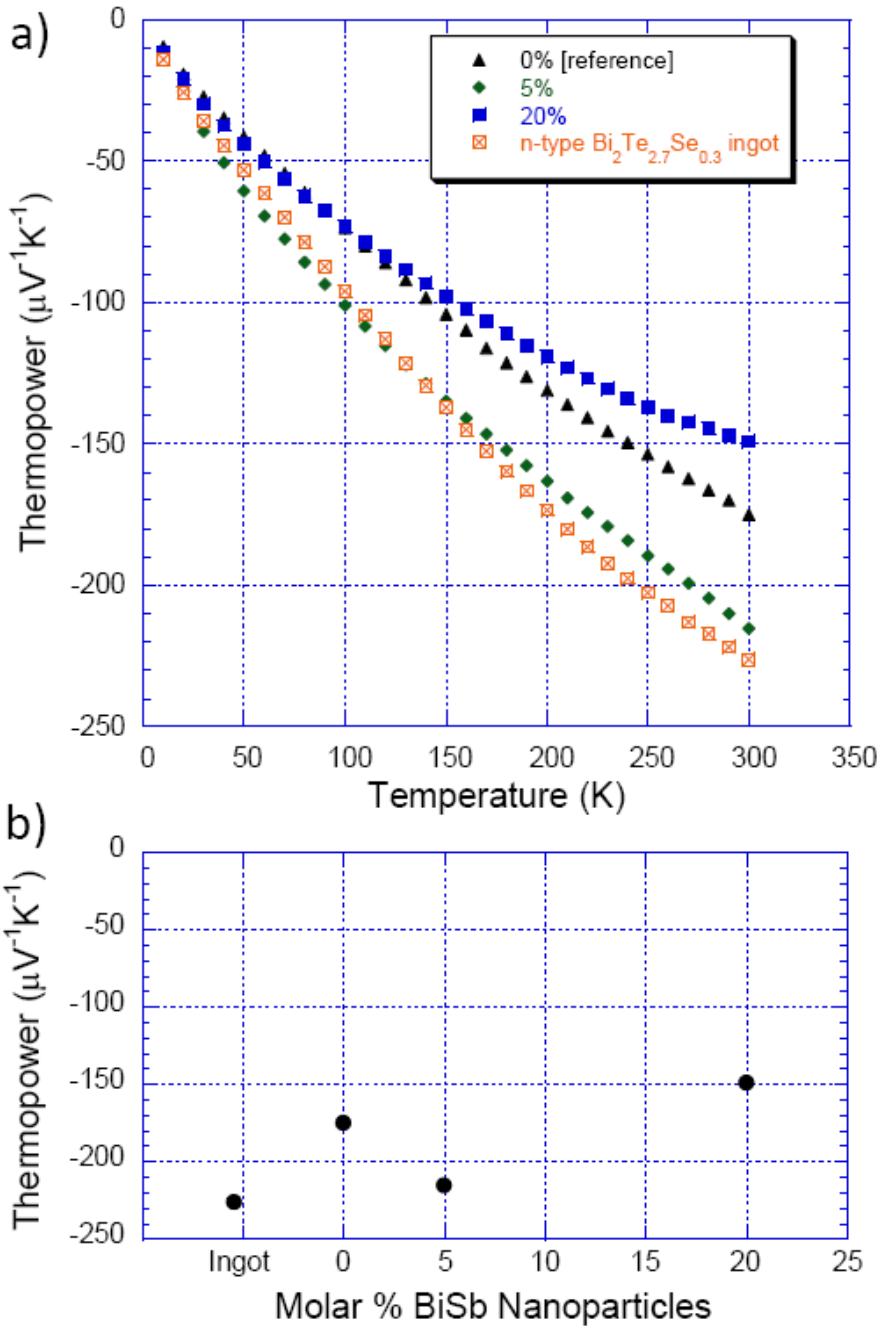

Figure 59. a) Thermopower vs. temperature data for the n-type BiSb nanocomposites, showing a mild change in curvature for the BiSb-containing samples. b) Thermopower vs. BiSb percentage, at 300 K.

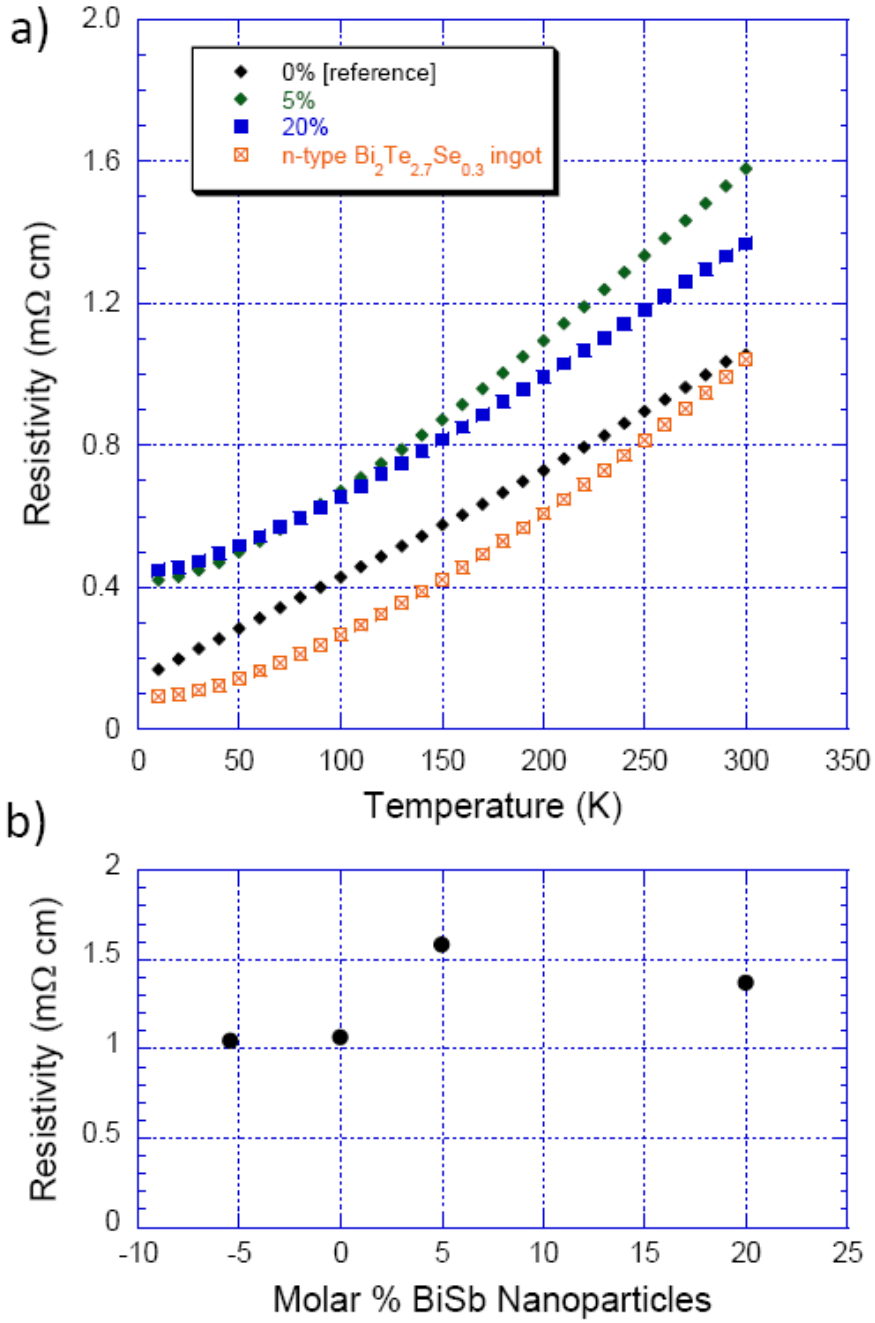

Figure 60. a) Resistivity vs. temperature data for the n-type BiSb nanocomposites. b) Resistivity vs. BiSb nanoparticle percentage, at 300 K.

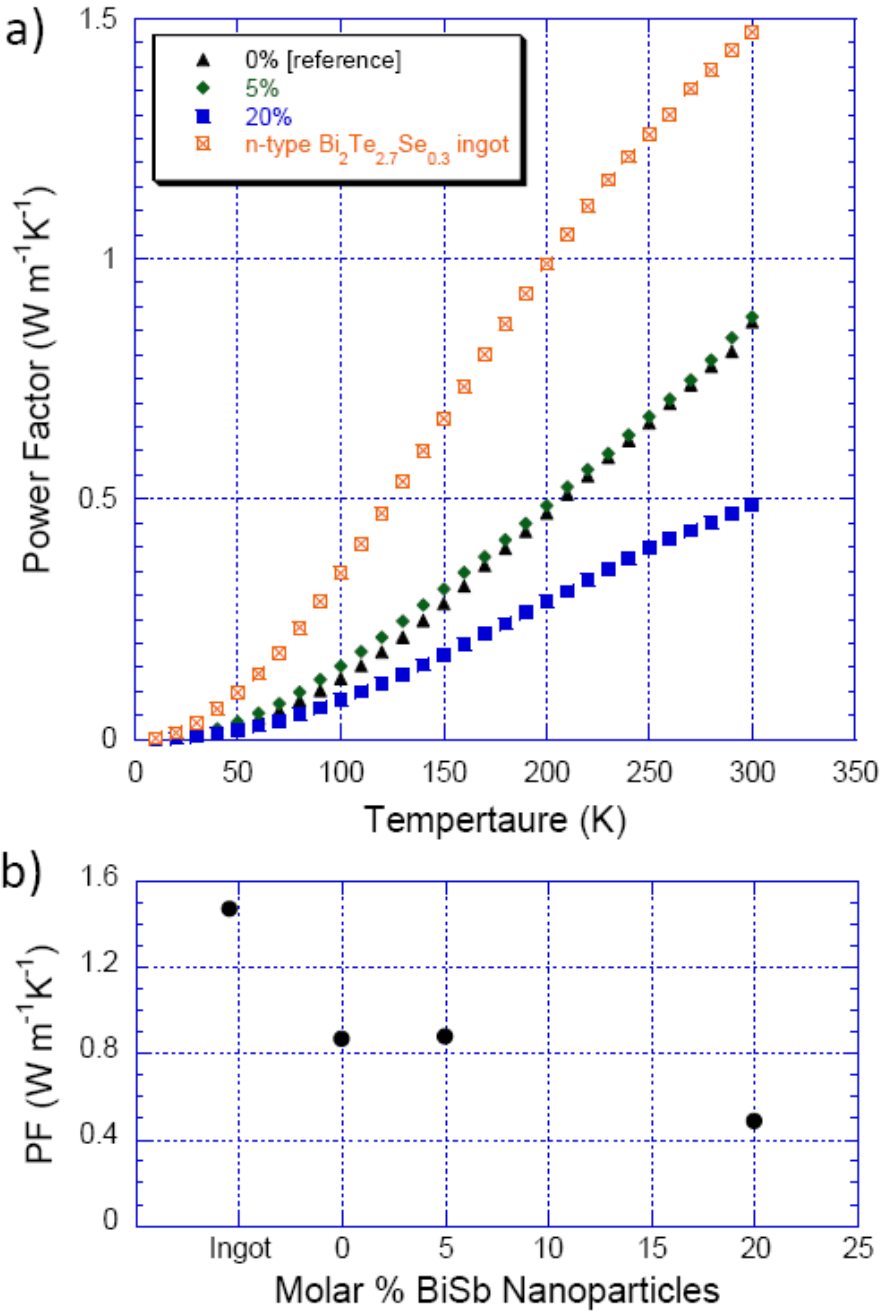

Figure 61. a) Power factor (PF) vs. temperature data for the n-type BiSb nanocomposites. b) PF vs. percentage of BiSb nanoparticles, at 300 K.

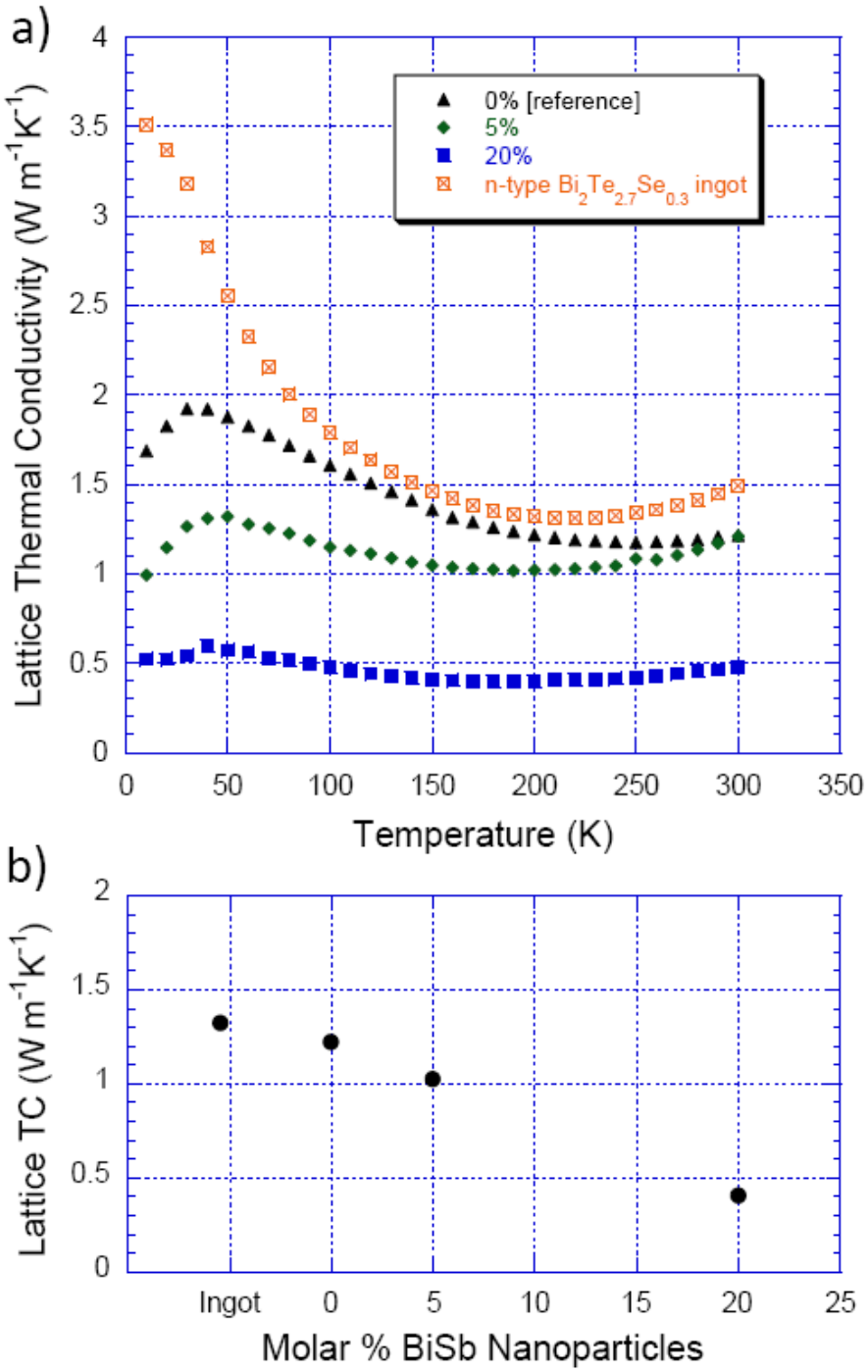

Figure 62. a) Lattice thermal conductivity (uncorrected) vs. temperature for the n-type BiSb nanocomposites, showing a dramatic reduction in TC for the 20% sample. b) Lattice TC vs. percentage of BiSb nanoparticles, at 200 K.

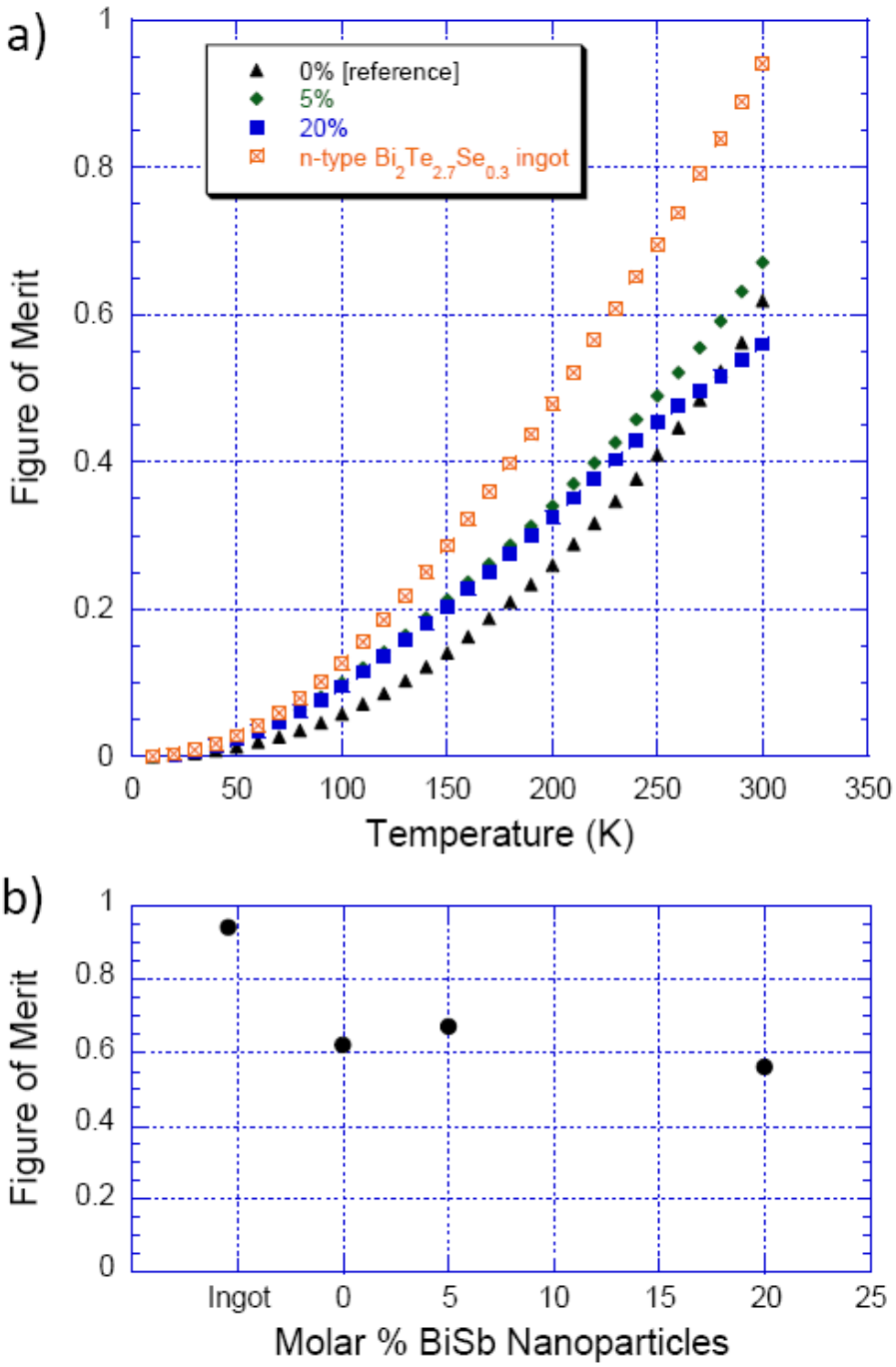

Figure 63. a) Figure of merit vs. temperature data for the n-type BiSb nanocomposites. b) ZT vs. percentage of BiSb nanoparticles, at 300 K.

Bi_2S_3 Nanocomposites

Another compound of interest to bismuth telluride-based nanocomposites due to its morphology was that of Bi_2S_3, which can be synthesized by the hydrothermal method in the form of nanowires. It was thought that this material might have the advantages of both a lattice mismatch with the bismuth telluride matrix as well as the potential for enhanced electron transport down the length of the nanowires. The hydrothermal method was adapted in this case by combining S or NaS_2 in distilled water at moderate temperatures, often in the presence of a surfactant such as thyoglycolic acid. The resultant nanowires have lengths ranging from hundreds of nanometers to several microns, and cross sectional areas that have dimensions on the order of 50-100 nm (figure 64a). These wires were incorporated via mechanical 3-axis mixing and hot pressing into a matrix of n-type $Bi_2Te_{2.7}Se_{0.3}$ particles that were first ground and sifted such that the result was a particle size distribution of approximately 5-15μm, as obtained in previous studies. Conditions of hot pressing in this case were 300-400^oC and 2.500 tons (~193.4 MPa). Samples were synthesized having 2, 5, and 10 molar % Bi_2S_3, along with a reference sample that contained 0 mol. % Bi_2S_3 nanowires. Figure 64b shows an SEM image of a typical nanocomposite after hot pressing. In the bottom, a $Bi_2Te_{2.7}Se_{0.3}$ matrix particle having a cross section of ~10μm is visible, while the upper part of the image shows a region where it appears as though the Bi_2S_3 nanowires have aggregated. The larger cross sections of what appear to be the nanowires likely indicate that some melting has occurred and that the nanowires have grown together to some extent under the hot pressing conditions.

Thermopower data shows an initial drop in thermopower magnitude followed by a slow increase proportional to the percentage of nanoparticles in the composite (figure 65). This trend is mirrored in the resistivity, with the 2% sample showing a sharp decrease in resistivity as compared to the reference sample, and the 5% and 10% samples representing a gradual rise in room temperature resistivity (figure 66b). Although some flattening of the resistivity vs. temperature curves as compared to the ingot occurs, the effect is present in the reference sample as well as the samples containing Bi_2S_3, and it cannot therefore be attributed solely to the presence of the nanowire additions. It is possible, however, that the low values of resistivity seen in these samples are attributable to the Bi_2S_3 nanowires enhancing electrical conduction to some extent. If this is the case, it is nevertheless clear that a saturation point is reached after which continued addition of nanowires is detrimental to the electrical conductivity, and that this point occurs below 5% of nanowires. From a standpoint of high power factor, it would appear as though percentages of nanowires in the range of 5% are most beneficial (figure 67)—otherwise nanowire introduction causes a reduction in the power factor. Figure 68 indicates that the effect of the nanowires upon the lattice thermal conductivity is minimal. Again, there is a reduction in the low temperature lattice TC peak that indicates an increase in boundary scattering for these samples as compared to the ingot, but there does not appear to be any further flattening of this peak beyond what is seen in the reference material. Further, lattice TC values taken at 200 K and plotted against the percentage of Bi_2S_3 nanowires used in the composites shows a minor increase in magnitude. The net result, then, is that changes in the figure of merit are again dominated by the effects of the nanowires upon

electrical transport, such that both nanocomposites show a substantial reduction in ZT as compared to the reference material (figure 69). Therefore it seems that while Bi_2S_3 nanowires are indeed beneficial for increasing the electrical conductivity in composites such as these, the negative effects upon the thermopower are sufficient to counteract any advantages gained in electrical conduction.

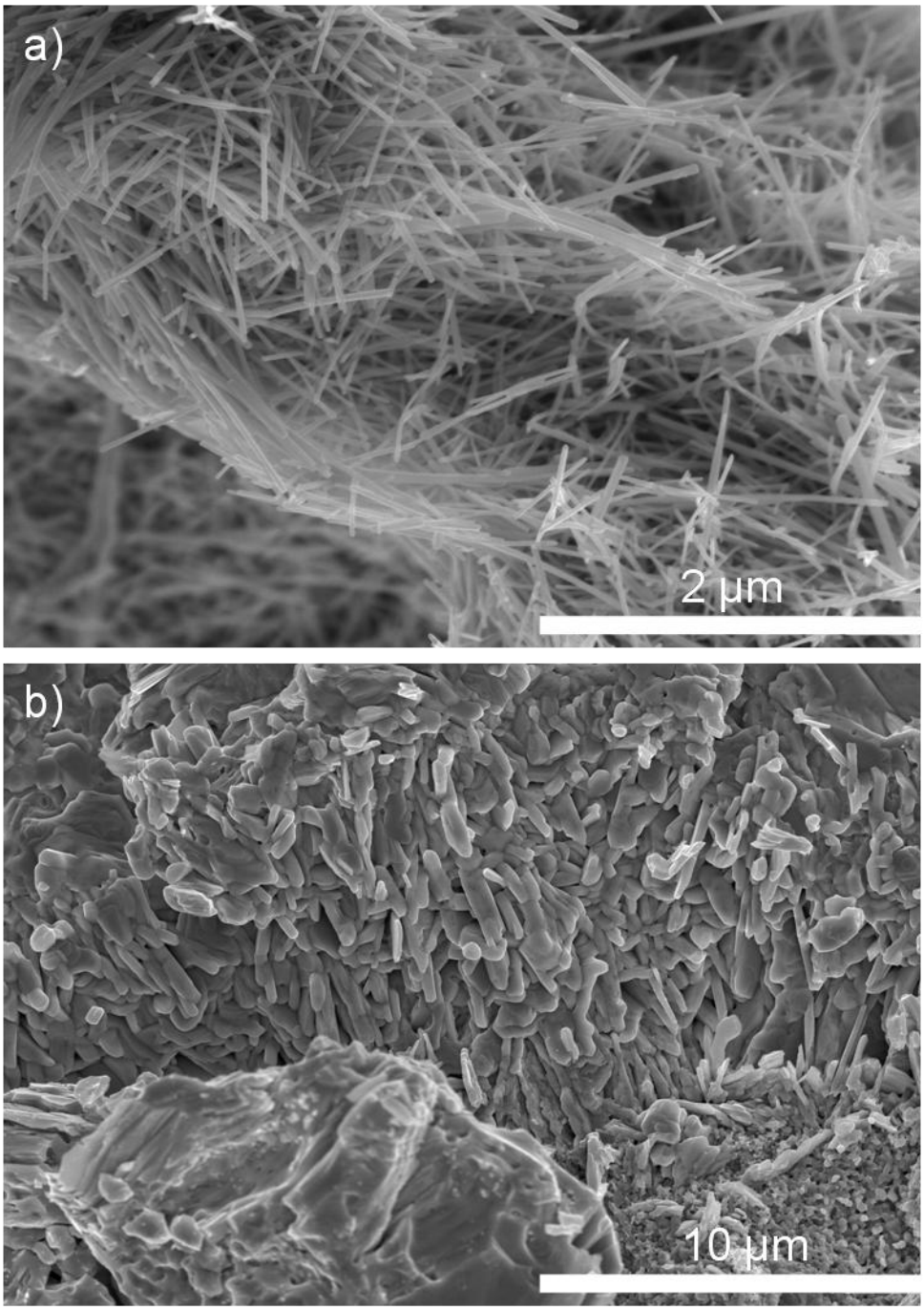

Figure 64. a) SEM image of Bi_2S_3 nanowires grown via the hydrothermal method. b) SEM of a Bi_2S_3-bismuth telluride nanocomposite after hot pressing. A large bismuth telluride matrix particle is visible at the bottom, and the nanowires appear to have grown together.

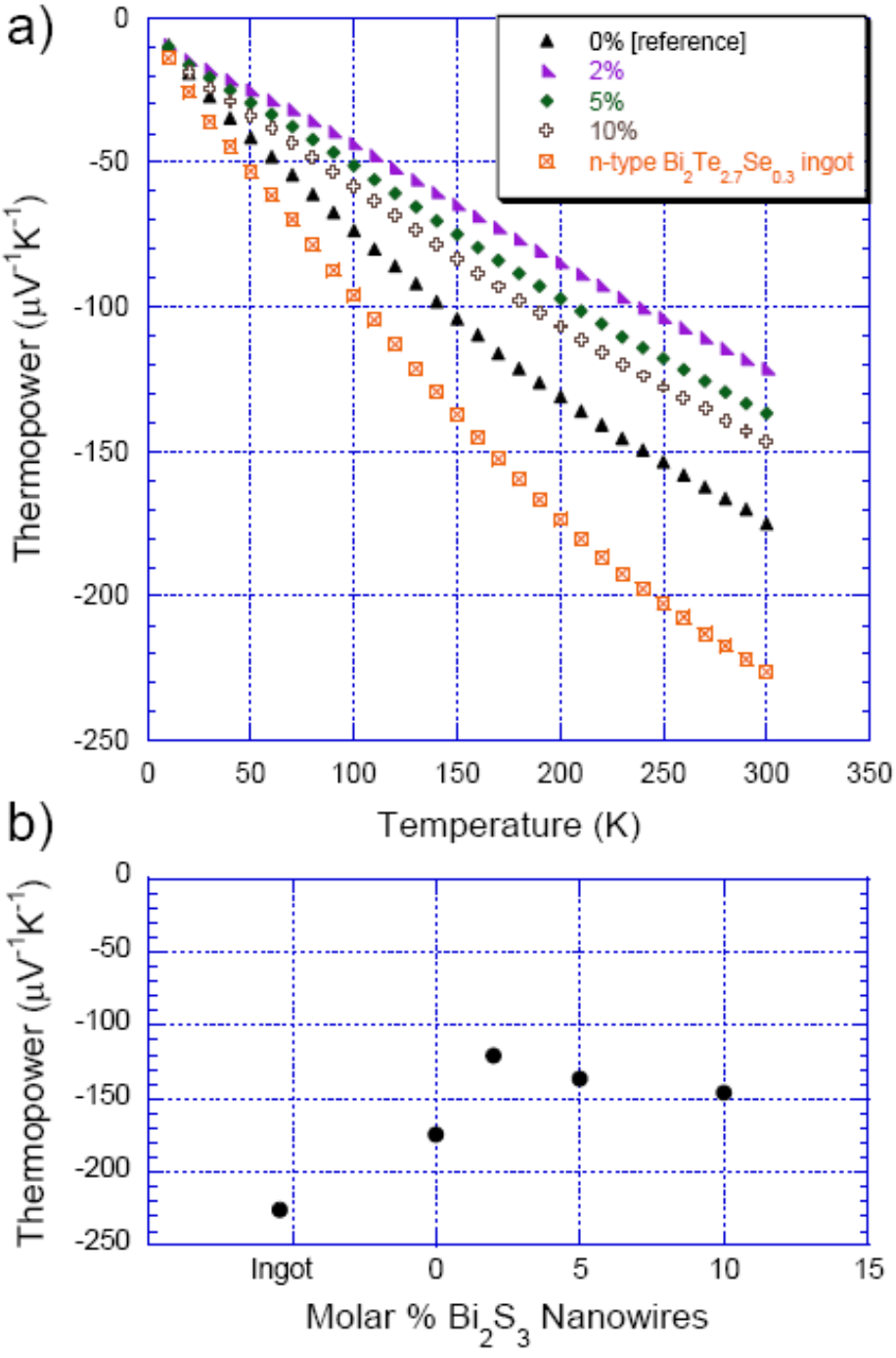

Figure 65. a) Thermopower vs. temperature data for the n-type Bi_2S_3 nanocomposites. b) Thermopower as a function of percentage of nanoparticles, at 300 K.

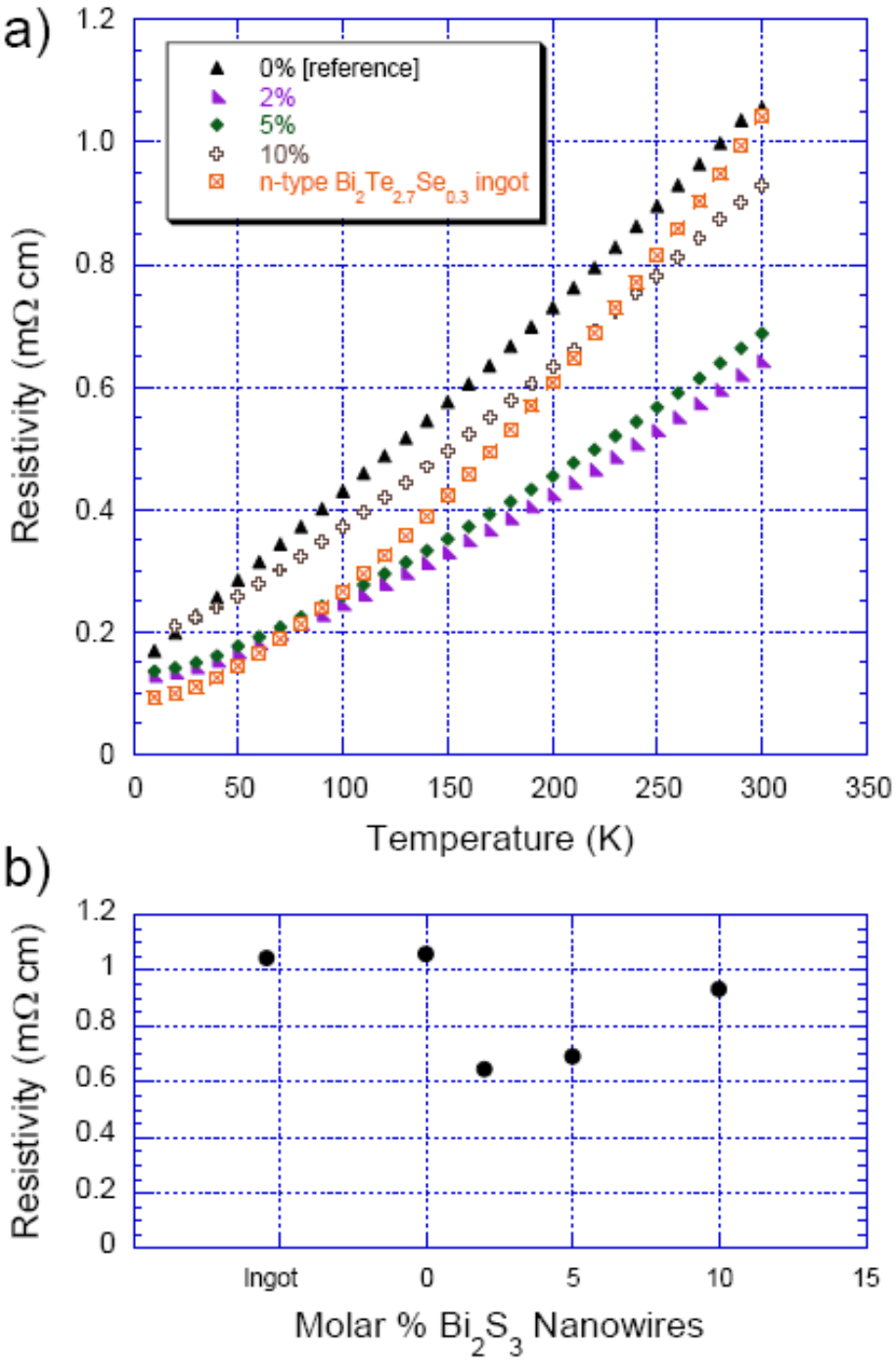

Figure 66. a) Resistivity vs. temperature data for the series of n-type Bi_2S_3 nanocomposites. b) Resistivity vs. percentage of nanoparticles, at 300 K.

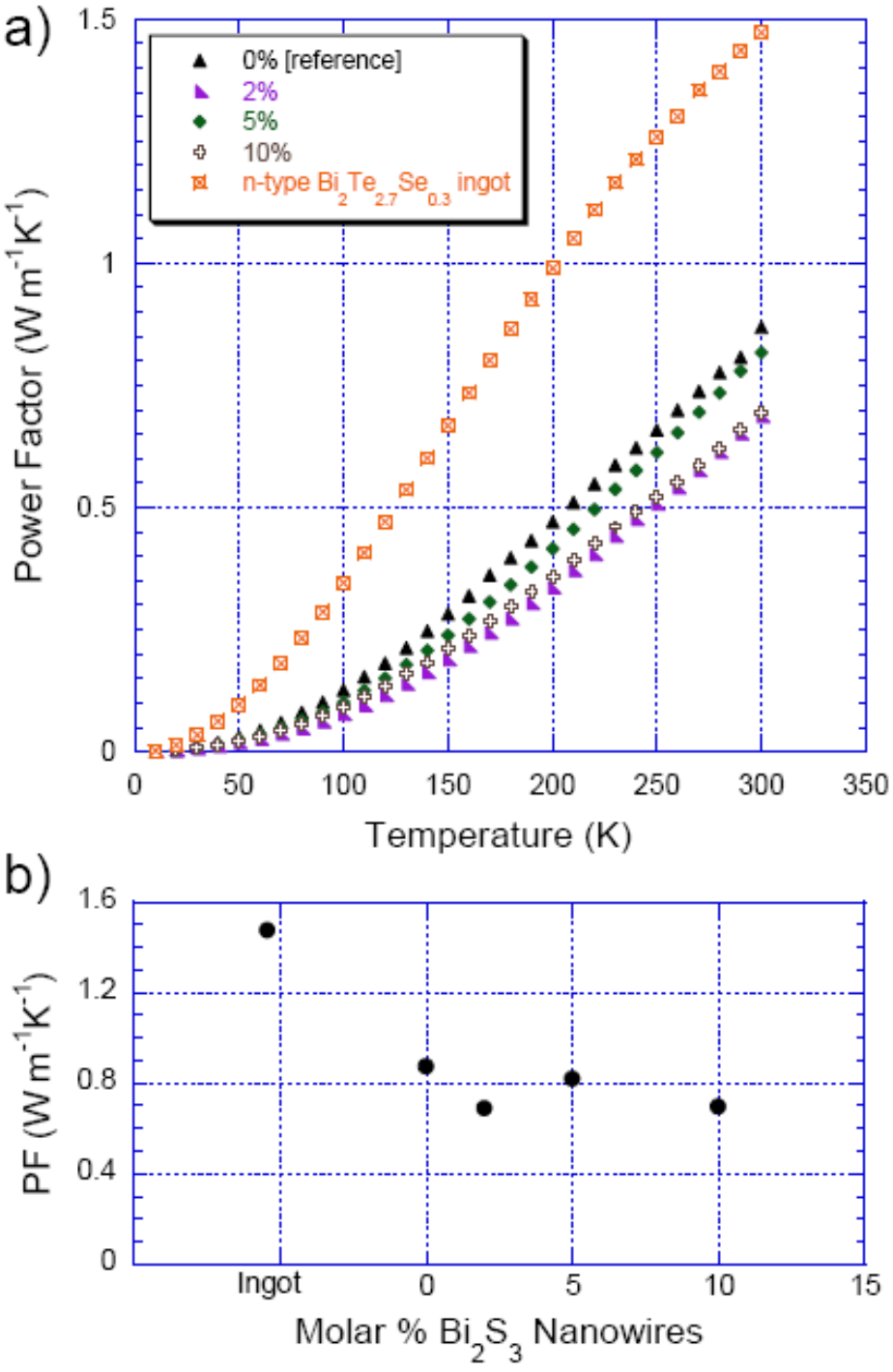

Figure 67. a) Power factor (PF) vs. temperature data for the series of n-type Bi_2S_3 nanocomposites. b) PF as a function of percentage of nanoparticles, at 300 K.

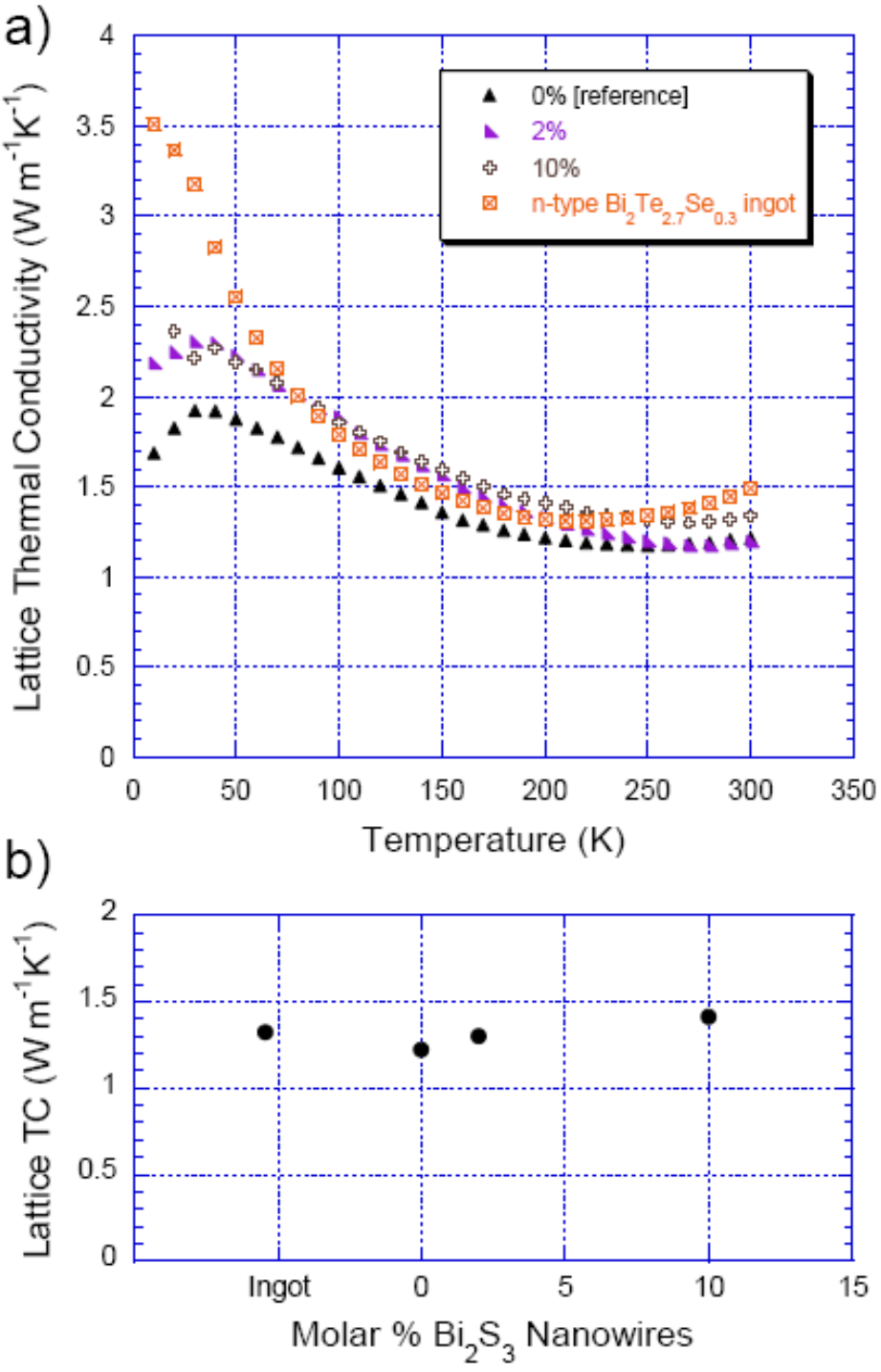

Figure 68. a) Lattice thermal conductivity vs. temperature data for the series of n-type Bi_2S_3 nanocomposites. b) Lattice thermal conductivity vs. percentage of nanoparticles, at 200 K.

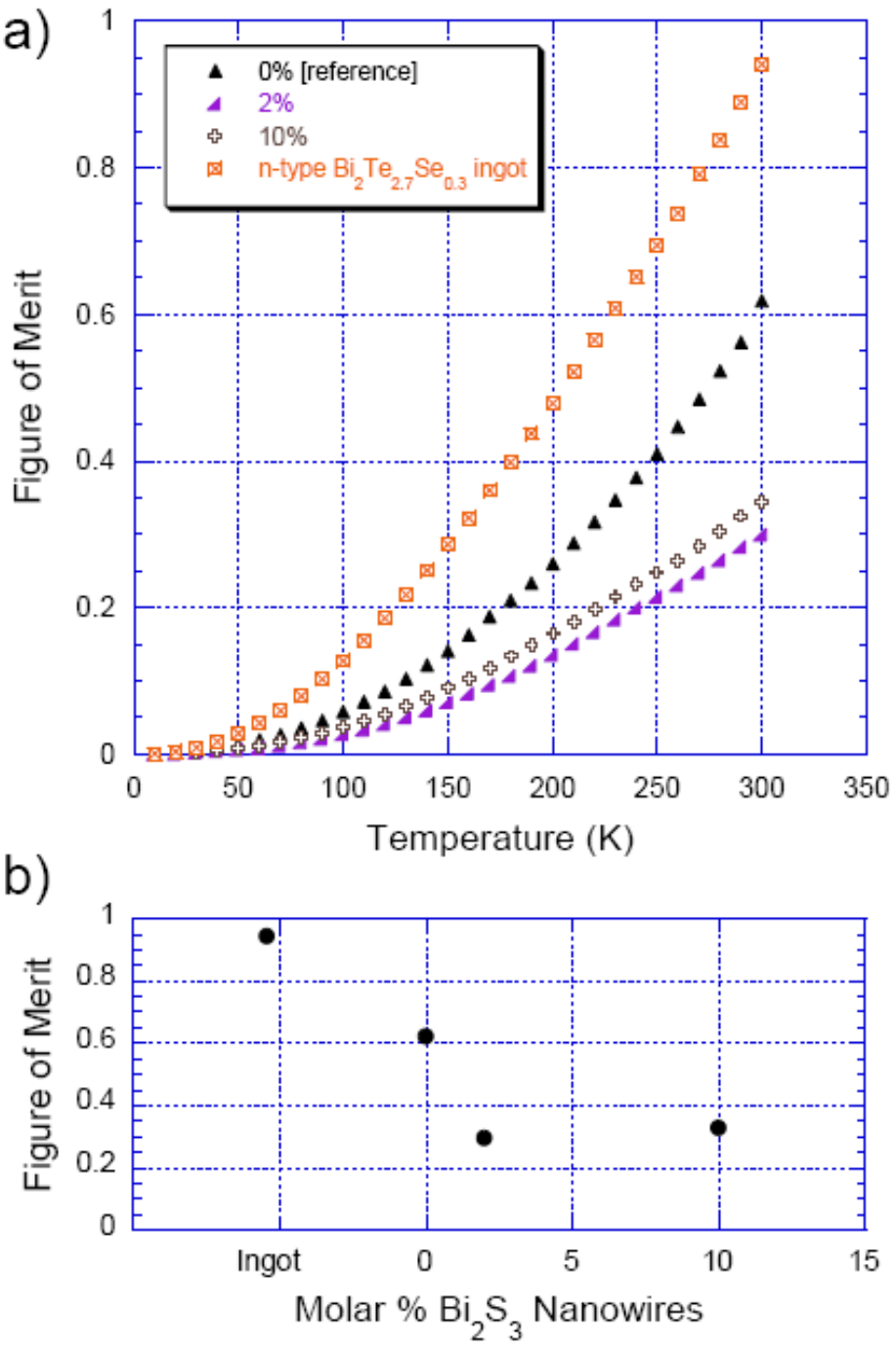

Figure 69. a) Figure of merit (ZT) vs. temperature data for the series of n-type Bi_2S_3 nanocomposites. b) ZT vs. percentage of nanoparticles, at 300 K.

Au / Ag Nanocomposites

One of the major difficulties in improving the efficiency of nanocomposites produced with a bismuth telluride matrix is the negative effect the nanoparticles have upon the electronic properties. Although nanoparticles have been shown to have a positive effect especially upon the low temperature thermal conductivity, in many cases the detriment posed to the electronic properties outweigh any benefits to the thermal conductivity. One method to circumvent this difficulty could be to incorporate nanoparticles with excellent electronic conductivities, such as Au or Ag, which are available commercially in colloidal form in sizes on the nanometer scale, into the matrix. While their excellent electrical conductivity could possibly increase the electronic part of the thermal conductivity, if the particle size is kept small enough, the particles could possibly serve as sites for point defect scattering of phonons, thereby decreasing the thermal conductivity. As phonon point defect scattering is an effect that comes into play at higher temperatures than boundary scattering of phonons, such an approach could potentially reduce the thermal conductivity in the temperature range of interest to bismuth telluride materials.

P-type $Bi_{0.4}Sb_{1.6}Te_3$ has a higher thermopower magnitude than the n-type sample (approximately 260 $\mu V\ K^{-1}$ at room temperature vs. -220 $\mu V\ K^{-1}$ for n-type $Bi_2Te_{2.7}Se_{0.3}$) and consequently a higher power factor. For this reason, the p-type ingot was selected as the matrix material for the Au and Ag nanoparticle inclusions. Colloids of Au nanoparticles are commercially available from Ted Pella, Inc., in diameters of 2 nm, 5 nm, and 20 nm, while Ag particles are only available at sizes of 20 nm. Fragments of the p-

type ingot were first ground via mortar and pestle and then sifted by a system of sieves, with an upper opening of 45 μm and a lower opening of 20 μm, the goal being a matrix grain size distribution of 20-45 μm, although previous studies indicate that the actual grain size will be somewhat smaller. Next, a specified volume of the Au or Ag colloid, determined by the molar percentage of nanoparticle that was desired in the nanocomposite, was decanted into a graduated cylinder. This calculation was based upon the published density of particles per mL for the given colloid [94], as well as upon the atomic weights of Au and Ag. The appropriate volume of the nanoparticle colloid was then mixed with a specified quantity of matrix material, measured by molar percentage, in a beaker that was placed on a hot-plate with a magnetic stirrer. The mixture was continuously stirred at low heat until it was reduced to a thick slurry, at which point the slurry was placed into a vacuum oven at low temperature ($< 50^{o}$C) to dry completely. After drying, the powders were inserted into either a 0.37 or 0.5 inch graphite die, briefly cold pressed, and then hot pressed at 350-400^{o} C and 1.500-1.650 tons for the 0.37 inch die (~211.9-233.1 MPa) or 3.000-3.200 tons for the 0.5 inch die (~232.1-247.6 MPa). In general, dies with larger inner diameters are less likely to break during hot pressing, even when the pressure applied to the sample is higher than what may be used for smaller I.D. dies. However, in the case of the Au / Ag colloids, the nanoparticles are so small and finely dispersed in the solutions that frequently a smaller I.D. had to be used because of the small volume of nanoparticles available. The following series of samples was grown by this method: 2, 5, and 20 nm Au at 0.025 mol. %, 20 nm Au and 20 nm Ag at 0.100 mol. %, and a 0% reference sample that was subjected to all the steps of the processing

used for the other samples, but with no nanoparticles added. Following hot pressing, the samples were imaged via SEM and samples were cut for low temperature electronic and thermal transport measurements.

Figure 70a shows an SEM image for a particle of the reference material prior to hot pressing. The overall particle size is approximately 30 x 50 μm, with the actual size of the matrix particles being on the order of 5-10 μm, similar to what was found in previous sections. Figure 70b shows a cross section of the sample whose composition is 0.100% 20 nm Au, after compaction by hot pressing. Here, the matrix particles can again be seen, but there are a couple of particles with sizes smaller than 1 μm that stand out in their response to the SEM beam (indicated by orange circles). These particles most likely represent moderate aggregations of the 20 nm Au particles that were added to the colloid, but they are rather hard to locate.

The effects of these nanoparticles upon the thermopower of the composites are presented in figure 71, as functions of thermopower, mol. %, and nanoparticle size. In figure 71a, the Au and Ag data are grouped by color, the two different percentages by filled or empty data points, and the nanoparticle sizes by the shape of the data markers. It is clear that the effect of the nanoparticles upon the thermopower is virtually none, whether the analysis is by temperature (71a), percentage (71b), or nanoparticle size (71c). This result is perhaps not entirely surprising, due to the small percentages in which these nanoparticles were added to the matrix powders, as well as the difficulty of locating the particles via SEM.

A consideration of the resistivity vs. temperature data shows little effect upon the curvature of the data trends, although there are slight changes in the residual resistivities (figure 72a). The mixture of metallic Au or Ag with semi-metallic bismuth telluride suggests that there should be some change in curvature, but again the small percentages of nanoparticles that were added, combined with the subtle differences between metallic and semi-metallic resistivity responses, cause the absence of any effects in this case to be inconclusive. Further analysis of the trends in nanoparticle percentage and size shows that while there is little change in resistivity when proceeding from the reference to the 2 nm or 5 nm Au samples, which were produced using 0.025% nanoparticles, the 0.025% 20 nm Au sample shows an increase of ~0.4 mΩ cm. When the mol. % is increased to 0.100% however, the resistivity value for this 20 nm Au sample returns to the value observed in the previous samples. When 20 nm Ag is introduced at 0.100 mol. %, the sample exhibits resistivity identical to the 0.025% 20 nm Au sample. The trend appears to be that larger particle sizes are detrimental to high conductivity values when introduced into the composites in small amounts, but that they are beneficial when the nominal percentages are increased. It is curious, however, that composites manufactured by incorporating Ag nanoparticles exhibit lower electrical conductivities than do the composites manufactured from Au nanoparticles, considering that Ag has a higher electrical conductivity than does Au [95].

The lattice thermal conductivity data (figure 73) indicates that the lattice TC tends to increase as the nanoparticle size increases, but then decreases if the nanoparticle percentage is further increased. This is most likely simply a reflection of the trend in the

electrical conductivity, since the calculated values of lattice TC depend on σ according to $\kappa_L = \kappa_T - L\sigma T$. The overall effect upon the ZT, then, is that small percentages of 2 nm particles and large percentages of 20 nm particles are beneficial for high ZT values, while the other samples show marked decreases in ZT (figure 74). Unfortunately, however, due to the small quantities of nanoparticles available and the difficulties in incorporating them into the composites, the final conclusion must be that the effects of Au or Ag nanoparticles upon these composites are inconclusive.

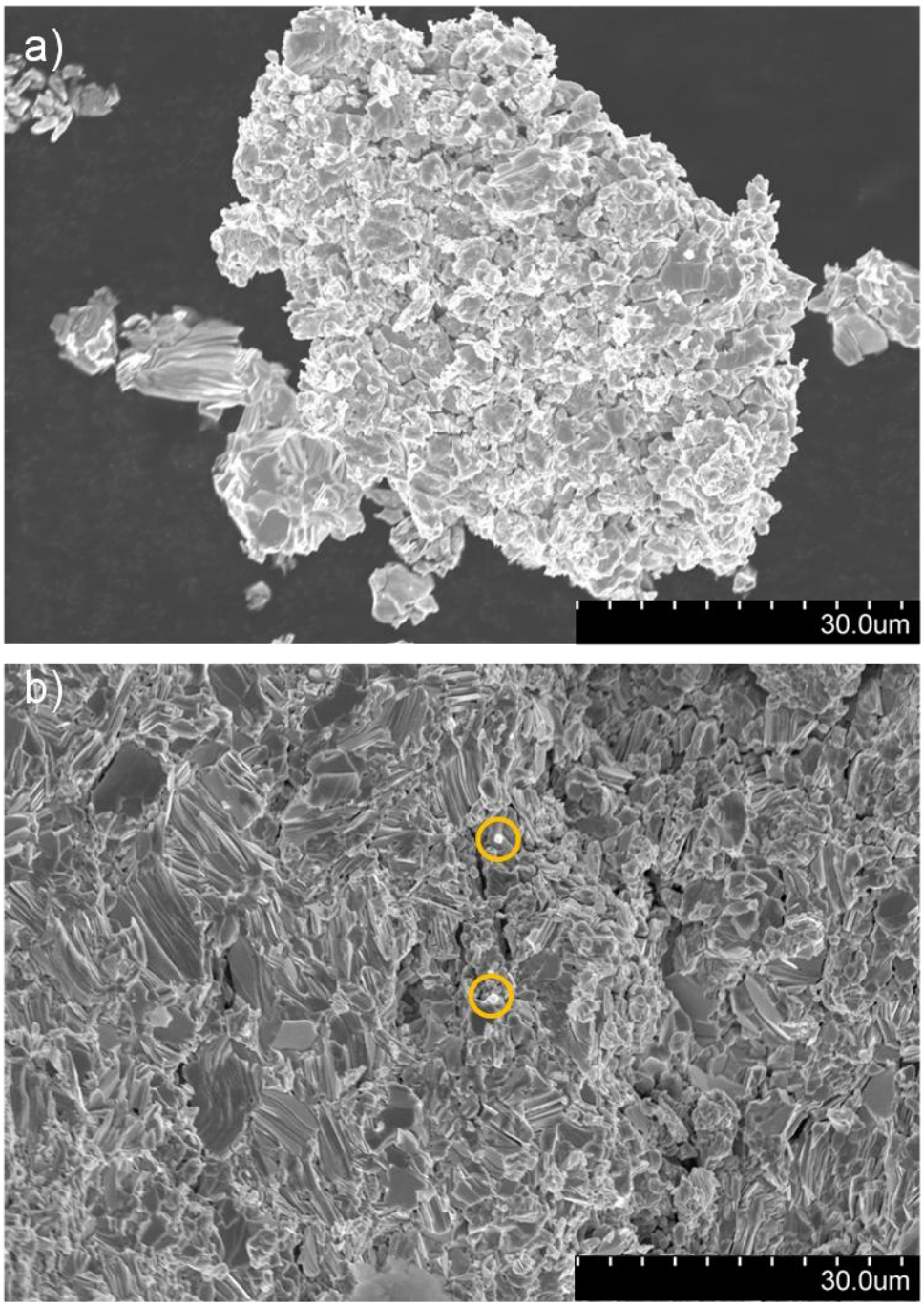

Figure 70. a) SEM image of the reference material for the p-type Au / Ag – bismuth telluride nanocomposites prior to hot pressing. b) SEM of a Au composite after hot pressing, with possible locations of Au nanoparticles highlighted.

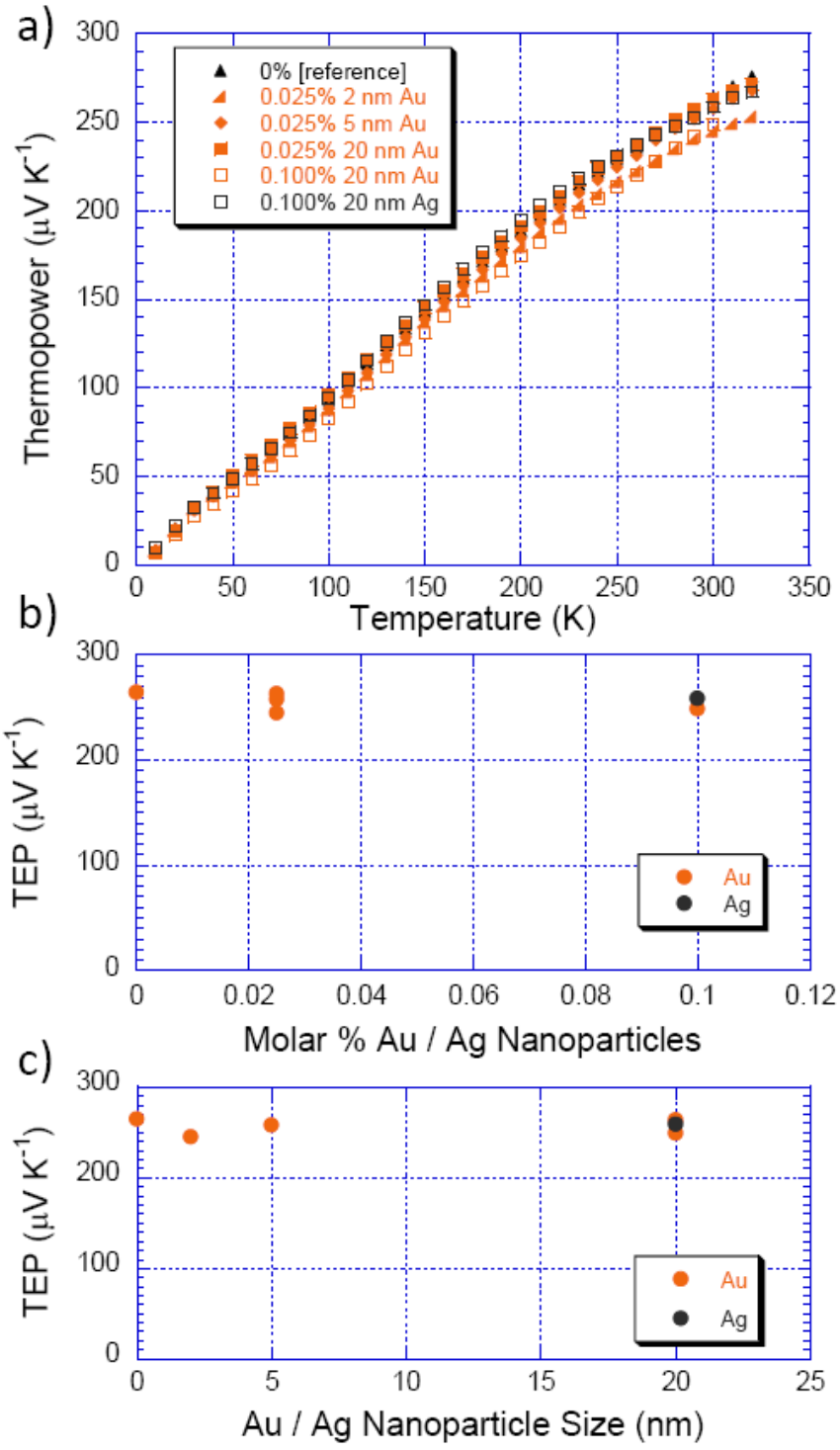

Figure 71. Thermopower (TEP) data for Au and Ag nanoparticles in a p-type bismuth telluride matrix as a function of a) temperature, b) percentage of nanoparticles, and c) nanoparticle size.

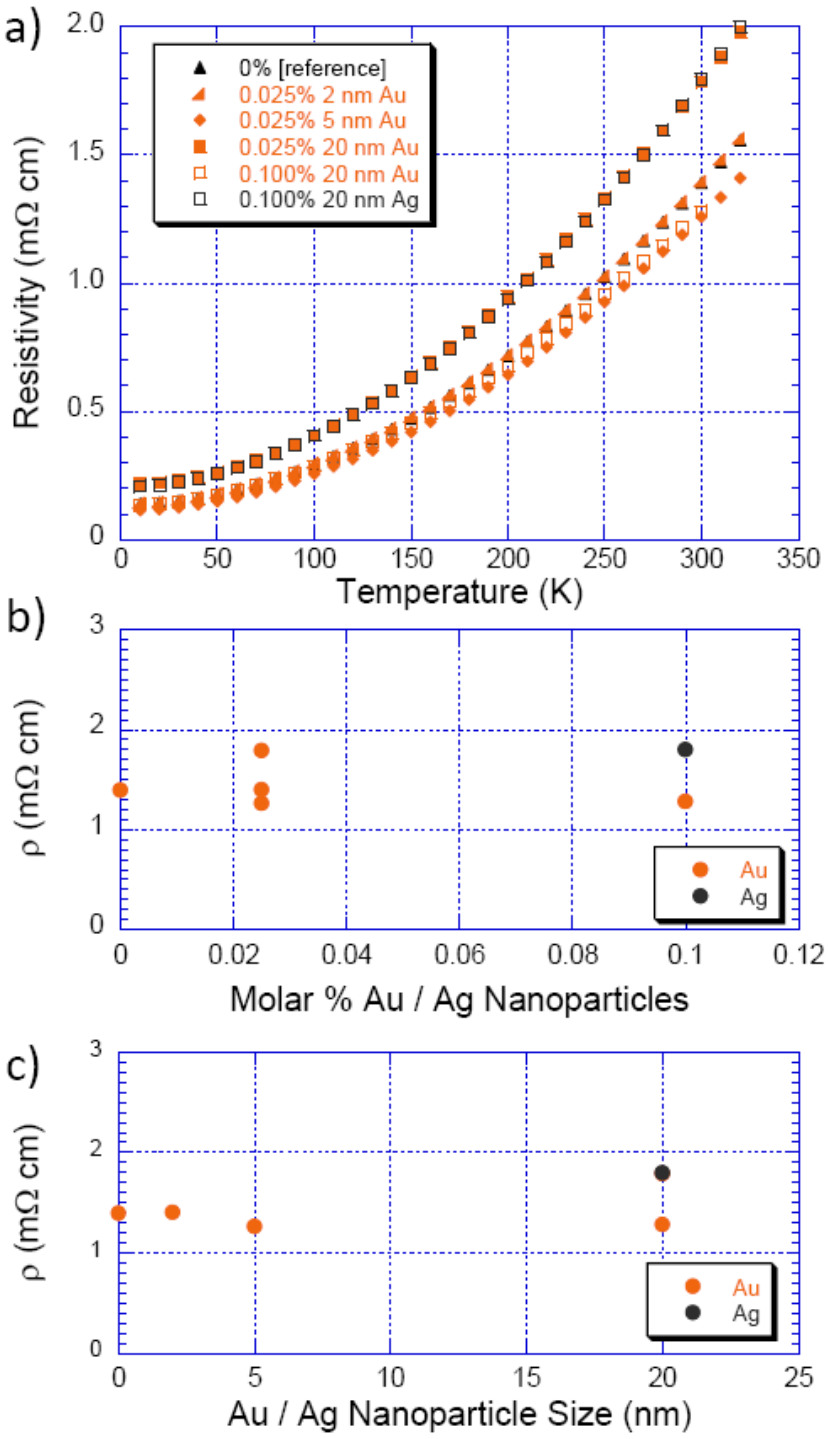

Figure 72. Resistivity (ρ) data for Au and Ag nanoparticles in a p-type bismuth telluride matrix as a function of a) temperature, b) percentage of nanoparticles, and c) nanoparticle size.

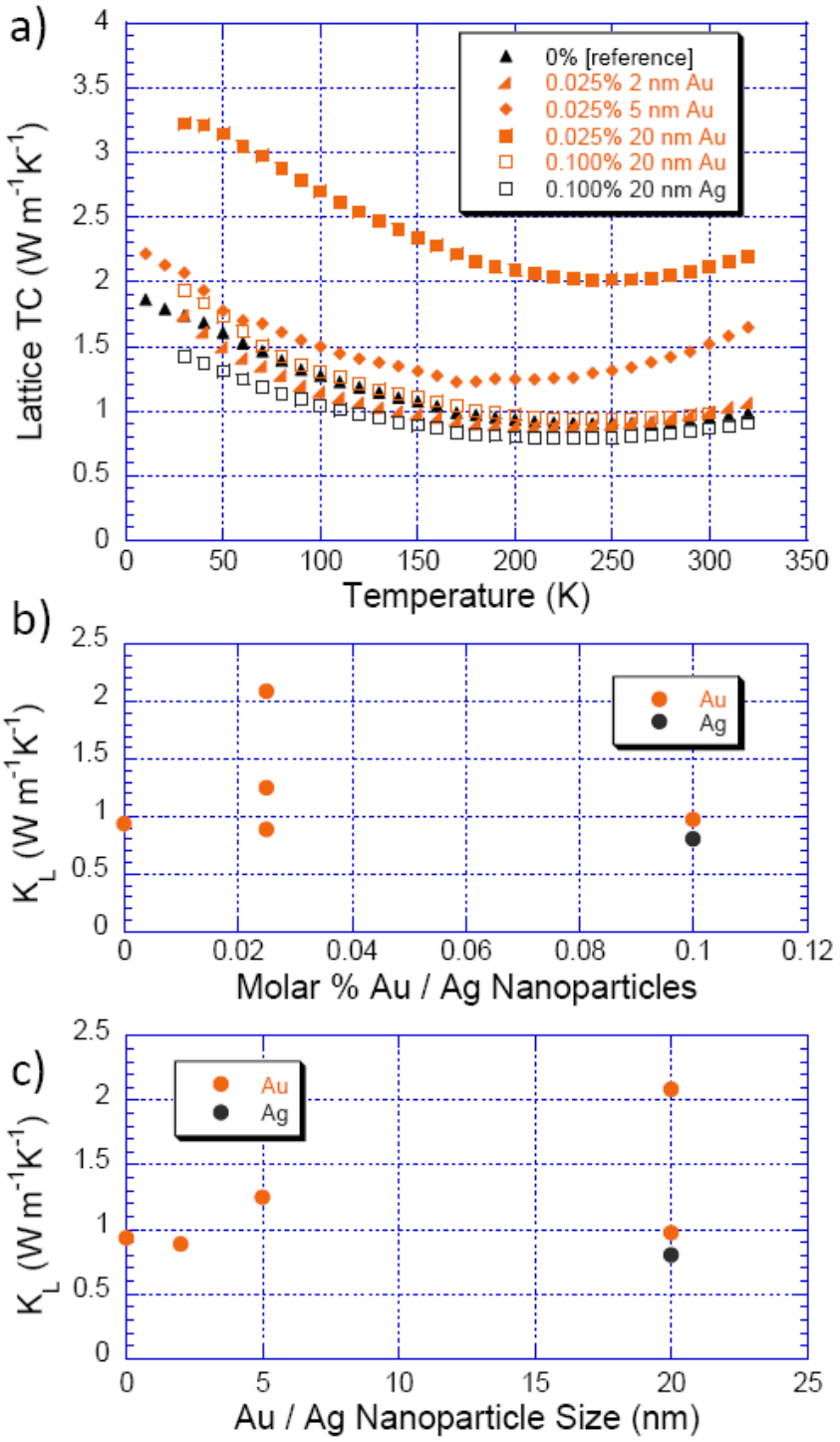

Figure 73. Lattice thermal conductivity data (κ_L) for Au and Ag nanoparticles in a p-type bismuth telluride matrix as a function of a) temperature, b) percentage of nanoparticles, and c) nanoparticle size.

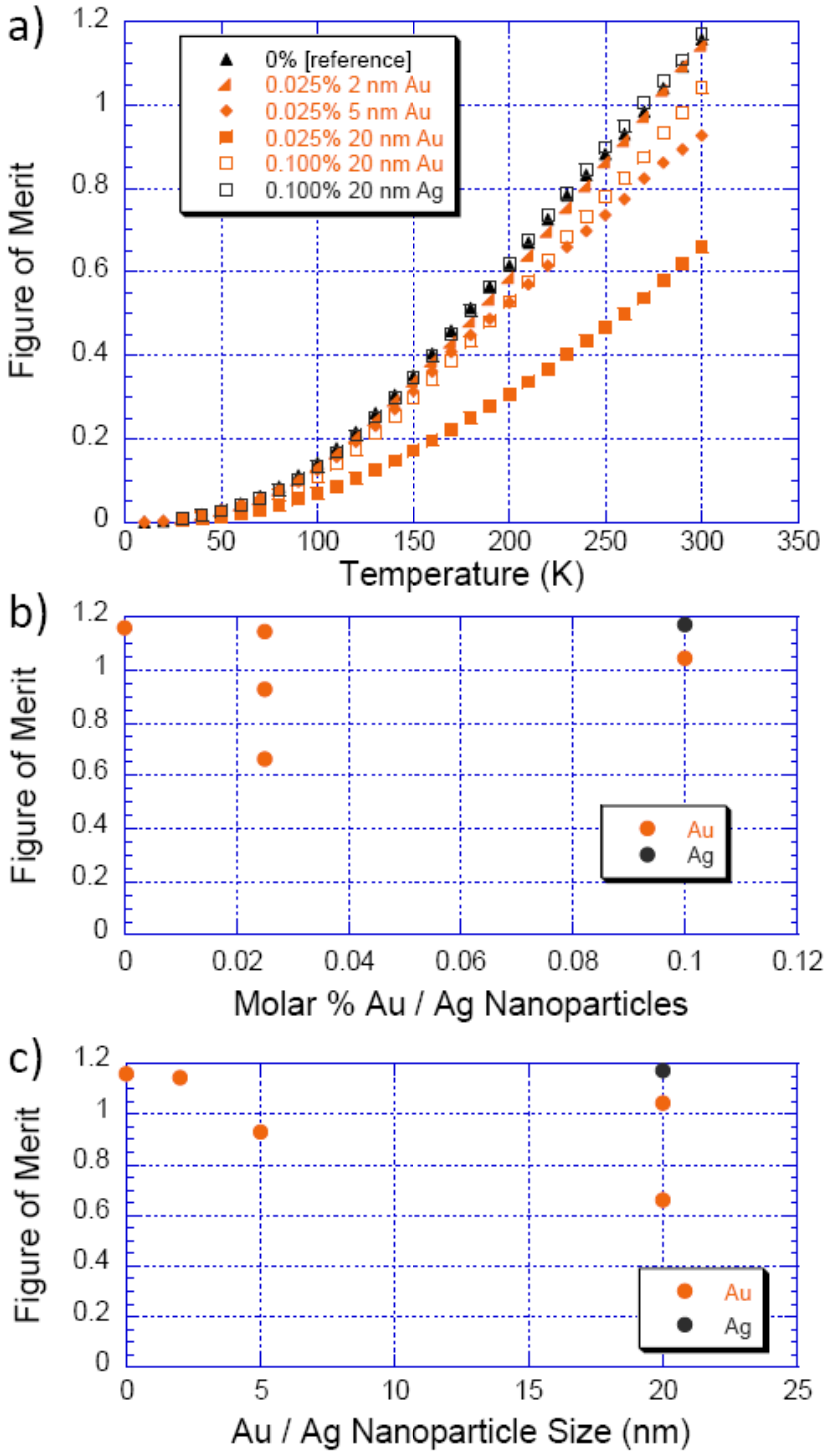

Figure 74. Figure of merit data for Au and Ag nanoparticles in a p-type bismuth telluride matrix as a function of a) temperature, b) percentage of nanoparticles, and c) nanoparticle size.

C_{60} Nanocomposites

Nanocomposites made using C_{60} are of interest due to the small particle diameter (~7 Å) and radically different lattice structure of C_{60} as opposed to bismuth telluride, which is expected to affect the thermal conductivity of these materials, ideally with minimal effect on the electronic properties. Further, much of the concern regarding diffusion or intergrowth between the nanoparticle inclusions and the matrix materials is eliminated by using materials that have such radically different structures and physical properties than the matrix. Already, in fact, it has been shown that fullerene additions are a viable method for increasing phonon scattering in Si-Ge alloys [96] as well as for reducing the thermal conductivity of $CoSb_3$ nanocomposites [30].

In order to investigate the effects of fullerenes upon the bismuth telluride system, a series of samples was manufactured by mixing dry powders of bismuth telluride with C_{60} and then hot pressing. The powders of bismuth telluride were obtained by grinding a p-type ingot ($Bi_{0.4}Sb_{1.6}Te_3$) by hand using a mortar and pestle, and then sifting these powders via a system of sieves. The matrix material was taken from between the 325 mesh sieve (~45μm opening) and the 450 mesh sieve (~32μm opening), and the matrix and nano-powders were mixed via a mechanical 3-axis mixer before being loaded into a 0.37 inch I.D. graphite die. Hot press conditions ranged from 300-400^oC at 1.500 tons pressure (212 MPa). Samples of 0.5, 1, 3, 5, and 8 molar percent C_{60} were produced in this way, as well as samples of 1 and 5 atomic percent C, which translates into 0.017 and 0.0875 molar percent C_{60}, respectively. A reference sample, having 0% fullerenes added, was also produced, using identical processing conditions. After hot pressing, the samples

were examined by Raman spectroscopy to verify that the fullerenes had survived the hot pressing. Figure 75 shows the Raman data for the reference sample, overlaid with data for samples that have increasing fullerene percentages. This graph shows an increase in the Raman peak characteristic of C_{60} that increases as the nominal percentage of C_{60} in the composites is increased, indicating that C_{60} has survived the hot pressing largely intact.

SEM images of fracture planes representative of these samples are presented in figure 76. In figure 76a, the presence of micron-sized and sub-micron-sized bismuth telluride matrix grains can be discerned, as well as large black regions that likely represent regions of high carbon concentration. These dark regions vary in distribution and in size, ranging from a few microns across to as much as 100-200 μm. In both figure 76a and 76b, it is apparent that the grain structure of the composite is largely preserved in these regions, and in figure 76b, in particular, the layered structure typical of the hot-pressed bismuth telluride matrix grains can be discerned in the large dark region. Figure 77a shows an SEM image of a polished surface of one of these composites, revealing a wider view of the dispersion and size of the dark regions. Figure 77b is a closer view of one of the sections where the apparent C_{60} dispersions are much smaller in size, and where two lighter regions are visible. During SEM imaging, energy dispersive x-ray diffraction (EDX) was taken in an attempt to better determine the distribution of elements throughout the sample. Figure 78 shows a low resolution SEM scan, in which three regions are visible, a grey background (spectrum 2), dark regions (spectrum 3), and a light inclusion area (spectrum 1). The quantitative results of EDX from each of these

regions are shown below the image, and the scan sampling area is indicated by a rectangular cross section marked on the SEM image. Spectrum 2 shows Bi, Te, and Sb in relative ratios that are consistent with the composition of the matrix material, $Bi_{0.4}Sb_{1.6}Te_3$, but with a large excess percentage of carbon also present. In spectrum 3, taken from a dark region, the carbon signal is nearly twice as strong, but a background signal from the matrix $Bi_{0.4}Sb_{1.6}Te_3$ material is still apparent. In spectrum 1, however, no carbon signal was detected, and the bismuth / telluride elemental counts are consistent with pure Bi_2Te_3 rather than the substitutionally-doped p-type matrix material.

This SEM study shows the strong tendency of C_{60} to aggregate, but it also indicates that the aggregate regions are not pure C_{60}, but rather a mixture of C_{60} and matrix particles. It is possible that the C_{60} is heavily coating the matrix grains in these dark regions, since EDX indicates that the matrix material is still present within them. The background signal of C_{60} throughout the composites suggests that despite its strong tendency to aggregate, C_{60} is nevertheless also dispersing throughout the samples to some degree, and it is likely present even in regions where there are not sufficient quantities of it to visually register on the SEM scan. The regions of pure Bi_2Te_3 are most likely due to local melting that occurs during hot pressing. Further work is underway in collaboration with the Air Force Research Lab to better investigate the microstructure of these composites [97].

Measurements of thermopower, resistivity, and thermal conductivity were performed on these samples from 10-300 K. From figure 79, it is apparent that the thermopower is quite robust for the samples, having a value of 274 ± 12μV/K at room

temperature, which is largely invariant from sample to sample as a function of temperature. There is, however, a slight tendency towards decreasing thermopower with increasing percentage of fullerenes (figure 79b). Figure 80 shows the resistivity as a function of temperature as well as of C_{60} molar percentage. All samples exhibit semi-metallic resistivity, characteristic of bismuth telluride, but there is a general trend towards higher residual resistivity with higher C_{60} molar percentage. As the data approaches room temperature, an increase in the curvature of the temperature response of the resistivity is noticeable in the 3, 5, and 8% C_{60} samples.

Figure 81a shows the lattice thermal conductivity as a function of temperature in the absence of a radiation loss correction. As the volume fraction of C_{60} increases, the low temperature disorder peak is almost completely suppressed (as, for example, in the 5 and 8 mol. % C_{60} samples), indicative of the expected increase in the level of boundary scattering in the samples that have the highest percentages of fullerenes. Figure 81b shows the trend in the lattice TC data at 200 K, prior to the onset of radiation effects. Here, there is little change in the data until the 1% sample, which shows a sharp decrease from the values for the previous three data points, and the following three samples exhibit a continued decrease in magnitude. Considering the response of the lattice TC to both temperature and volume fraction of C_{60}, then, it appears as though, as before, the major effect of the nanoparticle inclusions is to increase the degree of low temperature boundary scattering of phonons, but that this time the overall magnitude of the lattice TC is also decreased, after reaching a certain threshold of C_{60} molar percentage, which occurs at approximately 1 mol. % C_{60}.

The effect of porosity upon the thermal and electrical properties is also an important consideration for these composites. Figure 82a shows the density as a function of C_{60} percentage. Here it can be seen that while the density remains largely constant at low percentages of C_{60}, it decreases by as much as 20% in samples that have greater than 1 mol. % C_{60}. The change in density can be attributed to the addition of the low-density, cage-like fullerenes that have densities of ~1.6 g / cm^3 [98], rather than to a poor level of compaction in the composites. This point is established by figure 82b, which shows the percentage of theoretical density achieved in these composites as a function of molar percentage of C_{60}, where the theoretical density is calculated using the theoretical densities of $Bi_{0.4}Sb_{1.6}Te_3$ and C_{60} in the proper ratios. Thus, while the 0% sample has a theoretical density of 6.78 g / cm^3 (the value for $Bi_{0.4}Sb_{1.6}Te_3$), the theoretical density of an 8 molar % C_{60}-$Bi_{0.4}Sb_{1.6}Te_3$ composite is only 5.34 g / cm^3, due to the addition of low-density C_{60} molecules. The end result is that while the level of compaction of the composites is considerably good, the C_{60} inclusions nevertheless serve to increase the porosity of the samples. Moreover, a consideration of the carrier concentration and mobility, calculated from measurements of the Hall effect, indicates that there is not a clear relationship between the carrier concentration or the mobility and the percentage of C_{60} in the composites (figure 83). This consideration seems to support the conclusion that the direct effect of C_{60} upon the electronic properties is a minimal rather than a major effect, and that porosity is likely the predominant explanation for the changes in both the electrical and thermal transport.

The effects of porosity upon the relevant thermoelectric transport properties are shown in figure 84. Recall that the thermopower shows a decrease as a function of C_{60} percentage (figure 79), while the resistivity increases with the addition of C_{60} (figure 80). The combined effect is a decrease in the power factor corresponding to the decrease in density that is caused by the addition of fullerenes (figure 84a). A similar effect is observed in the lattice thermal conductivity (figure 84b). The net effect of C_{60} additions on the figure of merit, however, is less clear (figure 85). While the samples that have the highest concentrations of C_{60} exhibit moderate reductions in ZT as compared to the reference sample, the ZT response to fullerene additions in the intermediate range shows an initial decrease for the 0.0875% sample followed by an increase up to the 1% sample, which has a value of ZT that is higher than the reference material. The reason that this 1% C_{60} sample exhibits such a high ZT value is due to the fact that it lies right at the cusp of the rise in resistivity that occurs as more fullerenes are added to the composites (figure 80b) while also being situated near the beginning of the drop in thermal conductivity that occurs simultaneously with the rise in resistivity (figure 81b). It therefore lies just at the critical point where the thermal transport properties are degraded while the electrical properties are for the most part undisturbed. In general, though, the slight reduction in the thermal conductivity, particularly for the high percentage C_{60} samples, is enough to offset just slightly the losses observed in the power factor, with the result that while the ZT value worsens with the addition of C_{60}, it does not decrease as strongly as does the power factor for these samples.

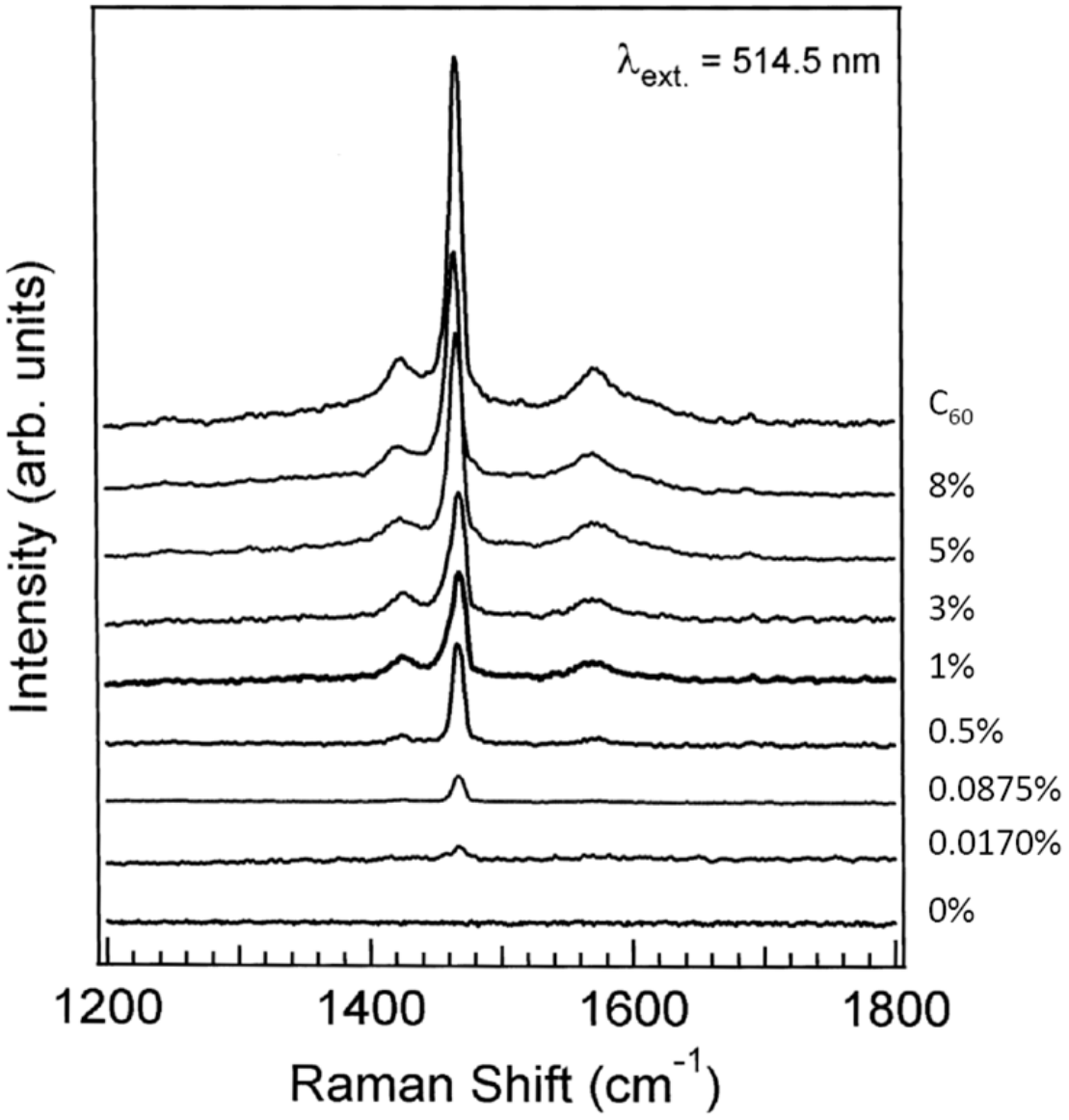

Figure 75. Raman shifts for a series of p-type C_{60} nanocomposites.

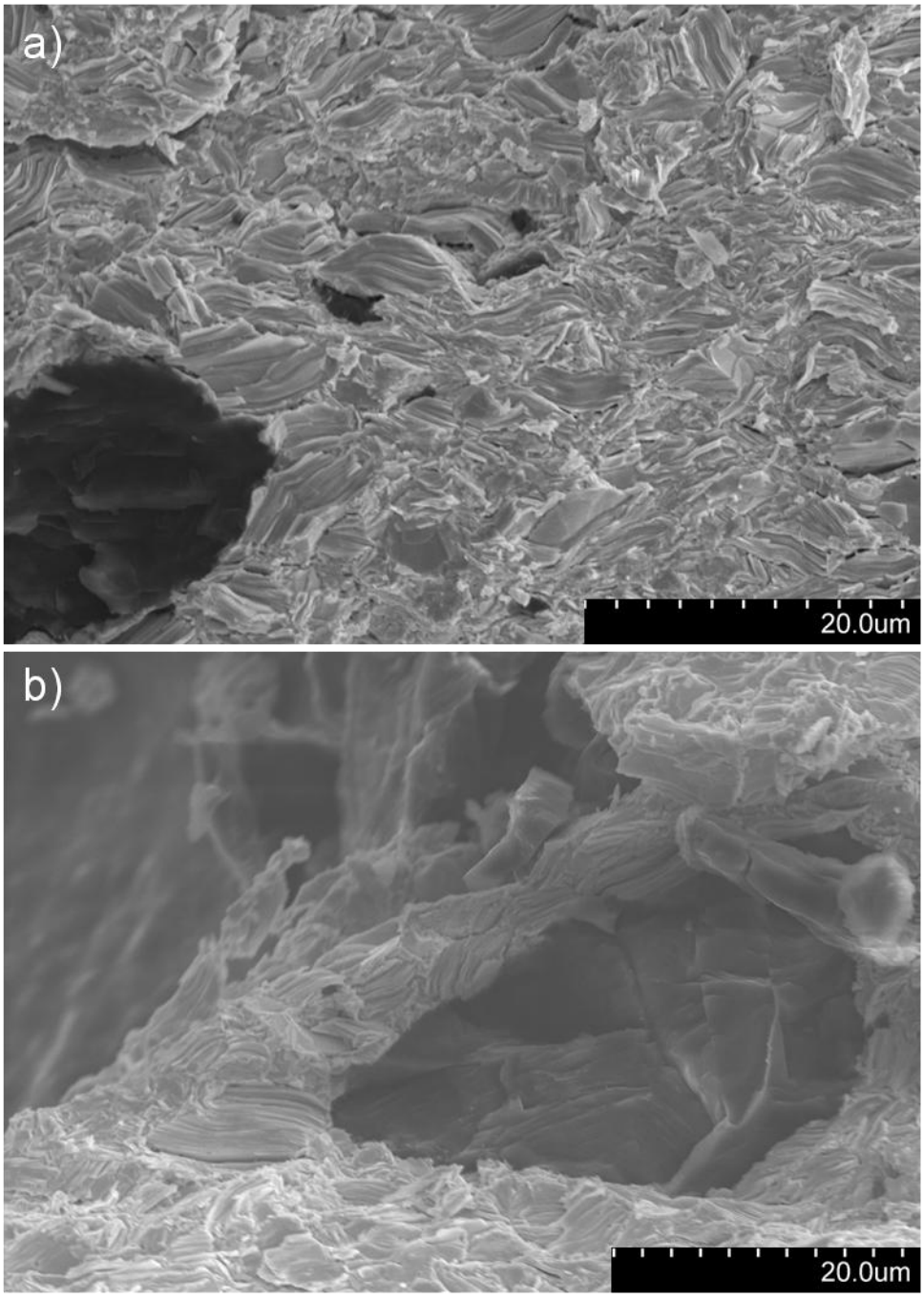

Figure 76. a) Fracture surface of a composite of C_{60} and p-type bismuth telluride, showing regions of matrix material and dark patches of apparent carbon concentration. b) Close view of a dark region, showing the layered structure of bismuth telluride to be present.

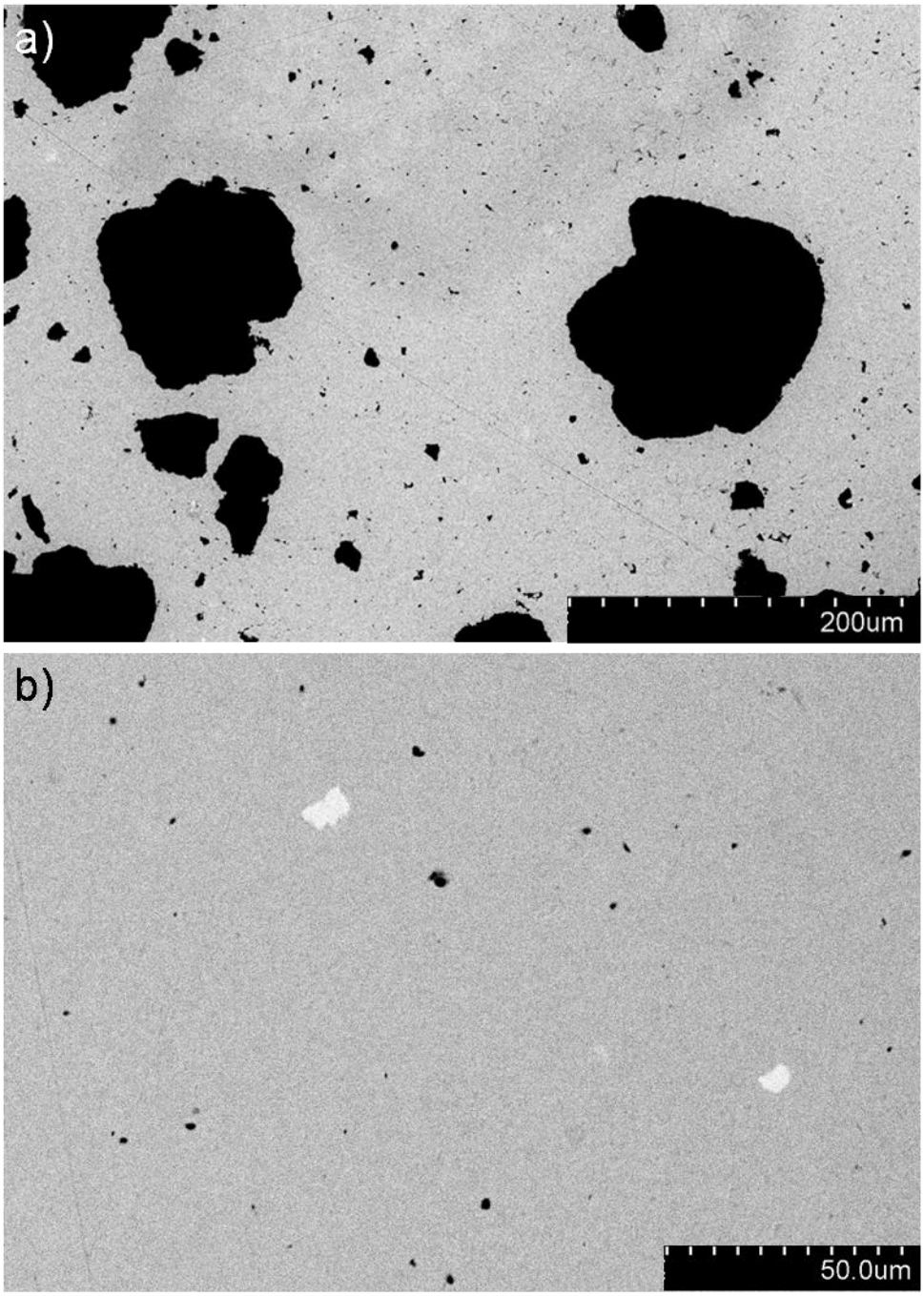

Figure 77. a) Wide view of a polished surface of a p-type C_{60} nanocomposite, showing dark aggregations on scales larger than 100 μm. b) Smaller dark aggregations, as well as two lighter regions.

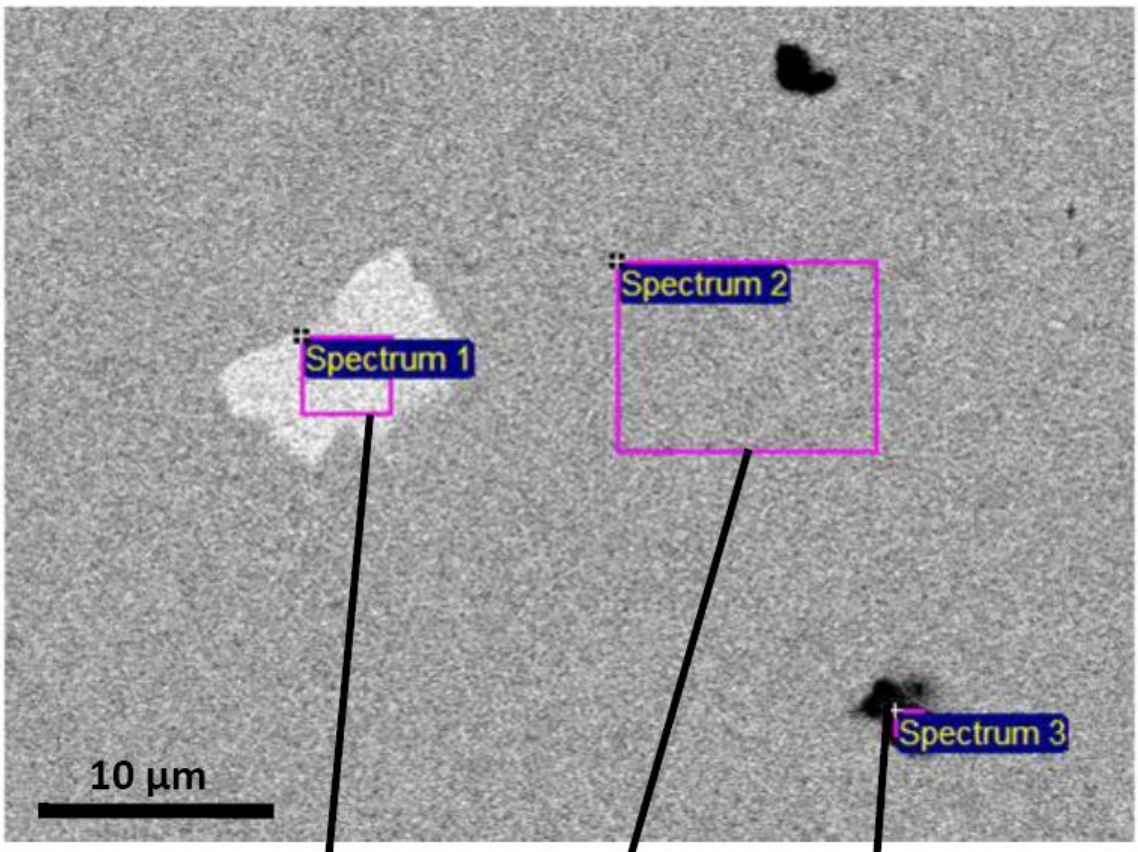

Element	Atomic%
Te	62.65
Bi	37.35

Element	Atomic%
C	37.96
Sb	19.01
Te	37.74
Bi	5.29

Element	Atomic%
C	64.83
Sb	10.44
Te	22.08
Bi	2.64

Figure 78. Low resolution SEM image of a polished surface of a p-type C_{60} nanocomposite, with EDX analysis of three regions.

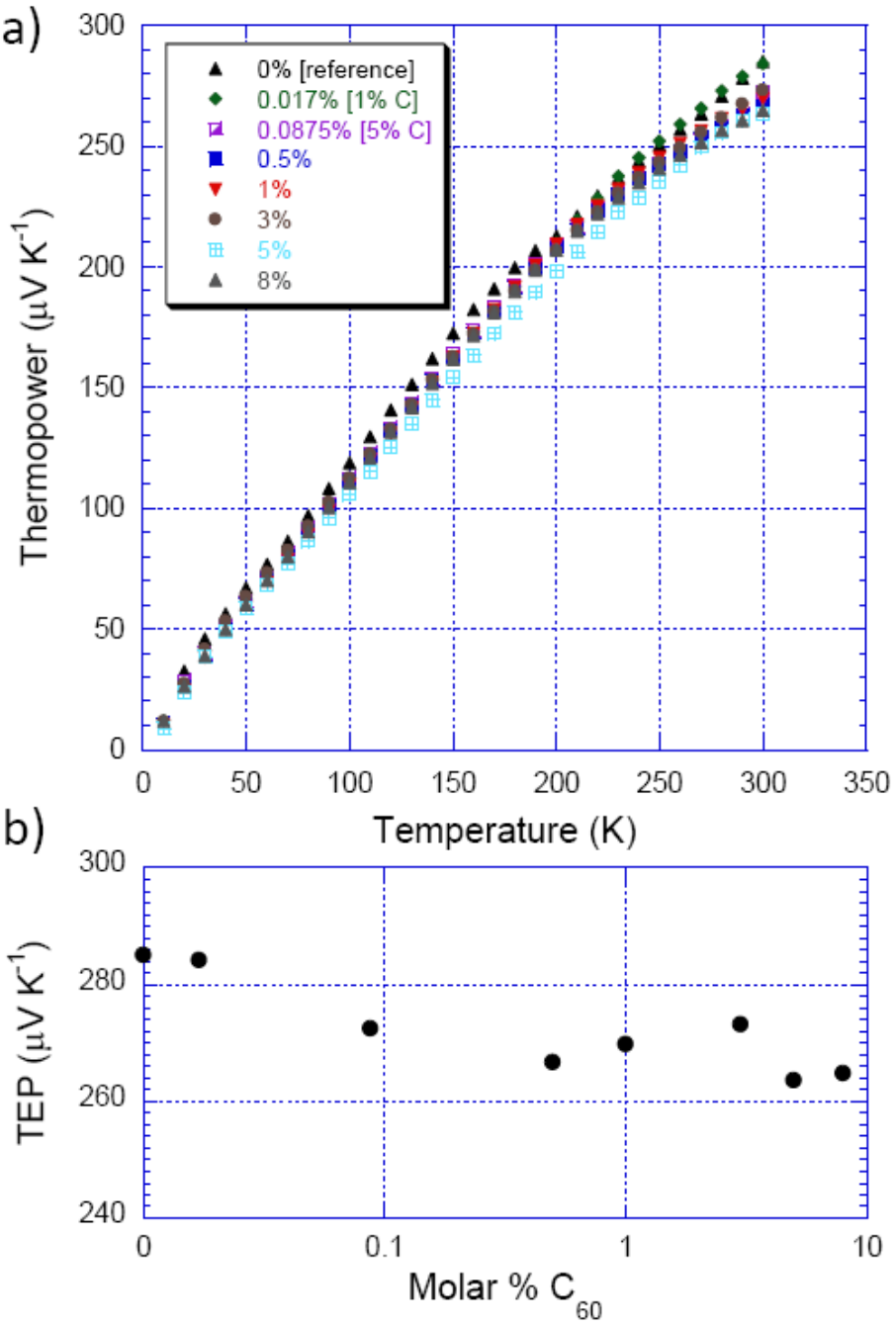

Figure 79. a) Thermopower (TEP) vs. temperature for p-type C_{60} nanocomposites. b) TEP vs. C_{60} percentage, at 300 K.

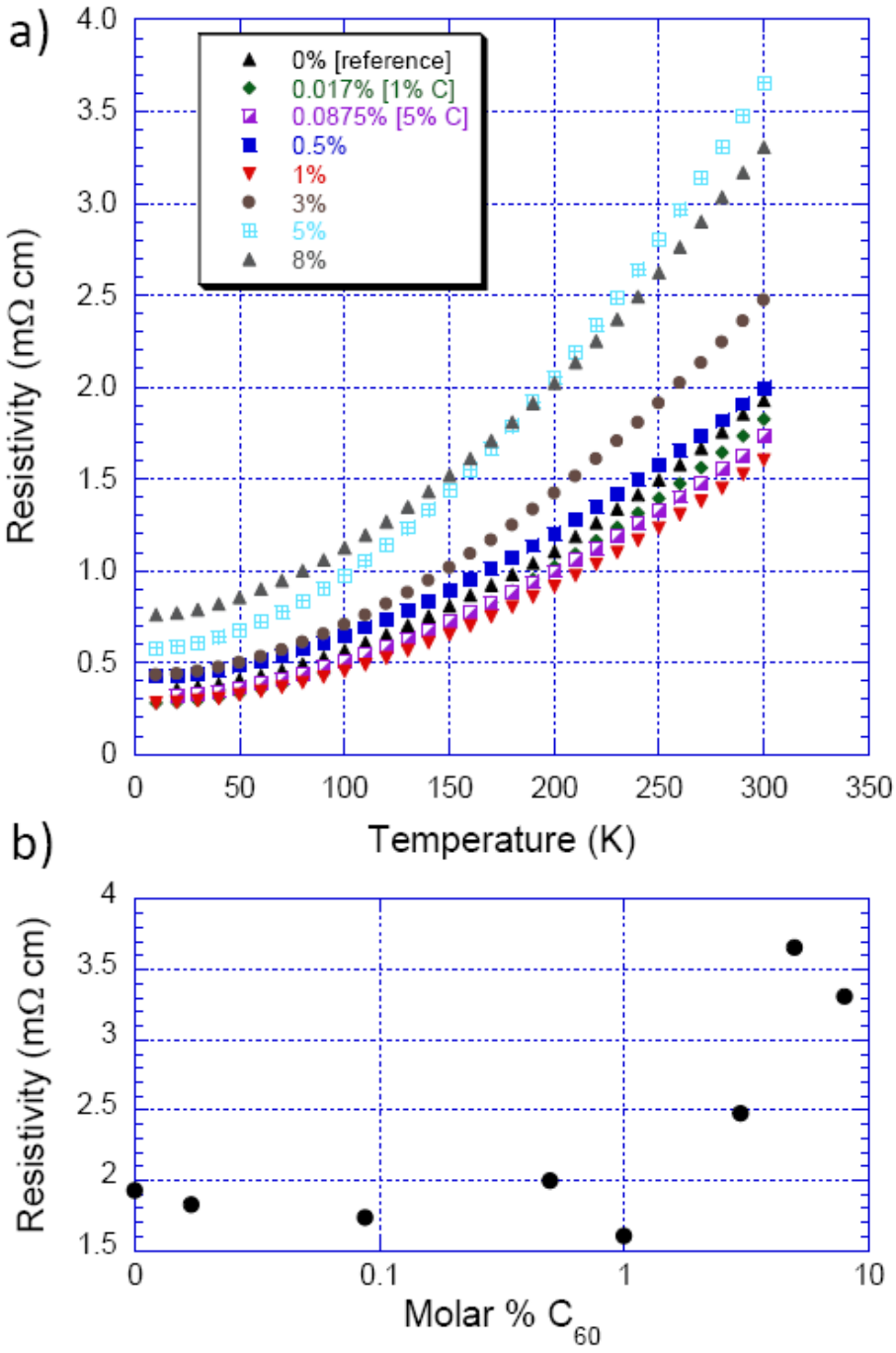

Figure 80. a) Resistivity vs. temperature for the p-type C_{60} nanocomposites. b) Resistivity as a function of fullerene percentage, at 300 K.

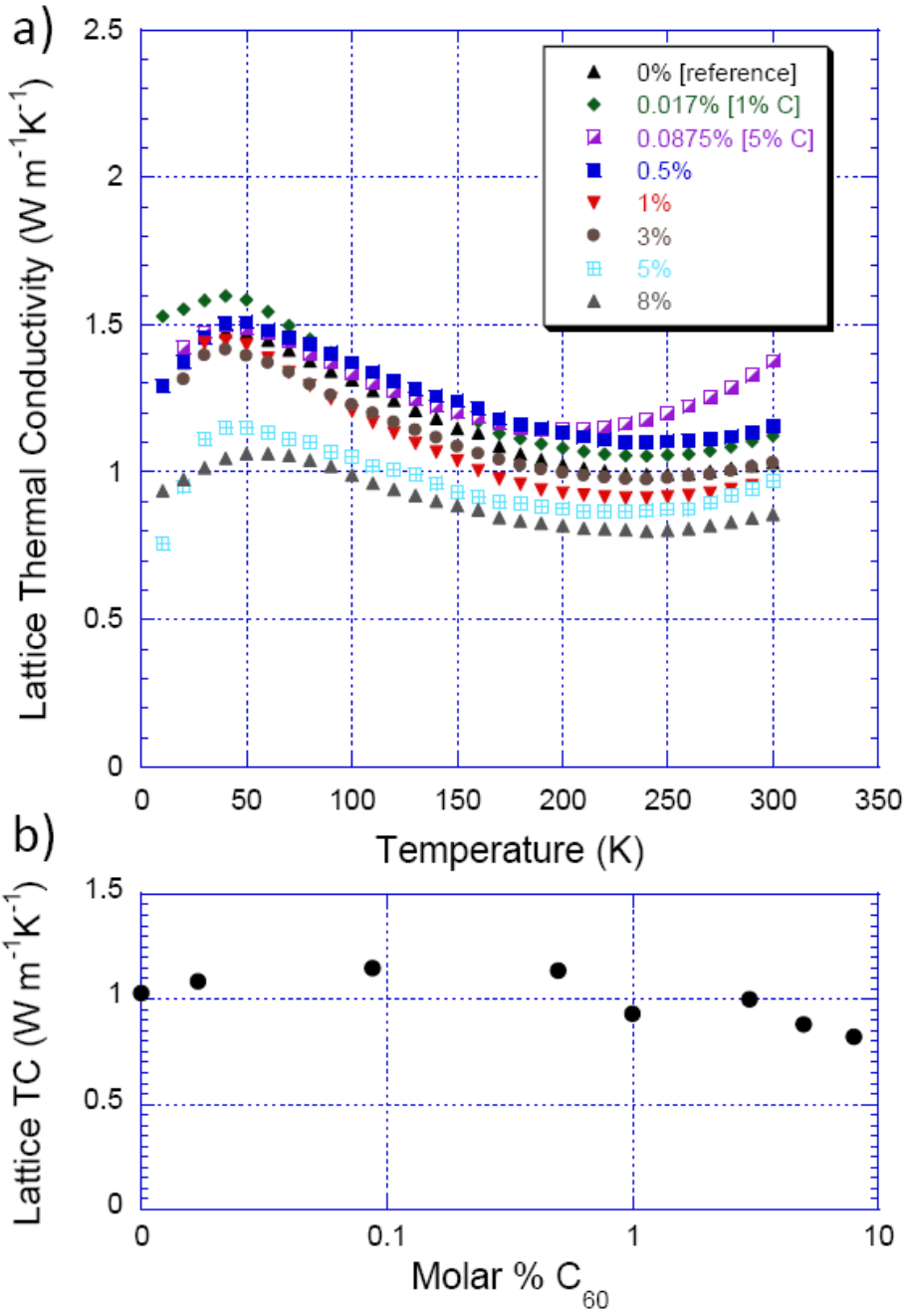

Figure 81. a) Lattice thermal conductivity (TC) vs. temperature for the p-type C_{60} nanocomposites. b) Lattice TC vs. percentage of C_{60}, at 200 K.

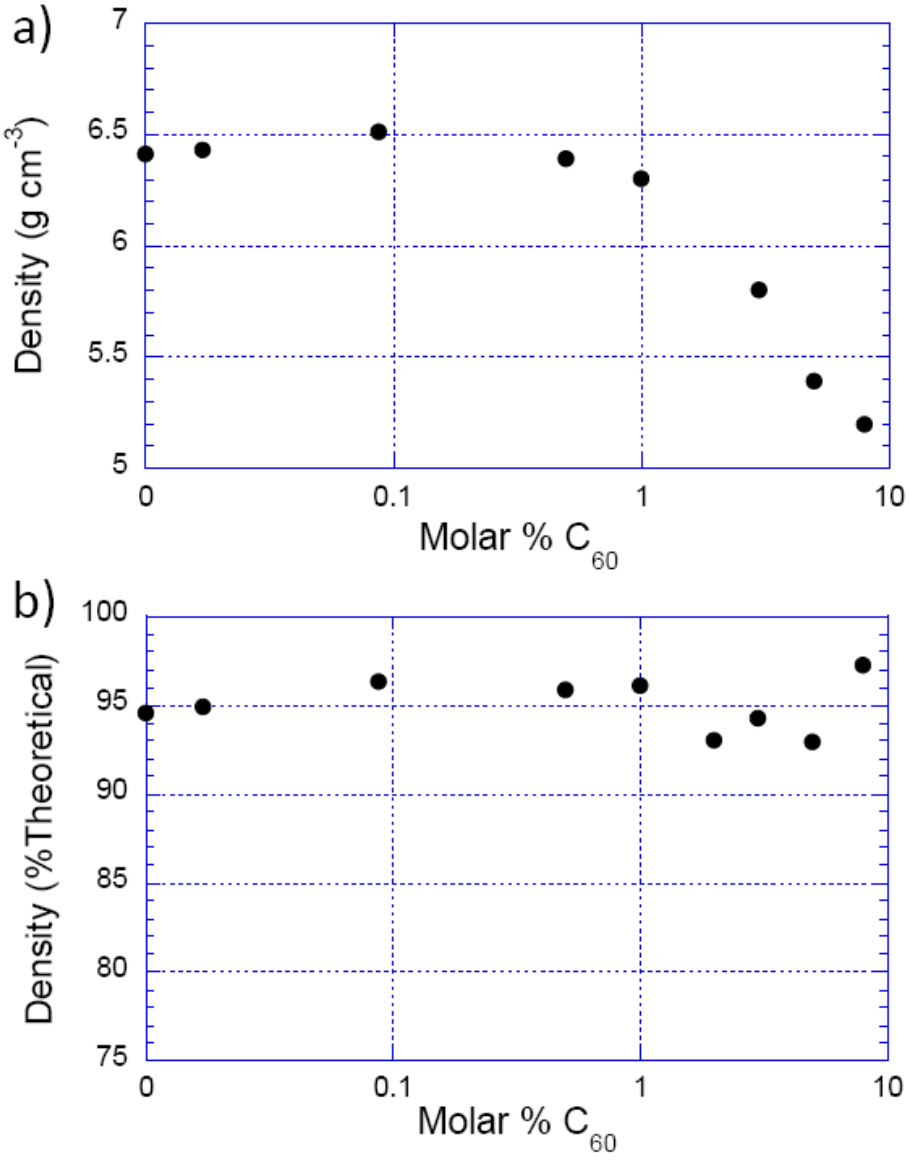

Figure 82. a) Absolute density vs. percentage of C_{60} b) Percentage of theoretical density vs. percentage of C_{60} for the p-type C_{60} composites.

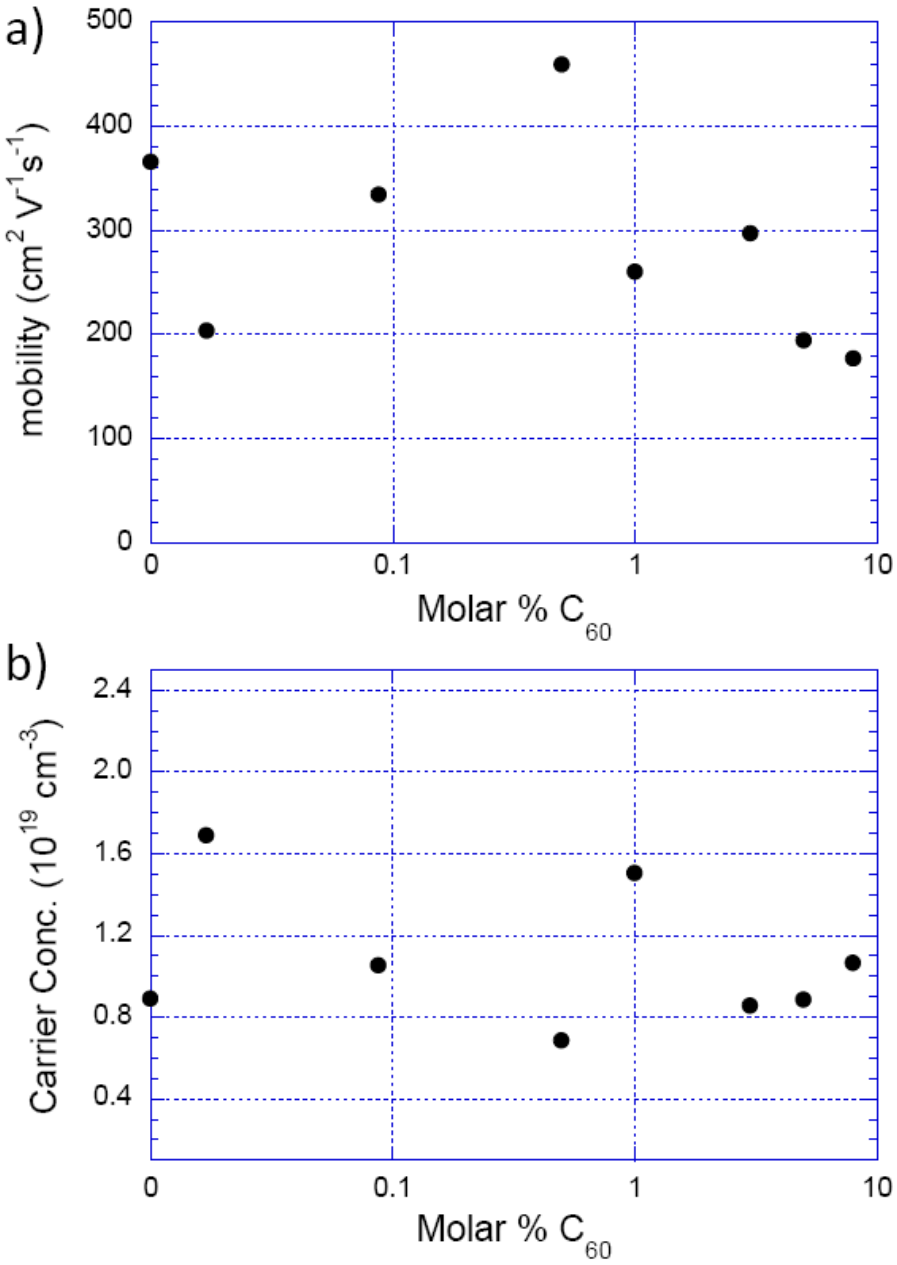

Figure 83. a) Mobility vs. percentage C_{60} for the series of p-type C_{60} nanocomposites, at 300 K. b) Carrier concentration vs. percentage C_{60}, at 300 K.

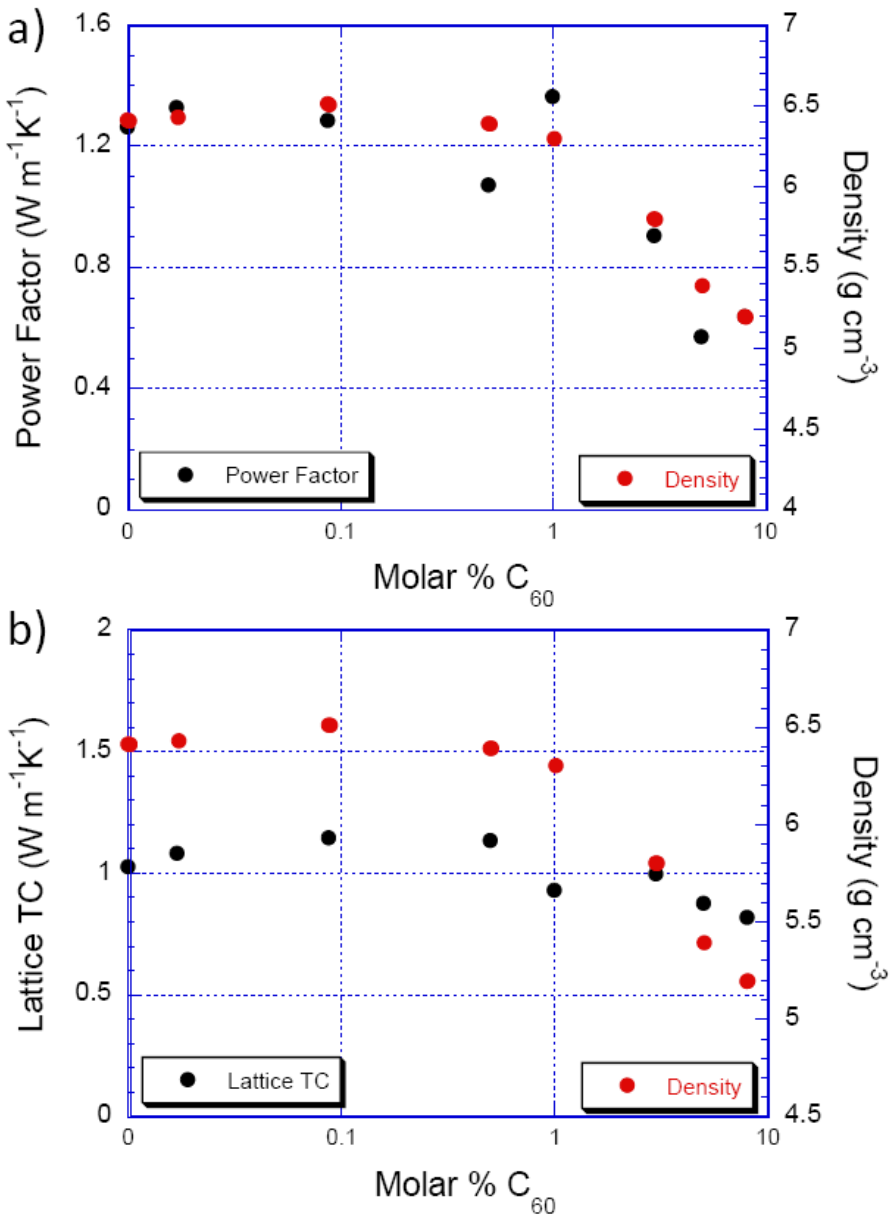

Figure 84. a) Power factor and density vs. percentage C_{60}. b) Lattice thermal conductivity at 200 K and density vs. percentage C_{60} for the series of p-type C_{60} nanocomposites.

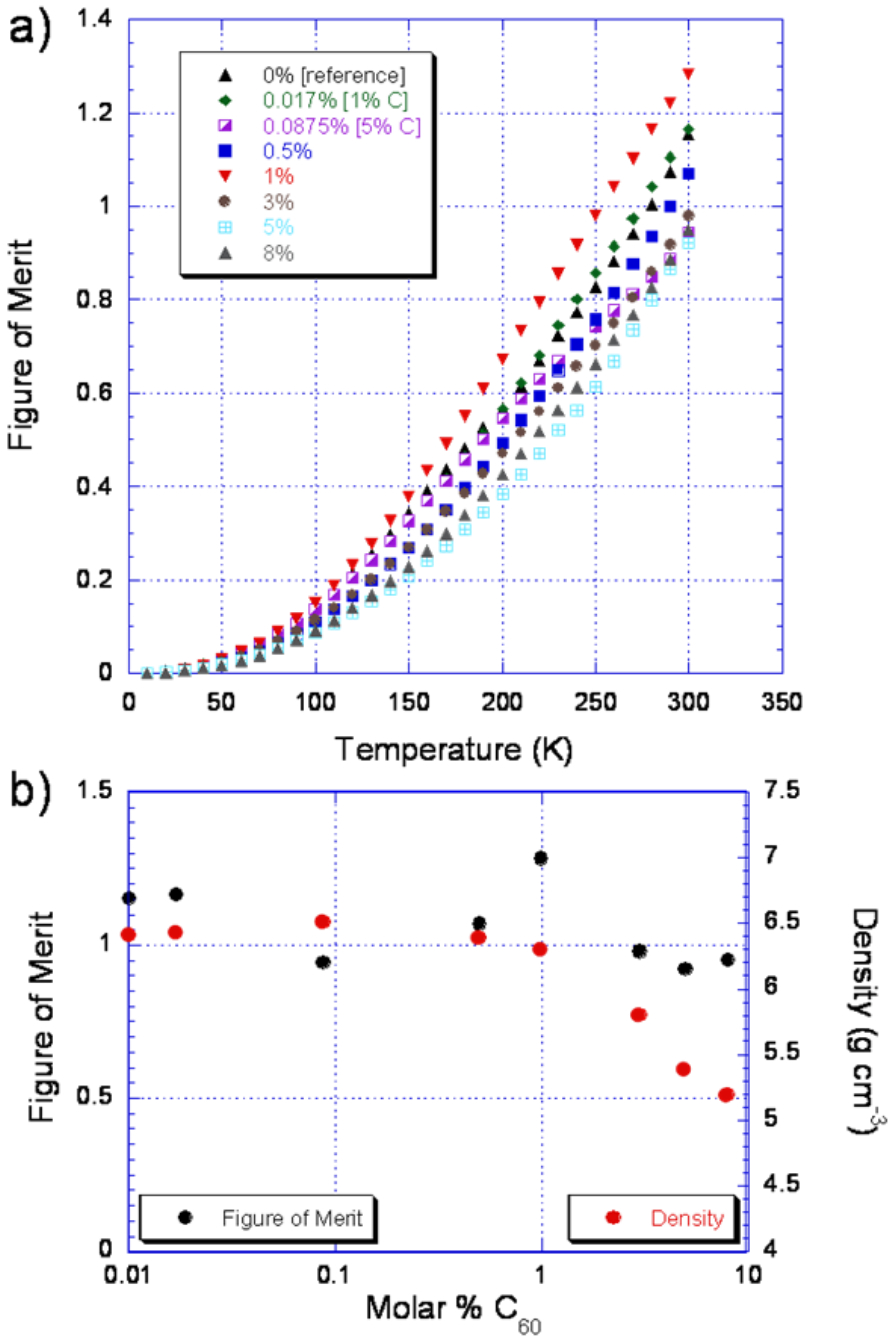

Figure 85. a) Figure of merit (ZT) vs. temperature for the series of p-type C_{60} nanocomposites. b) ZT and density vs. percentage of C_{60}, at 300 K.

SUMMARY

This study provides one of the first investigations of the effects of nanomaterials upon the thermal and electrical transport properties of nanocomposites formed using favorable thermoelectric materials as a matrix. The nanocomposites studied herein are also of value for investigating the viability of the uniaxial hot-pressing technique for producing such composites, as well as being of benefit for studying viable techniques of nanoparticle growth. While the end results have in most cases not been the formation of nanocomposites that have figures of merit that surpass the bulk materials, the effects of the nanomaterials upon the electrical and thermal properties nevertheless help illuminate interesting new directions for thermoelectric research of nanocomposites.

With regard to synthesis of materials, it has been shown that while CVD growth techniques can be utilized to produce high yields of nanoparticles of cubic crystal structures such as PbTe [79], the technique does not translate easily to materials such as bismuth telluride that have complex crystal structures composed of elements of widely varying volatility such as Bi and Te. Although the CVD technique was abandoned in favor of the more established growth technique of solvothermal synthesis in order to produce high yields of bismuth telluride nanoparticles, preliminary results indicate that it is possible that with continued research, the CVD technique could be tailored to achieve bismuth telluride nanoparticle crystal growth.

Uniaxial hot-pressing has been demonstrated to be a viable method for pellet compaction, capable of producing composites large and robust enough to undergo the processing that is necessary for low temperature thermal and electrical transport

properties measurements. Typical composite densities are above 93% of the theoretical value in most cases, but they can be as high as 98% in some composites. Alternative techniques such as spark plasma sintering (SPS) are of interest for use, however, since the slow pressing at moderately high temperatures provided by hot pressing can lead to an undesirably high degree of matrix-nanoparticle intergrowth. SPS uses large electrical currents to achieve highly controlled localized heating of a sample over a short period of time, and it may therefore provide a greater degree of control over the compaction of nanocomposites such as these. Further, mechanical 3-axis mixing appears simply to be a first step towards a method for achieving homogeneous distribution of nanoparticles throughout the composites, due to the evidence that 3-axis mechanical mixing followed by uniaxial hot-pressing results in a high degree of nanoparticle aggregation. With a greater degree of nanoparticle dispersion throughout the samples, the transport properties potential of these composites could be characterized more completely, and it is therefore of interest to continue to study various combinations of processing and consolidation techniques with respect to both the microstructure and transport behavior of such nanocomposites.

All of the nanomaterials used in this work have shown the ability to increase the degree of boundary scattering of both phonons and charge carriers, an effect that is primarily seen in the electronic mobility data and in the temperature dependence of the thermal conductivity at low temperatures. Processing techniques have contributed in some cases to masking the effect of the nanoparticles upon the transport properties, such as has been observed in the Bi_2Te_3 nanocomposites. The difficulty in isolating the effects

caused by sub-micron-sized Bi_2Te_3 nanoparticles from those due to the bismuth telluride matrix grains, which are themselves on size scales of only several microns or even sub-micron-sized, brings to light the implication that nanomaterials of compounds that differ in composition from the matrix material are likely to be of more interest than compounds of the same composition as the matrix. Using such materials would also reduce the potential for nanoparticles to grow into the matrix grains under the temperature and pressure conditions of the hot press. The composites formed by incorporating BiSb and Bi_2S_3 nanoparticles into the bismuth telluride matrix, for example, have exhibited marked differences in transport properties data as compared to the Bi_2Te_3 nanocomposites.

With regard to consolidation techniques, it is of interest that the lattice thermal conductivity values for the Bi_2Te_3 samples prepared by mixing (figure 51) have higher values at all temperatures than does the series of samples prepared by ball milling (figure 43). The ball-milled composites also show greater suppression of the low temperature lattice TC peak. Upon reflection, this effect matches well with the general decrease in the size of the matrix particles that is observed when ball milling is used, as it follows that ball milling produces a higher degree of grain structure disorder than does mechanical mixing, and thereby reduces the thermal conductivity more drastically. The high degree of charge carrier scattering evident in the resistivity values for the ball-milled samples, however, negates the benefits of decreased thermal conductivity in the ball-milled samples, with the result that the figure of merit in the ball-milled samples is not as good as the figure of merit of the mixed composites. It is also of note that the power factor values for the nanocomposites with the two highest percentages of nanoparticles as

prepared by mixing (figure 50b) are approximately the same as nearly all of the ball-milled nanocomposites (figure 42b). This observation further confirms that ball-milling produces an over-abundance of sub-micron-sized matrix grains. The uniform power factors observed in the ball-milled samples as well as in the 20 and 50% mixed samples also suggests that a saturation point has been reached with regards to harming the electronic properties. That is, ball milling decreases the power factor values, but it does so more uniformly than does mixing, and it has essentially the same effect as adding large quantities of nanoparticles to the matrix via mechanical mixing. Given this consideration, it seems possible that ball-milling may be a better method than mixing for improving the figure of merit of these materials.

Nanocomposites of C_{60} and $Bi_{0.4}Sb_{1.6}Te_3$ have shown marked decreases in the lattice thermal conductivity as a function of C_{60} percentage. This effect could be due to the lattice mismatch between C_{60} and $Bi_{0.4}Sb_{1.6}Te_3$, or it could simply be an artifact of the decrease in density that follows the addition of fullerenes to the composite. These nanocomposites have also shown marked increases in nanoparticle aggregation, the nature and extent of which that are still under investigation. Of interest is whether ball milling of matrix materials followed by fullerene addition, either by mechanical 3-axis mixing or by a method that would serve better to distribute the fullerenes, could result in improved materials properties. The study of Bi_2Te_3 nanoparticle-based composites has already shown ball milling to be advantageous from a standpoint of thermal conductivity. Where inclusions of such size as C_{60} are concerned, moreover, one need not worry that

the size of the matrix particles will be decreased to such a point as to be indistinguishable in effect from the nanoparticles.

The development of thermoelectric nanocomposites need not be limited merely to the bismuth telluride or lead telluride systems, however. One materials class that continues to have a large amount of uncharacterized parameter space, for bulk as well as nano-materials, is found in the half-Heuslers. Techniques developed in this study could be expanded upon and adapted in attempts to explore the transport properties response of nanocomposites of half-Heusler materials.

REFERENCES

1. T.J. Seebeck, "Magnetic Polarization of Metals and Minerals," *Abhandlungen der Deutschen Akademie der Wissenschaften zu Berlin,* 265 (1822-1823).

2. J.C. Peltier, "Nouvelles Experiences sur la Caloricite des Courans Electrique," *Ann. Chim*. LVI, 371 (1834).

3. W. Thompson, "On a Mechanical Theory of Thermoelectric Currents," *Proceedings of the Royal Society of Edinburgh,* 91 (1851).

4. A.F. Ioffe, *Semiconductor Thermoelements and Thermoelectric Cooling*. Infosearch ltd., London, 1957.

5. H.J. Goldsmid and R.W. Douglas, "The use of semiconductors in thermoelectric refrigeration," *Brit. J. Appl. Phys.* **5**, 386 (1954).

6. G.A. Slack, "New Materials and Performance Limits for Thermoelectric Cooling," In *CRC Handbook on Thermoelectrics*, ed. D.M. Rowe, pp. 407-40, CRC Press, Boca Raton, FL, 1995.

7. L.D. Hicks and M.S. Dresselhaus, "Effect of quantum-well structures on the thermoelectric figure of merit," *Phys. Rev. B.*, **47**, 12727 (1993).

8. R. Venkatasubramanian, E. Siivola, T. Colpitts, and B. O'Quinn, "Thin-film thermoelectric devices with high room-temperature figures of merit," *Nature* **413**, 597 (2001).

9. G.S. Nolas, J. Sharp, and H.J. Goldsmid. *Thermoelectrics: Basic Principles and New Materials Developments*. Springer, Berlin, 2001.

10. J. Yang and T. Caillat, "Thermoelectric Materials for Space and Automotive Power Generation," *MRS Bulletin* **31**, 224 (2006)

11. C. Kittel. *Introduction to Solid State Physics.* John Wiley & Sons, Inc., New York, 1976.

12. N.F. Mott, "Electrons in disordered structures," *Adv. Phys.* 16 (1967).

13. M.G. Kanatzidis, "The Role of Solid-State Chemistry in the Discovery of New Thermoelectric Materials," In *Semiconductors and Semimetals* vol. 69, ed. T.M. Tritt, pp. 51-100, Academic Press, New York, 2000.

14. B.C. Sales, D. Mandrus, and R.K. Williams, "Filled Skutterudite Antimonides: A New Class of Thermoelectric Materials," *Science* **272**, 1325 (1996)

15. C. Uher, "Skutterudites: Prospective Novel Thermoelectrics, "In *Semiconductors and Semimetals* vol. 69, ed. T.M. Tritt, pp. 139-253, Academic Press, New York, 2001.

16. S.J. Poon, "Electronic and Thermoelectric Properties of Half-Heusler Alloys," In *Semiconductors and Semimetals* vol. 70, ed. T.M. Tritt, pp. 37-75, Academic Press, New York, 2001.

17. I. Terasaki, Y. Ishii, D. Tanaka, K. Takahata, and Y. Iguchi, "Thermoelectric Properties of $NaCo_{2-x}Cu_xO_4$ Improved by the Substitution of Cu for Co," *Jpn. J. Appl. Phys.* **40**, L65 (2001).

18. B.C. Sales, B.C. Chakoumakos, D. Mandrus, and J.W. Sharp, "Atomic Displacement Parameters and the Lattice Thermal Conductivity of Clathrate-like Thermoelectric Compounds," *J. Solid State Chem.* **146**, 528 (1999).

19. G.S. Nolas, G.A. Slack, and S.B. Schujman, "Semiconductor Clathrates: A Phonon Glass Electron Crystal Material with Potential for Thermoelectric Applications," In *Semiconductors and Semimetals* vol. 69, ed. T.M. Tritt, pp. 255-300, Academic Press, New York, 2000.

20. T.M. Tritt and R.T. Littleton IV, "Thermoelectric Properties of the Transition Metal Pentatellurides: Potential Low-Temperature Thermoelectric Materials," In *Semiconductors and Semimetals* vol. 70, ed. T.M. Tritt, pp179-206, Academic Press, New York, 2001.

21. S. Iijima, "Helical Microtubules of Graphitic Carbon," *Nature* **354**, 56 (1991).

22. E.S. Rittner, "On the Theory of the Peltier Heat Pump," *J. Appl. Phys.* **30**, 702 (1959).

23. L.D. Hicks and M.S. Dresselhaus, "Thermoelectric figure of merit of a one-dimensional conductor," *Phys. Rev. B.,* **47**, 16631 (1993).

24. L.D. Hicks, T.C. Harman, X. Sun, and M.S. Dresselhaus, "Experimental study of the effect of quantum-well structures on the thermoelectric figure of merit," *Phys. Rev. B.,* **53**, R10493 (1996).

25. H. Beyer, J. Nurnus, H. Böttner, A. Lambrecht, T. Roch, and G. Bauer, "PbTe based superlattice structures with high thermoelectric efficiency," *Appl. Phys. Lett.* **80**, 1216 (2002).

26. T. Koga, S.B. Cronin, M.S. Dresselhaus, J.L. Liu, and K.L. Wang, "Experimental proof-of-principle investigation of enhanced $Z_{3D}T$ in (001) oriented Si/Ge superlattices," *Appl. Phys. Lett.* **77**, 1490 (2000).

27. J.P. Heremans, C.M. Thrush, D.T. Morelli, and M.C. Wu, "Thermoelectric Power of Bismuth Nanocomposites," *Phys. Rev. Lett.* **88**, 216801 (2002).

28. T.C. Harman, P.J. Taylor, M.P. Walsh, and B.E. LaForge, "Quantum Dot Superlattice Thermoelectric Materials and Devices," *Science* **297**, 2229 (2002).

29. K.F. Hsu, S. Loo, F. Guo, W. Chen, J.S. Dyck, C. Uher, T. Hogan, E.K. Polychroniadis, M.G. Kanatzidis, "Cubic $AgPb_mSbTe_{2+m}$ Bulk Thermoelectric Materials and High Figure of Merit," *Science* **303**, 818 (2004).

30. X. Shi, L. Chen, J. Yang, and G.P. Meisner, "Enhanced thermoelectric figure of merit of $CoSb_3$ via large-defect scattering," *Appl. Phys. Lett.* **84**, 2301 (2004).
P.W. Lange, "Ein Vergleich zwischen Bi_2Te_3 und Bi_2Te_3S," *Naturwissen.* **27**, 133 (1939).

32. J.R. Drabble, "The Physical Properties of Single Crystal Bismuth Telluride," In *Progress in Semiconductors* vol. 7, ed. A.F. Gibson, pp. 45-98, J. Wiley, New York, 1956.

33. M.H. Francombe, "Structure-cell data and expansion coefficients of bismuth telluride," *Brit. J. Appl. Phys.* **9**, 415 (1958)

34. J.R. Drabble and C.H.L. Goodman, "Chemical Bonding in Bismuth Telluride," *J. Phys. Chem. Solids* **5**, 142 (1958).

35. M.R. Thuler, R.L. Benbow, and Z. Hurych, "Synchrotron-Radiation Photoemission Study of the V-VI Layered Compounds Bi_2Te_3, Bi_2Se_3, Sb_2Te_3, and Sb_2Te_2Se," *Chem. Phys.* **71**, 265 (1982).

36. H. Scherrer and S. Scherrer, "Bismuth Telluride, Antimony Telluride, and Their Solid Solutions," In *CRC Handbook on Thermoelectrics*, ed. D.M. Rowe, pp. 211-37, CRC Press, Boca Raton, FL, 1995.

37. T.M. Tritt and M.A. Subramanian, "Thermoelectric Material, Phenomena, and Applications: A Bird's Eye View," *MRS Bulletin* **31**, 188 (2006).

38. S. Katsuki, "The Band Structure of Bismuth Telluride," *J. Phys. Soc. Japan* **26**, 58 (1969).

39. D.L. Greenaway and G. Harbeke, "Band Structure of Bismuth Telluride, Bismuth Selenide, and Their Respective Alloys," *J. Phys. Chem. Solids* **26**, 1585 (1965).

40. J.R. Drabble and R. Wolfe, "Anisotropic Galvanometric Effects in Semiconductors," *Proc. Phys. Soc. B* **69**, 1101 (1956).

41. J.R. Drabble, R.D. Groves, and R. Wolfe, "Galvanometric Effects in n-Type Bismuth Telluride," *Proc. Phys. Soc.* **71**, 430 (1958).

42. I.G. Ausin, "Infra-red Faraday Rotation and Free Carrier Absorption in Bi_2Te_3," *Proc. Phys. Soc.* **76**, 169 (1960).

43. D. Shoenberg, "The de Haas-van Alphen Effect," In *Progress in Low Temperature Physics* vol. 2, ed. C.J. Gorter, pp. 226-265, North-Holland Publishing Company, Amsterdam, 1957.

44. R.B. Mallinson, J.A. Rayne, and R.W. Ure, Jr., "de Haas-van Alphen Effect in n-Type Bi_2Te_3," *Phys. Letters* **19**, 545 (1965).

45. L.R. Testardi, P.J. Stiles, and E. Burstein, "de Haas-van Alphen and High Field Galvanomagnetic Studies of the Bi_2Te_3 Valence Band Structure," *Solid State Commun.* **1**, 28 (1963).

46. R.B. Mallinson, J.A. Rayne, and R.W. Ure, Jr., "de Haas-van Alphen Effect in n-Type Bi_2Te_3," *Phys. Rev.* **175**, 1049 (1968).

47. H.J. Goldsmid, "Recent Studies of Bismuth Telluride and Its Alloys," *J. Appl. Phys.* **32**, 2198 (1961).

48. P.M. Lee and L. Pincherle, "The Electronic Band Structure of Bismuth Telluride," *Proc. Phys. Soc.* **81**, 461 (1963).

49. L.M. Roth and P.N. Argyres, "Magnetic Quantum Effects," In *Semiconductors and Semimetals* vol. 1, ed. R.K. Willardson and A.C. Beer, pp. 159-202, Academic Press, New York, 1966.

50. H. Köhler, "Non-Parabolicity of the Highest Valence Band of Bi_2Te_3 from Shubnikov-de Haas Effect," *Phys. Stat. Sol. (b)* **74**, 591 (1976).

51. H. Köhler, "Non-Parabolic *E(k)* Relation of the Lowest Conduction Band in Bi_2Te_3," *Phys. Stat. Sol. (b)* **73**, 95 (1976).

52. G.A. Thomas, D.H. Rapkine, R.B. Van Dover, L.F. Mattheiss, W.A. Sunder, L.F. Schneemeyer, and J.V. Waszczak, "Large electronic-density increase on cooling a layered material: Doped Bi_2Te_3," *Phys. Rev. B* **46**, 1553 (1992).

53. S.K. Mishra, S. Satpathy, and O. Jepsen, "Electronic structure and thermoelectric properties of bismuth telluride and bismuth selenide," *J. Phys.: Condens. Matter* **9**, 461 (1997).

54. H.J. Goldsmid, "The Electrical Conductivity and Thermoelectric Power of Bismuth Telluride," *Proc. Phys. Soc.* **71**, 633 (1958).

55. C.B. Satterthwaite and R.W. Ure, Jr., "Electrical and Thermal Properties of Bi_2Te_3," *Phys. Rev.* **108**, 1164 (1957).

56. J.P. Fleurial, L. Gailliard, R. Triboulet, H. Scherrer, and S. Scherrer, "Thermal Properties of High Quality Single Crystals of Bismuth Telluride—Part I: Experimental Characterization," *J. Phys. Chem. Solids* **49**, 1237 (1988).

57. H.J. Goldsmid, "The Thermal Conductivity of Bismuth Telluride," *Proc. Phys. Soc. B* **69**, 203 (1956).

58. H.J. Goldsmid, "Heat Conduction in Bismuth Telluride," *Proc. Phys. Soc.* **72**, 17 (1958).

59. H.M. Rosenberg. *The Solid State*, Oxford University Press, New York, 1978.

60. D.J. Griffiths. *Introduction to Quantum Mechanics*, Prentice Hall, Upper Saddle River, 1995.

61. A.L. Pope, R.T. Littleton IV, and T.M. Tritt, "Apparatus for the rapid measurement of electrical transport properties for both "needle-like" and bulk materials," *Rev. Sci. Instr.* **72**, 3129 (2001).

62. N.D. Lowhorn, "Effect of Rare-Earth Doping on the Thermoelectric and Electrical Transport Properties of the Transition Metal Pentatelluride $HfTe_5$," Ph.D. Dissertation, Clemson University (2005).

63. C. Uher, "Thermal Conductivity of Metals," In *Thermal Conductivity: Theory, Properties, and Applications*, ed. T.M. Tritt, pp 21-91, Kluwer Academic / Plenum Publishers, New York, 2004.

64. J. Yang, "Theory of Thermal Conductivity," In *Thermal Conductivity: Theory, Properties, and Applications*, ed. T.M. Tritt, pp 1-20, Kluwer Academic / Plenum Publishers, New York, 2004.

65. A.L. Pope, B. Zawilski, and T.M. Tritt, "Description of removable sample mount apparatus for rapid thermal conductivity measurements," *Cryogenics* **41**, 725 (2001).

66. http://www.netzsch-thermal-analysis.com/en/products/detail/pid,26,t,2.html

67. W.J. Parker, R.J. Jenkins, C.P. Butler, and G.L. Abbott, "Flash Method of Determining Thermal Diffusivity, Heat Capacity, and Thermal Conductivity," *J. Appl. Phys.* **32**, 1679 (1961).

68. H.J. Goldsmid, "Bismuth Telluride," in *Materials Used in Semiconductor Devices*, ed. C.A. Hogarth, pp 165-197, John Wiley& Sons Ltd, New York, 1965.

69. T.C. Harman, B. Paris, S.E. Miller, and H.L. Goering, "Preparation and Some Physical Properties of Bi_2Te_3, Sb_2Te_3, and As_2Te_3," *J. Phys. Chem. Solids* **2**, 181 (1957).

70. L. Ainsworth, "Single Crystal Bismuth Telluride," *Proc. Phys. Soc. B* **69**, 606 (1956).

71. J. Black, E.M. Conwell, L. Seigle, and C.W. Spencer, "Electrical and Optical Properties of some $M_2^{V\text{-}B}N_3^{VI\text{-}B}$ Semiconductors," *J. Phys. Chem. Solids* **2**, 240 (1957).

72. G.J. Cosgrove, J.P. McHugh, and W.A. Tiller, "Effect of Freezing Conditions on the Thermoelectric Properties of $BiSbTe_3$ Crystals," *J. Appl. Phys.* **32**, 621 (1961).

73. Duan X. and Lieber C.M., "General Synthesis of Compound Semiconducting Nanowires," *Adv. Mater.* **12**, 198 (2000).

74. N. Gothard, M. Craps, A.M. Rao, and T.M. Tritt, "Thermoelectric Properties of Nanostructures Grown from Bi_2Te_3," *Proc. International Conference on Thermoelectrics*, IEEE Catalog 05TH8854C, Piscataway, NJ (2005).

75. J. Reppert, R. Rao, M. Skove, J. He, M. Craps, T. Tritt, and A.M. Rao, "Laser-assisted synthesis and optical properties of bismuth nanorods," *Chem. Phys. Lett.* **442**, 334 (2007).

76. R. Andrews, D. Jacques, A.M. Rao, F. Derbyshire, D. Qian, X. Fan, E.C. Dickey, and J. Chen, "Continuous Production of Aligned Carbon Nanotubes: A Step Closer to Commercial Realization," *Chem. Phys. Lett.* **303**, 467 (1999).

77. B. Sadanadan, T. Savage, S. Bhattacharya, T. Tritt, A. Cassell, M. Meyyappan, Z.R. Dai, Z.L. Wang, R. Zidan, and A.M. Rao, "Synthesis and Thermoelectric Power of Nitrogen-Doped Carbon Nanotubes," *J. Nanosci. Nanotech.* **3**, 99 (2003)

78. N. Gothard, C. Daraio, J. Gaillard, R. Zidan, S. Jin, and A.M. Rao, "Controlled Growth of Y-Junction Nanotubes using Ti-doped Vapor Catalyst," *Nano. Lett.* **4**, 213 (2004).

79. B. Zhang, J. He, and T.M. Tritt, "Size-selective high-yield growth of lead telluride (PbTe) nanocrystals using a chemical vapor deposition technique," *Appl. Phys. Lett.* **88**, 043119 (2006).

80. Marlow Industries, Inc., 10451 Vista Park Rd., Dallas, TX 75238

81. N. Gothard, B. Zhang, J. He, and T.M. Tritt, "CVD Growth of Nanostructures from Bi_2Te_3," *Mater. Res. Soc. Symp. Proc.* 886 (2005).

82. H. Okamoto and L.E. Tanner, In *Binary Alloy Phase Diagrams*, ed. T.B. Massalski, pp. 800-801, American Society for Metals, Metals Park, OH, 1986.

83. S.H. Yu, J. Yang, Y.S. Wu, Z.H. Han, J. Lu, Y. Wie, and Y.T. Qian, "A new low temperature one-step route to metal chalcogenide semiconductors: PbE, Bi_2E_3 (E = S, Se, Te)," *J. Mater. Chem.* **8**, 1949 (1998).

84. X.B. Zhao, X.H. Ji, Y.H. Yang, G.S. Cao, and J.P. Tu, "Hydrothermal synthesis and microstructure investigation of nanostructured bismuth telluride powder," *Appl. Phys. A* **80**, 1567 (2005).

85. X. Ji, B. Zhang, T.M. Tritt, J.W. Kolis, and A. Kumbhar, "Solution-Chemical Syntheses of Nano-Structured Bi_2Te_3 and PbTe Thermoelectric Materials," *J. Electron. Mater.* **36**, 721 (2007).

86. Thermal Technology, 1911 Airport Blvd., Santa Rosa, CA 95403.

87. Poco Graphite, Inc., 300 Old Greenwood Rd., Decatur, TX 76234

88. "Properties and Characteristics of Graphite For Industrial Applications," ed. R.G. Sheppard, D.M. Mathes, and D.J. Bray, Poco Graphite, Inc., Decatur, 2001.

89. http://www.edfagan.com/2006/?page_id=25

90. http://www.rembar.com/Molybdenum.htm

91. J.W. Orton and M.J. Powell, "The Hall Effect in polycrystalline and powdered semiconductors," *Rep. Prog. Phys.* **43**, 1263 (1980).

92. N. Gothard, X. Ji, J. He, and T.M. Tritt, "Thermoelectric and Transport Properties of *n*-type Bi_2Te_3 Nanocomposites," *J. Appl. Phys.* **103**, 054314 (2008).

93. G.E. Smith and R. Wolfe, "Thermoelectric Properties of Bismuth-Antimony Alloys," *J. Appl. Phys.* **33**, 841 (1962).

94. Ted Pella, Inc., P.O. Box 492447, Redding, CA 96049.

95. "Electrical Conductivity of Materials," *Release Draft R8418 Rev. 2*, Eddy Current Technology, 201A Horace Ave., Virginia Beach, VA 23462.

96. B.A. Cook, J.L Harringa, and S. Loughin, "Fullerite additions as a phonon scattering mechanism in p-type Si-20 at. % Ge," *Mat. Sci. Eng.* **B41**, 280 (1996).

97. N. Gothard, J.E. Spowart, and T.M. Tritt, "Nanocomposites of Bismuth Telluride and C_{60}," MS&T (2008).

98. H.W. Kroto, A.W. Allaf, and S.P. Balm, "C_{60}: Buckminsterfullerene," *Chem. Rev.* **91**, 1213 (1991).